(2)

AD_____

ASSESSMENT AND COMPUTERIZED MODELING OF THE ENVIRONMENTAL DEPOSITION OF MILITARY SMOKES

CHARACTERIZATION OF THE ATMOSPHERIC BOUNDARY LAYER IN COMPLEX TERRAIN AND RESULTS FROM THE AMADEUS SMOKE DISPERSION EXPERIMENTS

prepared by

D. F. Brown and W. E. Dunn
Department of Mechanical and Industrial Engineering
University of Illinois at Urbana-Champaign
Urbana, IL 61801
217-333-3832

December, 1991

Supported by

U. S. ARMY MEDICAL RESEARCH AND DEVELOPMENT COMMAND
Fort Detrick, Frederick, MD 21702-5012

Contract No. 90PP0819

Contracting Officer's Representative: Major John Young
Health Effects Research Division
U. S. ARMY BIOMEDICAL RESEARCH AND DEVELOPMENT LABORATORY
Fort Detrick, Frederick, MD 21702-5010

NOTICE

Disclaimer

The findings in this report are not to be construed as an official Department of the Army position unless so designated by other authorized documents.

Disposition

Destroy this report when it is no longer needed. Do not return it to the originator.

Unclassified

SECURITY CLASSIFICATION OF THIS PAGE

REPORT DOCUMENTATION PAGE

Form Approved OMB No. 0704-0188

1a. REPORT SECURITY CLASSIFICATION: Unclassified	1b. RESTRICTIVE MARKINGS
2a. SECURITY CLASSIFICATION AUTHORITY	3. DISTRIBUTION / AVAILABILITY OF REPORT: Approved for public release; distribution unlimited
2b. DECLASSIFICATION / DOWNGRADING SCHEDULE	
4. PERFORMING ORGANIZATION REPORT NUMBER(S)	5. MONITORING ORGANIZATION REPORT NUMBER(S)
6a. NAME OF PERFORMING ORGANIZATION: Argonne National Laboratory; 6b. OFFICE SYMBOL (If applicable)	7a. NAME OF MONITORING ORGANIZATION
6c. ADDRESS (City, State, and ZIP Code): 9700 South Cass Avenue, Argonne, IL 60439	7b. ADDRESS (City, State, and ZIP Code)
8a. NAME OF FUNDING / SPONSORING ORGANIZATION: U.S. Army Medical Research and Development Command; 8b. OFFICE SYMBOL (If applicable)	9. PROCUREMENT INSTRUMENT IDENTIFICATION NUMBER: 90PP0819
8c. ADDRESS (City, State, and ZIP Code): Fort Detrick, Frederick, Maryland 21702-5012	10. SOURCE OF FUNDING NUMBERS: PROGRAM ELEMENT NO. 62720A; PROJECT NO. 3E1-62720A835; TASK NO. CA; WORK UNIT ACCESSION NO. 291

11. TITLE (Include Security Classification)

(U) Assessment and Computerized Modeling of the Environmental Deposition of Military Smokes

12. PERSONAL AUTHOR(S)

D. F. Brown, W. E. Dunn

13a. TYPE OF REPORT	13b. TIME COVERED	14. DATE OF REPORT (Year, Month, Day)	15. PAGE COUNT
Final	FROM 7/1/90 TO 12/31/91	December 1991	172

16. SUPPLEMENTARY NOTATION Subtitle: Characterization of the Atmospheric Boundary Layer in Complex Terrain and Results from the AMADEUS Smoke Dispersion Experiments

17. COSATI CODES		
FIELD	GROUP	SUB-GROUP
04	01	
07	03	

18. SUBJECT TERMS (Continue on reverse if necessary and identify by block number)

RA 3, smoke, screening smoke, obscuring smoke, hexachloroethane, gas chromatography

19. ABSTRACT (Continue on reverse if necessary and identify by block number)

This report summarizes our analysis of the AMADEUS meteorological data Preliminary analysis (also given in Brown et al. 1990) of these data for each of the smoke-release periods include: (i) computation of averages of the surface-station and micrometeorological measurements (wind speed, wind direction, temperature), (ii) stability characterization by analysis of bulk Richardson numbers and wind direction standard deviations, (iii) examination of vertical heat and momentum fluxes from sonic-anemometer data, (iv) analysis of spectra computed using 1-Hz micrometeorological data and (v) determination of boundary-layer height from the instrumented balloon soundings. Additional results given in this report include: (i) an analysis of vertical wind profiles, (ii) comparisons of Meadowbrook data to similarity-based empirical relations and (iii) a comprehensive analysis of the nocturnal down-slope flows.

The results show that the meteorological data are consistent, both internally and with other studies of the atmospheric boundary layer. The daytime convective conditions reveal a high degree of coherency, whereas the nighttime stable conditions are more spatially heterogeneous and less coherent. Analysis of surface-station data has shown that the characteristics of the nocturnal downslope flows in the Meadowbrook valleys are influenced by a combination of local cooling, local surface conditions and mesoscale drainage flows external to the Meadowbrook system. These data appear to offer significant potential for improving the state of dispersion modeling in this important area.

20. DISTRIBUTION/AVAILABILITY OF ABSTRACT	21. ABSTRACT SECURITY CLASSIFICATION	
☐ UNCLASSIFIED/UNLIMITED ☒ SAME AS RPT. ☐ DTIC USERS	Unclassified	
22a. NAME OF RESPONSIBLE INDIVIDUAL: Mary Frances Bostian	22b. TELEPHONE (Include Area Code): 301-663-7325	22c. OFFICE SYMBOL: SGRD-RMI-S

DD FORM 1473, JUN 86 *Previous editions are obsolete.*

SECURITY CLASSIFICATION OF THIS PAGE

UN

FOREWORD

Opinions, interpretations, conclusions and recommendations are those of the author and are not necessarily endorsed by the U.S. Army.

AJP Where copyrighted material is quoted, permission has been obtained to use such material.

_____Where material from documents designated for limited distribution is quoted, permission has been obtained to use the material.

AJP Citations of commercial organizations and trade names in this report do not constitute an official Department of the Army endorsement or approval of the products or services of these organizations.

_____In conducting research using animals, the investigator(s) adhered to the "Guide for the Care and Use of Laboratory Animals," prepared by the Committee on Care and Use of Laboratory Animals of the Institute of Laboratory Animal Resources, National Research Council (NIH Publication No. 86-23, Revised 1985).

_____For the protection of human subjects, the investigator(s) have adhered to policies of applicable Federal Law 45CFR46.

A. J. Palicia Jr 12/31/91

PI Signature Date

EXECUTIVE SUMMARY

In the Fall of 1987, a team of researchers from the University of Illinois and Argonne National Laboratory undertook a series of smoke dispersion trials at a complex terrain site in Northern California as part of a larger program to develop an improved model for smoke dispersion. These field trials were carried out in cooperation with researchers from several organizations working under contract to the US Army Atmospheric Sciences Laboratory at White Sands Missile Range in New Mexico. These field studies are known as the AMADEUS Dispersion Experiments.

The following meteorological instrumentation was employed to assess atmospheric conditions during each of the smoke and tracer release periods:

1. An array of 14 surface stations (instrumented at a height of 10 m) was used to map the horizontal variation of the wind field over the site.

2. A micrometeorological tower was used to determine vertical profiles of wind and temperature to a 30-m height and to provide indirect measures of atmospheric stability through fluctuations in the wind velocity and temperature.

3. Two sonic anemometers were used to directly measure the vertical momentum and heat flux through the atmospheric boundary layer and thus provide additional data by which to characterize atmospheric stability.

4. Instrumented balloons were used to provide wind and temperature profiles to a height of several kilometers, allowing the thickness of the atmospheric boundary layer to be determined.

5. A mini-sodar, which employs reflected sound waves, was used to characterize the atmospheric boundary layer to a height of roughly 300 m.

This report summarizes our analysis of the AMADEUS meteorological data. Preliminary analysis (also given in Brown et al. 1990) of these data for each of the smoke-release periods include: (i) computation of averages of the surface-station and micrometeorological measurements (wind speed, wind direction, temperature), (ii) stability characterization by analysis of bulk Richardson numbers and wind direction standard deviations, (iii) examination of vertical heat and momentum fluxes from sonic-anemometer data, (iv) analysis of spectra computed using 1-hz micrometeorological data and (v) determination of boundary-layer height from the instrumented balloon soundings. Additional results given in this report include: (i) an analysis of vertical

wind profiles, (ii) comparisons of Meadowbrook data with similarity-based empirical relations and (iii) a comprehensive analysis of the nocturnal downslope flows.

The results show that the meteorological data are complete and internally consistent. The daytime convective conditions reveal a high degree of coherency, showing little variation in wind speed and temperature throughout the region. These results, however, show only limited agreement with empirical models based on similarity theory.

In general, the stable boundary layer is generally less well understood than is the convective boundary layer, especially in a complex terrain setting where conditions are very site specific. Our data for the nighttime stable conditions follow this same trend, exhibiting little coherency in temperature and stability across the site. The wind field, however, is almost always characterized by well-established downslope flows. Analysis of surface-station data has shown that the characteristics of the nocturnal downslope flows in the Meadowbrook valleys are influenced by a combination of local cooling, local surface conditions and mesoscale drainage flows external to the Meadowbrook system. These data appear to offer significant potential for im proving the state of dispersion modeling in this important area.

ACKNOWLEDGEMENT

We wish to acknowledge the contribution of the many organizations which participated in the AMADEUS dispersion experiments. The success of this study is a tribute to the professionalism of all those who were involved.

The contribution of two of our colleagues at the University of Illinois is especially noteworthy. Dr. James C. Liljegren and Dr. George E. DeVault were essential members of our field team and contributed much to the analysis and understanding of the data. Also significant is the effort of Mr. Daniel Maloney who assisted in reducing the surface-station data.

We also wish to thank Maj. John Young, Maj. David Parmer and Dr. Howard Bausum of the U. S. Army Biomedical Research and Development Laboratory for their important role in shaping the project. It is through their efforts that our involvement in the AMADEUS experiments was made possible. Moreover, their many helpful suggestions and insightful comments added enormously to the success of our effort.

TABLE OF CONTENTS

LIST OF FIGURES

LIST OF TABLES

NOMENCLATURE

Symbol	Meaning
c_p	Specific heat of air
d_i	Deviation used in computing σ_θ; lies in the interval (-180°, +180°)
E	Turbulent kinetic energy measured by sonic anemometer
f	Nondimensional frequency = nz/u
g	Acceleration of gravity
H	Heat flux
K_h	Eddy exchange coefficient for heat
K_m	Eddy exchange coefficient for momentum
L	Obukov length scale
l_ε	Kolmogorov microscale
mod	Modulo function; a mod b returns the remainder of a divided by b
N	Number of valid individual measurements in an average
N	Brunt-Väisälä frequency
n	Frequency; also used as counting index in computing averages
P	Atmospheric pressure
Q_o	Vertical-velocity/temperature correlation measured by sonic anemometer
R	Ideal gas constant for air
Ri	Gradient Richardson number
Ri_b	Bulk Richardson number
Ri_f	Flux Richardson number
S	Scalar-mean wind speed
s_i	An individual wind speed measurement which may be either a 1-s value or 1-min average
$S_{uu}(n)$	Single-sided power spectrum for u-velocity fluctuations
$S_{vv}(n)$	Single-sided power spectrum for v-velocity fluctuations
$S_{ww}(n)$	Single-sided power spectrum for w-velocity fluctuations
T	Mean temperature; an "i" subscript denotes an individual measurement and may be either a 1-s value or 1-min average
T_{2m}	Mean temperature at a height of 2 m
T_{10m}	Mean temperature at a height of 10 m
ΔT	Temperature difference; for example, $T_{10m} - T_{2m}$
$\forall T$	Temperature difference between an upper-valley station and Station A102

Symbol	Meaning
t	Time
U	Vector-mean wind speed; also the scalar mean of u
U_1	Scalar mean of u_1
U_2	Scalar mean of u_2
U_3	Scalar mean of u_3
u	Component of wind velocity in the direction of the mean wind; an "i" subscript denotes an individual measurement and may be either a 1-s value or 1-min average
u_1	First Cartesian (horizontal) component of the wind velocity; an "i" subscript denotes an individual measurement and may be either a 1-s value or 1-min average
u_2	Second Cartesian (horizontal) component of the wind velocity; an "i" subscript denotes an individual measurement and may be either a 1-s value or 1-min average
u_3	Third Cartesian (vertical) component of the wind velocity; an "i" subscript denotes an individual measurement and may be either a 1-s value or 1-min average
u_*	Friction velocity
V	Scalar mean of v; zero by definition
v	Component of wind velocity normal to the direction of the mean wind; an "i" subscript denotes an individual measurement and may be either a 1-s value or 1-min average
W	Scalar mean of w
w	Vertical component of wind velocity; an "i" subscript denotes an individual measurement and may be either a 1-s value or 1-min average
w_*	Convective velocity scale
z	Height above ground
z_i	Height of boundary layer; inversion height
z_o	Roughness height
z_u	Height at which wind speed or velocity is measured
z_{T1}, z_{T2}	Heights at which temperature is measured
ε	Turbulent dissipation rate
κ	von Kármán's constant = 0.4
Λ	Local Obukhov length
ϕ	Inclination of wind velocity
ρ	Density of air

Symbol	Meaning
σ_u	Standard deviation of u
σ_v	Standard deviation of v
σ_w	Standard deviation of w
σ_T	Standard deviation of T
σ_θ	Standard deviation of horizontal wind direction; an "i" subscript denotes an individual measurement and may be either a 1-s value or 1-min average
$\sigma_{\theta,1\ min}$	Standard deviation of horizontal wind direction computed from 1-min averages of θ
θ	Vector-mean wind direction; an "i" subscript denotes an individual measurement and may be either a 1-s value or 1-min average
θ	Potential temperature
θ_*	Potential temperature scale
τ	Shear stress
ν	Kinematic viscosity
ζ	Nondimensional height z/L

1. INTRODUCTION

1.1 The AMADEUS Smoke Dispersion Study

In order to more fully understand the meteorology and aerosol-dispersion characteristics of complex terrain environments and to obtain data for the use of dispersion model validation, a team of researchers from the University of Illinois (UIUC) and Argonne National Laboratory (ANL) undertook a series of smoke dispersion trials at a complex terrain site (the Meadowbrook Site) in Northern California. These experiments, known as the AMADEUS Dispersion Experiments, took place from late September to early October in 1987. This work was carried out under the sponsorship of the US Army Biomedical Research and Development Laboratory (USABRDL). These field trials were performed in cooperation with researchers from several organizations working under contract to the US Army Atmospheric Sciences Laboratory (ASL) located at White Sands Missile Range, New Mexico. The dispersion trials discussed herein represent only a small fraction of the total ASL effort, which had as its major objective the validation and improvement of certain wind field models developed by ASL. This larger effort, known as Project WIND, involved four major field studies with the dispersion trials of interest here being carried out during the fourth such study, referred to Phase IV.

The dispersion studies conducted at the Meadowbrook site produced a large amount of valuable data on atmospheric flow and dispersion in complex terrain. Two sets of dispersion experiments were actually conducted. In addition to the 12 fog-oil smoke trials of primary interest here, 11 SF_6-tracer releases were also made. The tracer gas was sampled over a larger but more sparse grid than was the smoke. Also, the tracer gas was collected using bag samplers, which give 5-min average values. These gas collectors were placed on the ground giving an effective sampling height of only a few centimeters. In contrast, the fog-oil smoke was collected using aspirated filter samplers operated over the full duration of the trial and was simultaneously sampled every second using an optical device. The smoke concentrations were measured at heights of 2 and 8 m using the filter samplers and at a single height of 2 m using the optical device. Depending on the trial, 30 to 40 locations were used for sampling the smoke. In addition to the average and real-time smoke dispersion data, aerial photographs of the smoke plume were taken for all but the nighttime smoke releases.

1.2 Overview

This report is presented in 3 major sections. In Chapter 2, the current state-of-the-art theory of atmospheric boundary-layer structure is introduced as a foundation for the discussion of the Meadowbrook results. In Chapter 3 the Meadowbrook atmospheric data are discussed in detail, and reduced data encompassing the times of the 12 fog-oil dispersion tests are presented. Concluding Chapter 3 is a discussion of the applicability of conventional flat-terrain analysis to our complex-terrain data. In Chapter 4 the nocturnal drainage flows which occurred at Meadowbrook are analyzed in detail, and characteristics influencing their development and behavior are discussed.

2. ATMOSPHERIC FLOW

Over the past 40 years, a large effort has been undertaken to develop the fundamental knowledge which is necessary in order to accurately understand and model the Earth's planetary boundary layer. In general, planetary boundary layers have a few aspects which delineate them from other fluid boundary layers commonly studied in engineering disciplines. The Earth's atmosphere has no horizontal boundaries, necessitating the development of appropriate horizontal length scales. Also, the atmosphere is characterized by local and regional thermal gradients which act to vertically separate it into several distinct regions. The energy which most influences the turbulence in the lower regions of atmosphere is obtained from surface heating and cooling. Large scale atmospheric flow, however, is driven by horizontal pressure forces created by global scale differential heating and is greatly influenced by Coriolis acceleration imparted from the Earth's rotation.

In most of the theoretical and observational analysis of the atmospheric boundary layer, its characteristics have been assumed to be decoupled from the rest of the atmosphere, and rotational effects have been neglected. In doing so, its statistics are dependent only on surface heat and momentum fluxes as well as boundary-layer height. This has proven to be a good strategy and has led to the development of useful similarity theories and turbulence parameterizations, many of which are obtainable from surface measurements.

Much of the current research into atmospheric-boundary-layer physics has been concentrated in determining the effects induced by complex (non-uniform) terrain. Terrain-generated buoyancy forces strongly influence the boundary-layer flows, whose characteristics may be very site-specific in nature. These added complexities make the interpretation of data and the generalization of results much more difficult.

2.1 Atmospheric Stability and Turbulence Classification

2.1.1 Thermal Stability and Boundary-layer Structure

The thermal stability of the atmosphere greatly influences its turbulence characteristics, the knowledge of which are important for accurate dispersion modeling. Thermal stability of the atmospheric boundary layer is directly dependent on its vertical temperature profile. To account for the reduction of pressure through the atmosphere, the potential temperature is often used to assess buoyancy, and hence stability. The potential temperature is defined as the temperature that a parcel of air will attain if it were isentropically compressed or expanded to 1000 mb. For a given temperature

and pressure, the potential temperature θ may by found by applying the simple thermodynamic relation

$$\theta = T\left(\frac{P_{oo}}{P}\right)^{R/c_p}, \qquad (2.1)$$

where P_{oo} is the standard reference pressure of 1000 mb, R is the ideal gas constant, c_p is the specific heat and both T and θ are absolute temperatures.

During the daytime, the lower atmosphere is usually characterized by an unstable boundary layer such as that shown in Figure 2.1(a). The formation and maintenance of the unstable boundary layer is driven by solar insolation which warms the ground and, through the agitation of mechanical turbulence, transfers this heat to the lowest layer of the atmosphere. Through this process, incident heat energy is continually transferred to the surface layer which, due to its instability at lower levels, forms large convective cells and a region of vigorous mixing. The height of these cells is determined by the lowest inversion in the potential temperature profile, for as the air crosses this inversion, it will no longer be warmer than its surroundings and rising will cease. Shortly after sunrise, this inversion will move upward from ground level and may reach a height of a kilometer or more by midday. As the inversion height increases, air is drawn into the boundary layer from a free-shear region known as the entrainment layer in order to conserve mass. During late afternoon, this inversion height quickly falls as the incoming solar radiation diminishes. About an hour before sunset, the ground will begin to radiate more heat to space than it receives from the sun, and ground level cooling will commence.

The cooling associated with long-wavelength radiation flux creates a completely different boundary-layer structure, which is not as clearly defined as that of the unstable boundary layer. The nocturnal boundary layer, which is much thinner than its unstable counterpart, is idealized in Figure 2.1(b). The lowest few kilometers of the atmosphere will usually experience radiational cooling, but cooling is greatest at the surface, strongly stratifying the air at the lowest levels. Shear-induced turbulence will act to vertically spread the cooling throughout the surface layer, while the stably stratified air will act to suppress turbulence created by ground level shear. The rapid dissipation of turbulent energy by the work done against gravity greatly confines the vertical size of eddies and limits turbulent exchange. Above the turbulent shear layer, the boundary layer is often only intermittently turbulent and may contain inertial gravity waves. In an average night, the potential temperature profile will have a strong positive slope at ground level, changing to a weaker positive slope at the top of the shear

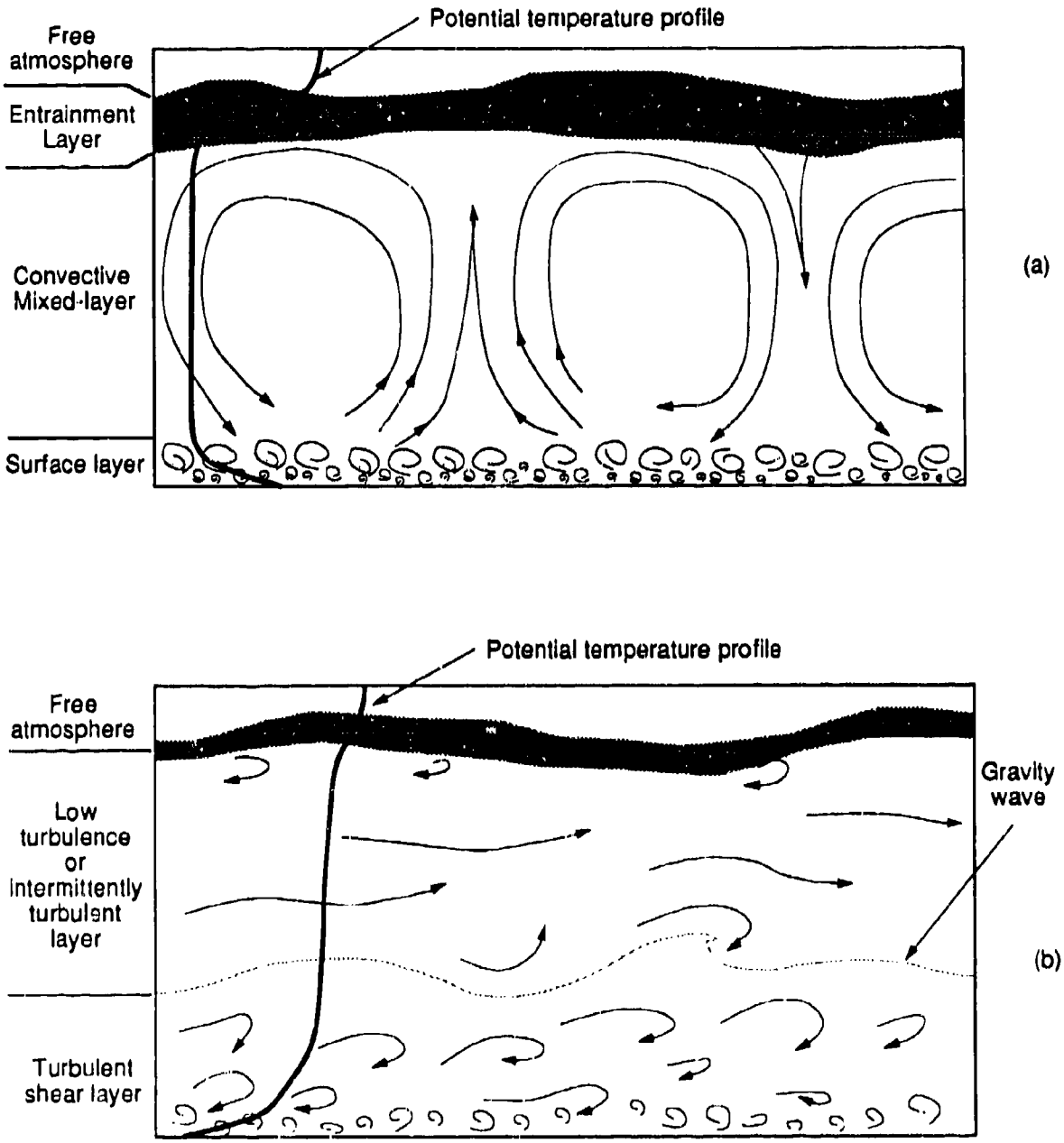

Figure 2.1 Idealized structure for (a) the unstable daytime boundary layer and (b) the stable nighttime boundary layer. Potential temperature profiles and important regions are shown. Figures adapted from Wyngaard (1985).

layer. This slope may diminish entirely at higher levels (>2000 m). Wind direction will often change considerably with height, and low-level jets are often present, creating a problem in conceptually defining the boundary layer and greatly complicating the analysis and interpretation of meteorological data.

In overcast conditions or when strong winds are present, the potential temperature profile is often roughly constant throughout the lower levels of the atmosphere. This will create an atmospheric boundary layer which is considered neutrally stratified. Since the atmosphere is not convective or stably stratified during these times, the shear-induced turbulence at the surface may extend throughout the entire boundary layer. Since buoyancy may be neglected, this situation greatly simplifies analysis and has been the basis for much theoretical atmospheric research.

2.1.2 Richardson Number

One of the most prevalent non-dimensional stability and turbulence classification parameters is the Richardson number, of which several forms have been developed. The gradient Richardson number is defined in terms of the vertical gradients of density and horizontal velocity as

$$Ri = \frac{g\,(\partial\rho/\partial z)}{\rho\,(\partial U/\partial z)^2}\,, \qquad (2.2)$$

where g is the acceleration of gravity, ρ is the density, U is the flow velocity and z is vertical position. (As discussed in Brunt, 1952, this is not the exact form first proposed by L. F. Richardson but was named in this honor). Richardson number relations employed in the atmospheric boundary layer, however, typically have the potential temperature gradient substituted for the density gradient. This substitution allows for convenient measurement of Richardson number but is thermodynamically imprecise, since there exists a distinction between adiabatic ($Ri(\theta) = 0$) and neutrally buoyant ($Ri(\rho) = 0$) stratification. However, the potential temperature based Ri does provide good empirical results in describing the atmospheric boundary layer, since "neutral" boundary layers (free of convection or thermal stratification) have been generally found to be adiabatic. The distinction between adiabatic and neutrally buoyant may become further clouded when moisture and condensation effects are considered. These subtle distinctions are beyond the scope of this report, and from this point only the potential-temperature Richardson number will be considered.

In his original analysis of buoyant fluid layers, Richardson first proposed that a positively buoyant fluid would become turbulent through natural convection if $Ri < 1$.

However, in the study of turbulent shear flows, the eddy exchange coefficients for heat and momentum (K_h and K_m, respectively) must be considered. Analysis of this problem with the gradient Richardson number and the eddy exchange coefficients leads to a critical Ri value of 0.25. (Miles, 1970). For Ri values above this limit, turbulence will be suppressed by buoyant stratification.

With the incorporation of the heat and momentum exchange coefficients, a flux Richardson number may be defined by

$$Ri_f = \frac{K_h}{K_m} Ri, \tag{2.3}$$

where substitution of the defined values for K_h and K_m, given by the following relations

$$\overline{u'w'} = -K_m\left(\frac{\partial U}{\partial z}\right) \tag{2.4}$$

$$\overline{w'T'} = -K_h\left(\frac{\partial \theta}{\partial z}\right), \tag{2.5}$$

leads to a relation between Ri_f and turbulent fluxes as

$$Ri_f = \frac{g\ \overline{w'T'}}{\theta\ \overline{u'w'}\left(\frac{\partial u}{\partial z}\right)}. \tag{2.6}$$

The flux Richardson number Ri_f is a ratio of the turbulence destruction rate by stable stratification to the turbulence-generation rate by shear, making it a measure of the relative importance of buoyancy in influencing turbulence behavior and boundary-layer dynamics. Large negative values of this parameter are indicative of unstable stratification and thus convective turbulence, whereas large positive values denote stable stratification which tends to suppress turbulent mixing. A flux Richardson number near zero indicates an absence of excess turbulence production or dissipation, implying neutrally buoyant stratification. As will be shown in Section 2.2.1, Ri_f is very similar to the Obukhov Length L.

An additional form of the Richardson number is the bulk Richardson number Ri_b. This parameter is based on the wind speed and change in temperature across a layer and is also strongly dependent on height. The gradients appearing in the gradient Richardson number are replaced by the corresponding finite differences ($\partial\theta/\partial z$ by $\Delta\theta/\Delta z$ and $\partial U/\partial z$ by $\Delta U/\Delta z$), and the potential temperature by that of the upper measuring location. These gradients are simplified by differencing the wind speed with respect to ground level (i.e. $u = 0$ at $z = 0$), while assuming θ_1 (usually measured at a

height of a few meters) is representative of temperature at ground level. Taking these assumptions into consideration, Ri_b is then given by

$$Ri_b = \frac{g\, z_2\, (\theta_2 - \theta_1)}{u_2^2\, \theta_2} \quad . \tag{2.7}$$

Since a wind speed measurement is required at only one location, this parameter is often favored over the gradient Richardson number for atmospheric studies. Besides the appeal of needing less on-site instrumentation, the ΔU term in the gradient Richardson number can be the source for large measurement errors, especially in the presence of light winds. Some researchers prefer to replace the height z_2 with the geometric mean of the heights which temperature are measured ($\sqrt{z_1 z_2}$). All Ri_b values given for the AMADEUS data were computed using Eq. 2.7, but care should be taken since certain empirical relations based on Ri_b call for the alternate height scale.

2.2 Similarity Theory and Scaling

2.2.1 Surface-layer Scaling Parameters

Although there were a number of valuable atmospheric field studies and experiments prior to the 1950's, the results that were obtained were not easily classified or comparable with those from other field studies. This situation was greatly improved when, in 1954, Monin and Obukhov published their similarity theories for the atmospheric surface layer. Beginning from the equations of fluid motion, they assumed all statistical properties to be invariant with time and direction and neglected viscous terms. Since their similarity relations pertained only to the surface layer, they also surmised that Coriolis and radiative effects could be excluded and that shear stress and heat flux are constant throughout the surface layer. With these restrictions, they deduced that turbulent structure could be evaluated with the knowledge of heat flux, friction velocity, buoyancy (g/T) and height. Within their new framework of surface-layer parameterizations, they recommended a vertical length scale z/L, a horizontal velocity scale u_* and a potential temperature scale θ_*. Subsequent field studies, most notably the Kansas Surface Layer Project of 1968, have demonstrated that many fundamental atmospheric statistics become generalized functions of the vertical scale z/L (hereafter referred to as ζ) when normalized by u_* and θ_*.

The friction velocity is related to the surface shear stress τ, which in turn is related to the cross correlation of the horizontal and vertical velocities.

$$u_* = \sqrt{\frac{\tau}{\rho}} = \sqrt{\overline{u'w'}} \qquad (2.8)$$

Analogously, the potential temperature scale is formed using the cross correlation of the vertical velocity and temperature, and is normalized by the friction velocity. These fluctuating vertical velocity and temperature components also define the heat flux at a given point in the atmosphere. These relations are

$$\theta_* = \frac{\overline{w'\theta_0'}}{u_*} \qquad (2.9)$$

and

$$H = \rho c_p \overline{w'\theta_0'} \qquad (2.10)$$

The Obukhov Length L is defined as the height where the energy contributions from surface generated shear and buoyancy production (or dissipation) are equivalent. In atmospheric boundary layer characterization, the dimensionless length scale $\zeta = z/L$ is usually preferred and is given by

$$\zeta = \frac{z}{L} = -\frac{g\, z\, \kappa\, \overline{w'\theta_0'}}{u_*^3\, \theta}. \qquad (2.11)$$

The turbulent flux terms $\overline{u'w'}\,\frac{\partial u}{\partial z}$ and $\overline{w'\theta'}\,\frac{g}{\theta}$, from which the Obukhov Length is derived, are essentially the same as those that appear in the flux Richardson number. The differences between Ri_f and ζ lie in that a near-surface logrithmic wind profile is assumed in the derivation of the Obukhov Length, allowing for the replacement of the the gradient $\frac{\partial u}{\partial z}$ by $u_*/\kappa z$. The negative sign is added to L so that z/L is in proper accordance with the Richardson number sign convention.

The assumptions that were imposed in the development of this similarity theory can be quite restrictive, but several field studies have demonstrated the applicability and usefulness of these parameters. The heat and momentum fluxes are not constant throughout the surface layer, but they have been shown to vary by only around 10% throughout this region. The assumption of homogeneous and stationary turbulence is usually valid in daytime convective conditions may easily be violated during stable conditions, or in inhomogeneous terrain. Also, as mentioned before, it has been assumed in the development of the Obukhov Length that a logarithmic wind profile exists at the surface. This also is valid in convective conditions, even in complex ter-

rain, but in stable conditions wind profiles may be seriously distorted in the presence of large roughness elements or hills. Regardless of surface characteristics, similarity theory may fail during periods of unsteady syncptic conditions of transitional meteorology.

2.2.2 Parameters Employed Outside the Surface Layer

Besides the Obukhov Length, another important length scale is the boundary-layer height z_i. During convective conditions, this is defined as the top of the well mixed layer and presents a practical upper limit for the vertical transport of pollutants. This limit evolves from a temperature inversion that forms during unstable conditions and presents a barrier that convective plumes usually will not penetrate.

In the convective boundary layer at heights above |L|, the wind field is dominated by convection instead of mechanical turbulence. The friction velocity, and hence Monin-Obukhov scaling, is not valid in this region since it lies above the influence of surface roughness elements. In order to cope with this problem, Deardorff (1970) introduced a mixed-layer scaling parameter w_* which incorporated the concept of a quasi-homogeneous layer in which the convective-eddy size is proportional to the boundary-layer height. Using the inversion height, heat flux, and surface temperature, he defined the convective velocity scale as

$$w_* = \left(\frac{g\, H\, z_i}{c_p\, \rho\, T_o} \right)^{1/3} = -u_* \left(\frac{z_i}{\kappa\, L} \right)^{1/3} \tag{2.12}$$

and since u_* is no longer a valid scaling parameter in this region, a convective temperature scale is defined using w_* instead of u_*.

$$T_* = \frac{\overline{w'\theta_o'}}{w_*} \tag{2.13}$$

2.2.3 Stable Boundary Layer Characterization

Unlike the unstable convective boundary layer, the stable boundary layer lacks the clear concept of vertical structure and boundary layer height. As a result, the turbulent structure lacks a parameterization like that found in the mixed-layer scaling for convective conditions. Since vertical motion is suppressed by the thermal stratification, large eddies, such as those in the convective boundary layer, do not extend across the boundary layer. This creates the need for an appropriate *local* length scale for turbulent exchange. In addition to these problems, turbulent energy varies strongly

with height and time, and the determination of its structure can be hindered by the coexistence of turbulence with anomalies such as gravity waves and Kelvin-Helmholz billows. Although no generally accepted parameterization for the turbulence structure exists, local scaling parameters have been suggested by a few investigators. The most notable is that of Nieuwstadt (1984), who introduced the local Obukhov Length Λ as an extension of the Monin-Obukhov similarity to the stable boundary layer. This local length scale is given by

$$\Lambda = \frac{\tau^{3/2}\,\theta}{g\ \kappa\ z\ \overline{w'\theta'}} . \qquad (2.14)$$

This is similar in form to the Obukhov Length, but all fluxes are height dependent and no longer influenced by surface values. Nieuwstadt went on to demonstrate how z/Λ can be used to scale turbulent quantities above the surface layer much like z/L does in convective conditions.

In addition to local scaling parameters, a few appropriate length scales have been proposed concerning nocturnal boundary layer height. In most circumstances, a surface "inversion" exists, the height of which can be defined as where either the potential temperature gradient becomes small (Yu, 1978) or the negative heat flux caused by turbulent transport (in weak stability) or radiative cooling decreases to a threshold value (Melagarejo and Deardorff, 1974). The turbulent shear-layer depth (mixing depth) is usually lower than the inversion height and more difficult to qualitatively define, much less quantitatively assess from ground-level measurements. In many circumstances, especially in the presence of strong cooling and light winds or above the surface layer, the wind-field turbulence may locally collapse into regions of laminar motion. These regions can extend to ground level reducing the shear boundary layer to a few meters. The depth of the turbulent shear layer, as opposed to "inversion height," is of the most concern in dispersion modeling. Unfortunately, many issues concerning the characterization of the turbulent shear layer have yet to be adequately resolved.

2.3 Flux Profile Relationships

The profiles of temperature and velocity can be described as functions of ζ using the scaling parameters described in Section 2.2.1 These profiles may be written in the following form

$$\frac{du}{dz} = \frac{u_*}{\kappa z}\,\phi_m(\zeta) \tag{2.15}$$

$$\frac{d\theta}{dz} = \frac{\theta_*}{\kappa z}\,\phi_h(\zeta), \tag{2.16}$$

where ϕ_m and ϕ_h are unique functions of ζ. Several investigations have been undertaken in an effort to determine empirical functions for ϕ_m and ϕ_h. The most commonly used forms are those proposed by Businger et al. (1971). Using data from the Kansas Surface Layer Project in 1968, Businger developed the following similarity functions:

$$\begin{aligned} \phi_m &= (1-\gamma\zeta)^{-1/4} \qquad -2 < \zeta < 0 \\ &= 1-\beta\zeta \qquad\quad 0 < \zeta < 1.5 \end{aligned} \tag{2.17}$$

$$\begin{aligned} \phi_h &= R\,(1-\gamma'\zeta)^{-1/2} \qquad -2 < \zeta < 0 \\ &= R-\beta'\zeta \qquad\quad 0 < \zeta < 1.5 \end{aligned} \tag{2.18}$$

where $\gamma = 15$, $\gamma' = 9$, $\beta = \beta' = 4.7$, and $R = 0.74$. The upper bounds of $|\zeta|$ given in these expressions are suggested on the basis that the data used in the development of these relations covers only this range. Comparison of these relations with the Kansas data (Businger et al. 1971) is very good for $\zeta < 0$, but for $\zeta > 0$ the scatter in the data becomes quite large, emphasizing the problem in characterizing the stable boundary layer, even on very ideal terrain. Also, the von Kármán constant κ has been determined to be 0.35, in disagreement with the generally accepted value of 0.4. In a re-examination of the Kansas data, Wieringa (1980) suggested that anemometer overspeeding may be the cause of this low estimation of κ, but no general consensus exists in the literature. Dyer (1974) suggested relations of the same form as Eqs 2.17 and 2.18, but with $\kappa = 0.4$, $\gamma = 16$, $\gamma' = 16$, $\beta = \beta' = 5.0$, and $R = 1.0$.

The above relations may be integrated to give the velocity and temperature profiles with L, u_* and θ_* being independent parameters. An additional quantity that becomes important at this point is the lower bound of these integrations, the roughness length z_o. Employing the concept of z_o and integrating Eqs 2.17 and 2.18, the integrated profiles evolve in the following form

$$u(z) = \frac{u_*}{\kappa}\left[\ln\frac{z}{z_o} - \Psi_m(\zeta) + \Psi_m\left(\frac{z_o}{L}\right)\right] \tag{2.19}$$

$$\theta(z) - \theta(z_o) = R\,\frac{\theta_*}{\kappa}\left[\ln\frac{z}{z_o} - \Psi_h(\zeta) + \Psi_h\left(\frac{z_o}{L}\right)\right]. \tag{2.20}$$

Using the above relations and Businger's similarity function given by Eqs 2.18 and 2.19, Paulson (1970) procured the following expressions for Ψ_m and Ψ_h

$$\Psi_m(\zeta) = \begin{cases} \ln\left[\left(\frac{1+x}{2}\right)^2\left(\frac{1+x^2}{2}\right)\right] - 2\tan^{-1}(x) + \frac{\pi}{2} & \zeta < 0 \\ -\beta\,\zeta & \zeta \geq 0 \end{cases} \qquad (2.21)$$

$$\Psi_h(\zeta) = \begin{cases} 2\ln\left(\frac{1+y}{2}\right) & \zeta < 0 \\ -\frac{\beta'}{R}\zeta & \zeta \geq 0 \end{cases} \qquad (2.22)$$

where $x = \phi_m = (1-\gamma\zeta)^{1/4}$

$y = \phi_h = (1-\gamma'\zeta)^{1/2}$.

Using these profile relations, the surface-layer fluxes can be estimated from a knowledge of the wind and temperature profiles, and several methods for accomplishing this exist in the literature. The U. S. Environmental Protection Agency (EPA) recommends the use of a least-squares method by Nieuwstadt (1978) when wind speed and temperature data are available at three or more levels. As implied, this method fits Eqs. 2.21 and 2.22 to the wind and temperature profile data, minimizing the error at the individual measurement locations. However, the iterative solution of this problem is often very slow to converge and is not robust. With these problems, slight irregularities in wind and temperature profiles may cause a complete failure of convergence or gross errors in flux estimates.

When fewer than 3 levels of temperature and wind speed data are available, but temperature measurements at 2 heights are available, the EPA recommends the use of a method by Irwin and Binkowski (1980). This method only requires the knowledge of the bulk Richardson number, defined by Eq. 2.7, and an estimate of the roughness length. The solution procedure centers around a functional relationship between Ri_b and L as being

$$\frac{z_2}{L} = \frac{\kappa F^2}{G} Ri_b \,. \qquad (2.23)$$

The empirical forms for F and G are developed from the integral forms presented in Eqs. 2.21 and 2.22 and are given by

$$\kappa F = \frac{\kappa\, u}{u_*} \tag{2.24}$$

$$= \begin{cases} \ln\left[\left(\frac{z_2}{z_o}\right)\left(\frac{\eta_o^2+1}{\eta_2^2+1}\right)\left(\frac{\eta_o+1}{\eta_2+1}\right)^2\right] + 2\tan^{-1}\left(\frac{\eta_o-\eta_2}{1+\eta_o\eta_2}\right) & L < 0 \\ \ln\left(z_2/z_o\right) + \beta\, z_2 / L & L \geq 0 \end{cases}$$

$$\kappa G = \frac{\kappa\, \Delta\theta\, u_*}{-\overline{w'\theta'}} \tag{2.25}$$

$$= \begin{cases} R \ln\left[\left(\frac{z_2}{z_1}\right)\left(\frac{\lambda_2+1}{\lambda_1+1}\right)^2\right] & L < 0 \\ \ln\left(z_2/z_1\right) + \beta'\left(z_2 - z_1\right) / L & L \geq 0 \end{cases}$$

where

$$\eta_2 = \left(1-\gamma\, z_2 / L\right)^{1/4}$$
$$\eta_o = \left(1-\gamma\, z_o / L\right)^{1/4}$$
$$\lambda_1 = \left(1-\gamma'\, z_1 / L\right)^{1/2}$$
$$\lambda_2 = \left(1-\gamma'\, z_2 / L\right)^{1/2},$$

where the values of β, β', γ, γ', R and κ are those given by Dyer (1974). This method is fairly robust and produces satisfactory results, but the inherent sensitivity to z_o is cause for some concern. The algorithm also tends to overestimate the value of $|L|$, sometimes by as much as 100%. Based upon comparison with Kansas and Minnesota data, the authors recommend underestimating z_o to provide more accurate results.

Roughness Length Determination

Given the wide application of the aforementioned methods for determining surface-layer parameters given profile or Ri_b data, the estimation of the roughness length z_o evolves as an important issue. In a physical sense, z_o is a measure of the eddy size at the surface and characterizes the efficiency of momentum transport at this level. Early investigators attempted to relate z_o to the actual height of the roughness elements. In particular, Nikuradse (1933) proposed the proportional relation $z_o = z_r/30$. These approaches, however, are physically unrealistic since surface-eddy size should

depend not only on roughness element size, but also on the distribution and arrangement of these elements. Over flat terrain, the roughness height is most easily determined by plotting the wind speed with respect to ln(z). If a logarithmic profile exists near the surface, z_o is determined by linearly extrapolating the profile to where the wind speed is zero. If the tower is on a small rise or trough, a displacement length may be necessary to correct between local and upwind ground level.

Typically, one will not have a velocity profile from which to compute roughness length, and a estimate based on surroundings will be necessary. Table 2.1 lists approximate values for z_o for a variety of uniform surfaces as given by Randerson (1984) and EPA (1988).

Table 2.1 Approximate values of roughness length for a variety of surfaces in uniform terrain as given by Randerson (1984) and EPA (1988).

Terrain description	z_o (m)
Smooth ice or mud	0.00005
Snow covered smooth ground	0.0001
Open sea with > 5 km fetch	0.0002
Grass lawn up to 1cm high	10^{-3}
Grass lawn up to 5 cm high	10^{-2}
Farmland, corn / hedges	0.1
High crops with scattered obstacles	0.3
Parkland, other larger obstacles	0.5
Centers of large towns, forests	0.5 -1.0

Most often, however, terrain is not uniform and z_o will be characterized by isolated large obstacles and other surface anomalies. In these cases z_o may be very difficult to estimate, since z_o can vary with wind direction, wind speed and stability. Roughness length assessment is further complicated in complex terrain, since u_* may vary with height, violating the assumption of a logarithmic profile and making the determination of z_o difficult even when employing a micrometeorological tower. Intuition and experience are most often the best tools for the determination of z_o in these conditions, although a few empirical relations have proven to be of some use. In particular, the EPA recommends the use of a procedure which employs the standard deviation of wind velocity and is given by

$$\frac{\sigma_u}{u} = \frac{1}{\ln (z/z_o)} . \qquad (2.26)$$

This relation, however, is only recommended when the 10-m wind speed is above 5 m/s.

2.4 Complex Terrain Effects

2.4.1 Principles of Gravity-Induced Flows

Much of the recent work in the field of boundary-layer meteorology has been concentrated in determining the effects induced by the local and regional terrain. The addition of heterogeneous terrain transforms the analysis of surface-flow characteristics from a one-dimensional (vertical) into a two- and more often three-dimensional problem. Shallow, near-surface density gradients are the driving mechanisms for these flows, which can cover regional areas cover up to 100 km on the slopes of mountain ranges or less than 1 km on an interior valley slope. Since these density gradients are created by the surface heat flux, factors which affect radiational exchange, such as low-level cloud cover, local humidity, and soil characteristics, have the strongest influence on the development and maintenance of valley flows. Depending on the size of the valley wind system and the overlying meteorological conditions (weather), the surface layer flows in complex terrain can sometimes be considered decoupled from geostrophic flow.

The simplicity of the gravity-induced buoyancy forces that drive these flows often overshadows the complexities that can arise in their character. These diurnal characteristics are governed by the surface heat flux and the temperature gradients in the first few hundred meters of the atmosphere. In the day solar heating warms the air at the surface, which proceeds to flow upslope due to its buoyancy. Then during late afternoon and night, long-wavelength radiational cooling will begin, the surface heat flux will reverse, and a positive potential temperature gradient will form. This gradient will cause the wind field to reverse direction and flow downslope. In the morning, the solar warming will reverse the near-surface potential temperature gradient and initiate upslope flow.

The most complex and difficult-to-handle of these two flow regimes are the nocturnal drainage flows. The lack of strong vertical mixing and restricted transverse mixing cause surface-induced flow disturbances to be transported downwind for considerable distances. In deep valleys weaker flows may form on the sidewalls, often with depths less than 10-m. These flows may interact with, often oscillating, valley

drainage flows and create turbulent shear zones which may significantly affect the diffusion of pollutants (Shinn et. al. 1989). Many site-specific flow regimes, such as those created in the confluence of two valleys (i.e. at Meadowbrook), must be analyzed with care, since their characteristics are difficult to compare with those from other sites, let alone lend themselves to a generalized treatment. These topics will be further discussed in Chapter 4.

2.4.2 Similarity Relations in Complex Terrain

The flat-terrain similarity relations introduced at the beginning of this chapter employed many assumptions which are easily violated in complex terrain. Problems may arise from the existence of multiple internal sublayers in airflow over terrain of heterogeneous roughness or the formation of nonideal wind profiles that include very low level jets and other anomalies. Also, surface heat flux is often heterogeneous and unsteady due to variations in ground cover and solar angle of incidence .

In *local* regions of homogeneous terrain surrounded by larger regions of complex terrain, such as that seen in the main valley at the Meadowbrook unstable dispersion site, terrain effects in unstable convective conditions may sometimes be disregarded. Horizontal length scales associated with these conditions are usually rather small. This causes the wind field at a particular location to appear horizontally homogeneous and its statistics to be stationary. These small length scales result from the disruption of the surface layer by convective thermals which entrain the surface air and exchange it with air from the well-mixed layer. Since any particular parcel of air is present on the ground for only a short period of time, the wind field cannot retain terrain information for more than a few hundred meters and will not have the ability to reflect the upwind terrain in its temperature and velocity profiles.

During stable drainage conditions, however, flat-terrain surface-layer similarity is almost always inapplicable. Generalized surface-layer similarity is very difficult to conceive due to the long length scales and site-specific conditions. In these conditions, however, there lies a great need for a proper understanding of the flow physics, since pollutants will be transported at low levels for considerable distances.

2.5 Variance and Spectra

As discussed in the first part of this chapter, the development and use of surface-layer similarity is important for the proper treatment of meteorological data. However, the dispersion of aerosol contaminants is governed by the *actual* turbulent fluctuations

present in the flow. Although impossible to analyze in an exact sense, turbulent fluctuations may be handled very nicely statistically. The most common method of characterization for these fluctuations is the standard deviation (or variance) of the wind components. Skewness and kurtosis (third and fourth moment statistics) are also used, especially with the analysis of vertical velocity fluctuations in unstable stratification (which do not exhibit Gaussian behavior), but these are mostly used for modeling and are seldom measured and analyzed in atmospheric flows.

Also significant are the spectra, which characterize the distribution of turbulent energy with respect to frequency. The spectra, which may be computed using the Fourier transform, is fundamental in determining which length scales are important and how energy is transferred within the flow. By definition, the variance can be expressed as the integration of the spectra from wave numbers from 0 to infinity.

2.5.1 Standard Deviations of Wind Components

Derivation of turbulent statistics such as variance, skewness, etc., is not possible using the similarity theories presented earlier. However, the similarity parameters described in Section 2.2 are often used in the *normalization* of these statistics and in the *development* of empirical correlations based on observations. Fitting into the overall framework of the Monin-Obukhov similarity theory, standard deviations have been shown to be functions of ζ and u_* in regions where similarity is applicable. Of course, complex terrain and other non-ideal factors may introduce additional scaling parameters.

Neutrally stratified air is most easily handled, since buoyancy is not a factor and ζ approaches zero. Data for these conditions have shown that the standard deviations for all three velocity components are directly proportional to the friction velocity, with constants of proportionality differing between the components. In an extensive review of these constants from several investigations, Panofsky and Dutton (1984) concluded that

$$\sigma_u = (2.39 \pm 0.03) u_*, \quad (2.27a)$$

$$\sigma_v = (1.92 \pm 0.05) u_* \quad (2.27b)$$

and

$$\sigma_w = (1.25 \pm 0.03) u_*. \quad (2.27c)$$

Correlations for velocity fluctuations based on ζ in stable air are tenuous at best. When ζ is not large, the above relations for neutral conditions may be used. However, for larger values of ζ, wind speeds are often low, and large low-frequency undulations

in wind direction are common. Variances under these conditions are more likely to be affected by the slowly meandering wind field than by the turbulent fluctuations, which are more important to dispersion.

In unstable stratification, horizontal velocity fluctuations depend on the movement of large convection cells, which naturally scale with boundary-layer height. Thus, there should be little or no height dependence. Panofsky et al. (1977) developed the following height-independent empirical relation applicable to both σ_u and σ_v

$$\sigma_v \sim \sigma_u = u_* \left(12 - 0.5 \frac{z_i}{L}\right)^{1/3} \tag{2.28}$$

Højstrup (1982) incorporating a weak dependence on height, especially for small |L|, and different forms for σ_u and σ_v proposed

$$\left(\frac{\sigma_u}{u_*}\right)^2 = 0.6\left(-\frac{z_i}{L}\right)^{2/3} + 4.8 \frac{(1-z/z_i)^2}{(1+15\, z/z_i)^{2/3}} \tag{2.29a}$$

and

$$\left(\frac{\sigma_v}{u_*}\right)^2 = 0.7\left(-\frac{z_i}{L}\right)^{2/3} + 2.7 \frac{(1-z/z_i)^2}{(1+2.8\, z/z_i)^{2/3}} \,. \tag{2.29b}$$

For the vertical velocity in the surface layer, Panofsky et al. (1977) and Højstrup (1982) both recommend relations which scale to the *local* height instead of boundary-layer height. Højstrup, however, incorporated a dependence on z/z_i, providing three relations. Panofsky suggests

$$\sigma_w = 1.25\, u_* \left(1 - 3\, \zeta\right)^{1/3} \qquad z < h \tag{2.30}$$

whereas Højstrup suggests

$$\sigma_w = u_* \left(1.5 + 3.8\, |\, \zeta\, |^{2/3}\right)^{1/2} \qquad z/h \sim 0.001 \tag{2.31a}$$

$$\sigma_w = u_* \left(1.5 + 2.9\, |\, \zeta\, |^{2/3}\right)^{1/2} \qquad z/h \sim 0.01 \tag{2.31b}$$

$$\sigma_w = u_* \left(1.1 + 1.7\, |\, \zeta\, |^{2/3}\right)^{1/2} \qquad z/h \sim 0.1 \tag{2.31c}$$

The difference in scaling between the horizontal and vertical velocity variations lies in the supposition that the prominent velocity component of the large convection eddies will be horizontal at ground level. This dictates that these cells, which scale with the boundary layer height, induce the largest horizontal velocity fluctuations. The vertical velocity fluctuations, however, are influenced by a large range of eddies whose size depends on their proximity to the ground.

Even though some experimental data exists for vertical velocity fluctuations above the surface layer (Deardorff, 1970, Caughey and Palmer, 1979), the scatter in the data do not lend themselves to an easily definable empirical relation. The appropriate scaling parameters for this region are w_* and h (Smith and Blackall, 1979), and several empirical forms using these have been suggested. However, the differences in these relations above the surface layer are extreme.

Complex terrain will generally increase the estimates of horizontal standard deviations, since the wind will be able to retain information about upstream conditions for long distances. The proportionality constants presented earlier for neutral to moderately stable conditions can exceed twice their flat-terrain estimates for mean-wind and transverse velocity fluctuations. In unstable conditions, similarity-based estimates may underestimate observations, but these discrepancies can often be neglected. Regardless of stability, small eddies, which quickly adjust to terrain, characterize vertical velocity fluctuations in the surface layer. Hence, complex terrain effects on σ_w are greatly reduced.

2.5.2 Spectra of Wind Components

Physically speaking, the variances of the velocity components are a measure of the turbulent energy in the atmosphere, and the spectra display how this energy is distributed with respect to frequency. When displayed on a log-log scale, as is almost always done with atmospheric spectra, velocity spectra for mesoscale time scales have a characteristic shape into which three regions of turbulent energy exchange are commonly delineated. The energy containing subrange is located at lower frequencies and is classified as the region where energy enters the flow. The addition of this energy is most often through mesoscale processes or mechanical turbulence. The inertial subrange is distinguished as a region where no energy enters or leaves the flow but is cascaded from lower to higher frequencies. The region of its influence is characterized by a -5/3 power law and is easily discernible on the log-log scale. The dissipation subrange is where viscous forces convert the mechanical energy into heat and is applicable for all wavelengths less than the Kolmogorov microscale. The length scale associated with the Kolmogorov microscale may be interpreted as the size of the smallest eddies and is given by

$$l_\varepsilon = \left(\frac{\nu}{\varepsilon} \right)^{1/4} , \qquad (2.32)$$

where v is the kinematic viscosity and ε is the turbulent dissipation rate. For air at sea level, the eddy size associated with the Kolmogorov microscale is about a millimeter.

Unstable Spectra

Ideal unstable velocity spectra are characterized by a family of curves which may be delineated with respect to z/h and stability. Appropriate normalization, however, has been shown to collapse the spectra for all to a single curve in the inertial subrange. For these spectra, Højstrup (1982) proposed a model which incorporated a mixed-layer component and a shear-generated component. Højstrup hypothesized that the interaction between the components is sufficiently small to allow them to be modeled separately. From this basis, he developed the following models for unstable spectra which are functions of z, z_i, L, u_* and frequency, and calibrated these with data from the Minnesota and Kansas boundary-layer experiments,

$$\frac{nS_{uu}}{u_*^2} = \frac{0.5\, f_i}{(1+2.2\, f_i)^{5/3}} \left(-\frac{z_i}{L}\right)^{2/3} + \frac{105\, f_{ru}}{(1+33\, f_{ru})^{5/3}} \frac{(1-z/z_i)^2}{(1+15\, z/z_i)^{2/3}} \qquad (2.33a)$$

$$\frac{nS_{vv}}{u_*^2} = \frac{0.95\, f_i}{(1+2.0\, f_i)^{5/3}} \left(-\frac{z_i}{L}\right)^{2/3} + \frac{17\, f_{rv}}{(1+9.5\, f_{rv})^{5/3}} \frac{(1-z/z_i)^2}{(1+2.8\, z/z_i)^{2/3}} \qquad (2.33b)$$

$$\frac{nS_{ww}}{u_*^2} = \left[\frac{f^2 + (0.3z/z_i)^2}{f^2+.023}\right]^{1/2} \frac{0.95\, f_i}{(1+2.0\, f_i)^{5/3}} \left(-\frac{z_i}{L}\right)^{2/3} + \frac{2\, f\, (1-z/z_i)^2}{(1+5.3f)^{5/3}}, \qquad (2.33c)$$

where $f = \frac{n\,z}{u}$, $f_i = \frac{n\,z_i}{u}$, $f_{ru} = \frac{f}{1+15\, z/z_i}$, and $f_{rv} = \frac{f}{1+2.8\, z/z_i}$

These are usually plotted with respect to f, which is a non-dimensional frequency. Højstrup's variance relations given earlier are merely integrations of the above spectral relations.

Stable Spectra

Spectra in stable conditions are less well understood and thus more difficult to accurately model. The spectral forms in these conditions are fundamentally different in that effects of both waves and turbulence may be present. The majority of wave activity is due to oscillations which develop from the suppression of turbulence by negative

buoyancy. The waves associated with the oscillations are called gravity waves By equating the buoyancy force to the vertical acceleration, the frequency of the resulting sinusoidal solution is

$$N = \left(\frac{g}{\theta} \frac{\partial \theta}{\partial z} \right)^{1/2} . \qquad (2.34)$$

This frequency is known as the Brunt-Väisälä frequency and is real in positive potential temperature gradients and imaginary in negative ones. Hence, N is only an appropriate analysis parameter in stable conditions. Another form of wave activity is Kelvin-Helmholz instabilities, which develop in free shear layers. Although Kelvin-Helmholz instability has not been extensively studied in ground-level atmospheric flows, the mechanisms for their existence are present in nocturnal downslope flows, especially in highly stable conditions when intense low-level jets may develop. The formation and subsequent breakdown of Kelvin-Helmholz billows may be partially responsible for intermittent turbulence observed during these conditions.

In the examination of spectra from stable conditions, a low-frequency wave subrange can sometimes be located in the vicinity of the Brunt-Väisälä frequency. This will produce a gap between a wave and shear generated components, although the mechanical component must be rather small for a distinction to be clear. The dependence of spectra on gravity waves is somewhat troublesome, since gravity waves are strongly terrain dependent and may travel great distances undisturbed. More importantly, their contribution in the dispersion of pollutants is minimal, even though their apparent contribution to turbulent energy may be significant on the spectral level.

Another fundamental problem in the measurement of stable spectra is that turbulence may be very weak or non-existent. Caughey (1977) analyzed data from the Minnesota experiments and found that spectral estimates fell to near noise levels for Ri values above about 0.2. This is what one may anticipate though, since for Ri > .25 atmospheric flow may well be laminar as was discussed in Section 2.1.2. Low wind speeds may also lead to large errors in spectral estimates due to the threshold level of the instrumentation. These issues are discussed further in Section 3.3 where the spectra of Meadowbrook data are presented.

Local Isotropy

In turbulence, isotropy describes a condition where statistics are invariant with respect to direction. Implications of isotropy include the independence of all velocity

components from each other and identical variances for each component. In the atmospheric boundary layer, isotropy is not observed, but it may exist at sufficiently high frequencies, leading to the concept of local isotropy.

The spectra of the three velocity components may be used to determine if local isotropy prevails at a given point. The main significance of local isotropy in atmospheric flows is determining at what frequency isotropy will prevail, since eddies with frequencies higher than this will not be distorted by the ground level roughness elements. For increasing frequencies, local isotropy prevails at the frequency where the spectra ratios S_{vv} / S_{uu} and S_{ww} / S_{uu} converge to constant values of 1.28 and 1.33 respectively.

3 ANALYSIS OF MEADOWBROOK METEOROLOGICAL DATA

3.1 Overview of Meteorological Measurements

3.1.1 Site Characteristics

The Meadowbrook dispersion site, fog-oil sampling grids, and meteorological instrumentation are shown in Figs. 3.1, 3.2 and 3.3. This site is located approximately 20 miles east of Red Bluff, California in the foothills of the Sierra-Nevada Mountains and consists of a forked creek valley with surrounding slopes rising to a height of about 250 m above the valley floor. These slopes are covered with deciduous and coniferous trees reaching heights of 25 m, although the average height of the surrounding forest is about 8 to 10 m. The relatively flat main valley, which is about 800 m across at its widest point, lies west of the confluence formed by the joining of Plum Creek with Paynes Creek. These two creeks flow down from the higher elevations east of the valley. The cleared areas paralleling each of the two creeks narrow and eventually vanish as elevations increase.

The surface meteorology of the site is dominated by mesoscale slope flows which arise from the Boise-Cascade mountains that lie to the west of the site. At night, colder, denser air flows down these mountain slopes into the valley; whereas during the day, warmer, buoyant air flows up these slopes from the lower elevations. These mountains also strongly affect local climate by blocking much of the moist air traveling east from the Pacific Ocean thus giving rise to dry conditions. The decreased cloud cover and humidity throughout the atmosphere results in very strong daytime heating and nocturnal cooling. The intense daytime heating is responsible for temperatures in excess of 40 °C on occasions during the testing period. Nocturnal cooling and stratification are equally intense with temperatures below 10 °C occurring in the lower areas of the test site, and temperature differences between the valley floor and ridge tops approaching 15 °C on very clear nights. The meteorology of the test area is well established, both through the nature of the terrain and through three previous large-scale wind field studies carried out in Phases I – III of Project WIND.

To effectively utilize the diurnal wind characteristics present at Meadowbrook, two smoke release locations and associated sampling grids were established. One, known as the "unstable release point," is located at the west end of the valley floor as shown in Fig. 3.2. This release point was used for daytime experiments when upslope winds were anticipated. The "unstable" designation comes from the fact that a highly convective, unstable atmospheric boundary layer is expected under these conditions.

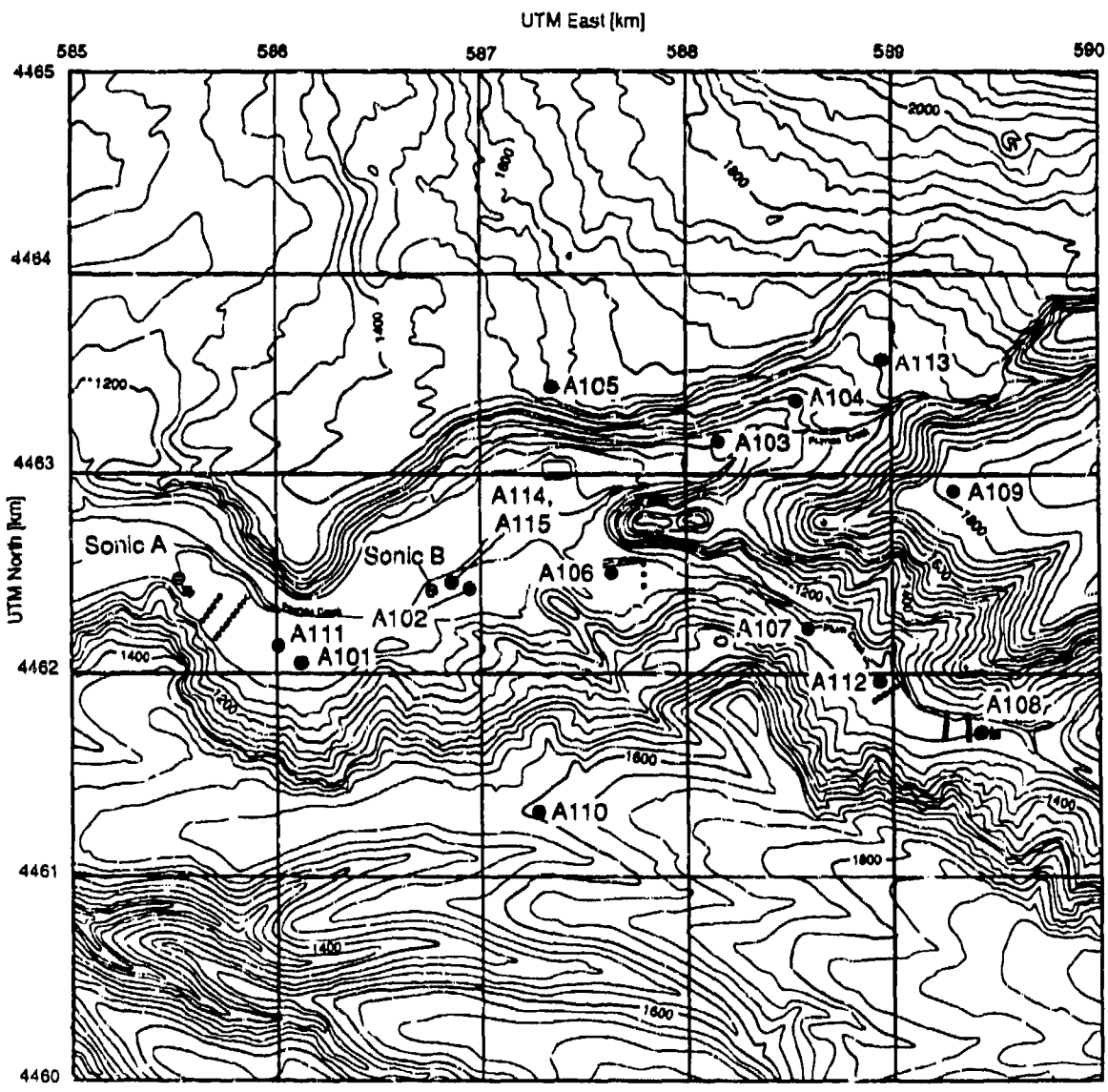

Figure 3.1 Topographical map of the Meadowbrook Site. Elevations are in feet above sea level with contour lines at increments of 40 feet. The horizontal scale is in Universal Transverse Mercator coordinates, with the grid marked in km. The topographical information is taken from the USGS map of Inskip Hill, California.

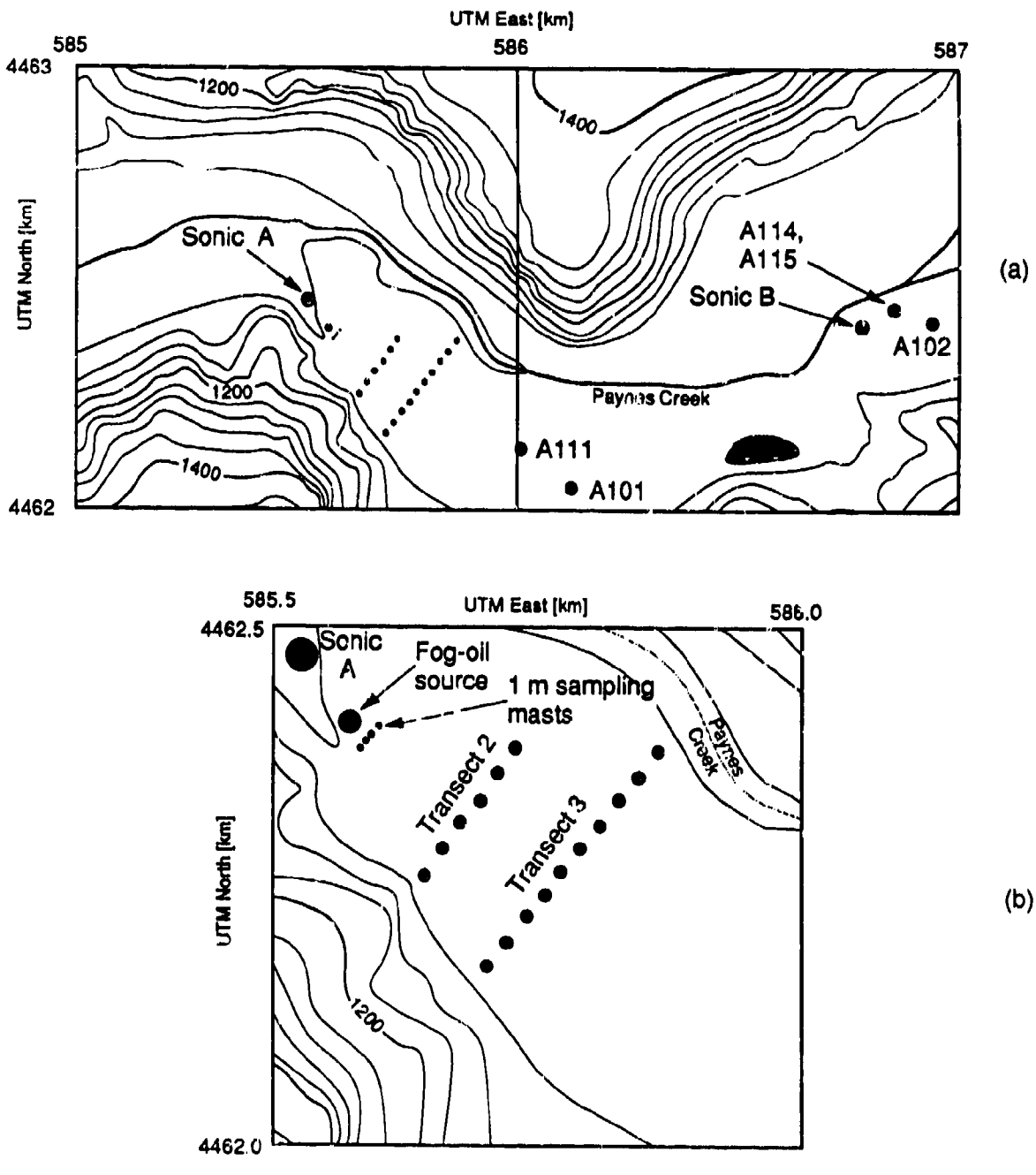

Figure 3.2 Close-up views of the "unstable" test area showing (a) locations of relevant meteorological instrument towers and (b) enlarged view of the sampling transects. The horizontal scale is in Universal Transverse Mercator coordinates, with the grid marked in km. Elevations are in feet above sea level with contour lines at increments of 40 feet The topographical information is taken from the USGS map of Inskip Hill, California.

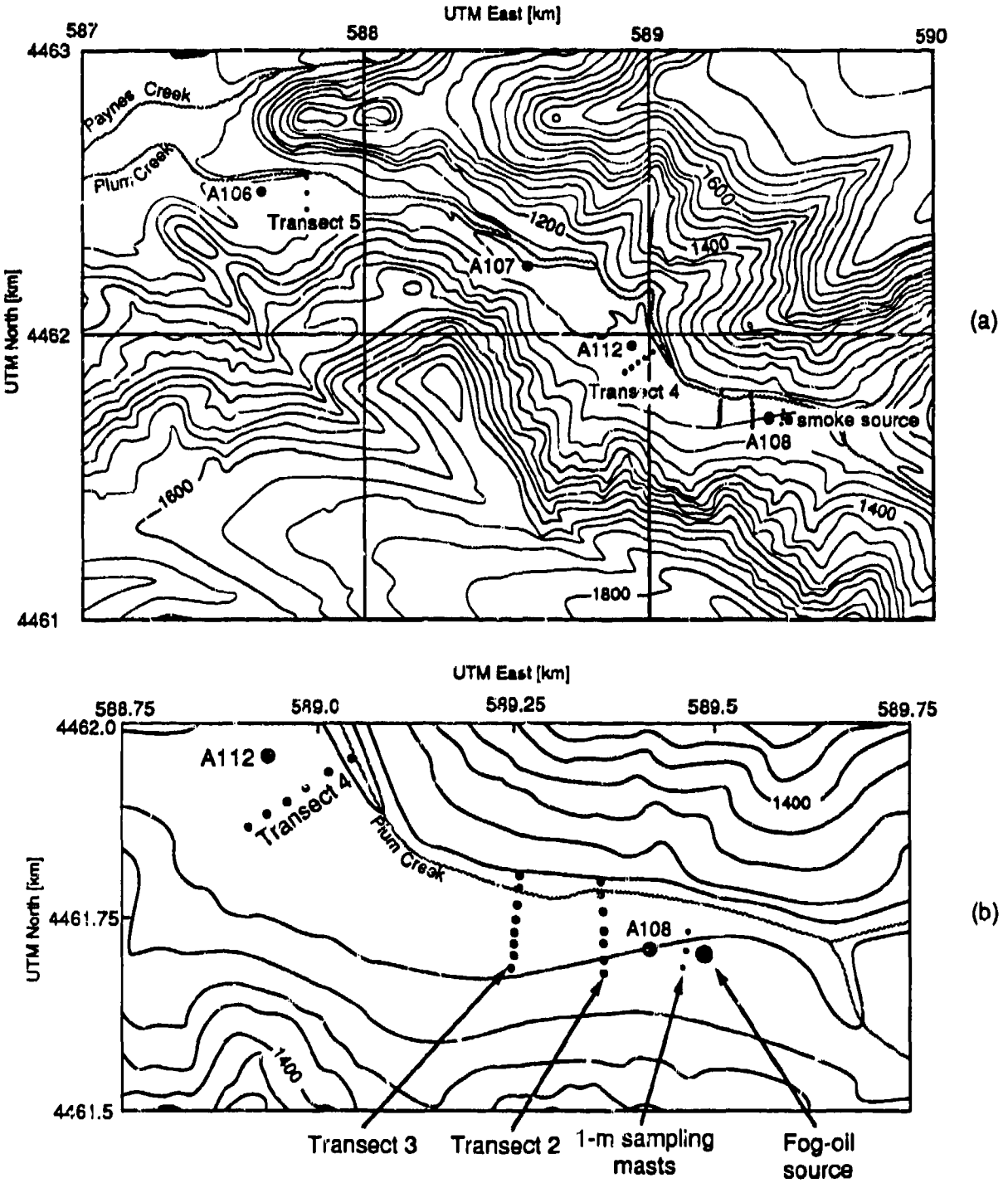

Figure 3.3 Close-up views of the stable test area showing (a) location of relevant meteorological instruments and (b) enlarged view of the sampling transects. The horizontal scale is in Universal Transverse Mercator coordinates, with the grid marked in km. Elevations are in feet above sea level with contour lines at increments of 40 feet. The topographical information is taken from the USGS map of Inskip Hill, California.

The second location, known conversely as the "stable release point," lies in the upper reaches of the cleared area of the Plum Creek valley and is shown in Fig. 3.3. This location was used for the nighttime and early morning smoke releases when downslope winds and a stable atmospheric boundary layer were anticipated. The commonly employed terms "stable" and "unstable" must be carefully applied, however, since their specific meanings may become clouded in a complex terrain setting such as the Meadowbrook Site, where local stability may be extremely heterogeneous. Although somewhat vague, these terms provide a simple, convenient and easily understood method of distinguishing the two types of smoke releases. Moreover, the use of these labels has become so widespread in the AMADEUS literature that adopting a new terminology now would only serve to greatly confuse matters.

Near the unstable release point, the wind is predominantly from northwest to southeast, following the curvature of the valley. Samplers were operated along three transects to a distance of 250 m from the source as shown in Figs. 3.1 and 3.2. The high dilution rate of the smoke as well as strong vertical lifting under highly convective conditions precluded measurement at greater distances, and for most of the tests diminished the concentrations at the third transect. Because of the limited distance involved and the relatively flat terrain of the valley floor, little if any complex terrain effects on the dispersion were experienced.

Near the stable release point, the wind follows the gradient of the terrain quite well. The smoke dispersion characteristics may be very sensitive to the *local* stability and surface roughness, especially in the near-field region. Five rows of samplers spanning the width of the creek valley and covering a downwind distance to 2 km were used to sample the smoke released from this location as shown in Figs. 3.1 and 3.3. In a few of the tests, samplers located on the third transect of the unstable-release-point grid were also operated to give a total sampling distance of more than 3 km.

In total, twelve smoke releases were made: five from the unstable release point and seven from the stable release point. The trials ranged from 12 to 67 minutes in duration with the majority of the releases lasting between 30 minutes and an hour. Seven of the trials (four unstable and three stable) were conducted under clear skies; the remaining five were carried out under partly cloudy conditions. Five of the seven releases at the stable release point were made in the early morning hours shortly before the transition from downslope to upslope flow occurred.

3.1.2 Surface Stations

An array of surface stations was used to map the wind field over the Meadowbrook site. In its simplest form, a surface station measures the wind speed, (horizontal) wind direction and temperature at a height 10 m above the ground. At some of the stations, a second temperature measurement at a height of 2 m was added to determine the vertical temperature gradient (lapse rate). Using the lapse rate, atmospheric stability can be inferred using the bulk Richardson number described in Section 2.1, although the validity of this procedure is a matter of some controversy in the literature. In some instances, these basic data are supplemented by additional measurements such as the soil temperature, the solar heat flux and the humidity.

During the AMADEUS Dispersion Experiments, thirteen 10-m surface stations equipped with cup anemometers and direction vanes were used. In addition, a 30-m micrometeorological instrument tower was located in the center of the valley floor as is more fully described later. Cup anemometers and direction vanes were mounted on this tower at the 10-m and 30-m levels. Thus, a total of 14 surface wind-field measurements were made at the 10-m level and an additional measurement was made at the 30-m level, creating a total of 15 measurements.

In addition to the cups and vanes, the 30-m tower was also equipped with three-component propeller anemometers at heights of 2, 4, 8, 16 and 30 m. The coexistence of two different types of instruments at the 30-m level allows readings from the two types to be compared. This comparison reveals that the cup anemometer reads consistently higher than the propeller anemometer by 10 to 20%. A similar comparison between the cup anemometer reading at the 10-m height and a value interpolated from the 8-m and 16-m propeller measurements yields the same conclusion. Based on the fact that the instruments were calibrated before use, the most likely explanation for this disparity lies in the response characteristics of the cup anemometer in a horizontally and vertically fluctuating wind field. Discussions with the scientists from the NOAA Atmospheric Research Laboratory who were responsible for operating these instruments confirmed the fact that their cup anemometers do, in fact, typically read higher than their propeller anemometers by the same percentage as was observed in this study.

Three different organizations were involved in gathering the surface-station data as follows:

1. Eight of the 15 stations, designated A101, A102 and A105-A110, were operated by the Physical Sciences Laboratory of New Mexico State University, Las Cruces, New Mexico. All eight of these stations were equipped with wind and temperature instruments at the 10-m level. The temperature difference between the 2-m and 10-m levels was also measured as was the soil temperature. These stations ran continuously (except for unscheduled down time) over the 17-day period during which the trials were conducted. One-minute averages were computed from 1-s samples by the data acquisition equipment in the field. These 1-min averages were saved and ultimately transferred to floppy disk.

2. Two of the 15 stations, designated A103 and A104, were operated by Nowcasting of Chico, California. Wind and temperature measurements were made at the 10-m level, but no auxiliary temperature measurements were made. Moreover, the temperature sensor on Station A103 exhibited a very slow response time as compared with the other surface-station sensors. These stations ran continuously for most of the testing period, although Station A103 did not operate during the first three smoke trials. One-minute averages were computed in the field from 1-s samples by the data acquisition equipment. These 1-min averages were saved and ultimately transferred to floppy disk.

3. Five of the 15 stations, designated A111 through A115, were operated by the NOAA Atmospheric Research Laboratory of Idaho Falls, Idaho. As previously noted, Stations A114 and A115 correspond to cup anemometers and direction vanes mounted at the 10-m and 30-m levels of the 30-m instrument tower. The temperature for Station A115 was taken as the value recorded by the micrometeorological sensor mounted at the 30-m level. Lacking a corresponding measurement at the 10-m level, we elected to use the actual value at the 8-m level rather than a value interpolated from the 8-m and 16-m data. These five stations were operated only during the smoke and tracer release periods. The data were sampled at 1-s intervals using a centralized data acquisition system. The 1-s data were transferred directly to nine-track magnetic tape, and 5-min averages were simultaneously produced for use by the Test Officer. We used the 1-s data on tape to generate 1-min averages of the same type available for the other surface stations.

3.1.3 Micrometeorological Measurements

As was previously discussed, a 30-m tower equipped with wind and temperature instruments at five levels (2 m, 4 m, 8 m, 16 m and 30 m) was operated by the NOAA Atmospheric Research Laboratory of Idaho Falls, Idaho. Propeller anemometers were used to measure all three components of the wind velocity, and the data were sampled

remotely at a 1-hz rate. In addition, unidirectional laser anemometers were used to measure the bulk flow velocity through the valley at three levels.

The micrometeorological data serve two primary purposes: (a) to characterize the vertical variation in the mean wind speed, mean wind direction and mean temperature, and (b) to provide information on the turbulent components and fluxes present in the wind and temperature fields from which the structure of the atmospheric boundary layer may be inferred. Momentum and heat fluxes may be found by directly analyzing the actual turbulent fluctuations of velocity and temperature (eddy correlation) or by profile fitting as was discussed in Section 2.3. Unfortunately, direct methods require fast-response instrumentation and generally fail for 1-hz data.

In processing the data, it was discovered that for several of the test periods a discrepancy existed in the wind direction between the propellers and the vane at the 30-m level. The worst of these are for (a) records starting at 21:00 on September 24 and ending at 02:40 on September 25 for which the disparity is 15-20°, (b) records starting at 02:15 on September 27 and ending at 07:50 on September 27 for which the disparity is 65-70° and (c) records starting at 09:40 on September 28 and ending at 13:45 on September 28 for which the disparity is 20°. NOAA-ARL personnel reported that, due to difficulties in maintaining the alignment of the wind vane, several adjustments to the instrument were required during the course of the field study. Considering these problems, we assumed that the wind vane was in error. For the test periods mentioned above, the data for Station A115, reported in Section 3.2, have been corrected.

3.1.4 Surface Momentum and Heat Flux Measurements

Two sonic anemometers (designated A and B) were operated by researchers from Risø National Laboratory in Denmark. Sonic Anemometer A, which only operated during the daytime dispersion tests, was located at UTM coordinates 4462474 N and 585523 E, which is about 100-m northwest from our unstable release point. Sonic Anemometer B, which operated almost continuously between September 21, 1987 and October 4, 1987, was located at UTM coordinates 4462417 N and 586756 E, which is about 100 m west of 30-m micrometeorological instrument tower (Station A114 and A115). Figs. 3.1 and 3.2 show the location of the two anemometers within the test area.

These two instruments recorded temperature and tri-directional wind-speed data at a 20-hz rate. With this rapid response time, it is possible to directly measure the turbulent momentum and heat fluxes in the vertical direction, and thus provide direct

information on atmospheric stability. However, these data exhibit considerable variation with time as eddies of various sizes pass by the measuring point. To partially overcome the transient nature of these measurements, the 20-hz data were averaged into 10-min data on site. Only the 10-min averages were available for the analysis considered here.

Caution must be exercised in the interpretation of sonic-anemometer data, since the turbulent fluxes are measured at a single point and may not be representative of the entire area. This is an important consideration for our data, since the meteorology at the Meadowbrook site is very heterogeneous, especially at night.

3.1.5 Instrumented Balloon Soundings

Attention thus far has been focused on near-ground flow patterns and the stability of the atmospheric boundary layer. An equally important parameter for dispersion modeling in unstable conditions is the atmospheric boundary-layer height. As discussed in Chapter 2, the unstable boundary layer is characterized by a strong capping inversion which lies near the ground at dawn and rises to an asymptotic height of as much as several kilometers over the course of the day. Bright sunny days with intense ground heating, such as are typical of the Meadowbrook Site, give rise to highly convective boundary layers. Determining the height of the boundary layer under stable conditions is more problematic, since the current understanding of stable-boundary-layer physics is poor and the vertical extent of the boundary layer is not so readily apparent.

An instrumented balloon can be used to determine the vertical wind and temperature structure of the atmosphere to a height of several kilometers and, if required, to heights of tens of kilometers. This device consists of a large, helium-filled balloon outfitted with a small instrument package which can measure pressure and temperature and radio this information to a ground-level tracking dish. The balloon is allowed to rise freely and its position is tracked by the ground station. Simultaneously, the instrument package telemeters backs the pressure and temperature data. Using the time history of the balloon position, the pressure data (from which height can be computed) and the temperature data, it is possible to determine vertical wind and temperature profiles.

Balloon soundings of this type can be used to determine an unstable boundary layer height using one of two methods. If a sounding is made during the day, the temperature inversion should be readily apparent and the height of the boundary layer

immediately evident (at least in principle). Alternatively, the sounding can be made very early in the morning when the inversion is near the ground. To obtain the mixing height for any specific time of day, one combines the vertical profile of potential temperature thus determined with the local ground-level potential temperature measured directly at the time of interest. This method of determining mixing height is routine in boundary-layer meteorology and has been found to give estimates which are within 50% of the actual value (Pendergast, 1984). Lacking a valid sounding, one can estimate the mixing height from solar heating considerations (based on time of day, time of year and cloud cover information) or by a spectral method presented later.

A valid sounding taken close to the time of the test is available for only one of our daytime releases. Morning soundings are available for three of the other four daytime releases. No upper air data are available for the one remaining daytime trial nor are any data available for the seven nighttime and early morning releases.

3.1.6 Mini-sodar Measurements

A mini-sodar device was operated periodically during the study by researchers from the Meteorological Section of the Environmental Research Division of Argonne National Laboratory. This device uses reflected sound waves to characterize the structure of the atmospheric boundary layer to a height of 300 m. Unfortunately, these data are not in a useful form at the present time, and thus have not been analyzed here.

3.2 Surface Station Data

3.2.1 Measurement Locations

The layout of fixed instrumentation at the Meadowbrook Site was shown previously in Fig. 3.1. Table 3.1 gives the latitude and longitude of Stations A101–A110 and A114/115 as determined by ASL-contractor personnel. The Universal Transverse Mercator (UTM) coordinates which we calculated from these values are also given. The locations of Stations A111-A113, in UTM coordinates, were supplied to us by the NOAA-ARL personnel who operated the stations. The latitude and longitude coordinates were determined by the ASL contractor using a Loran-C electronic positioning system rather than by ground-based surveying. Although the readings are reported to a *resolution* of 1" in both latitude and longitude, which translates into an uncertainty of 24 m in latitude and 31 m in longitude at this site, the *accuracy* of the measurements is generally believed to be between 2" and 10", depending on the quality and type of

instrument being used. With these potential inaccuracies in mind, the uncertainty in the horizontal positions determined from the reported latitude and longitude coordinates is expected to be between 50 and 250 m.

Table 3.1 Coordinates and elevations of meteorological surface stations as determined by ASL contractor personnel.

Station	Latitude	Longitude	UTM north	UTM east	Elevation [m]
A101	40°18'24"	121°59'11"	4462055	586104	321
A102	40°18'36"	121°58'37"	4462423	586903	323
A103	40°18'59"	121°57'43"	4463130	588173	370
A104	40°19'13"	121°57'21"	4463560	588690	449
A105	40°19'09"	121°58'18"	4463438	587350	465
A106	40°18'37"	121°58'06"	4462454	587632	332
A107	40°18'22"	121°57'29"	4461993	588502	355
A108	40°18'08"	121°56'54"	4461563	589324	390
A109	40°18'52"	121°56'55"	4462915	589301	554
A110	40°18'00"	121°58'21"	4461317	587279	491
A111	N/A	N/A	4462288	585924	321
A112	N/A	N/A	4462000	588909	369
A113	N/A	N/A	4463576	588955	457
A114/A115	40°18'37"	121°58'39"	4462454	586856	322

Due to the inaccuracies inherent in the Loran-C system, many of the surface station locations reported by the ASL contractor are substantially in error. This presents a serious problem, since the Meadowbrook site is characterized by complex terrain and very inhomogeneous meteorology. In an effort to resolve this problem, aerial photographs, ground-level photographs and UIUC/ANL survey information were analyzed to pinpoint the location of the stations.

Station A114/115 can be seen in aerial photographs, and its reported location appears to be correct. The UIUC/ANL team surveyed the unstable grid relative to Stations A114, A101 and A111. Using this survey information combined with the known location of Station A114/115, Stations A101 and A111 can be correctly located. Station A102 can also be recognized in an aerial photograph; it is about 40 m east of its reported location. The UIUC/ANL team used Stations A106, A108 and A112 as reference points in surveying the stable grid. Since Transects 4 and 5 are visible in the aerial photographs, these three stations can be correctly located from the UIUC sur-

vey. Using the elevation, temperature and wind direction data, we concluded that the reported location of Station A107 was grossly in error. We hypothesized that the station was, in fact, located in the middle of the Plum Creek valley. A personal communication with the ASL Project Leader (Mr. Ron Cionco) confirmed this suspicion and pinpointed the location as the narrowest point of the Plum Creek valley. During this communication, it was also discovered that the reported location of Station A104 was substantially in error, and the correct location was established. Unfortunately, no such supplementary information was available by which to correctly locate Stations A103, A105, A109, A110 and A113. These stations are outside the sampling grids used in the smoke trials and thus knowing their precise location is less critical. Table 3.2 summarizes the revised locations and the errors for the eight stations for which corrected locations were determined.

Table 3.2 Coordinates of meteorological surface stations as determined by the UIUC/ANL team. The difference column gives the horizontal distance between the location shown and that determined by ASL-contractor personnel as presented in Table 3.1.

Tower	UTM north	UTM east	Difference from reported [m]
A101	4462053	586125	21
A102	4462423	586942	39
A104	4463534	588369	322
A106	4462502	587632	48
A107	4462236	588501	243
A108	4461710	589422	177
A111	4462139	586010	123
A112	4461960	588937	49

3.2.2 Surface-station Data Reduction

Averages of the surface-station data were computed for each of the 12 smoke releases. In addition, two quantities commonly used to characterize the turbulent nature of the boundary layer were calculated from the surface-station data. One is the standard deviation of the horizontal wind direction σ_θ, and the other is the bulk Richardson number, which can be calculated for those stations where two temperature measurements are available. For the purposes of this evaluation, the analysis was carried out for time periods beginning with the start of each smoke release and ending

10 min. after the smoke release was terminated. The extension of the averaging period allowed time for the smoke plume to move off the sampling grid.

Scalar and Vector Averages

Scalar averaging is used in the analysis of wind speed and temperature data. For example, the *scalar*-mean wind speed S is determined from

$$S = \frac{1}{N} \sum_{n=1}^{N} s_i \,, \tag{3.1}$$

where s_i represents an individual 1-min scalar-average wind speed and N is the number of valid measurements included in the average. Average temperature is computed in the same manner.

Vector averaging is also required in the analysis of wind speed data when computing the *vector*-mean wind speed. The vector mean differs from the scalar mean in that it represents the average component of the individual wind vectors in the vector-mean wind direction. The computation of the vector-mean wind speed proceeds as follows. One must first compute the component averages U_1 and U_2 where

$$U_1 = \frac{1}{N} \sum_{n=1}^{N} u_i \, (\cos \theta_i) \tag{3.2}$$

and

$$U_2 = \frac{1}{N} \sum_{n=1}^{N} u_i \, (\sin \theta_i) \,. \tag{3.3}$$

Here, θ_i represents an individual 1-min average wind direction. The vector-mean wind speed U and vector-mean wind direction θ are then given by

$$U = \sqrt{U_1^2 + U_2^2} \tag{3.4}$$

and

$$\theta = \arctan (U_2, U_1) \,, \tag{3.5}$$

where arctan represents the full-circle arctangent function yielding values between 0° and 360°.

Once the vector-mean wind direction θ is determined, the individual wind velocity measurements can be resolved into their mean-wind component u_i and their cross-wind component v_i given by

Once the vector-mean wind direction θ is determined, the individual wind velocity measurements can be resolved into their mean-wind component u_i and their cross-wind component v_i given by

$$u_i = s_i \cos(\theta_i - \theta) \tag{3.6}$$

and

$$v_i = s_i \sin(\theta_i - \theta) . \tag{3.7}$$

It is easily shown that the (scalar) mean value of u is the vector-mean wind speed U and that the (scalar) mean value of v is 0. Because the cosine function appearing in Eqn. 3.6 is always less than or equal to one, it follows that each u_i is less than or equal to each s_i and thus that U is less than or equal to S, the equality being true only if the wind direction is constant (i.e., $\theta_i = \theta$, for all i).

Turbulence and Stability Estimation

Although surface-station data are primarily used to characterize the mean wind and temperature fields, estimates of atmospheric stability may be obtained from either of two alternative methods. The first method uses σ_θ, the standard deviation of the horizontal wind direction, and the second method utilizes the vertical temperature gradient to estimate stability through the Richardson number concept. Since only one wind speed is available, we used the bulk Richardson number described in Chapter 2 and defined from surface-station measurements as

$$Ri_b = \frac{g\, z_2 [T_2 - T_1 + \gamma \Delta z]}{S^2 T_2} , \tag{2.7}$$

where the bracket term is simply the potential temperature difference. As is shown, this may be computed using the *actual* temperature difference with the addition of the $\gamma\Delta z$ correction, where γ is the adiabatic lapse rate and Δz is the vertical distance between the temperature measurements.

Although conceptually simple, the computation of σ_θ is plagued with several difficulties. The fundamental problem lies in the fact that θ is periodic. Consider, as a simple illustration of this problem, the average of the two measurements: 355° and 5°. The mean computed by conventional methods is 180°, and the standard deviation is 247.5° both of which are in gross error (The correct results are 0° and 7.1°, respectively). To avoid this difficulty, one can first determine the vector mean wind direction θ

as noted above and then compute the standard deviation from the individual values d_i given by

$$d_i = (\theta_i - \theta + 540°) \bmod 360° - 180° , \tag{3.8}$$

where the modulo arithmetic indicated in Eqn. 3.8 has the net effect of mapping each individual deviation into the interval (-180°, +180°). For example, a simple arithmetic difference of 270° becomes an adjusted difference of 90°.

Some authors define the root mean square of these deviations as σ_θ. However, this definition introduces a systematic bias in the results, because the mean deviation may not be 0. For this reason, we employ the following definition which removes the effect of the non-zero mean deviation.

$$\sigma_{\theta,1\text{-min}} = \left[\left(\frac{1}{N-1} \sum_{i=0}^{N} d_i^2 \right) - \frac{N}{N-1} \left(\frac{1}{N} \sum_{i=0}^{N} d_i \right)^2 \right]^{1/2} . \tag{3.9}$$

Here, we use the special notation $\sigma_{\theta,1\text{-min}}$ to emphasize the fact that the surface data consist of 1-min averages of the wind speed and direction. However, when averages based solely on the one-minute data are used, the value of σ_θ is substantially underestimated. A more accurate estimate of the variance includes two terms: (i) the variance of the one-minute data as above and (ii) the mean of the individual variances $\sigma_{\theta i}^2$ associated with each one-minute record. Incorporating both components, the expression for σ_θ becomes

$$\sigma_\theta = \left[\sigma_{\theta,1\text{-min}}^2 + \frac{1}{N} \sum_{i=0}^{N} \sigma_{\theta i}^2 \right]^{1/2} . \tag{3.10}$$

The individual variances $\sigma_{\theta i}^2$ were recorded by dataloggers at each surface station. However, the dataloggers did not compute σ_θ directly. They used an approximation that allowed them to compute σ_θ using the scalar-averaged and vector averaged wind speeds. This approximation is

$$\sigma_{\theta i} \approx \frac{180° \sqrt{2}}{\pi} \left(1 - \frac{u_i}{s_i} \right)^{1/2}$$

$$\approx 81° \left(1 - u_i / s_i \right)^{1/2} . \tag{3.11}$$

Results and Discussion

A synopsis of the surface-station data for each of the 12 smoke trials is given in Tables 3.3 - 3.14. In these tables, the string "-99999" indicates that greater than 50% of the data in the averaging period were bad for that variable. For those cases with less than 50% bad data, the number of bad minutes is explicitly indicated in footnotes. The notation "N/A" indicates that a particular item was not measured or is not computable. All times given are local time (PDT).

Examination of these results reveals that the maximum wind speed varies between about 3 and 6 m/s. For the daytime trials, the range of wind speeds over the test area is within a factor of 3, whereas the variation can be as much as a factor of 10 at night. Wind speeds below 0.5 m/s should be interpreted with caution, since this value is near the threshold of the anemometers used on the surface stations. The temperatures follow the expected diurnal characteristics of the site being between roughly 10 °C and 15 °C during the nighttime and early morning tests and between roughly 25 °C and 40 °C during the daytime tests. The temperature inhomogeneity for the nighttime and early morning tests is much larger than for the daytime tests. Specifically, the inhomogeneity is seen to be between 5 °C and 12 °C for the nighttime and early morning trials, but typically less than 2 °C for the daytime trials. The value of σ_θ is apparently smaller for the stable nighttime and early morning releases, although a few very large values of σ_θ are seen at night when wind speeds are low. This reflects the problems associated with defining σ_θ under light wind conditions. The bulk Richardson number shows significant inhomogeneity (as much as a factor of 100) across the test area under stable nighttime and early morning conditions. In contrast, the inhomogeneity under unstable daytime conditions is much smaller, being consistently less than a factor of 10.

The considerable inhomogeneity of the surface-station data underscores not only the complexity of the wind field at this site but also the very difficult problem of characterizing the atmospheric boundary layer in simple terms.

3.3 Synopsis of the Micrometeorological Data

3.3.1 Data Reduction

The reduction of the micrometeorological data proceeded in a manner similar to that previously described for the surface-station data. Three important distinctions exist, however.

Table 3.3 Synopsis of surface-station data for Test 0921871. Smoke was released from 14:30 to 15:00. The unstable release point was used.

Station	S [m/s]	U [m/s]	θ [°]	σ_θ [°]	T_{10m} [C]	T_{2m} [C]	T_{soil} [C]	Ri_b
A101	-99999	-99999	-99999	-99999	-99999	-99999	-99999	-99999
A102	3.510	3.139	306.3	27.97	38.15	39.03	53.60	-0.020
A103	-99999	-99999	-99999	-99999	-99999	N/A	N/A	N/A
A104	-99999	-99999	-99999	-99999	-99999	N/A	N/A	N/A
A105	3.951	3.701	308.5	20.99	38.04	38.85	53.14	-0.015
A106	3.474	3.214	288.3	26.19	38.26	39.16	49.90	-0.022
A107	3.156	2.883	320.4	24.39	38.54	39.40	53.67	-0.025
A108	4.172	3.982	280.7	19.20	37.94	38.79	51.02	-0.014
A109	3.876	3.668	295.1	25.87	36.87	38.27	55.57	-0.028
A110	3.771	3.529	332.9	20.93	37.19	38.08	51.51	-0.018
A111	5.902	5.536	318.9	20.65	N/A	N/A	N/A	N/A
A112	3.912	3.714	318.1	18.05	N/A	N/A	N/A	N/A
A113	4.097	3.391	274.2	41.97	N/A	N/A	N/A	N/A
A114	4.329	3.951	297.7	25.18	38.65	39.17	N/A	-0.006
A115	4.659	4.290	298.5	23.92	38.28	39.17	N/A	N/A

Notes:

1. All wind speed and direction measurements are at 10 m, except for Station A115 which is at 30 m.
2. All upper temperature measurements (T_{10m}) are at 10 m as implied by the subscript, except for Station A114 which is at 8 m and Station A115 which is at 30 m.
3. All lower temperature measurements (T_{2m}) are at 2 m as implied by the subscript.
4. Soil temperature measurements (T_{soil}) are a depth of 0.1 m.

Table 3.4 Synopsis of surface-station data for Test 0923871. Smoke was released from 14:00 to 15:31. The smoke moved off the grid at 14:50. The unstable release point was used.

Station	S [m/s]	U [m/s]	θ [°]	σ_θ [°]	T_{10m} [C]	T_{2m} [C]	T_{soil} [C]	Ri_b
A101	2.867	2.374	296.3	42.94	30.20	30.70	48.24	-0.017
A102	2.718	2.398	275.9	30.29	29.84	30.82	50.84	-0.039
A103	-99999	-99999	-99999	-99999	-99999	N/A	N/A	N/A
A104	2.512	2.213	236.6	43.99	30.07	N/A	N/A	N/A
A105	2.465	2.094	276.2	34.83	29.56	30.29	49.50	-0.035
A106	2.566	2.370	290.5	23.86	30.27	31.25	45.70	-0.044
A107	1.954	1.417	334.1	66.07	30.58	31.68	50.12	-0.086
A108	2.347	2.066	303.0	34.87	30.02	31.06	48.63	-0.057
A109	2.357	2.299	265.7	20.53	29.03	30.14	52.04	-0.060
A110	2.205	1.523	227.5	49.67	29.09	29.94	48.33	-0.052
A111	3.733	3.024	315.2	49.26	N/A	N/A	N/A	N/A
A112	2.559	2.127	320.6	42.86	N/A	N/A	N/A	N/A
A113	3.406	3.048	246.1	29.66	N/A	N/A	N/A	N/A
A114	3.245	2.905	269.4	27.57	30.41	31.11	N/A	-0.016
A115	3.377	3.060	264.3	26.55	30.06	31.11	N/A	N/A

Notes:

1. All wind speed and direction measurements are at 10 m, except for Station A115 which is at 30 m.
2. All upper temperature measurements (T_{10m}) are at 10 m as implied by the subscript, except for Station A114 which is at 8 m and Station A115 which is at 30 m.
3. All lower temperature measurements (T_{2m}) are at 2 m as implied by the subscript.
4. Soil temperature measurements (T_{soil}) are a depth of 0.1 m.

Table 3.5 Synopsis of surface-station data for Test 0925871. Smoke was released from 00:18 to 01:03. The stable release point was used.

Station	S [m/s]	U [m/s]	θ [°]	σ_θ [°]	T_{10m} [C]	T_{2m} [C]	T_{soil} [C]	Ri_b
A101	1.182	1.099	121.7	22.36	16.41	15.65	14.67	0.204
A102	0.389	0.328	66.64	48.47	15.59	14.20	12.76	3.308
A103	-99999	-99999	-99999	-99999	-99999	N/A	N/A	N/A
A104	2.770	2.641	52.73	17.08	15.62	N/A	N/A	N/A
A105	2.370	2.332	118.6	10.28	17.29	17.02	17.80	0.021
A106	2.079	1.967	88.00	21.51	16.51	16.00	18.17	0.046
A107	1.622	1.550	165.5	17.07	15.99	15.17	15.92	0.116
A108	1.932	1.889	114.4	11.76	15.27	14.29	17.08	0.097
A109	1.954	1.944	55.65	10.94	19.53	19.25	17.84	0.031
A110	2.002	1.978	96.37	9.143	18.90	18.45	18.73	0.044
A111	0.324	0.323	190.2	0.208	N/A	N/A	N/A	N/A
A112	3.085	3.070	155.8	5.585	N/A	N/A	N/A	N/A
A113	3.041	3.011	99.96	8.009	N/A	N/A	N/A	N/A
A114	0.468	0.385	71.66	53.36	15.56	14.35	N/A	1.578
A115	1.307	1.291	66.47	10.46	16.24	14.35	N/A	N/A

Notes:

1. All wind speed and direction measurements are at 10 m, except for Station A115 which is at 30 m.
2. All upper temperature measurements (T_{10m}) are at 10 m as implied by the subscript, except for Station A114 which is at 8 m and Station A115 which is at 30 m.
3. All lower temperature measurements (T_{2m}) are at 2 m as implied by the subscript.
4. Soil temperature measurements (T_{soil}) are a depth of 0.1 m.
5. 1 bad minute was excluded in computing the 2-m temperature for Station A114.
6. 3 bad minutes were excluded in computing the 10-m temperature for Station A114.
7. 1 bad minute was excluded in computing the 10-m temperature for Station A115.
8. 2 bad minutes were excluded in computing the 10-m temperature for Station A115.

Table 3.6 Synopsis of surface-station data for Test 0926871. Smoke was released from 12:00 to 13:07. The unstable release point was used.

Station	S [m/s]	U [m/s]	θ [°]	σ_θ [°]	T_{10m} [C]	T_{2m} [C]	T_{soil} [C]	Ri_b
A101	4.856	4.721	302.4	34.41	25.34	26.22	41.64	-0.011
A102	3.735	3.331	299.7	40.65	25.40	26.27	44.77	-0.019
A103	4.242	3.933	238.4	30.15	26.78	N/A	N/A	N/A
A104	2.486	1.922	249.5	59.97	25.96	N/A	N/A	N/A
A105	4.214	3.961	314.5	36.38	25.15	26.08	41.25	-0.016
A106	3.538	3.263	291.0	34.14	25.69	26.64	37.51	-0.023
A107	3.043	2.796	316.6	41.13	25.80	26.68	45.58	-0.028
A108	4.032	3.871	279.9	32.51	25.26	26.26	41.91	-0.019
A109	2.688	2.576	294.4	35.75	24.20	25.75	45.72	-0.067
A110	3.786	3.552	315.3	42.11	24.25	25.23	42.21	-0.021
A111	6.505	6.343	316.6	30.23	N/A	N/A	N/A	N/A
A112	4.198	4.057	313.6	28.68	N/A	N/A	N/A	N/A
A113	3.666	3.098	308.2	44.04	N/A	N/A	N/A	N/A
A114	4.475	4.026	294.4	46.78	26.21	26.79	N/A	-0.007
A115	4.722	4.353	291.0	27.09	25.81	26.79	N/A	N/A

Notes:

1. All wind speed and direction measurements are at 10 m, except for Station A115 which is at 30 m.
2. All upper temperature measurements (T_{10m}) are at 10 m as implied by the subscript, except for Station A114 which is at 8 m and Station A115 which is at 30 m.
3. All lower temperature measurements (T_{2m}) are at 2 m as implied by the subscript.
4. Soil temperature measurements (T_{soil}) are at depth of 0.1 m.
5. 1 bad minute was excluded in computing the vector speed and direction for Station A112.
6. 1 bad minute was excluded in computing the vector speed and direction for Station A113.

Table 3.7 Synopsis of surface-station data for Test 0927871. Smoke was released from 03:19 to 03:39. The stable release point was used.

Station	S [m/s]	U [m/s]	θ [°]	σ_θ [°]	T_{10m} [C]	T_{2m} [C]	T_{soil} [C]	Ri_b
A101	1.055	0.920	117.6	28.17	13.23	11.75	8.263	0.480
A102	0.348	0.218	91.02	69.02	11.50	9.928	5.349	4.696
A103	2.880	2.821	64.33	11.94	12.77	N/A	N/A	N/A
A104	3.819	3.741	54.14	11.27	12.55	N/A	N/A	N/A
A105	2.25[illegible]	2.216	113.5	10.01	16.76	16.06	13.35	0.052
A106	2.0[illegible]	1.959	103.1	19.10	12.60	11.38	13.00	0.110
A107	1.3[illegible]	1.325	139.0	15.14	12.04	10.27	9.758	0.339
A108	1.866	1.833	98.54	10.70	11.95	9.737	11.61	0.226
A109	0.868	0.746	20.11	32.54	21.65	20.87	12.93	0.377
A110	0.646	0.555	138.0	35.80	19.70	17.82	14.24	1.571
A111	2.507	2.392	145.4	17.44	N/A	N/A	N/A	N/A
A112	2.101	2.059	156.8	14.50	N/A	N/A	N/A	N/A
A113	3.483	3.457	80.30	7.269	N/A	N/A	N/A	N/A
A114	0.671	0.556	74.32	36.88	11.42	9.235	N/A	1.372
A115	1.213	1.124	13.47	23.32	13.05	9.235	N/A	N/A

Notes:

1. All wind speed and direction measurements are at 10 m, except for Station A115 which is at 30 m.
2. All upper temperature measurements (T_{10m}) are at 10 m as implied by the subscript, except for Station A114 which is at 8 m and Station A115 which is at 30 m.
3. All lower temperature measurements (T_{2m}) are at 2 m as implied by the subscript.
4. Soil temperature measurements (T_{soil}) are a depth of 0.1 m.
5. 3 bad minutes were excluded in computing the 10-m temperature for Station A115.

Table 3.8 Synopsis of surface-station data for Test 0927872. Smoke was released from 06:44 to 06:54. The stable release point was used.

Station	S [m/s]	U [m/s]	θ [°]	σ_θ [°]	T_{10m} [C]	T_{2m} [C]	T_{soil} [C]	Ri_b
A101	1.232	1.079	132.3	31.24	11.56	10.39	6.403	0.283
A102	0.648	0.425	98.63	51.68	9.870	8.232	3.937	1.418
A103	-99999	-99999	-99999	-99999	-99999	N/A	N/A	N/A
A104	3.601	3.568	57.50	7.609	10.67	N/A	N/A	N/A
A105	2.227	2.178	113.9	12.35	15.72	14.96	11.88	0.057
A106	2.836	2.780	99.05	11.61	11.86	10.98	11.52	0.041
A107	1.818	1.765	146.9	13.74	10.51	8.841	7.890	0.183
A108	2.562	2.541	102.0	7.438	9.763	7.847	10.05	0.105
A109	1.338	1.311	114.6	21.87	20.28	19.25	10.93	0.208
A110	2.002	1.994	146.9	5.190	18.02	16.39	13.11	0.144
A111	2.402	2.232	158.0	23.00	N/A	N/A	N/A	N/A
A112	3.096	3.077	157.8	6.425	N/A	N/A	N/A	N/A
A113	3.100	3.062	82.58	9.310	N/A	N/A	N/A	N/A
A114	1.022	0.901	76.79	32.00	9.635	8.253	N/A	0.393
A115	1.509	1.488	9.496	9.026	11.59	8.253	N/A	N/A

Notes:

1. All wind speed and direction measurements are at 10 m, except for Station A115 which is at 30 m.
2. All upper temperature measurements (T_{10m}) are at 10 m as implied by the subscript, except for Station A114 which is at 8 m and Station A115 which is at 30 m.
3. All lower temperature measurements (T_{2m}) are at 2 m as implied by the subscript.
4. Soil temperature measurements (T_{soil}) are a depth of 0.1 m.
5 1 bad minute was excluded in computing the vector speed and direction for Station A109.

Table 3.9 Synopsis of surface-station data for Test 0928871. Smoke was released from 10:29 to 10:54. The unstable release point was used.

Station	S [m/s]	U [m/s]	θ [°]	σ_θ [°]	T_{10m} [C]	T_{2m} [C]	T_{soil} [C]	Ri_b
A101	2.740	2.702	301.4	9.667	25.70	26.32	37.32	-0.024
A102	2.585	2.542	265.9	10.54	26.18	27.01	40.31	-0.037
A103	-99999	-99999	-99999	-99999	-99999	N/A	N/A	N/A
A104	2.517	2.430	226.7	14.73	26.90	N/A	N/A	N/A
A105	2.058	1.885	286.5	23.30	26.46	27.09	36.00	-0.043
A106	2.313	2.267	259.4	11.45	26.70	27.47	31.06	-0.042
A107	1.864	1.727	326.7	22.58	27.29	28.00	38.64	-0.059
A108	2.213	2.112	308.9	16.96	26.87	28.02	32.22	-0.072
A109	-99999	-99999	-99999	-99999	-99999	-99999	-99999	-99999
A110	1.687	1.637	324.3	13.69	25.76	26.45	38.11	-0.071
A111	3.700	3.650	306.6	9.499	N/A	N/A	N/A	N/A
A112	2.355	2.139	327.2	24.96	N/A	N/A	N/A	N/A
A113	2.934	2.831	236.6	15.62	N/A	N/A	N/A	N/A
A114	3.136	3.101	258.3	8.946	26.77	27.18	N/A	-0.09
A115	2.508	2.461	286.1	11.40	26.54	27.18	N/A	N/A

Notes:

1. All wind speed and direction measurements are at 10 m, except for Station A115 which is at 30 m.
2. All upper temperature measurements (T_{10m}) are at 10 m as implied by the subscript, except for Station A114 which is at 8 m and Station A115 which is at 30 m.
3. All lower temperature measurements (T_{2m}) are at 2 m as implied by the subscript.
4. Soil temperature measurements (T_{soil}) are a depth of 0.1 m.

Table 3.10 Synopsis of surface-station data for Test 0930871. Smoke was released from 06:48 to 07:28. The stable release point was used.

Station	S [m/s]	U [m/s]	θ [°]	σ_θ [°]	T_{10m} [C]	T_{2m} [C]	T_{soil} [C]	Ri_b
A101	1.528	1.441	121.9	19.15	18.89	17.12	12.07	0.265
A102	0.946	0.853	78.45	26.80	18.02	15.25	9.410	1.072
A103	2.531	2.453	82.01	13.71	18.09	N/A	N/A	N/A
A104	3.000	2.862	42.17	16.26	17.73	N/A	N/A	N/A
A105	3.110	3.048	116.3	11.39	20.81	20.12	16.75	0.026
A106	3.217	3.161	79.98	10.83	19.61	18.79	16.72	0.029
A107	1.942	1.854	159.7	17.43	16.34	15.83	13.11	0.231
A108	2.405	2.329	112.4	14.75	17.21	14.55	14.19	0.160
A109	-99999	-99999	-99999	-99999	-99999	-99999	-99999	-99999
A110	1.712	1.688	112.4	9.821	25.20	23.22	17.60	0.231
A111	3.137	3.037	155.9	14.54	N/A	N/A	N/A	N/A
A112	3.746	3.730	159.3	5.228	N/A	N/A	N/A	N/A
A113	4.410	4.295	94.20	13.11	N/A	N/A	N/A	N/A
A114	1.465	1.391	74.19	19.69	17.79	15.41	N/A	0.306
A115	2.052	2.005	74.27	13.22	18.96	15.41	N/A	N/A

Notes:

1. All wind speed and direction measurements are at 10 m, except for Station A115 which is at 30 m.
2. All upper temperature measurements (T_{10m}) are at 10 m as implied by the subscript, except for Station A114 which is at 8 m and Station A115 which is at 30 m.
3. All lower temperature measurements (T_{2m}) are at 2 m as implied by the subscript.
4. Soil temperature measurements (T_{soil}) are a depth of 0.1 m.

Table 3.11 Synopsis of surface-station data for Test 1001871. Smoke was released from 06:52 to 07:32. The stable release point was used.

Station	S [m/s]	U [m/s]	θ [°]	σθ [°]	T_{10m} [C]	T_{2m} [C]	T_{soil} [C]	Ri_b
A101	1.359	1.216	119.4	26.82	20.32	18.56	14.08	0.332
A102	0.944	0.770	93.50	52.05	19.32	17.55	11.35	0.696
A103	2.252	2.009	91.60	28.82	19.80	N/A	N/A	N/A
A104	3.922	3.642	52.45	22.01	20.36	N/A	N/A	N/A
A105	2.803	2.742	120.6	12.08	21.98	21.31	17.79	0.032
A106	3.438	3.313	78.56	18.52	20.53	20.12	18.73	0.014
A107	2.322	2.225	161.2	16.78	19.27	18.20	14.86	0.071
A108	2.745	2.669	112.1	13.56	18.02	16.13	15.49	0.088
A109	2.949	2.926	61.08	11.35	27.33	26.31	19.28	0.041
A110	1.979	1.762	100.8	32.83	24.80	23.29	19.55	0.133
A111	2.787	2.686	148.0	15.32	N/A	N/A	N/A	N/A
A112	3.733	3.693	157.5	8.690	N/A	N/A	N/A	N/A
A113	4.103	3.716	90.89	26.16	N/A	N/A	N/A	N/A
A114	1.379	1.221	81.78	28.83	19.05	17.45	N/A	0.234
A115	2.243	2.197	80.74	12.32	20.25	17.45	N/A	N/A

Notes:

1. All wind speed and direction measurements are at 10 m, except for Station A115 which is at 30 m.
2. All upper temperature measurements (T_{10m}) are at 10 m as implied by the subscript, except for Station A114 which is at 8 m and Station A115 which is at 30 m.
3. All lower temperature measurements (T_{2m}) are at 2 m as implied by the subscript.
4. Soil temperature measurements (T_{soil}) are a depth of 0.1 m.

Table 3.12 Synopsis of surface-station data for Test 1002871. Smoke was released from 07:17 to 07:47. The stable release point was used.

Station	S [m/s]	U [m/s]	θ [°]	σ_θ [°]	T_{10m} [C]	T_{2m} [C]	T_{soil} [C]	Ri_b
A101	1.542	1.484	112.7	15.33	18.90	17.78	14.99	0.170
A102	0.745	0.685	76.10	34.68	18.01	16.33	12.46	1.067
A103	1.989	1.933	85.07	13.22	18.41	N/A	N/A	N/A
A104	3.249	3.102	51.00	17.30	18.78	N/A	N/A	N/A
A105	2.930	2.897	115.1	8.395	20.48	20.02	18.37	0.021
A106	2.157	2.068	94.06	16.23	18.73	18.11	18.11	0.050
A107	1.513	1.429	159.6	19.27	18.28	16.26	14.72	0.308
A108	1.944	1.890	104.3	13.75	17.37	15.22	15.97	0.199
A109	2.217	2.172	56.79	14.97	24.80	24.15	18.51	0.049
A110	1.409	1.374	104.5	12.76	23.16	21.94	19.37	0.216
A111	2.914	2.855	148.7	11.38	N/A	N/A	N/A	N/A
A112	3.189	3.177	157.3	5.066	N/A	N/A	N/A	N/A
A113	3.534	3.482	100.7	9.951	N/A	N/A	N/A	N/A
A114	1.257	1.219	72.34	18.44	18.01	16.78	N/A	0.220
A115	1.915	1.887	74.17	10.57	18.77	16.78	N/A	N/A

Notes:

1. All wind speed and direction measurements are at 10 m, except for Station A115 which is at 30 m.
2. All upper temperature measurements (T_{10m}) are at 10 m as implied by the subscript, except for Station A114 which is at 8 m and Station A115 which is at 30 m.
3. All lower temperature measurements (T_{2m}) are at 2 m as implied by the subscript.
4. Soil temperature measurements (T_{soil}) are a depth of 0.1 m.
5. 1 bad minute was excluded in computing the 10-m temperature for Station A111

Table 3.13 Synopsis of surface-station data for Test 1002872. Smoke was released from 12:16 to 12:34. The unstable release point was used.

Station	S [m/s]	U [m/s]	θ [°]	σ_θ [°]	T_{10m} [C]	T_{2m} [C]	T_{soil} [C]	Ri_b
A101	2.098	2.005	283.6	17.77	30.09	30.50	43.57	-0.024
A102	2.798	2.710	247.9	14.51	30.07	30.95	43.81	-0.033
A103	3.131	2.975	240.9	18.61	31.97	N/A	N/A	N/A
A104	2.951	2.794	220.3	18.88	30.58	N/A	N/A	N/A
A105	2.214	2.023	283.1	24.14	29.85	30.55	47.25	-0.041
A106	2.531	2.446	260.8	16.39	30.39	31.34	41.06	-0.044
A107	1.834	1.670	311.0	28.90	30.81	31.64	48.17	-0.072
A108	1.757	1.513	277.6	35.32	30.47	31.59	46.11	-0.109
A109	2.021	1.962	265.5	20.12	29.72	30.96	49.18	-0.092
A110	1.844	1.720	320.0	20.90	29.03	29.84	46.64	-0.070
A111	2.868	2.666	289.3	22.35	N/A	N/A	N/A	N/A
A112	0.225	0.190	74.11	32.29	N/A	N/A	N/A	N/A
A113	3.574	3.419	226.2	17.10	N/A	N/A	N/A	N/A
A114	3.506	3.421	244.2	12.51	30.40	31.15	N/A	-0.014
A115	3.430	3.354	250.3	12.07	30.05	31.15	N/A	N/A

Notes:

1. All wind speed and direction measurements are at 10 m, except for Station A115 which is at 30 m.
2. All upper temperature measurements (T_{10m}) are at 10 m as implied by the subscript, except for Station A114 which is at 8 m and Station A115 which is at 30 m.
3. All lower temperature measurements (T_{2m}) are at 2 m as implied by the subscript.
4. Soil temperature measurements (T_{soil}) are a depth of 0.1 m.

Table 3.14 Synopsis of surface-station data for Test 1003871. Smoke was released from 06:56 to 07:27. The stable release point was used.

Station	S [m/s]	U [m/s]	θ [°]	σ_θ [°]	T_{10m} [C]	T_{2m} [C]	T_{soil} [C]	Ri_b
A101	1.153	1.045	114.8	25.19	18.29	16.96	14.19	0.355
A102	0.659	0.432	122.6	63.18	17.68	15.38	12.98	1.851
A103	-99999	-99999	-99999	-99999	-99999	N/A	N/A	N/A
A104	2.830	2.754	63.14	12.70	17.96	N/A	N/A	N/A
A105	2.716	2.682	131.1	9.152	20.67	19.93	17.78	0.037
A106	2.394	2.133	81.94	50.65	18.93	18.26	18.02	0.044
A107	1.917	1.822	163.3	18.12	18.57	17.43	14.82	0.111
A108	3.032	2.977	115.3	10.78	18.05	17.04	16.09	0.040
A109	3.005	2.984	84.22	10.33	25.49	24.57	17.87	0.036
A110	2.148	2.104	96.12	21.00	23.51	22.46	18.81	0.081
A111	2.596	2.468	144.2	18.18	N/A	N/A	N/A	N/A
A112	3.419	3.389	157.1	7.796	N/A	N/A	N/A	N/A
A113	3.676	3.579	79.30	13.41	N/A	N/A	N/A	N/A
A114	0.827	0.584	116.6	62.96	17.28	15.84	N/A	0.579
A115	1.611	1.579	85.52	13.62	18.56	15.84	N/A	N/A

Notes:

1. All wind speed and direction measurements are at 10 m, except for Station A115 which is at 30 m.
2. All upper temperature measurements (T_{10m}) are at 10 m as implied by the subscript, except for Station A114 which is at 8 m and Station A115 which is at 30 m.
3. All lower temperature measurements (T_{2m}) are at 2 m as implied by the subscript.
4. Soil temperature measurements (T_{soil}) are a depth of 0.1 m.

1. The analysis of the micrometeorological data was completed using the 1-s data read directly from tape, whereas the analysis of the surface-station data was made using 1-min averages. Thus, no adjustment to σ_θ (as in Eqn. 3.9) is necessary for these data.

2. The wind velocity was specified by the three Cartesian components u_1, u_2, and u_3, instead of speed and direction. In the first step of the analysis, averages of the three components are computed separately from the following expressions.

$$U_1 = \frac{1}{N}\sum_{n=1}^{N} u_{1i} , \tag{3.18}$$

$$U_2 = \frac{1}{N}\sum_{n=1}^{N} u_{2i} \tag{3.19}$$

and

$$U_3 = \frac{1}{N}\sum_{n=1}^{N} u_{3i} , \tag{3.20}$$

where u_{1i}, u_{2i}, u_{3i} represent individual 1-s measurements. Next, the vector-mean wind speed and direction are found from Eqns. 3.4 and 3.5 which are repeated here for the convenience of the reader.

$$U = \sqrt{U_1^2 + U_2^2}$$

$$\theta = \arctan (U_2, U_1)$$

Third, each of the 1-s wind velocity vectors is transformed into its mean-wind, cross-wind and vertical components using the three relationships

$$u_i = s_i \cos (\theta_i - \theta) ,$$

$$v_i = s_i \sin (\theta_i - \theta)$$

and

$$w_i = u_{3i} , \tag{3.21}$$

where

$$s_i = \sqrt{u_{1i}^2 + u_{2i}^2} . \tag{3.22}$$

Lastly, standard deviations are computed for the components u, v, and w.

3. The averaging period was chosen to assure compatibility with the spectral analysis of the u, v and w fluctuations presented in Section 3.3.2. Thus, the averaging period is not exactly the same as that used for the surface station data, although the net effect of this difference is expected to be small.

The synopsis of the micrometeorological data for each of the 12 smoke trials is given in Tables 3.15 to 3.26. In these tables, the string "-99999" is used to indicate that a valid average could not be computed. It is readily apparent that there are several occasions when one or more of the tower levels was inoperative. The 4-m level is particularly troublesome in this regard. Also, a significant number of bad data are present in the original records for some cases. Despite this limitation, we felt that a valid average could be obtained in most instances, and have reported the results as such.

3.3.2 Power Spectra

As discussed previously in Section 2.5.2, the power spectra of the velocity fluctuations provide valuable information about the structure of the atmospheric boundary layer. Specifically, analysis of spectra allows one to determine the scale of motions which most contribute to horizontal and vertical mixing. The spectra also allow the consistency of the data between the various measurement levels to be assessed and comparisons with other studies of the atmospheric boundary layer to be made.

Two alternative methods are available to compute the single-sided power spectrum. One method, which we call the "direct method," involves the direct computation of the autocorrelation function of the velocity fluctuations. The autocorrelation function is then integrated to obtain the spectra. This method is very accurate but is also computationally expensive. A second method, which we call the "indirect method," relies on the use of Fast Fourier Transform techniques to decompose individual segments of the data into their sine and cosine components. These transformed data are then ensemble averaged to obtain the spectra. Because the individual data segments may have sharp discontinuities at the boundaries which may lead to excessive noise in the high frequency end, a filter function is applied to the data to reduce end values and all derivatives thereof to zero.

In order that we might be able to detect changes in the meteorological conditions during a single smoke release, we have elected to use the indirect method. This method generates a number of short-term spectra which can be analyzed for consistency. Of special concern are those tests which were conducted just before an expected transitional period.

Table 3.15 Synopsis of the micrometeorological data for Test 0921871. Smoke was released from 14:30 to 15:00. The unstable release point was used.

Level	U [m/s]	S [m/s]	W [m/s]	θ [°]	T [C]
2 m	2.639	3.000	-0.0620	301.9	39.17
4 m	2.915	3.283	-0.1325	298.1	38.79
8 m	3.184	3.553	-0.1555	297.6	38.65
16 m	3.318	3.697	-0.3584	300.7	38.50
30 m	3.331	3.748	-0.1245	301.5	38.28

Level	σ_u [m/s]	σ_s [m/s]	σ_v [m/s]	σ_w [m/s]	σ_θ [°]	σ_t [C]
2 m	1.011	1.067	1.467	0.2114	28.9	0.24
4 m	1.150	1.183	1.535	0.2965	28.3	0.24
8 m	1.194	1.205	1.586	0.4014	27.3	0.23
16 m	1.167	1.177	1.639	0.5695	27.0	0.23
30 m	1.198	1.173	1.700	0.7115	28.2	0.20

Table 3.16 Synopsis of the micrometeorological data for Test 0923871. Smoke was released from 14:00 to 15:31. The smoke moved off the grid at 14:50. The unstable release point was used.

Level	U [m/s]	S [m/s]	W [m/s]	θ [°]	T [C]
2 m	2.120	2.382	0.0086	270.4	31.11
4 m	2.214	2.495	-0.0631	269.0	30.62
8 m	2.382	2.655	0.0078	269.6	30.41
16 m	2.458	2.588	-0.1515	276.1	30.26
30 m	2.512	2.771	0.0889	267.5	30.06

Level	σ_u [m/s]	σ_s [m/s]	σ_v [m/s]	σ_w [m/s]	σ_θ [°]	σ_t [C]
2 m	1.044	0.950	0.997	0.1911	31.4	0.35
4 m	1.099	1.002	1.059	0.2452	31.6	0.34
8 m	1.138	1.045	1.082	0.3162	29.1	0.34
16 m	1.095	1.063	0.765	0.4372	20.4	0.31
30 m	1.082	0.952	1.052	0.5852	28.2	0.30

Table 3.17 Synopsis of the micrometeorological data for Test 0925871. Smoke was released from 00:18 to 01:03. The stable release point was used.

Level	U [m/s]	S [m/s]	W [m/s]	θ [°]	T [C]
2 m	0.198	0.369	0.0230	121.0	14.35
4 m	0.229	0.363	0.0075	93.4	-99999
8 m	0.302	0.465	0.0242	67.0	15.56
16 m	0.577	0.631	-0.0539	78.4	15.91
30 m	1.203	1.218	0.0246	86.7	16.24

Level	σ_u [m/s]	σ_s [m/s]	σ_v [m/s]	σ_w [m/s]	σ_θ [°]	σ_t [C]
2 m	0.231	0.176	0.273	0.0553	70.4	0.46
4 m	0.213	0.186	0.262	0.0738	54.9	-99999
8 m	0.283	0.225	0.308	0.0586	64.2	0.35
16 m	0.316	0.285	0.215	0.0760	31.1	0.15
30 m	0.361	0.353	0.174	0.1537	11.6	0.18

Table 3.18 Synopsis of the micrometeorological data for Test 0926871. Smoke was released from 12:00 to 13:07. The unstable release point was used.

Level	U [m/s]	S [m/s]	W [m/s]	θ [°]	T [C]
2 m	2.583	2.992	0.0210	293.1	26.79
4 m	-99999	-99999	-99999	-99999	-99999
8 m	3.156	3.560	-0.1115	292.0	26.21
16 m	3.295	3.682	-0.2265	296.7	26.07
30 m	3.286	3.691	0.0728	295.8	25.81

Level	σ_u [m/s]	σ_s [m/s]	σ_v [m/s]	σ_w [m/s]	σ_θ [°]	σ_t [C]
2 m	1.260	1.235	1.489	0.2403	33.4	0.79
4 m	-99999	-99999	-99999	-99999	-99999	-99999
8 m	1.436	1.382	1.600	0.4350	31.2	0.71
16 m	1.371	1.336	1.613	0.6119	29.2	0.69
30 m	1.372	1.301	1.624	0.7838	32.4	0.66

Table 3.19 Synopsis of the micrometeorological data for Test 0927871. Smoke was released from 03:19 to 03:39. The stable release point was used.

Level	U [m/s]	S [m/s]	W [m/s]	θ [°]	T [C]
2 m	0.474	0.628	0.0210	98.8	9.24
4 m	-99999	-99999	-99999	-99999	-99999
8 m	0.432	0.621	-0.0256	82.2	11.42
16 m	0.556	0.729	-0.0661	58.4	12.27
30 m	1.050	1.120	0.0726	83.1	13.05

Level	σ_u [m/s]	σ_s [m/s]	σ_v [m/s]	σ_w [m/s]	σ_θ [°]	σ_t [C]
2 m	0.365	0.263	0.326	0.0631	53.3	0.82
4 m	-99999	-99999	-99999	-99999	-99999	-99999
8 m	0 266	0.210	0.415	0.0817	48.4	0.32
16 m	0.225	0.248	0.482	0.0738	42.7	0.26
30 m	0.327	0.302	0.370	0.1573	22.0	0.32

Table 3.20 Synopsis of the micrometeorological data for Test 0927872. Smoke was released from 06:44 to 06:54. The stable release point was used.

Level	U [m/s]	S [m/s]	W [m/s]	θ [°]	T [C]
2 m	0.332	0.582	0.0163	101.0	8.25
4 m	-99999	-99999	-99999	-99999	-99999
8 m	0.589	0.770	-0.0395	73.6	9.64
16 m	0.968	1.058	-0.1090	72.1	10.52
30 m	1.358	1.377	0.0452	79.6	11.59

Level	σ_u [m/s]	σ_s [m/s]	σ_v [m/s]	σ_w [m/s]	σ_θ [°]	σ_t [C]
2 m	0.371	0.300	0.425	0.0714	62.1	0.65
4 m	-99999	-99999	-99999	-99999	-99999	-99999
8 m	0.491	0.410	0.417	0.1152	47.0	0.50
16 m	0.522	0.488	0.383	0.0654	27.3	0.31
30 m	0.377	0.371	0.218	0.1819	10.2	0.16

Table 3.21 Synopsis of the micrometeorological data for Test 0928871. Smoke was released from 10:29 to 10:54. The unstable release point was used.

Level	U [m/s]	S [m/s]	W [m/s]	θ [°]	T [C]
2 m	2.517	2.549	0.0560	260.4	27.18
4 m	-99999	-99999	-99999	-99999	-99999
8 m	2.728	2.757	-0.0072	259.9	26.77
16 m	2.590	2.619	-0.1558	261.2	26.77
30 m	2.131	2.167	0.0117	262.2	26.54

Level	σ_u [m/s]	σ_s [m/s]	σ_v [m/s]	σ_w [m/s]	σ_θ [°]	σ_t [C]
2 m	0.511	0.501	0.386	0.1367	9.5	0.24
4 m	-99999	-99999	-99999	-99999	-99999	-99999
8 m	0.515	0.507	0.388	0.2148	8.6	0.18
16 m	0.552	0.539	0.369	0.2607	9.2	0.19
30 m	0.552	0.545	0.383	0.2977	11.0	0.22

Table 3.22 Synopsis of the micrometeorological data for Test 0930871. Smoke was released from 06:48 to 07:28. The stable release point was used.

Level	U [m/s]	S [m/s]	W [m/s]	θ [°]	T [C]
2 m	0.705	0.775	0.0188	91.4	15.41
4 m	0.829	0.889	0.0324	83.4	16.75
8 m	0.953	1.049	-0.0278	70.1	17.79
16 m	1.258	1.339	-0.0371	74.8	19.08
30 m	1.739	1.778	0.0390	81.0	18.96

Level	σ_u [m/s]	σ_s [m/s]	σ_v [m/s]	σ_w [m/s]	σ_θ [°]	σ_t [C]
2 m	0.397	0.374	0.294	0.0686	30.4	0.66
4 m	0.348	0.332	0.306	0.1071	25.3	0.44
8 m	0.330	0.301	0.418	0.0958	26.9	0.25
16 m	0.438	0.413	0.435	0.1270	22.7	0.20
30 m	0.532	0.512	0.342	0.2004	13.9	0.17

Table 3.23 Synopsis of the micrometeorological data for Test 1001871. Smoke was released from 06:52 to 07:32. The stable release point was used.

Level	U [m/s]	S [m/s]	W [m/s]	θ [°]	T [C]
2 m	0.329	0.593	0.0087	96.0	17.45
4 m	0.504	0.678	0.0096	88.1	18.32
8 m	0.669	0.844	-0.0181	78.3	19.05
16 m	1.164	1.286	-0.0010	85.4	19.61
30 m	1.915	1.951	0.0799	87.7	20.25

Level	σ_u [m/s]	σ_s [m/s]	σ_v [m/s]	σ_w [m/s]	σ_θ [°]	σ_t [C]
2 m	0.324	0.303	0.480	0.0900	67.0	0.67
4 m	0.334	0.364	0.477	0.1237	45.9	0.43
8 m	0.424	0.407	0.501	0.1253	42.6	0.31
16 m	0.524	0.506	0.528	0.1612	28.3	0.22
30 m	0.643	0.633	0.353	0.2252	12.0	0.24

Table 3.24 Synopsis of the micrometeorological data for Test 1002871. Smoke was released from 07:17 to 07:47. The stable release point was used.

Level	U [m/s]	S [m/s]	W [m/s]	θ [°]	T [C]
2 m	0.576	0.609	0.0156	94.9	16.78
4 m	0.671	0.698	0.0101	86.1	17.55
8 m	0.813	0.878	-0.0443	68.4	18.01
16 m	1.187	1.233	-0.0524	76.7	18.56
30 m	1.709	1.738	-0.0014	82.4	18.77

Level	σ_u [m/s]	σ_s [m/s]	σ_v [m/s]	σ_w [m/s]	σ_θ [°]	σ_t [C]
2 m	0.421	0.400	0.145	0.0616	37.4	0.47
4 m	0.437	0.422	0.151	0.0965	25.4	0.36
8 m	0.490	0.460	0.286	0.0963	30.6	0.30
16 m	0.543	0.506	0.272	0.1221	20.3	0.14
30 m	0.583	0.570	0.290	0.1821	11.9	0.30

Table 3.25 Synopsis of the micrometeorological data for Test 1002872. Smoke was released from 12:16 to 12:34. The unstable release point was used.

Level	U [m/s]	S [m/s]	W [m/s]	θ [°]	T [C]
2 m	2.499	2.582	0.0605	245.3	31.15
4 m	2.533	2.623	-0.0406	242.2	30.69
8 m	2.700	2.775	0.0306	244.5	30.40
16 m	2.805	2.875	-0.1622	245.8	30.29
30 m	2.934	2.998	0.0266	246.8	30.05

Level	σ_u [m/s]	σ_s [m/s]	σ_v [m/s]	σ_w [m/s]	σ_θ [°]	σ_t [C]
2 m	0.705	0.689	0.630	0.1577	15.4	0.37
4 m	0.678	0.669	0.671	0.2004	15.7	0.31
8 m	0.686	0.680	0.633	0.2594	13.9	0.32
16 m	0.625	0.611	0.614	0.3651	13.1	0.31
30 m	0.530	0.513	0.602	0.4368	12.3	0.29

Table 3.26 Synopsis of the micrometeorological data for Test 1003871. Smoke was released from 06:56 to 07:27. The stable release point was used.

Level	U [m/s]	S [m/s]	W [m/s]	θ [°]	T [C]
2 m	0.202	0.589	0.0200	197.3	15.84
4 m	0.222	0.589	-0.0048	158.1	16.50
8 m	0.284	0.634	-0.0031	135.1	17.28
16 m	0.786	0.871	-0.0089	107.3	-99999
30 m	1.482	1.521	0.0704	94.7	18.56

Level	σ_u [m/s]	σ_s [m/s]	σ_v [m/s]	σ_w [m/s]	σ_θ [°]	σ_t [C]
2 m	0.465	0.247	0.388	0.0700	85.0	0.92
4 m	0.351	0.268	0.496	0.1103	70.3	0.78
8 m	0.389	0.255	0.484	0.1140	69.6	0.58
16 m	0.545	0.483	0.278	0.1472	48.6	-99999
30 m	0.696	0.682	0.316	0.2094	19.7	0.21

We chose an interval length of 512 s and divided the data record over the course of a single trial into overlapping segments of this length. By this we mean that the first segment runs from 1 to 512 s, the second segment from 257 to 768 s, the third segment from 513 to 1024 s, and so on. Overlapping segments are known to reduce aliasing and distortion in the high frequency end of the spectral estimate and reduce random error by providing additional estimates in the ensemble. Since meteorological data usually do not exhibit sharp peaks in their spectra, we used a Hanning filter function to smooth the endpoints of each segment. Each of these segments was then decomposed into its sine and cosine components using the Fast Fourier Transform, and the resulting decompositions were ensemble averaged to obtain the raw spectra. These raw spectra were then normalized by the ensemble average of the segment variances and smoothed by summing the spectrum over specific frequency intervals and assigning the net result to the mid-point of the interval. The intervals were chosen to keep $\Delta n/n$ roughly constant, where Δn and n are the width and midpoint of the interval, respectively.

Both methods discussed earlier do not provide a convenient mechanism for handling bad and missing data. Since the number of such data was quite small (<10), we elected to repair the data records by interpolating replacement values for the bad data. These few replacement values were only used for computing the spectra and do not affect the other results generated from the 1-s measurements.

The frequency-weighted, single-sided power spectra for the fluctuating components of wind velocity are presented in Figs. 3.4 – 3.15. For each figure, we have (a) $S_{uu}(n)$, the spectrum of the velocity fluctuations in the direction of the mean wind, (b) $S_{vv}(n)$, the spectrum of the velocity fluctuations in the direction normal to the mean wind, (c) $S_{ww}(n)$, the spectrum of the velocity fluctuations in the vertical direction and (d) the spectral ratios $S_{vv}(n) / S_{uu}(n)$ and $S_{ww}(n) / S_{uu}(n)$. These spectral ratios assist in determining if the turbulence may be considered locally isotropic.

As a group, the unstable daytime tests give the most coherent spectra with little variation between the levels for the mean-wind and cross-wind components. For the vertical spectra the upper levels have a greater fraction of energy in the low frequency range. This indicates that the scale of the turbulent motion increases with height as is usually observed. Moreover, most of the unstable cases show a fair degree of isotropy in the horizontal plane. Considering the overall coherence and the near-ideal high-frequency behavior of the unstable Meadowbrook spectra, comparison to flat-terrain spectra may allow a distinction to be made between eddy sizes which are terrain influenced and those that are not.

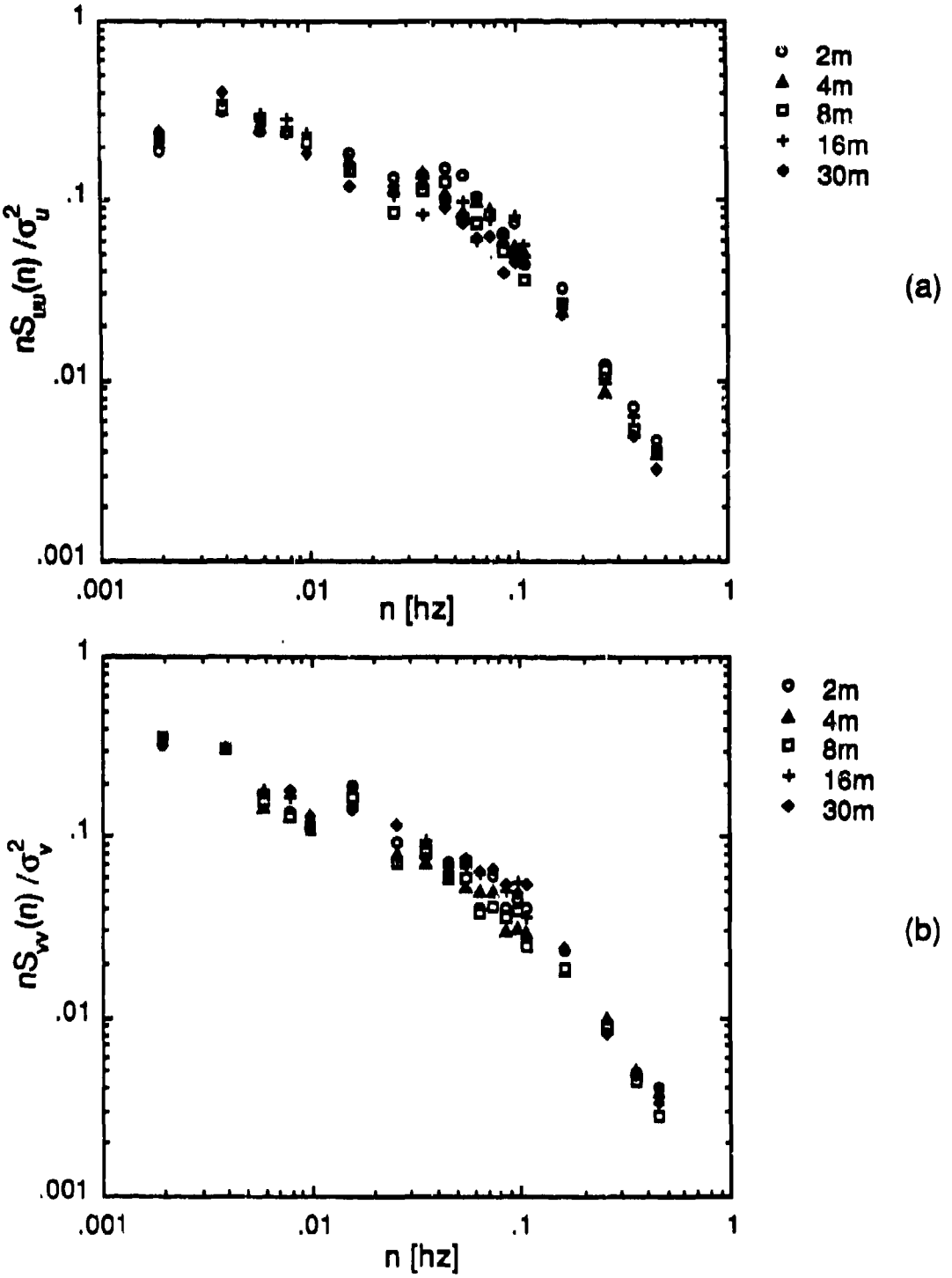

Figure 3.4 Spectra for Test 0921871 (a) mean-wind component and (b) cross-wind component. Smoke was released from 14:30 to 15:00. The unstable release point was used.

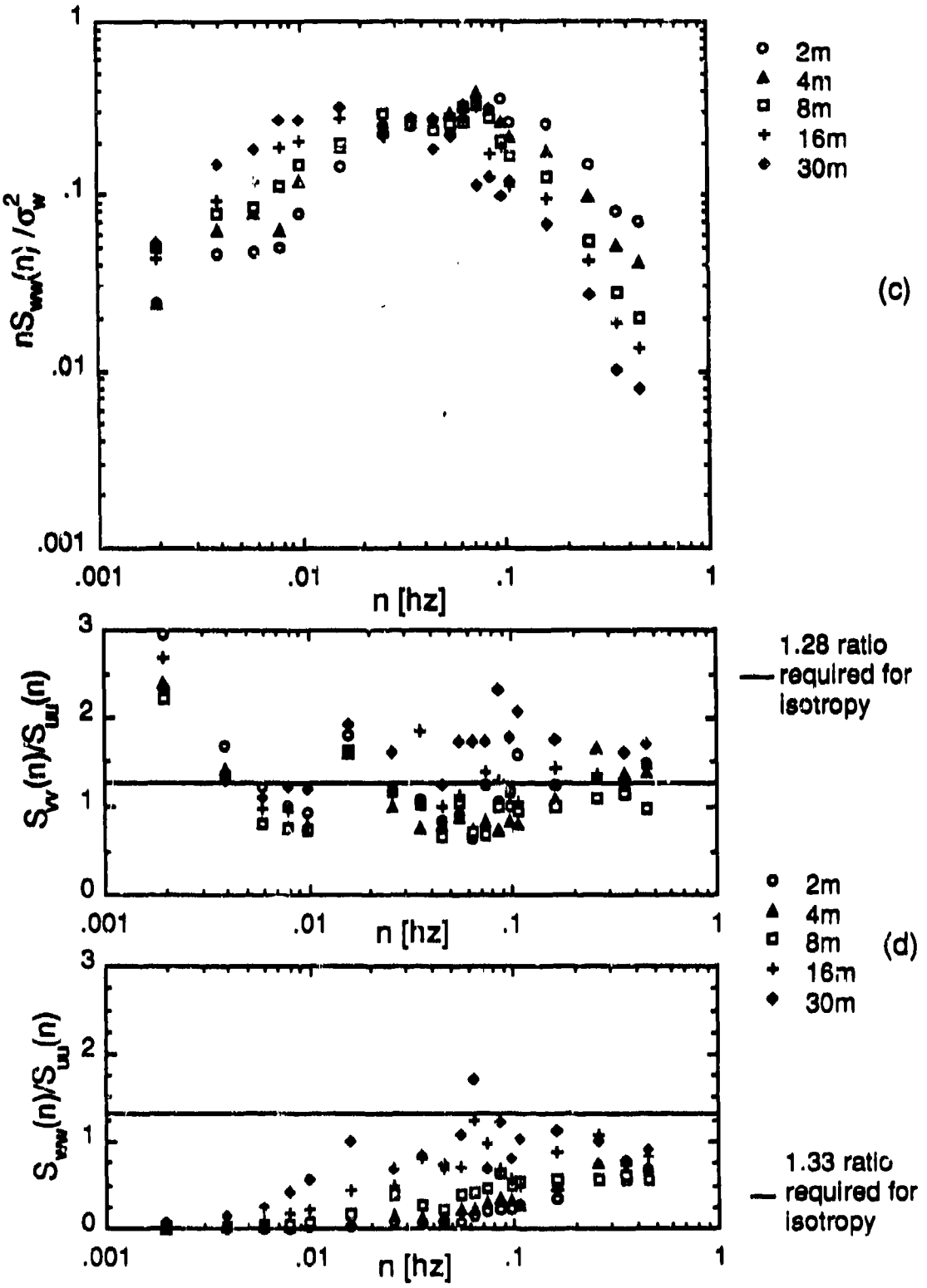

Figure 3.4 Spectra for Test 0921871 (c) vertical component and (d) spectral ratios. Smoke was released from 14:30 to 15:00. The unstable release point was used.

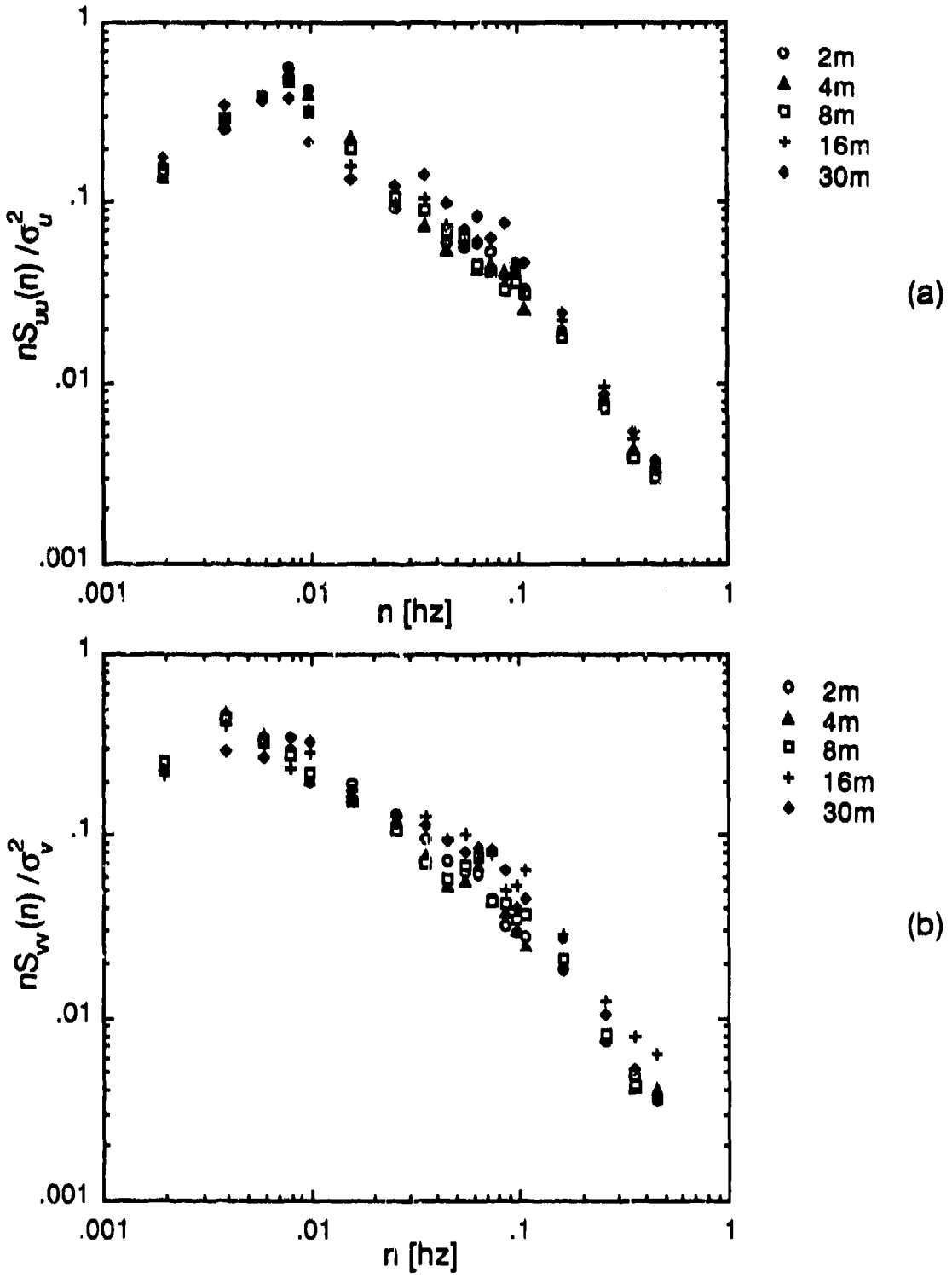

Figure 3.5 Spectra for Test 0923871 (a) mean-wind component and (b) cross-wind component. Smoke was released from 14:00 to 14:50. The smoke moved off the grid at 14:50. The unstable release point was used.

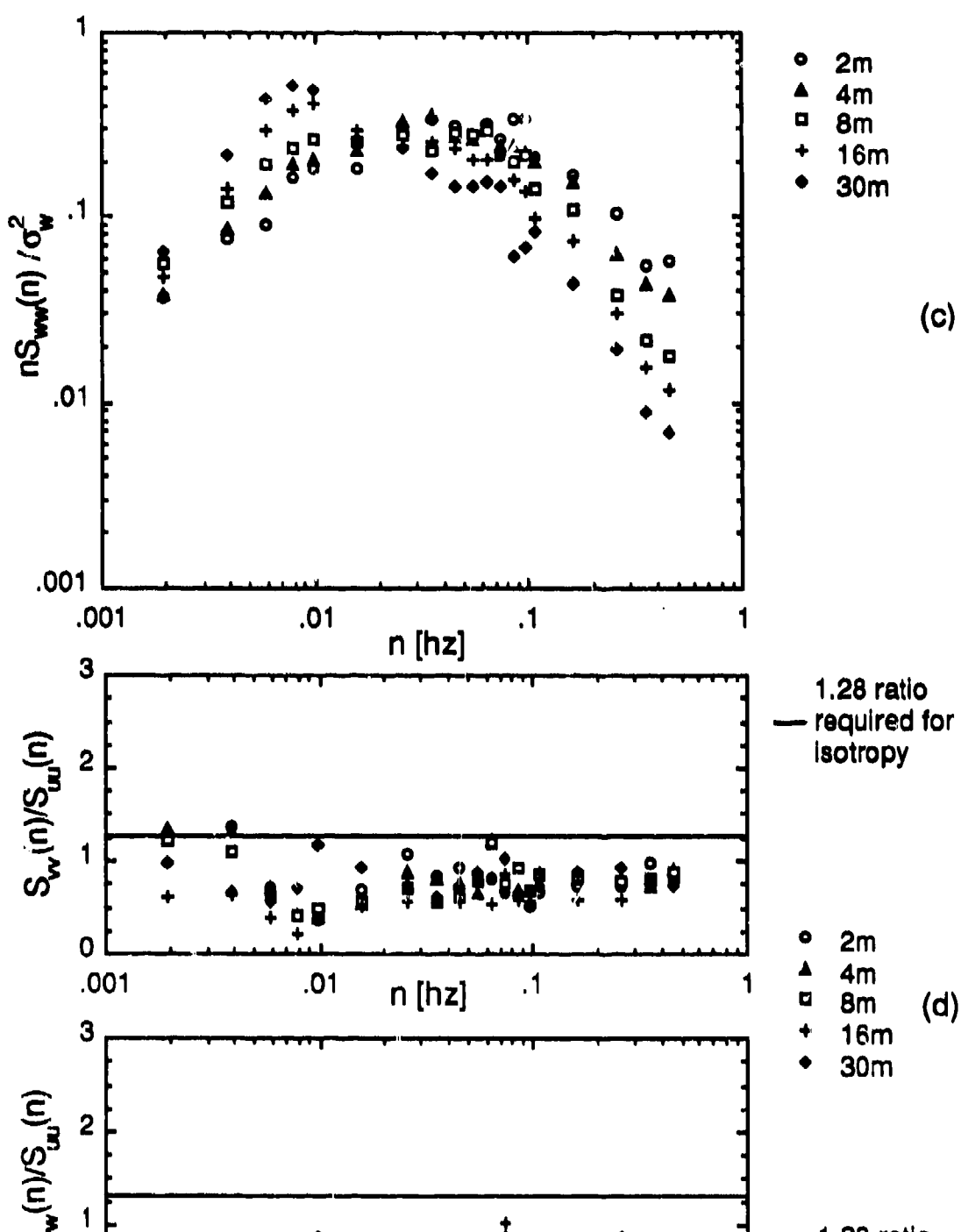

Figure 3.5 Spectra for Test 0923871 (c) vertical component and (d) spectral ratios. Smoke was released from 14:00 to 14:50. The smoke moved off the grid at 14:50. The unstable release point was used.

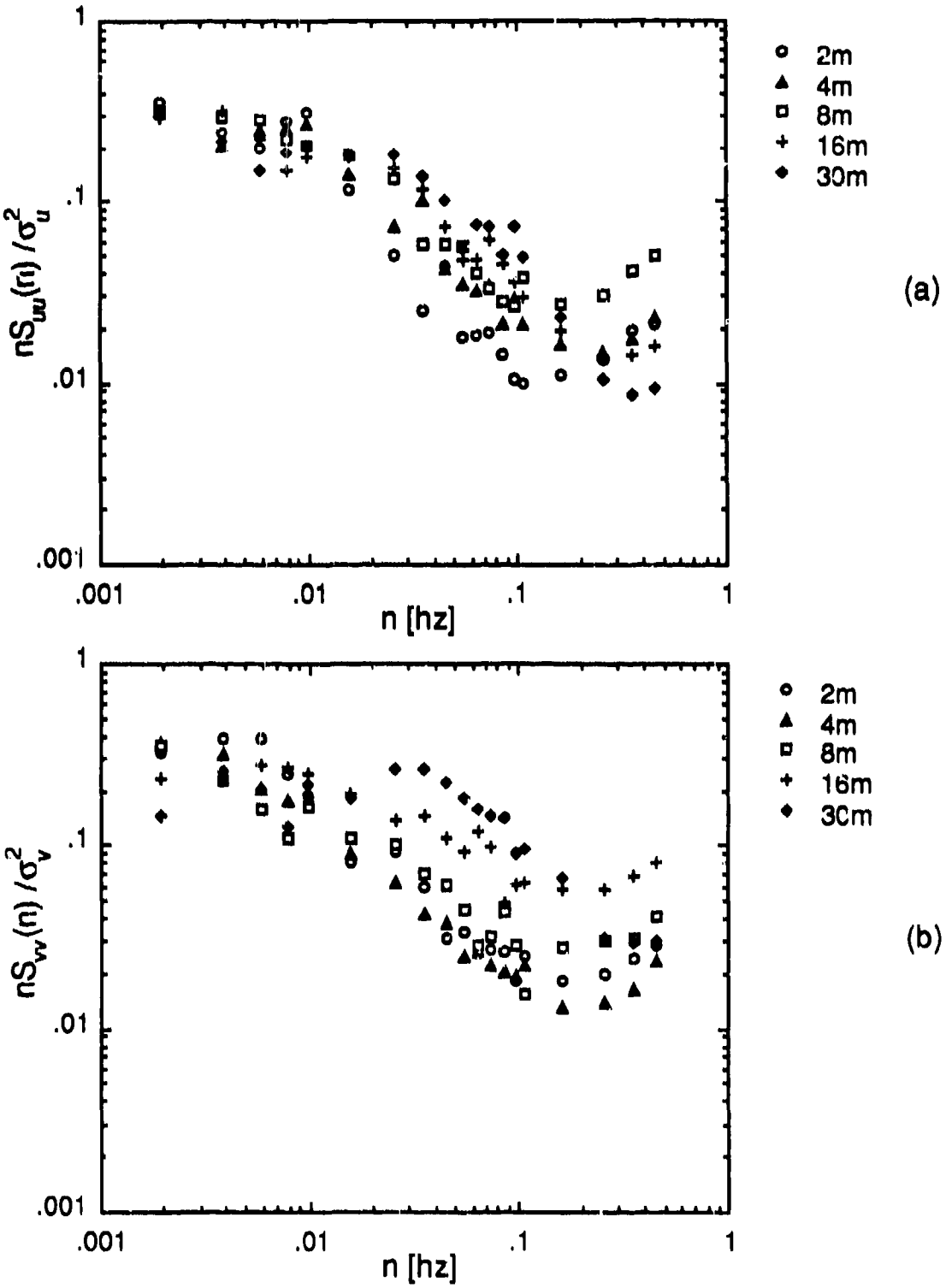

Figure 3.6 Spectra for Test 0925871 (a) mean-wind component and (b) cross-wind component. Smoke was released from 00:18 to 01:03. The stable release point was used.

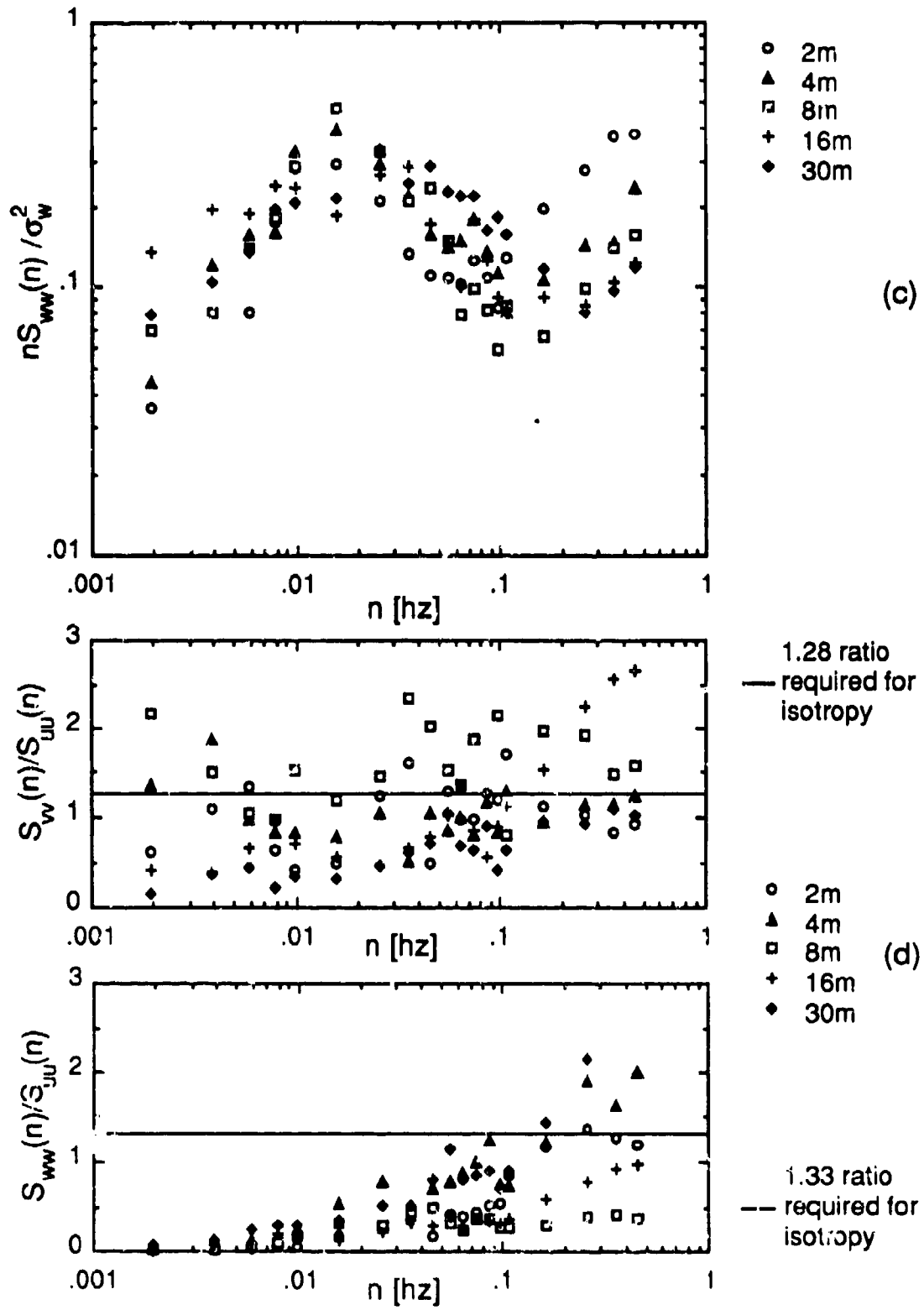

Figure 3.6 Spectra for Test 0925871 (c) vertical component and (d) spectral ratios. Smoke was released from 00:18 to 01:03. The stable release point was used.

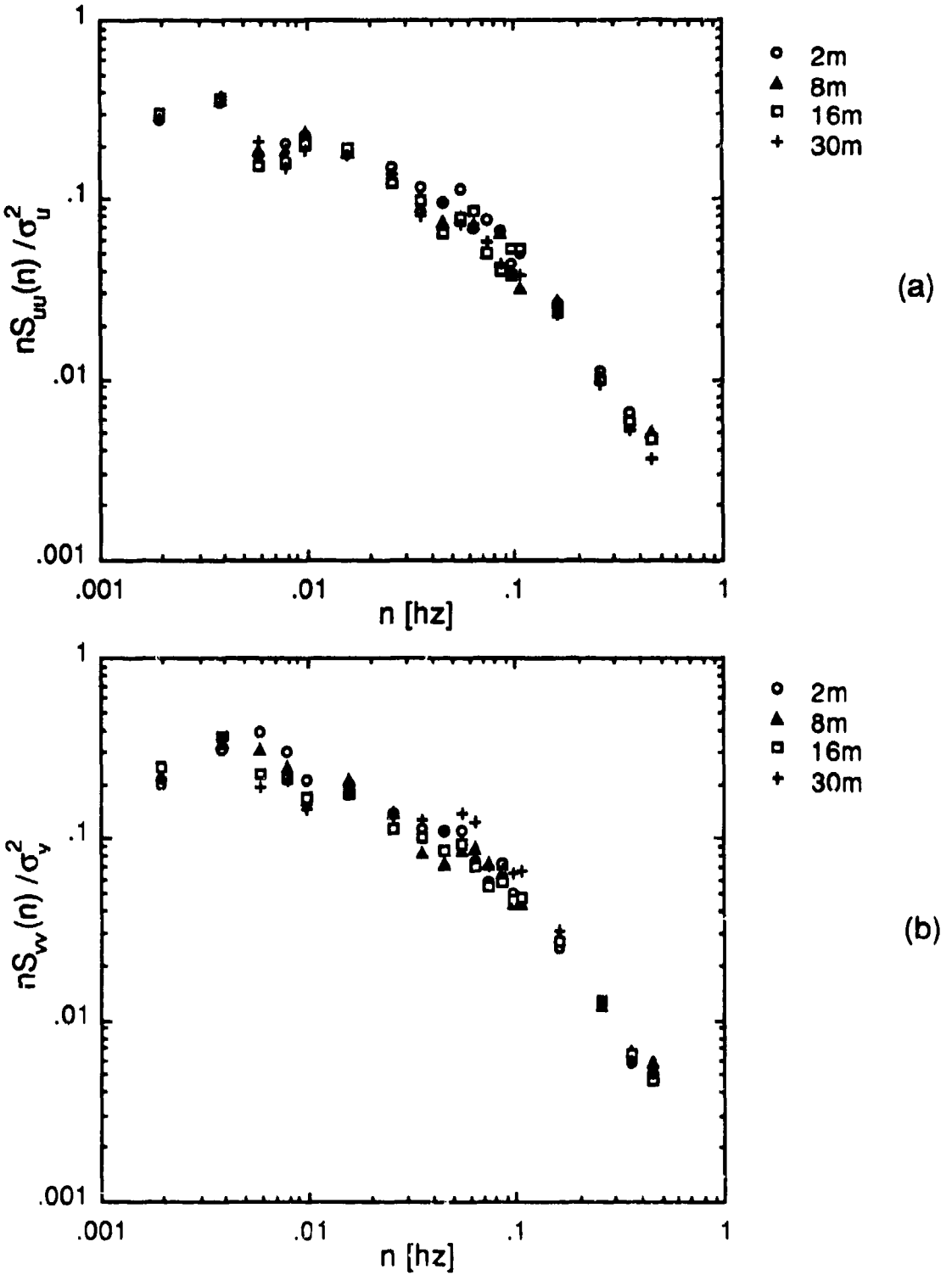

Figure 3.7 Spectra for Test 0926871 (a) mean-wind component and (b) cross-wind component. Smoke was released from 12:00 to 13:07. The unstable release point was used.

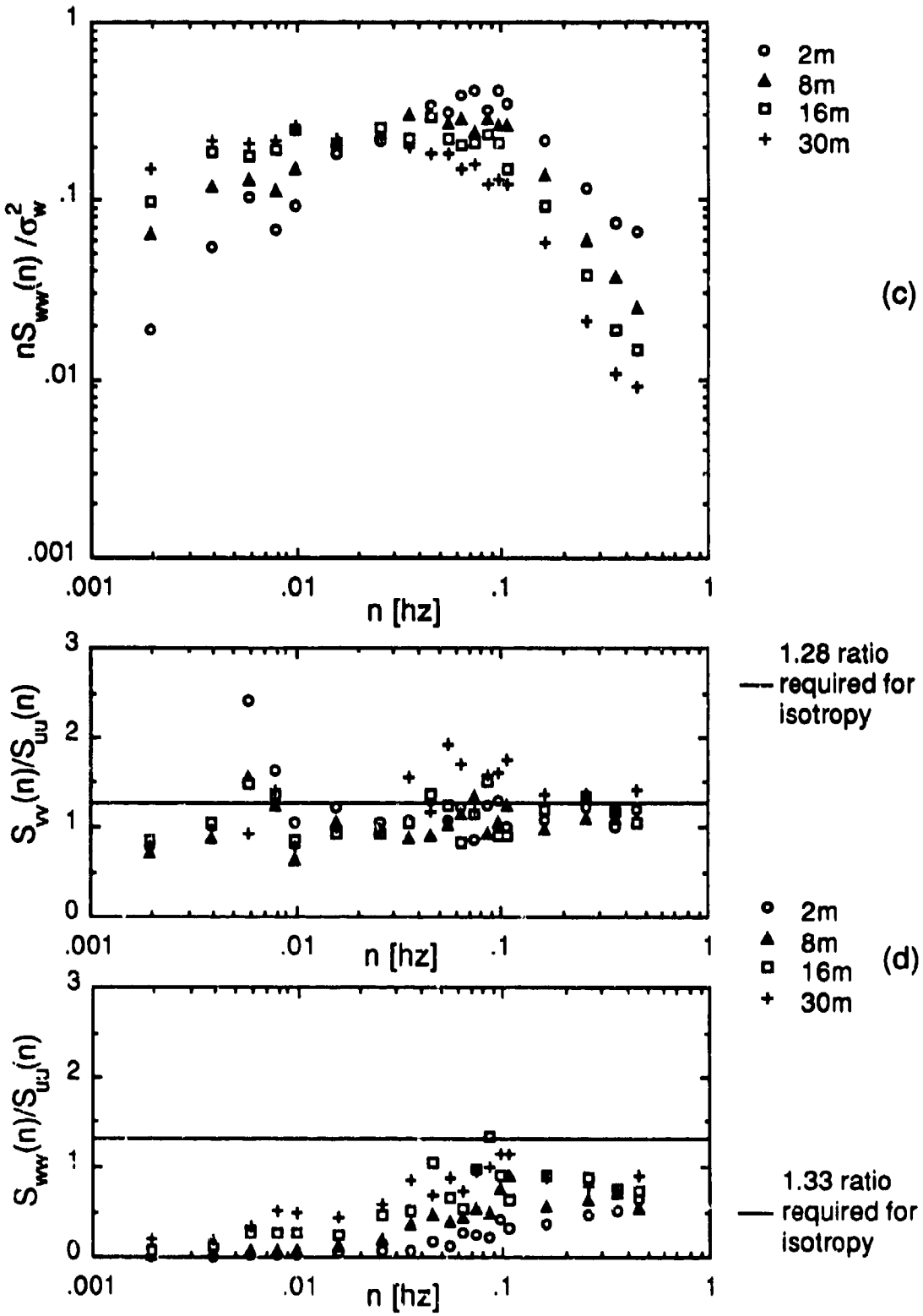

Figure 3.7 Spectra for Test 0926871 (c) vertical component and (d) spectral ratios. Smoke was released from 12:00 to 13:07. The unstable release point was used.

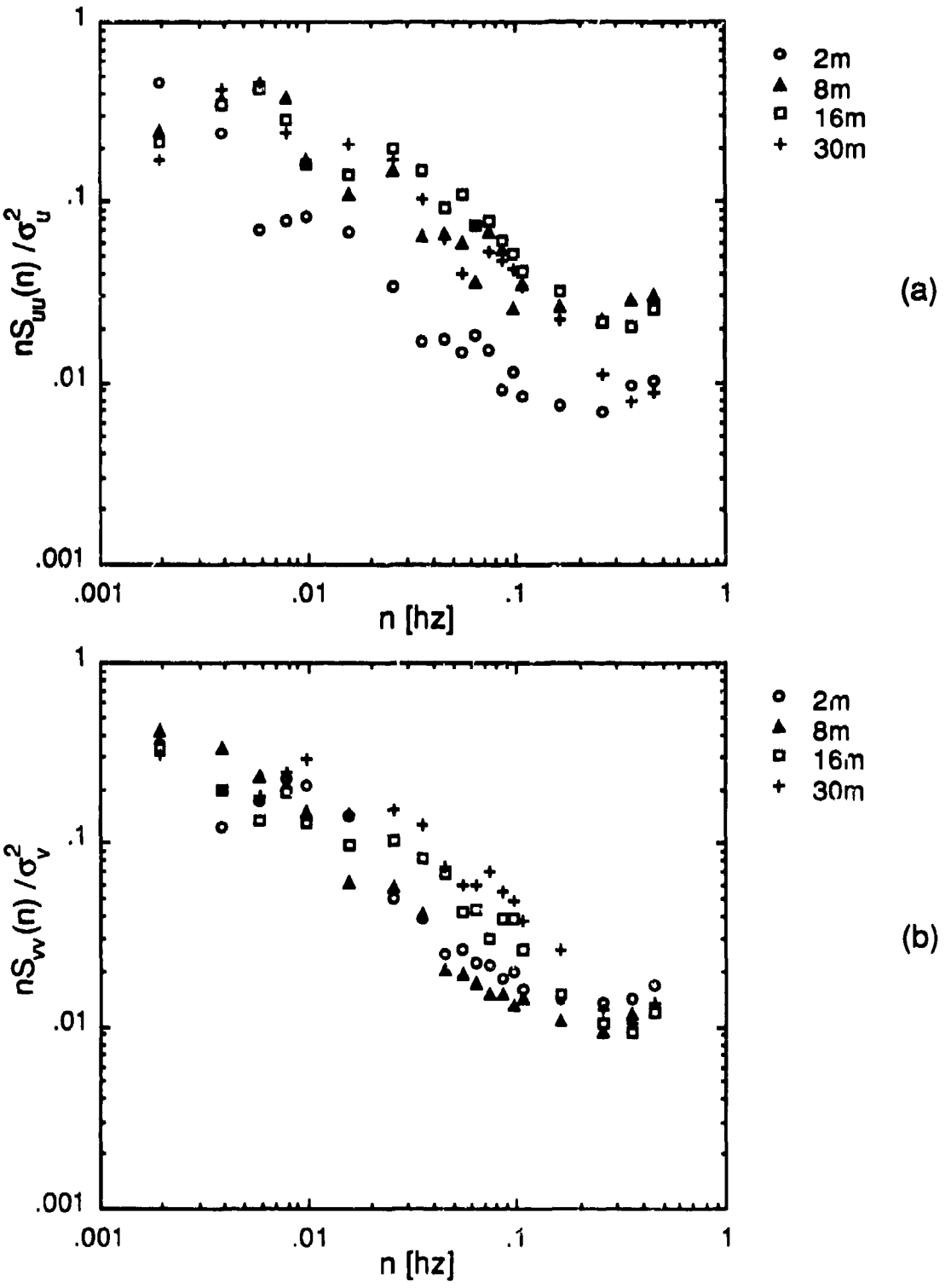

Figure 3.8 Spectra for Test 0927871 (a) mean-wind component and (b) cross-wind component. Smoke was released from 03:19 to 03:39. The stable release point was used.

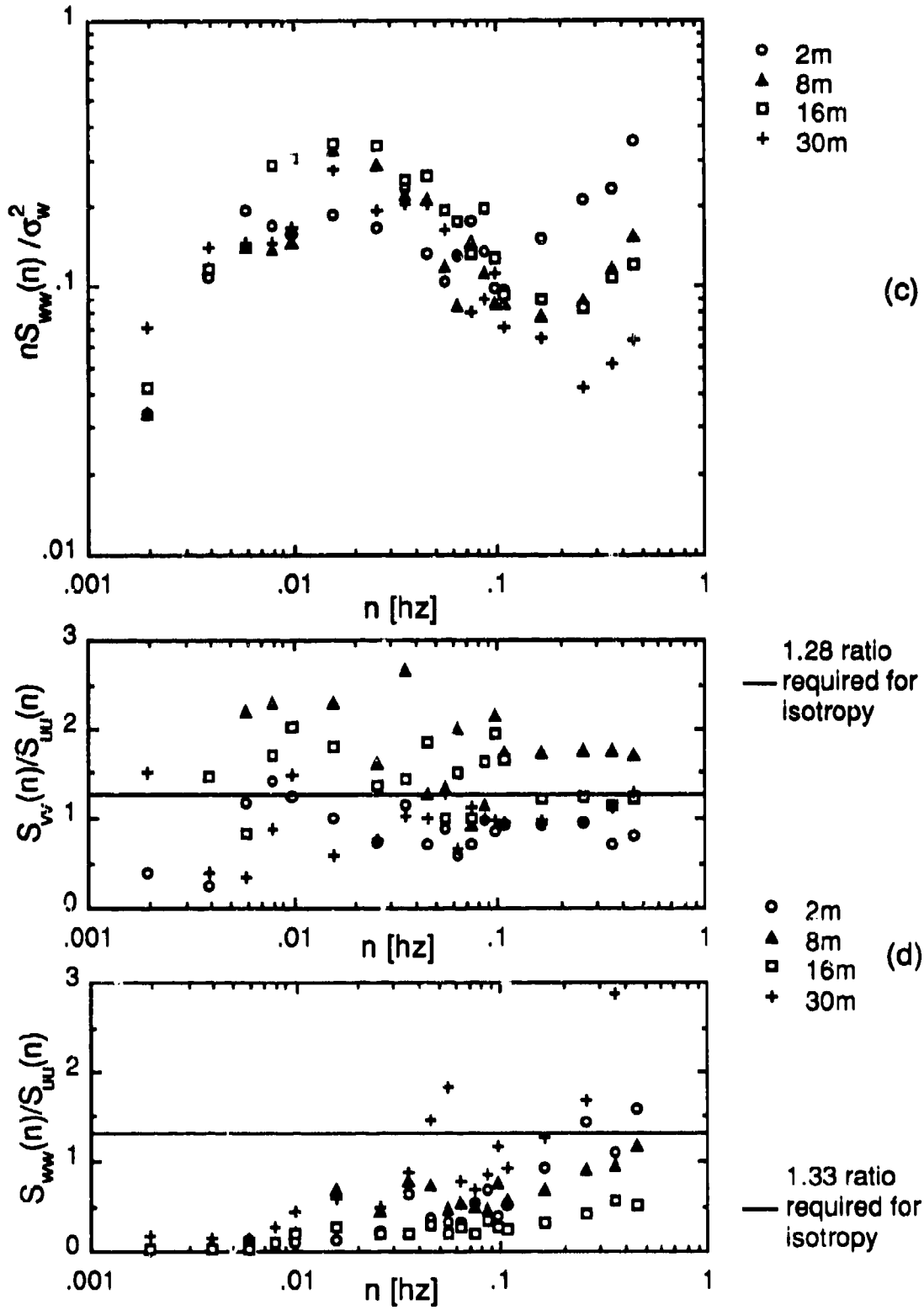

Figure 3.8 Spectra for Test 0927871 (c) vertical component and (d) spectral ratios. Smoke was released from 03:19 to 03:39. The stable release point was used.

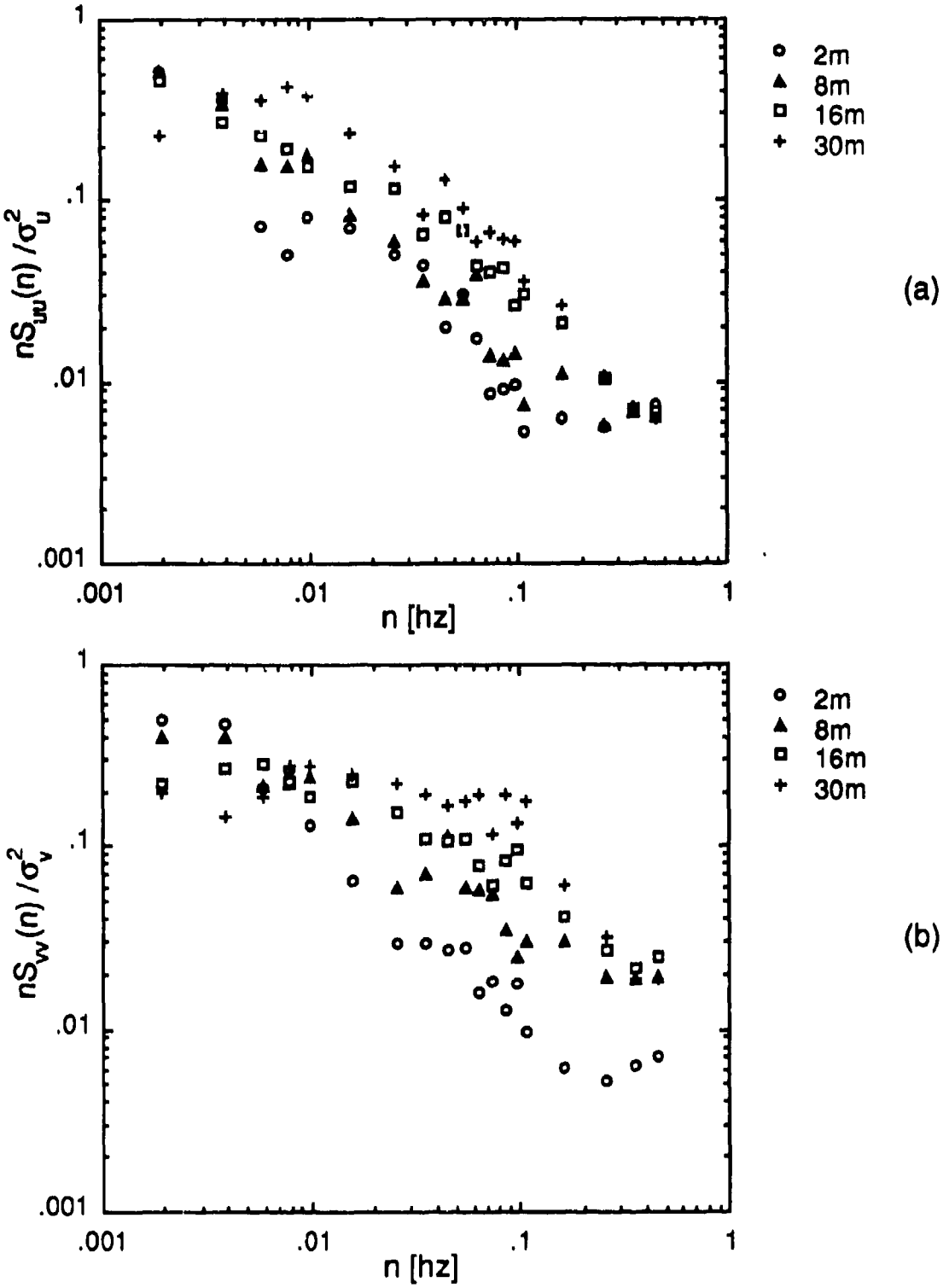

Figure 3.9 Spectra for Test 0927872 (a) mean-wind component and (b) cross-wind component. Smoke was released from 06:44 to 06:54. The stable release point was used.

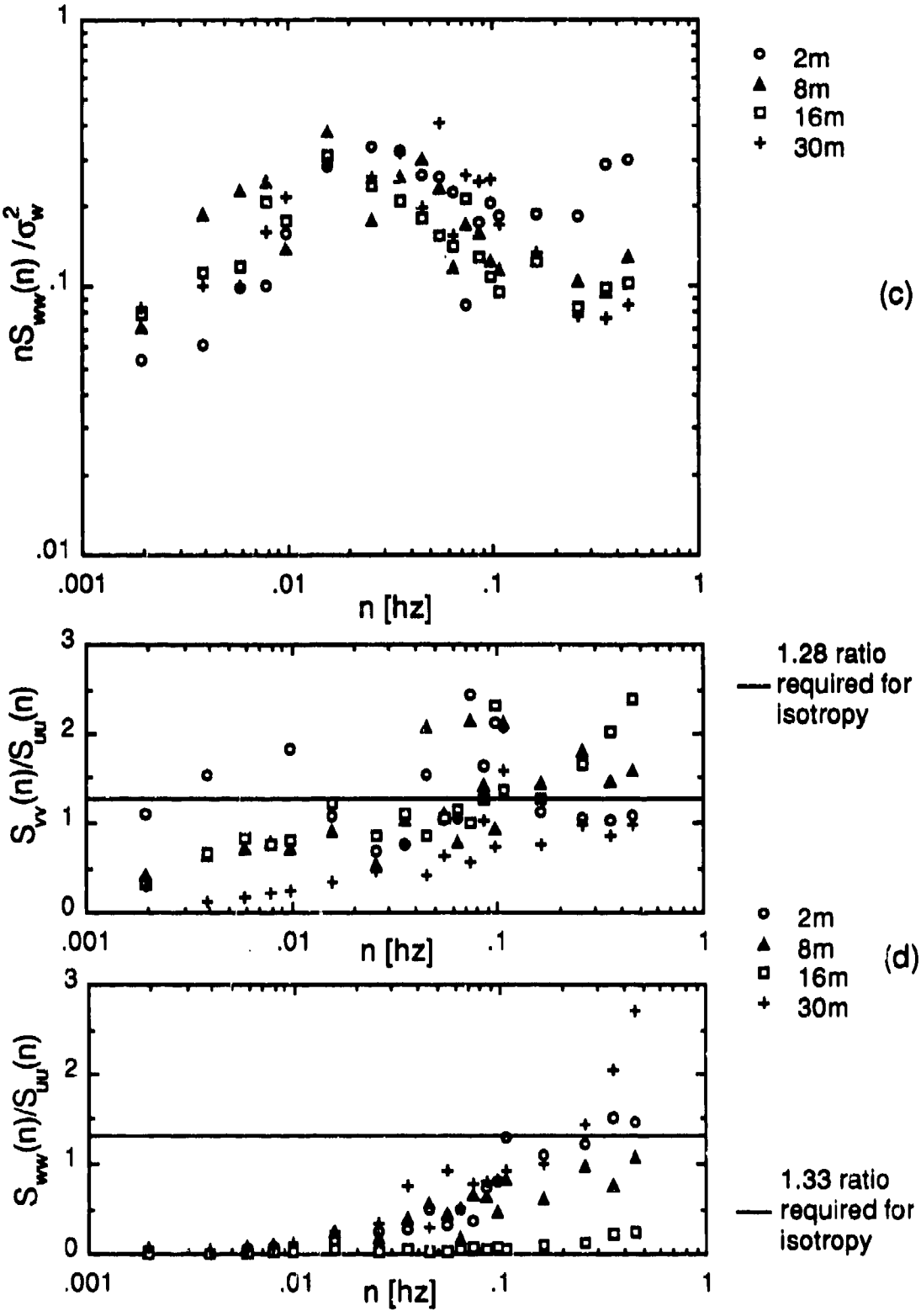

Figure 3.9 Spectra for Test 0927872 (c) vertical component and (d) spectral ratios. Smoke was released from 06:44 to 06:54. The stable release point was used.

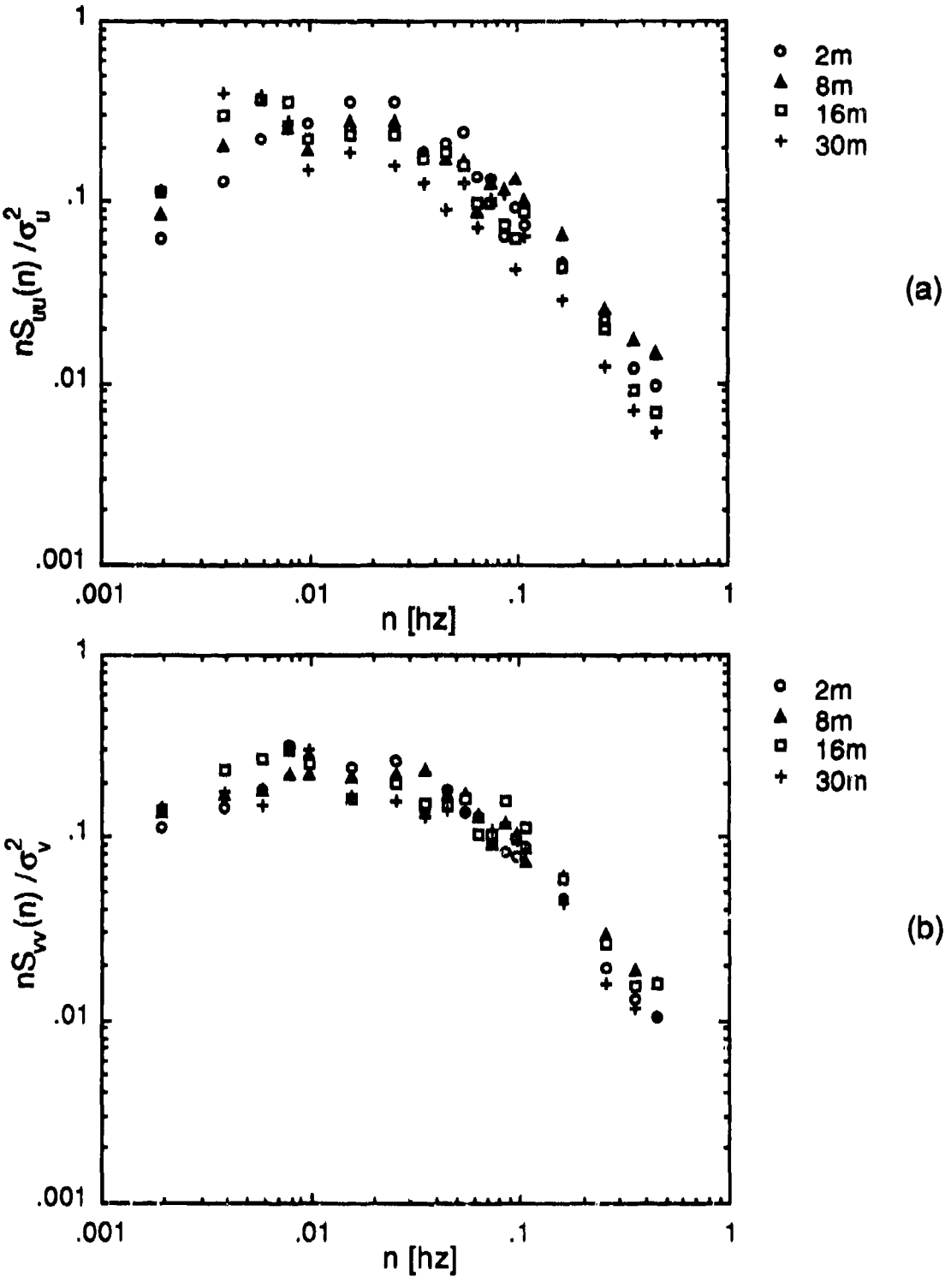

Figure 3.10 Spectra for Test 0928871 (a) mean-wind component and (b) cross-wind component. Smoke was released from 10:29 to 10:54. The unstable release point was used.

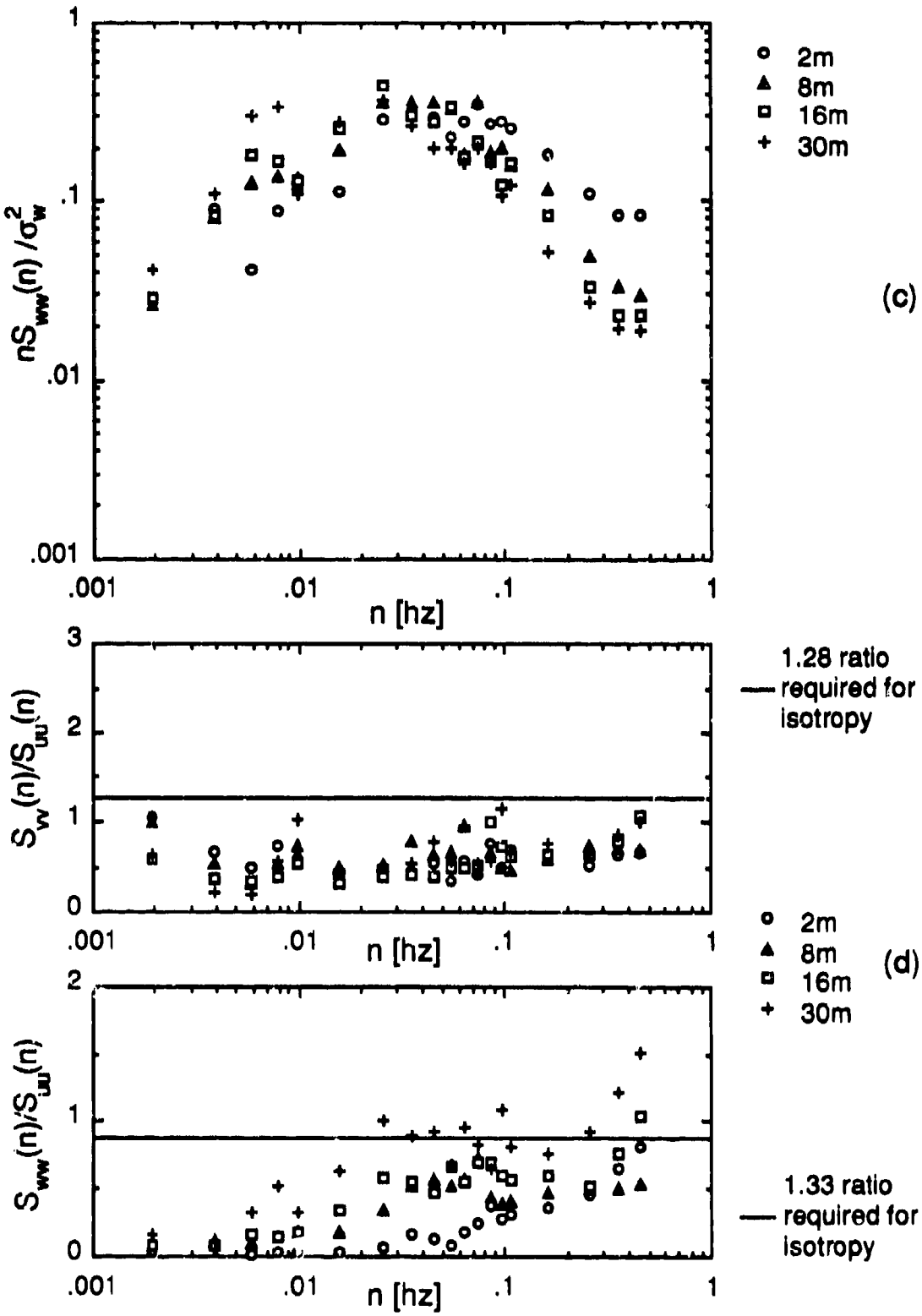

Figure 3.10 Spectra for Test 0928871 (c) vertical component and (d) spectral ratios. Smoke was released from 10:29 to 10:54. The unstable release point was used.

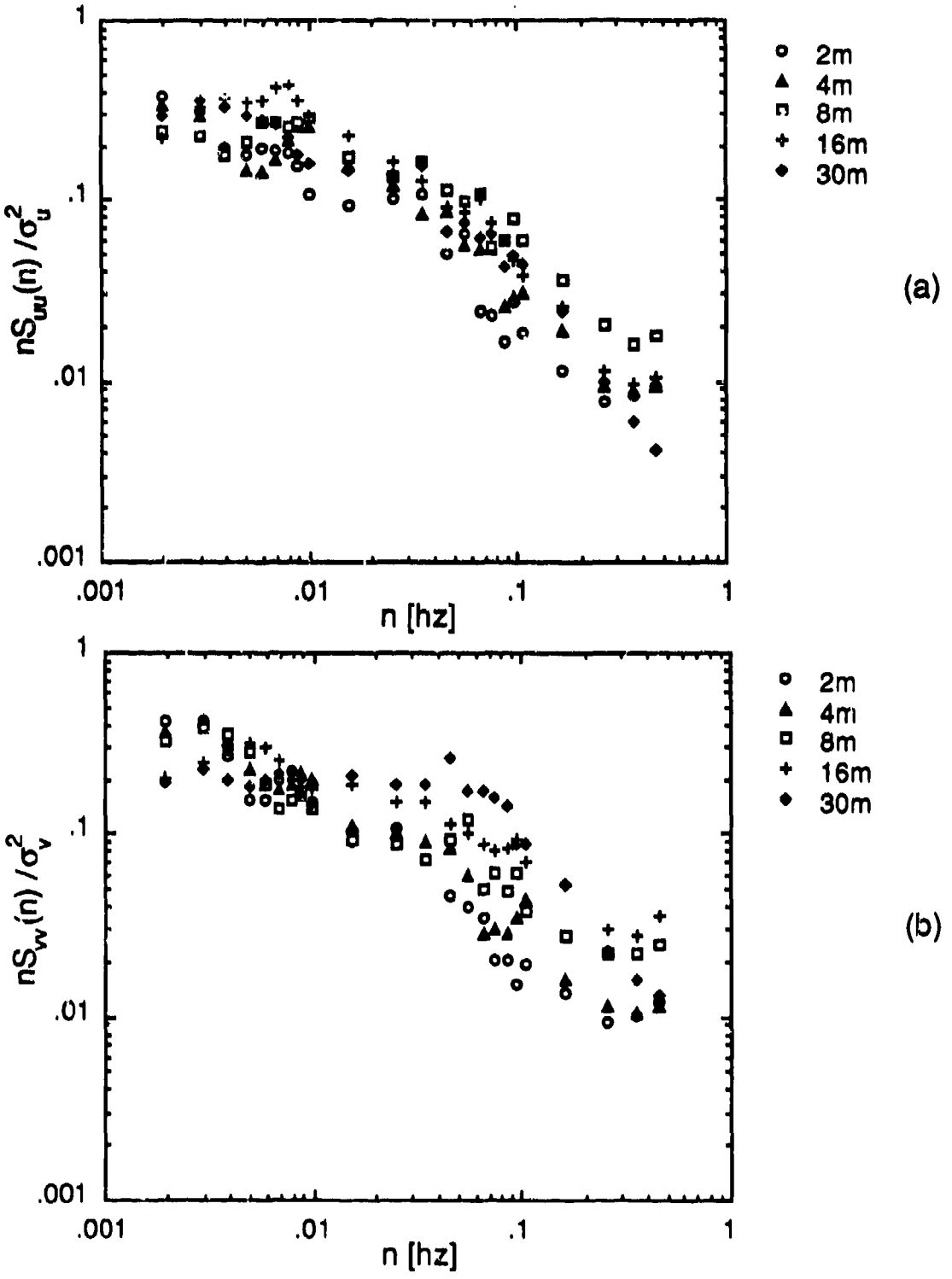

Figure 3.11 Spectra for Test 0930871 (a) mean-wind component and (b) cross-wind component. Smoke was released from 06:48 to 07:28. The stable release point was used.

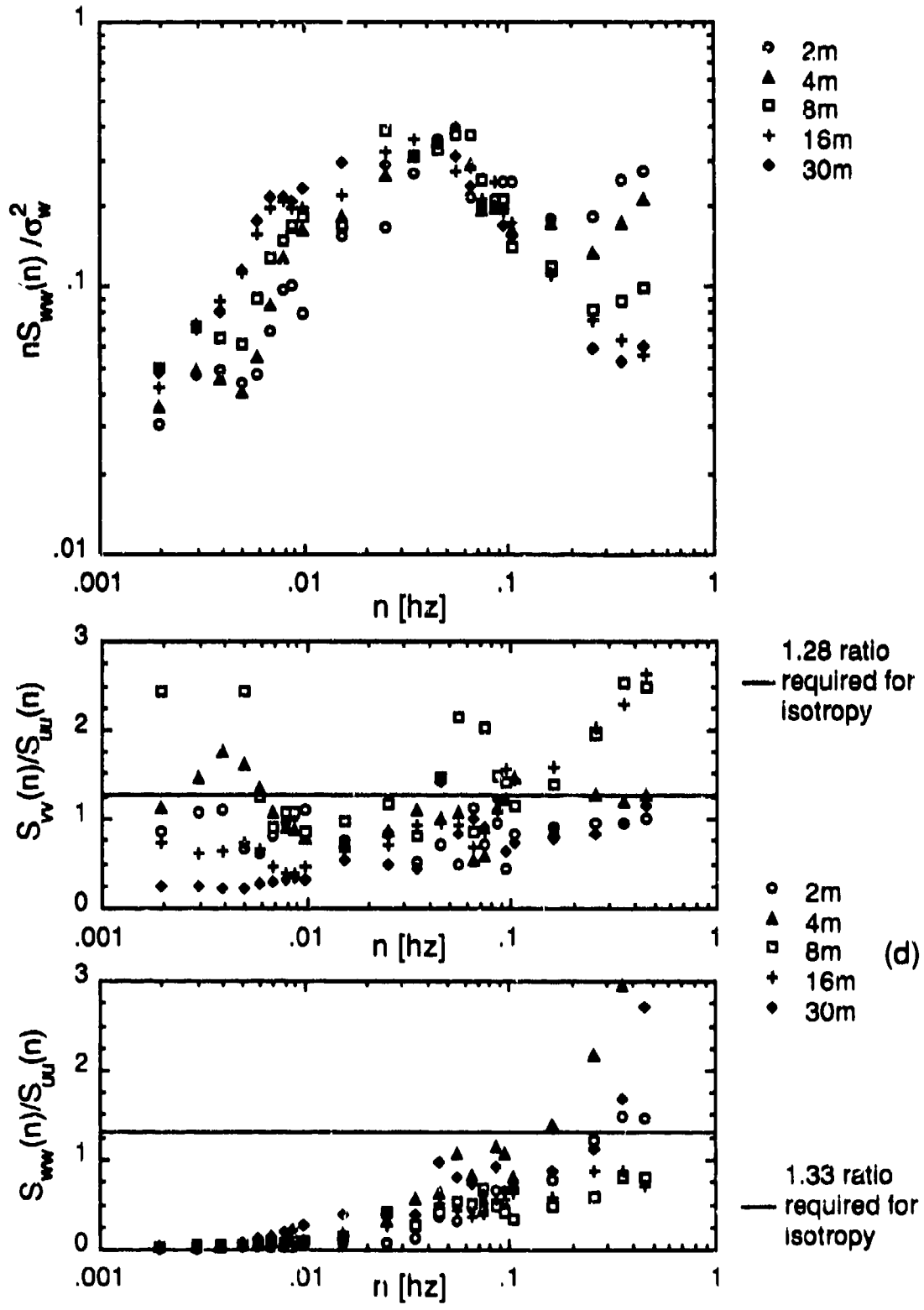

Figure 3.11 Spectra for Test 0930871 (c) vertical component and (d) spectral ratios. Smoke was released from 06:48 to 07:28. The stable release point was used.

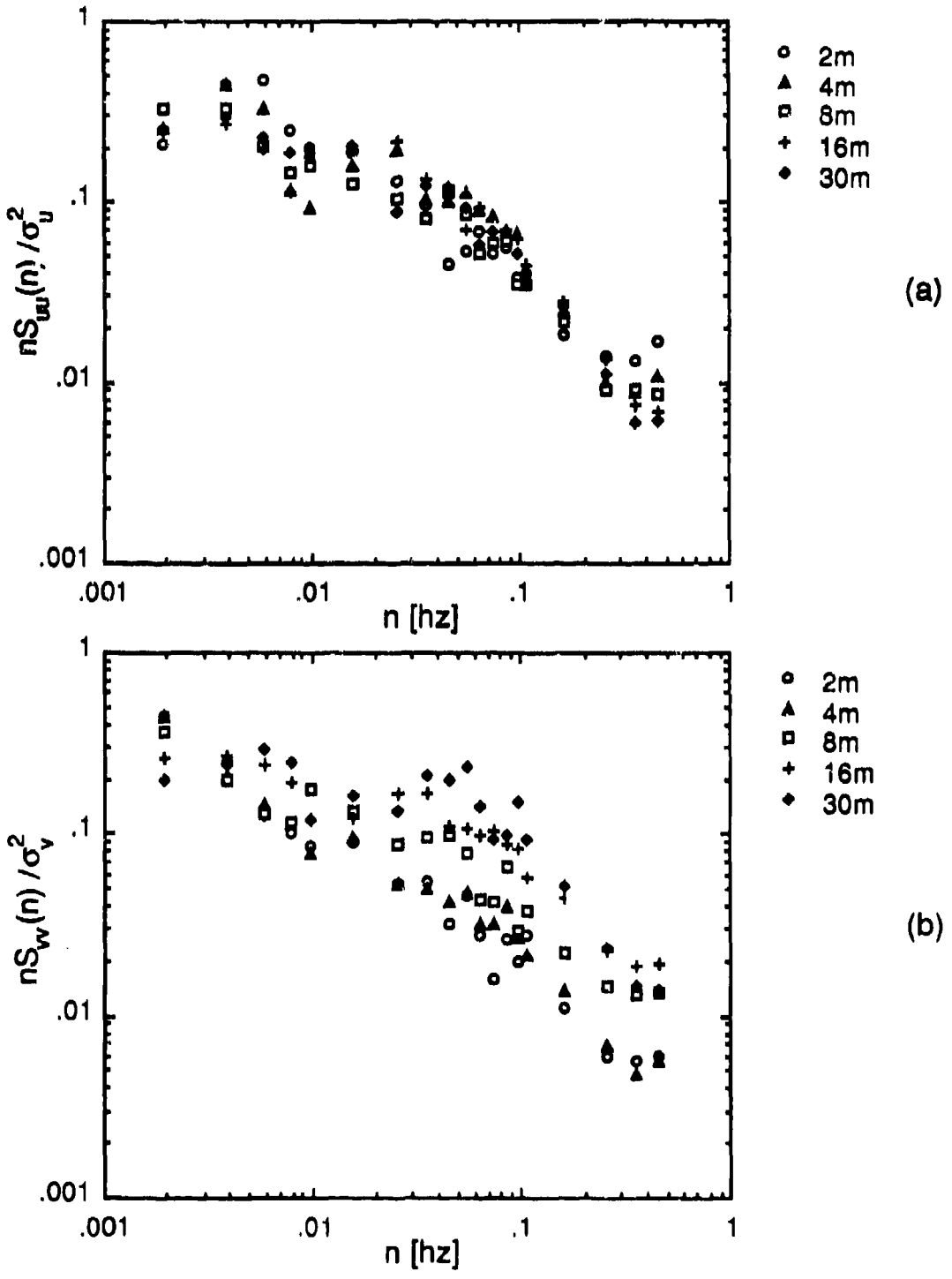

Figure 3.12 Spectra for Test 1001871 (a) mean-wind component and (b) cross-wind component. Smoke was released from 06:52 to 07:32. The stable release point was used.

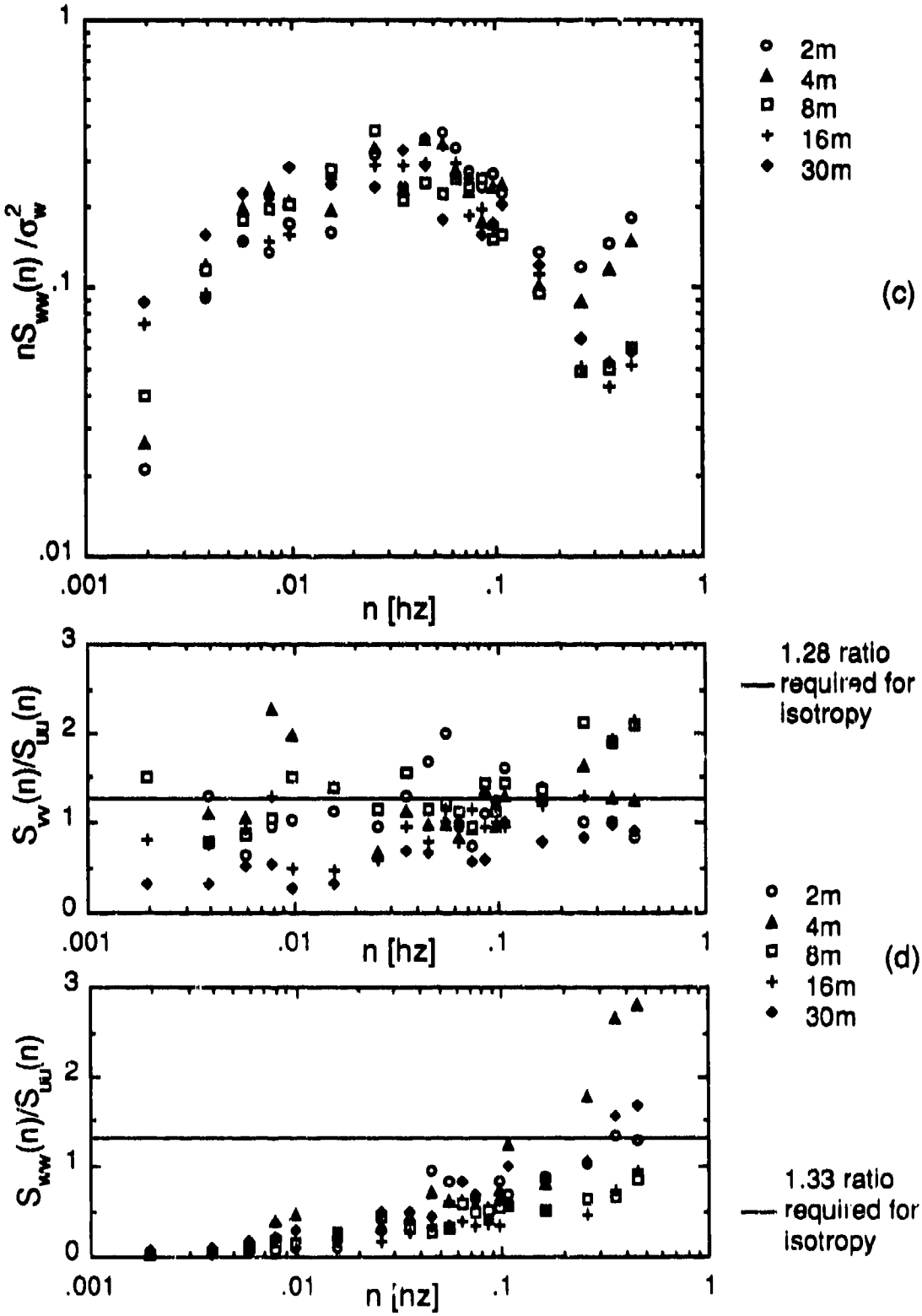

Figure 3.12 Spectra for Test 1001871 (c) vertical component and (d) spectral ratios. Smoke was released from 06:52 to 07:32. The stable release point was used.

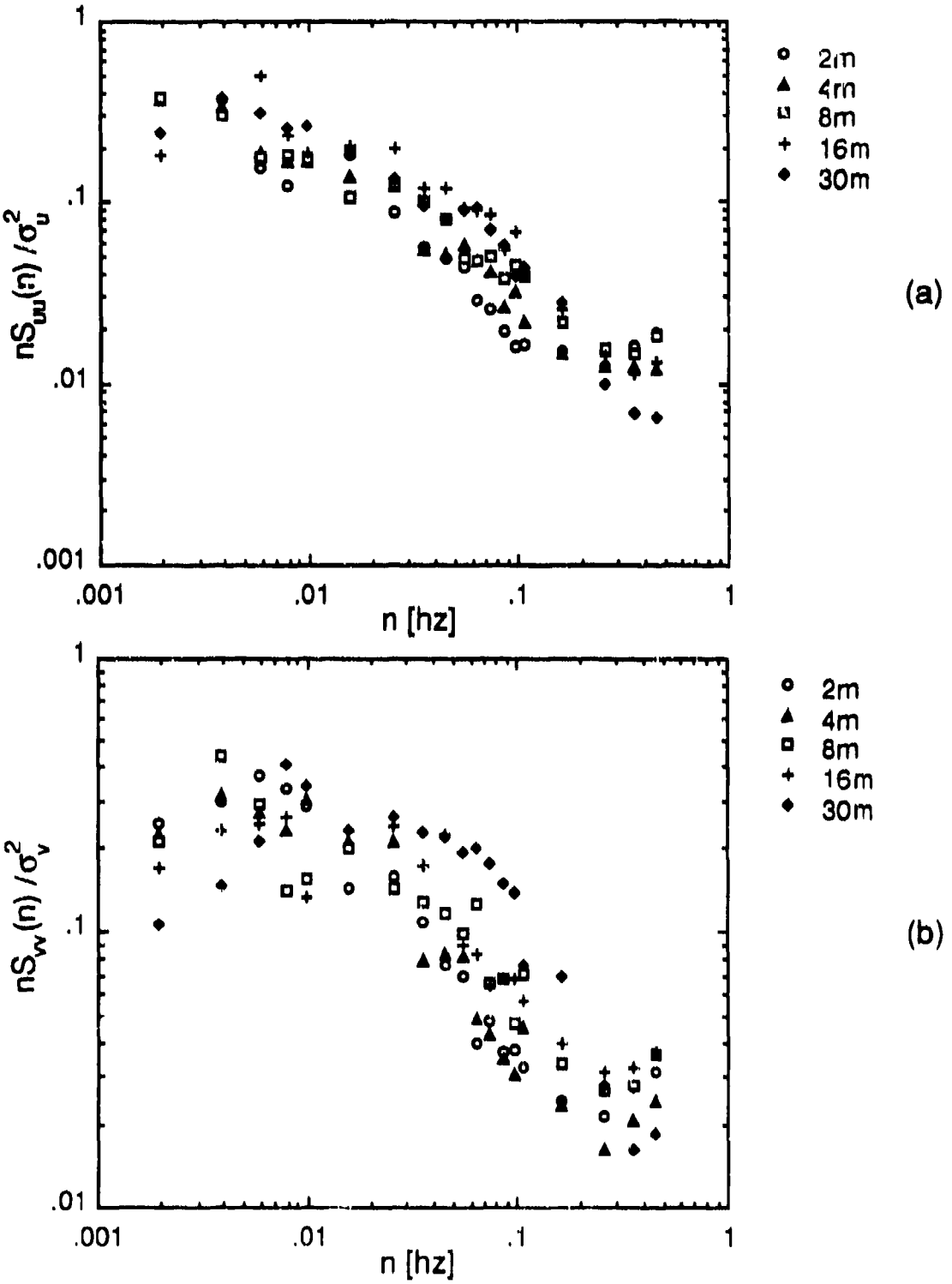

Figure 3.13 Spectra for Test 1002871 (a) mean-wind component and (b) cross-wind component. Smoke was released from 07:17 to 07:47. The stable release point was used.

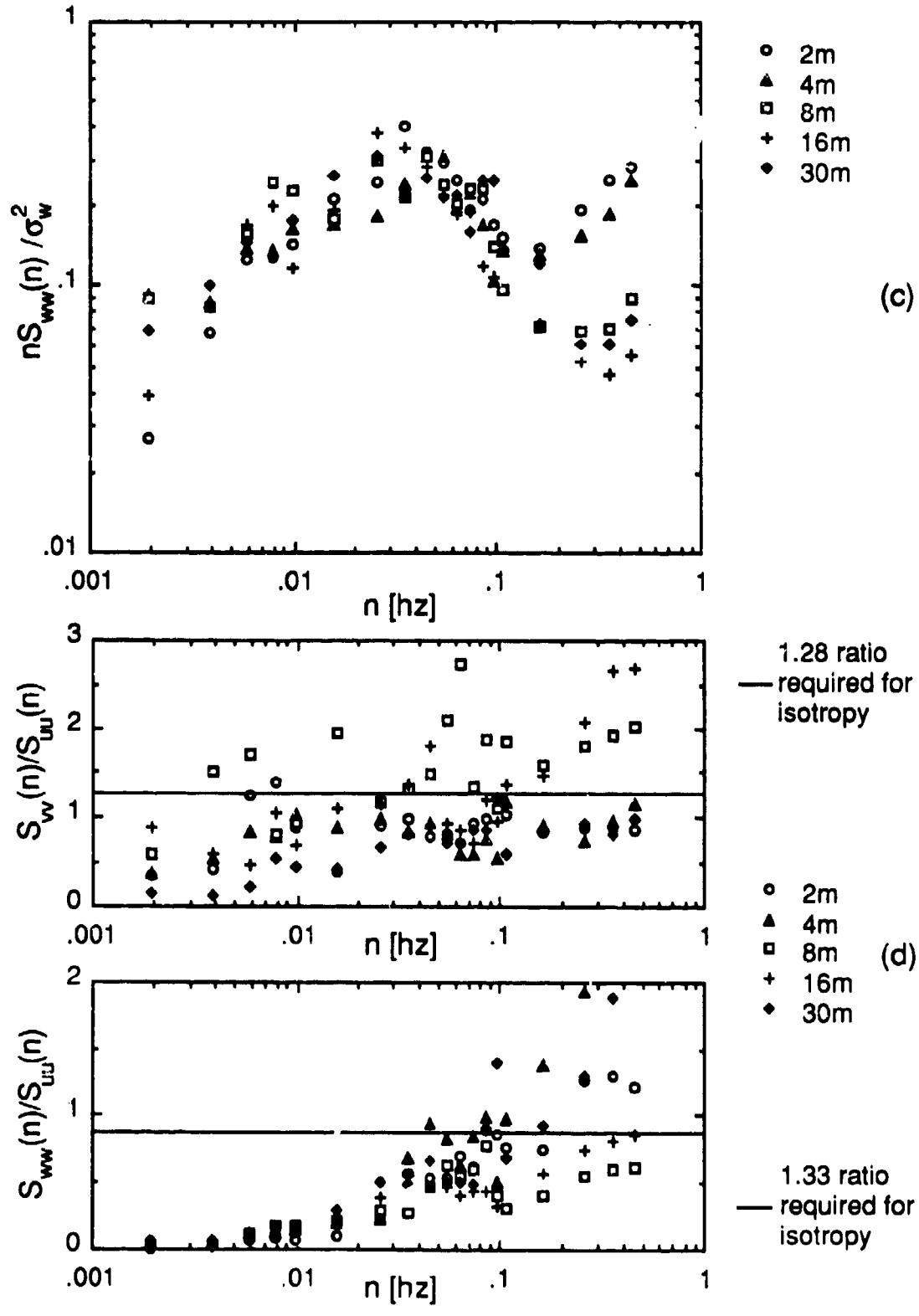

Figure 3.13 Spectra for Test 1002871 (c) vertical component and (d) spectral ratios. Smoke was released from 07:17 to 07:47. The stable release point was used.

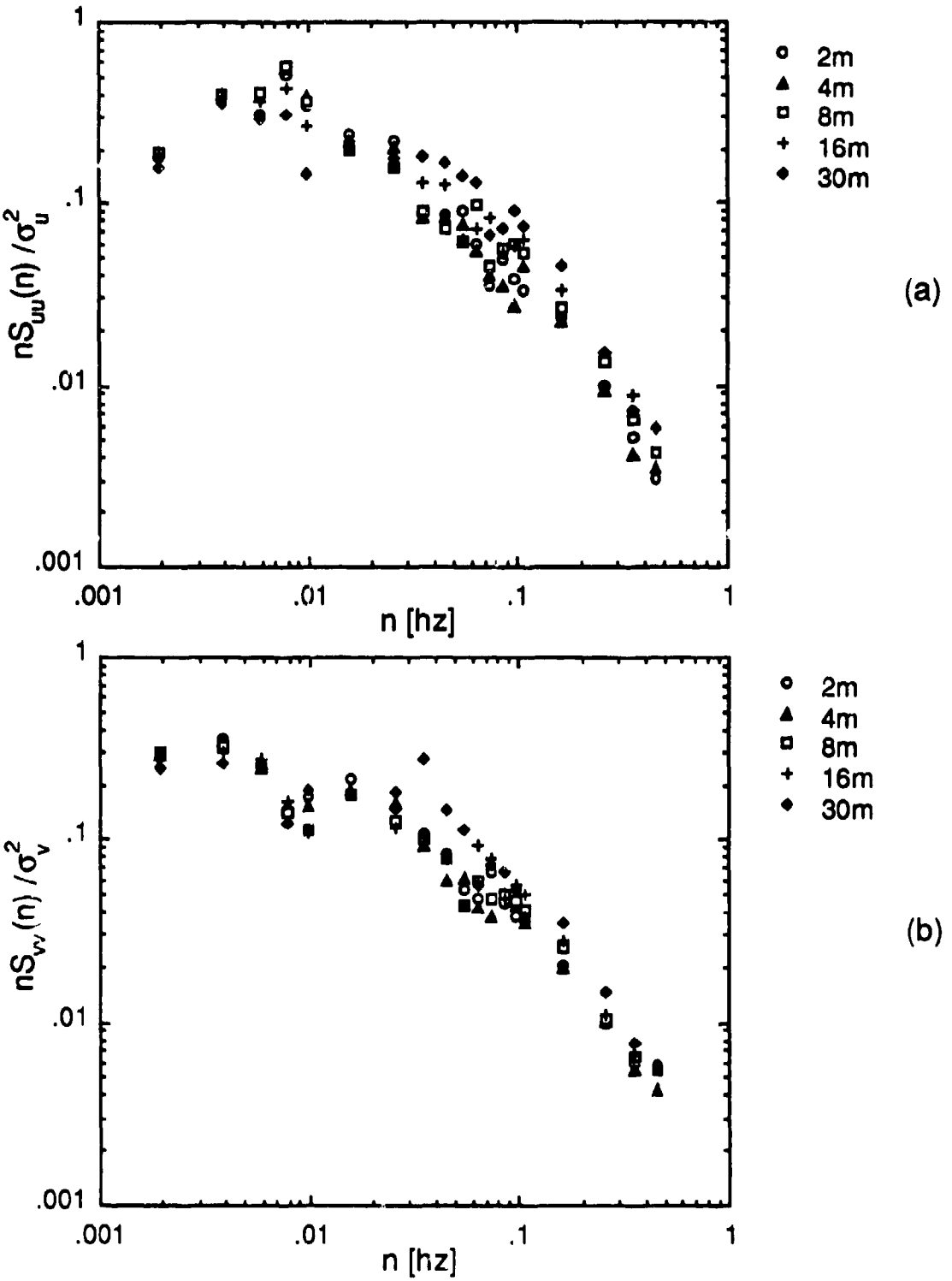

Figure 3.14 Spectra for Test 1002872 (a) mean-wind component and (b) cross-wind component. Smoke was released from 12:16 to 12:34. The unstable release point was used.

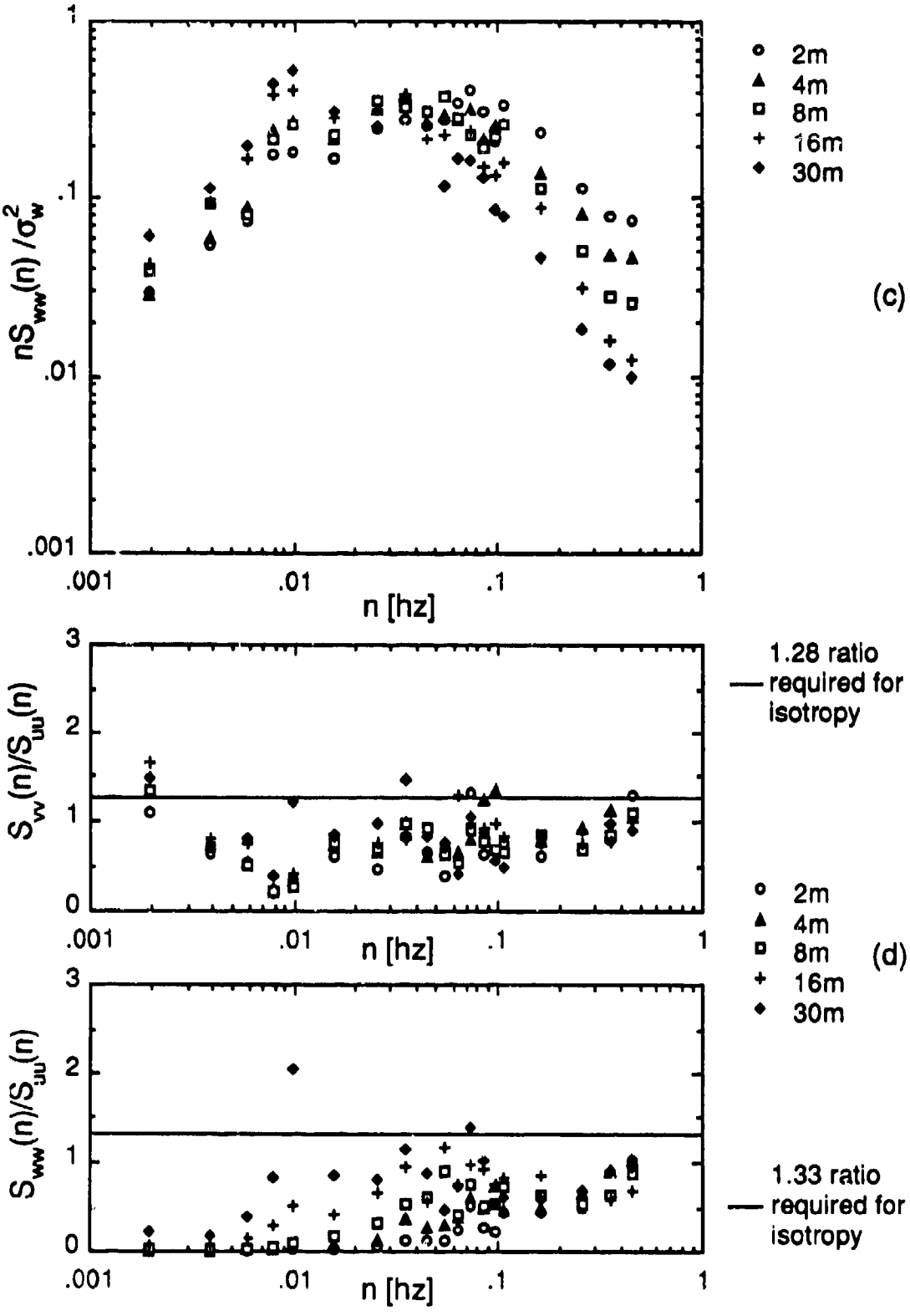

Figure 3.14 Spectra for Test 1002872 (c) vertical component and (d) spectral ratios. Smoke was released from 12:16 to 12:34. The unstable release point was used.

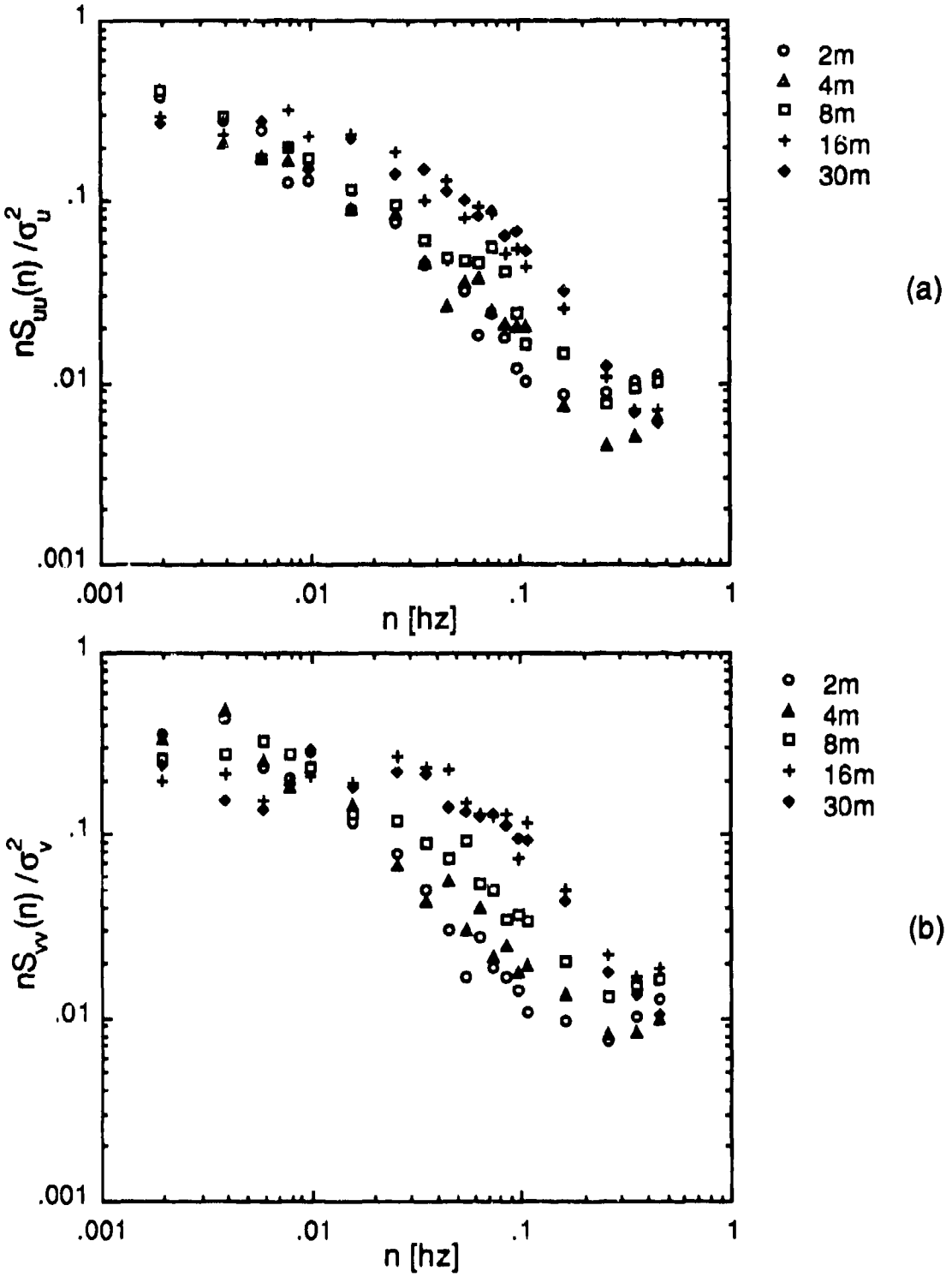

Figure 3.15 Spectra for Test 1003871 (a) mean-wind component and (b) cross-wind component. Smoke was released from 06:56 to 07:27. The stable release point was used.

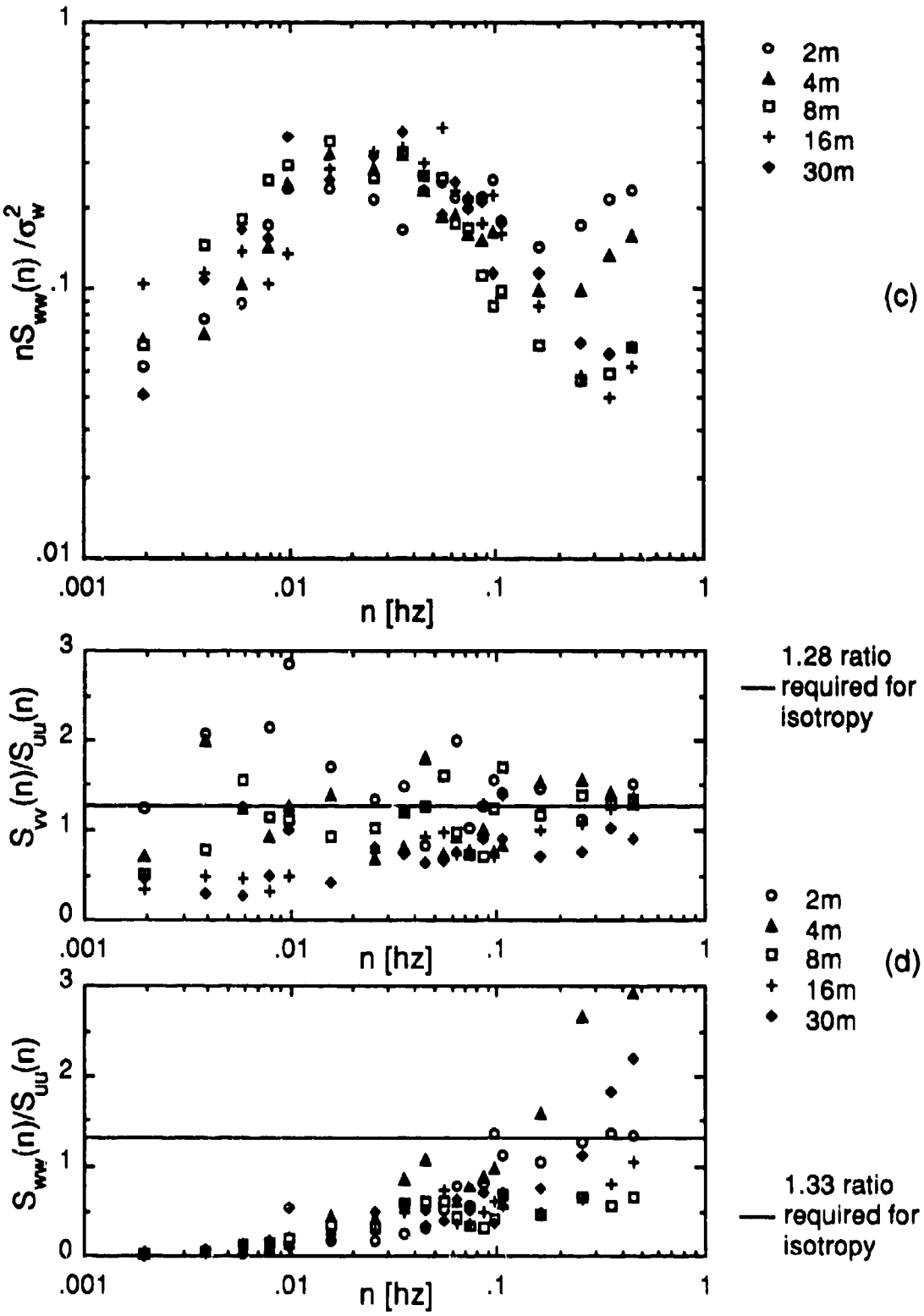

Figure 3.15 Spectra for Test 1003871 (c) vertical component and (d) spectral ratios. Smoke was released from 06:56 to 07:27. The stable release point was used.

In contrast to those from the unstable tests, the spectra computed for the stable tests are quite chaotic. The individual spectra show limited form, but significant variations are present between the different levels of the tower. These variations may be attributed to a general loss of turbulent kinetic energy at the lower levels. This energy loss is indicative of a very weak wind field and reflects the laminar characteristics expressed by the large values of Ri_b (see Section 3.2). For some of the stable tests local maxima in the transverse and vertical spectra occur at frequencies between 0.03 - 0.08 hz at the 30-m level. This frequency range corresponds closely to the Brunt-Väisälä frequency, repeated here for convenience

$$N = \left(\frac{g}{\theta} \frac{\partial \theta}{\partial z} \right)^{1/2} .$$

This correlation between N and our 30-m data indicates that inertial oscillations may be present in the core of the drainage flow and, more importantly, are predictable from simple theory and ground-level measurements.

Many of the stable spectra show unusual behavior on the high frequency end. This is especially prevalent in the vertical velocity spectra. The cause of these "tails" has been thoroughly investigated and two potential causes have been dismissed. The first suspected cause was momentary periods of strong turbulence which would occur a few times during a test period. The data were filtered to remove these large variations, but this had a negligible effect on the spectra. It was also surmised that these tails could be the result of discretization errors, but corrections for this problem had little effect. We believe these tails are not an actual characteristic of the flow field, and work is still continuing in the area.

3.4 Upper-air Data

3.4.1 Description of the Balloon-sounding Data

Ten instrumented balloon soundings were made during the course of the AMADEUS Dispersion Experiments. In this context a sounding is a vertical profile from ground level to heights of several kilometers with a 10 - 50-m vertical resolution. The dates, times (PDT) and maximum heights reached are summarized in Table 3.27 below. The soundings were made available to us in the from of photocopies of the printer outputs produced in the field; the format of these outputs varied from case to case. The data on these sheets were manually transferred to computer compatible form. Because over 28 full pages of numerical values were involved, the data were

first entered by one person and then independently checked by two others. In this way, the integrity of the data was ensured.

Table 3.27 Upper-air balloon soundings for Meadowbrook study.

Date	Start	Stop	Max. height (m)
9/23	13:21	13:36	1400
9/24	20:19	20:36	6000
9/26	07:48	08:06	6900
9/27	01:24	01:53	5600
9/28	07:17	07:44	8000
9/29	18:50	19:17	8000
9/30	15:34	16:02	7500
10/01	11:16	11:26	2100
10/02	09:06	09:27	2100
10/03	16:19	16:46	6300

Our primary interest in the instrumented-balloon data lies in determining the mixing heights for the unstable release periods. Two methods of making this determination are possible depending on the period during which the sounding is available. If a sounding is available at or very near the time of the test, the mixing height may be determined directly by locating the first inversion in the potential temperature profile. If synchronous sounding data are not available, then the ground-level temperature at the time of the test can be used in conjunction with a morning sounding to estimate the mixing height. This estimate is made by determining the height at which the potential temperature equals the surface-level potential temperature at the time of interest.

Boundary-layer heights for stable conditions may also be inferred from sounding data as was discussed in Chapter 2, although the methodology employed with these estimates has not been well established. Fortunately, the need for boundary-layer heights is not as crucial for the prediction of dispersion under these stratified conditions.

3.4.2 Potential Temperature Profiles and Mixing Heights for Daytime Releases

The potential temperature profiles determined from the 10 upper-air soundings are presented in Figs. 3.16– 3.25. No *sounding-based* estimate of the mixing height is

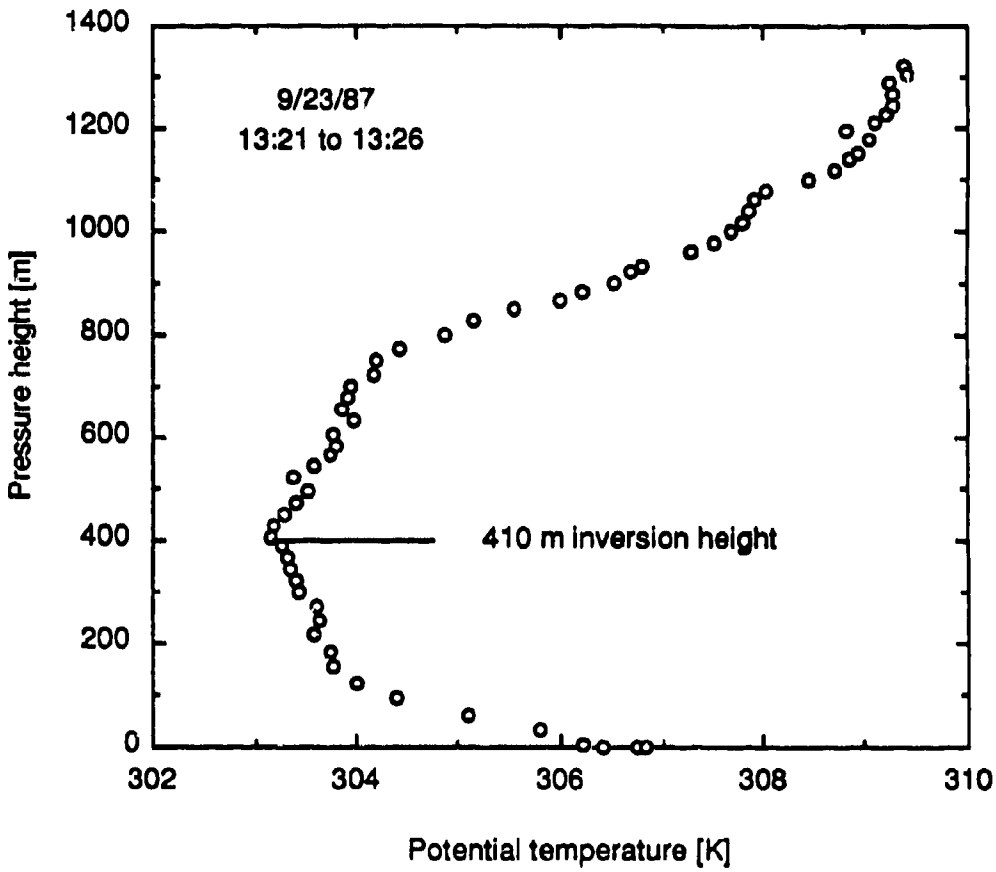

Figure 3.16 Potential temperature profile for Setember 23, 1987. This sounding was taken immediately prior to Test 0923871. An inversion at 410 m is clearly visible.

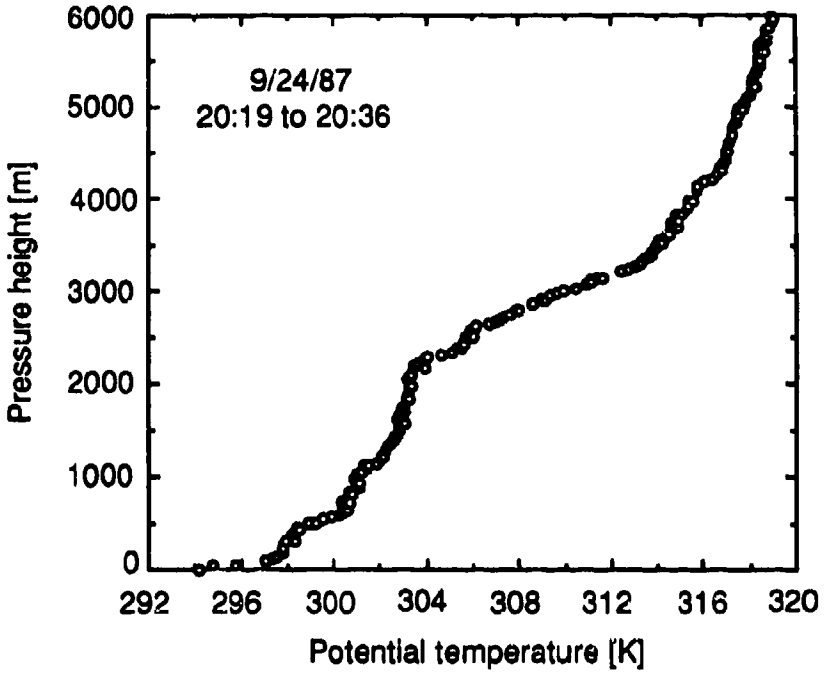

(a)

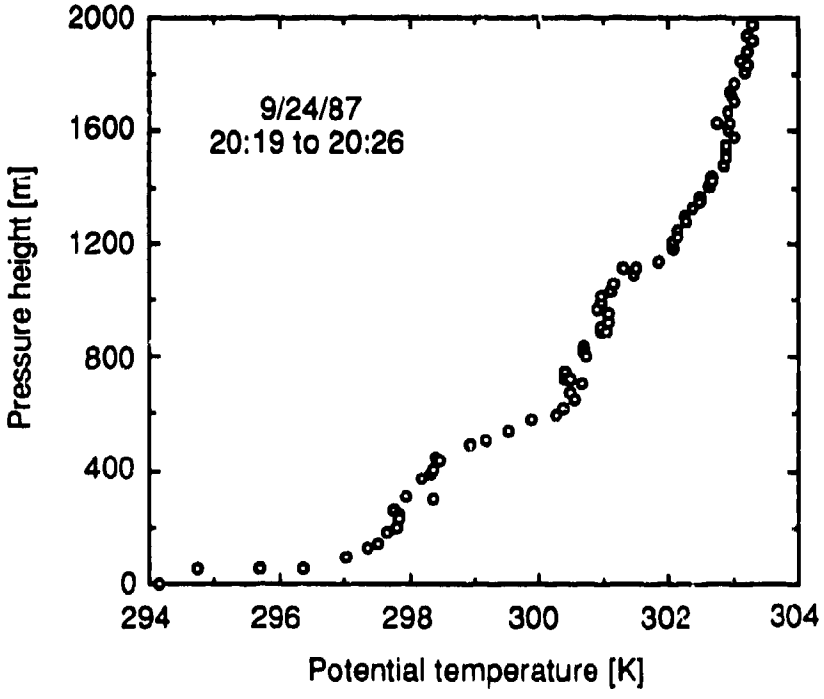

(b)

Figure 3.17 Potential temperature profile for September 24, 1987 (a) to a height of 6000 m and (b) to a height of 2000 m.

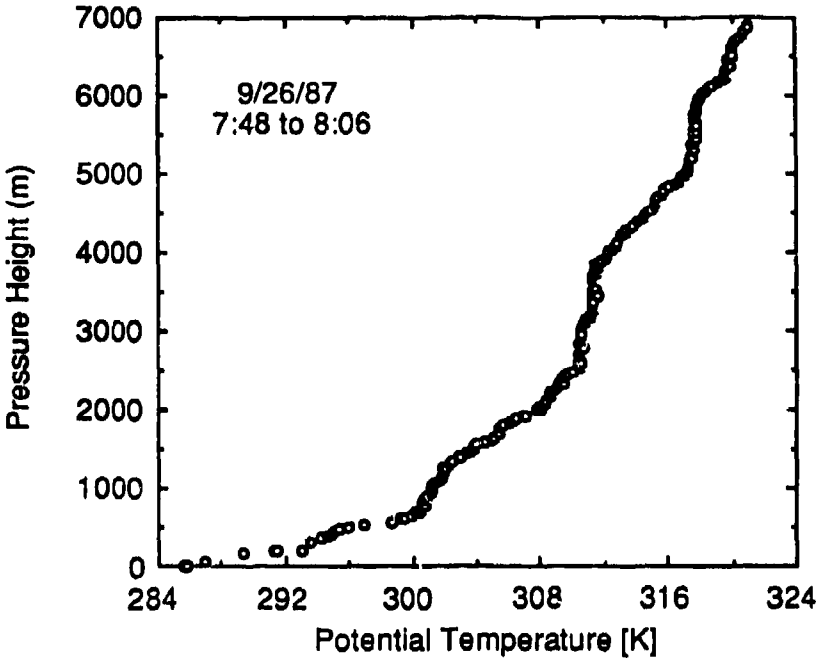

(a)

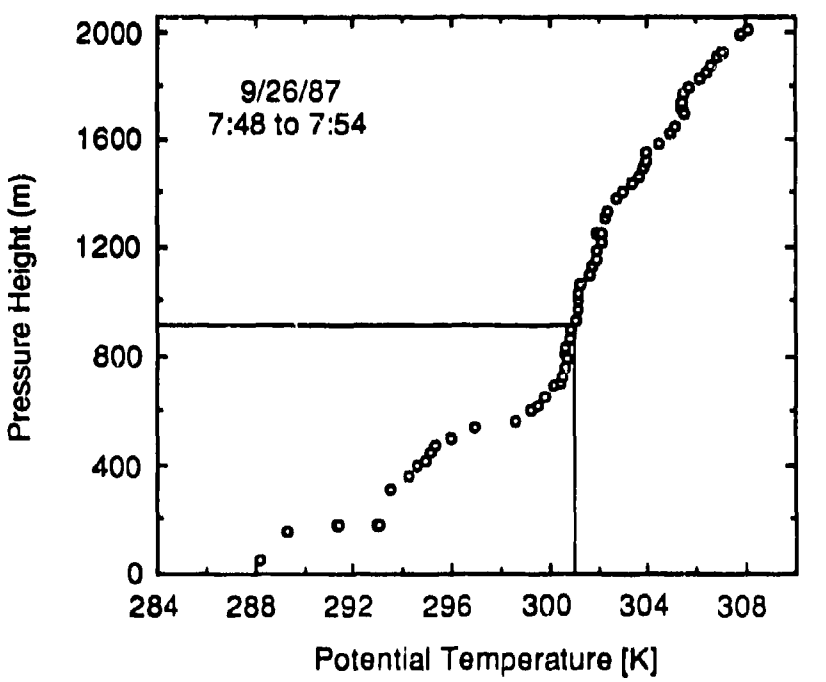

(b)

Figure 3.18 Potential temperature profile for September 26, 1987. (a) to a height of 6900 m and (b) to a height of 2000 m. The potential temperature at time of Test 0926871 was used with the morning profile to obtain a boundary layer height of 915 m for this test.

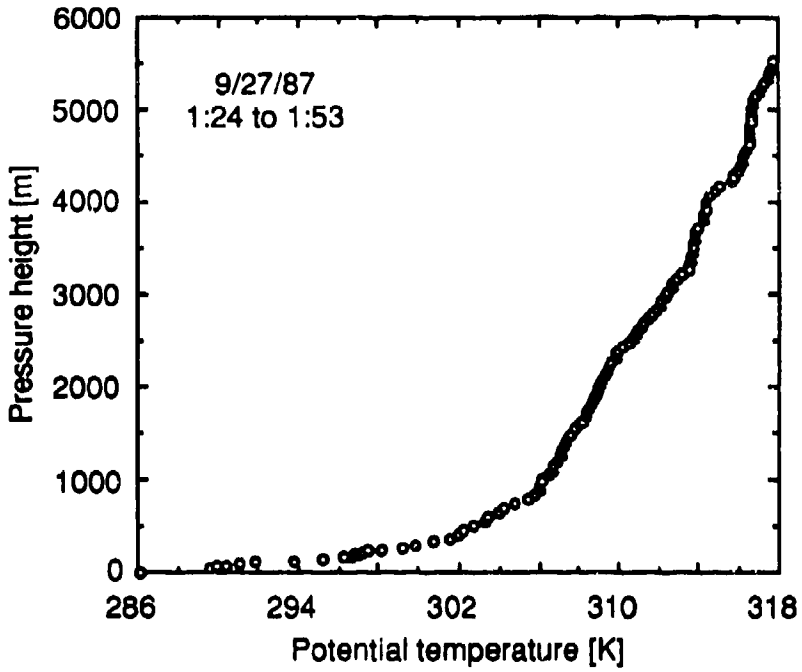

(a)

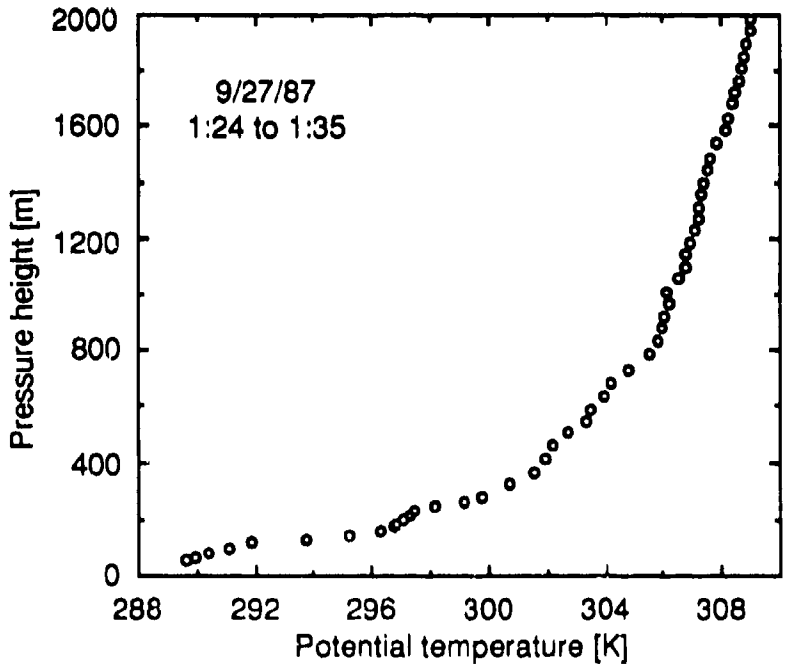

(b)

Figure 3.19 Potential temperature profile for September 27, 1987 (a) to a height of 5600 m and (b) to a height of 2000 m.

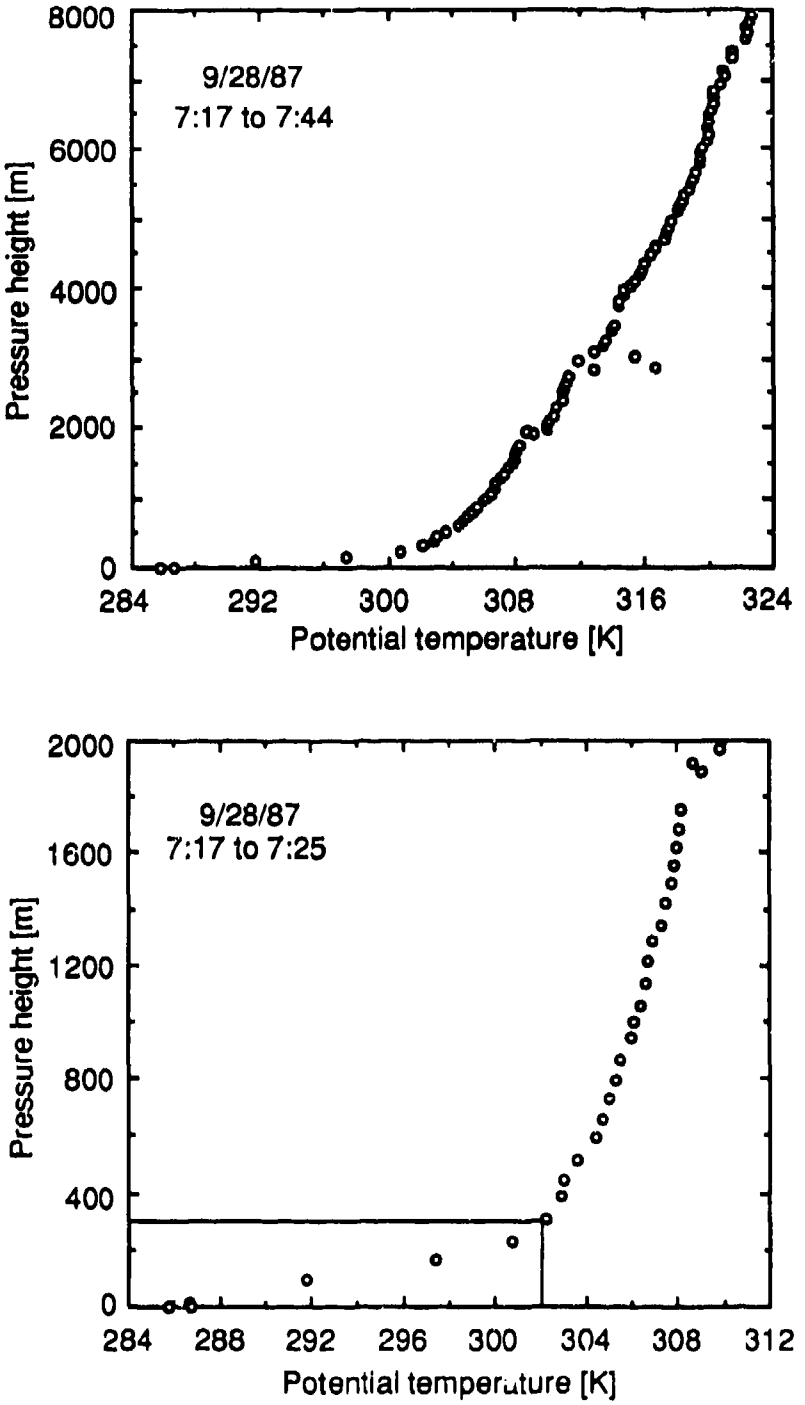

Figure 3.20 Potential temperature profile for September 28, 1987 (a) to a height of 8000 m and (b) to a height of 2000 m. The potential temperature at time of Test 0928871 was used with the morning profile to obtain a boundary-layer height of 300 m for this test.

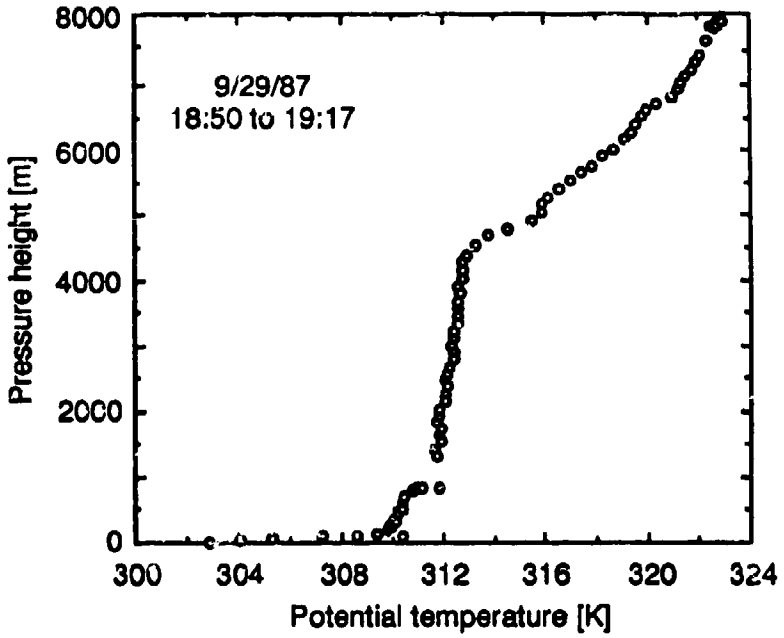

(a)

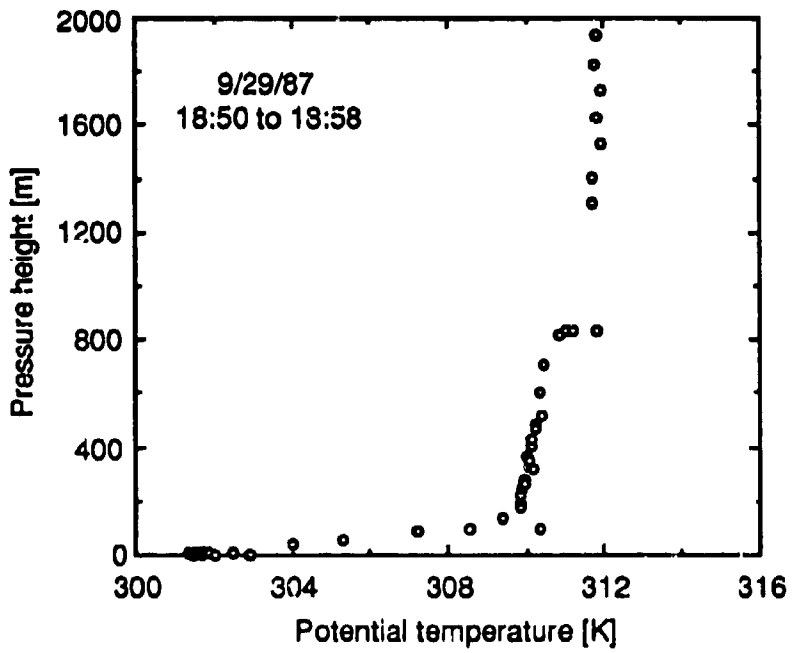

(b)

Figure 3.21 Potential temperature profile for September 29, 1987 (a) to a height of 8000 m and (b) to a height of 2000 m.

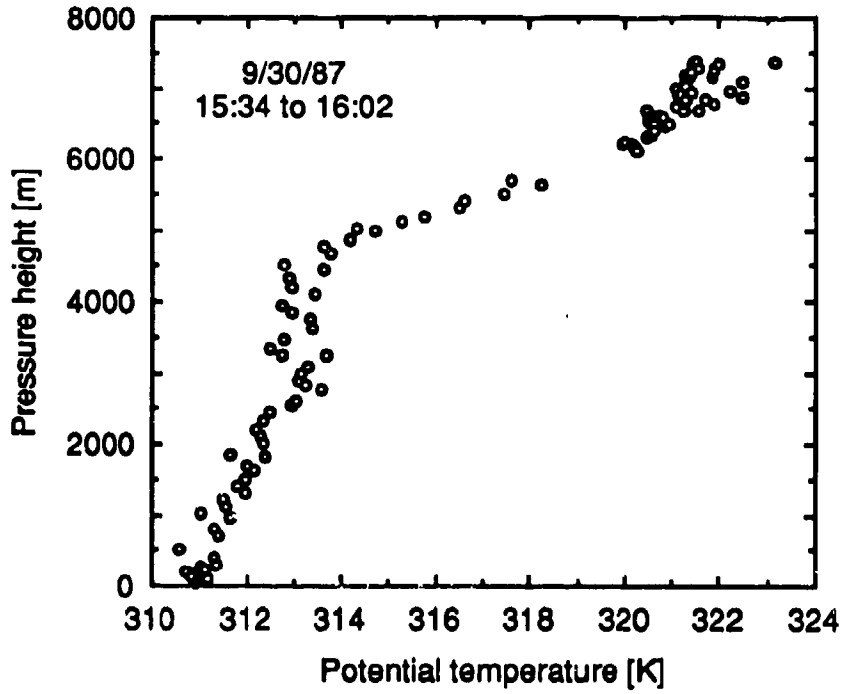

(a)

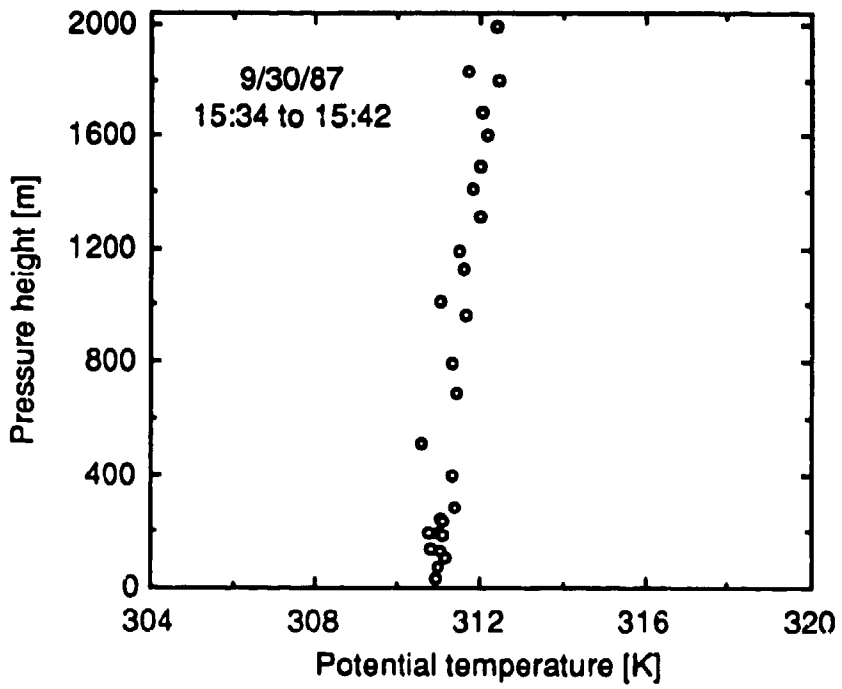

(b)

Figure 3.22 Potential temperature profile for September 30, 1987 (a) to a height of 7600 m and (b) to a height of 2000 m

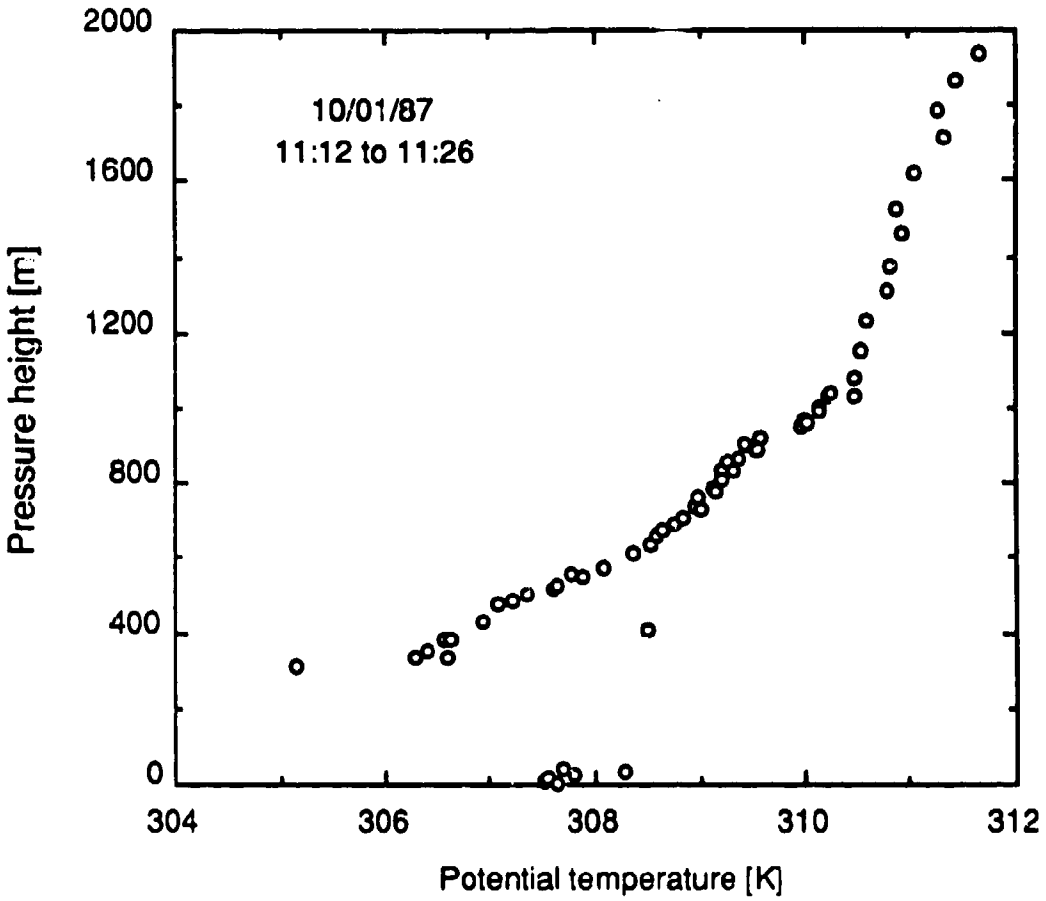

Figure 3.23 Potential temperature profile for October 1, 1987.

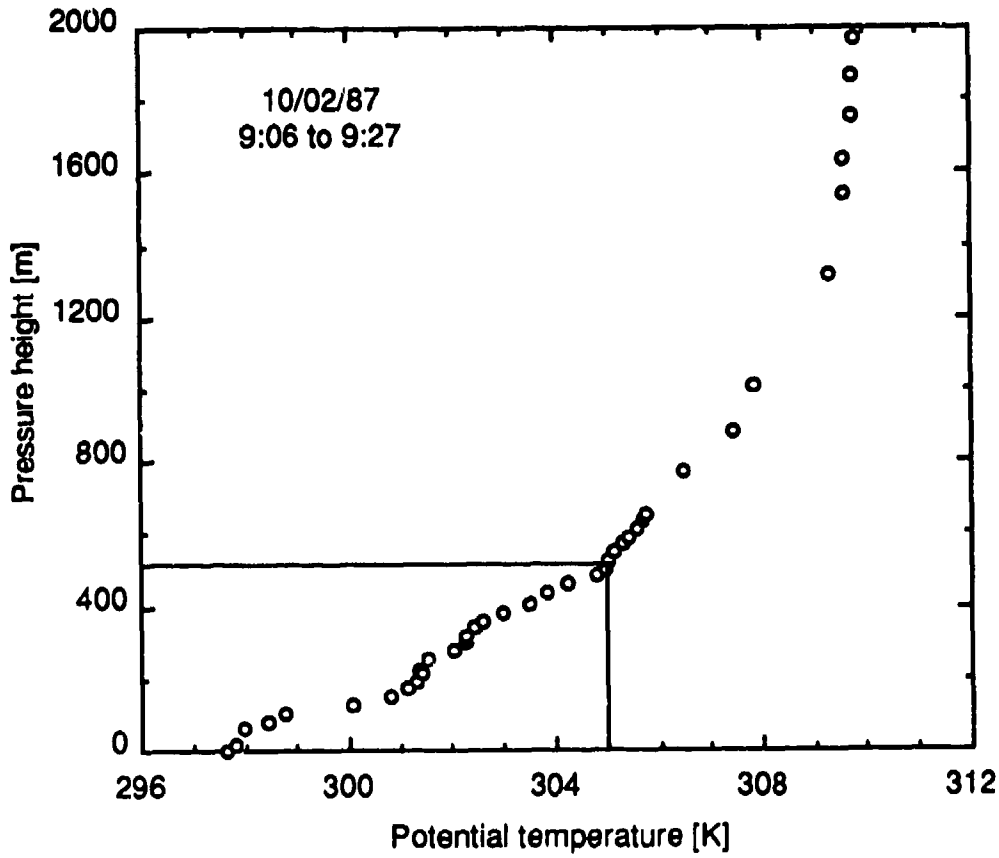

Figure 3.24 Potential temperature profile for October 2, 1987. The boundary-layer height of 520 m for Test 1002672 was obtained by intersecting the potential temperature at the time of the test with the morning potential temperature profile.

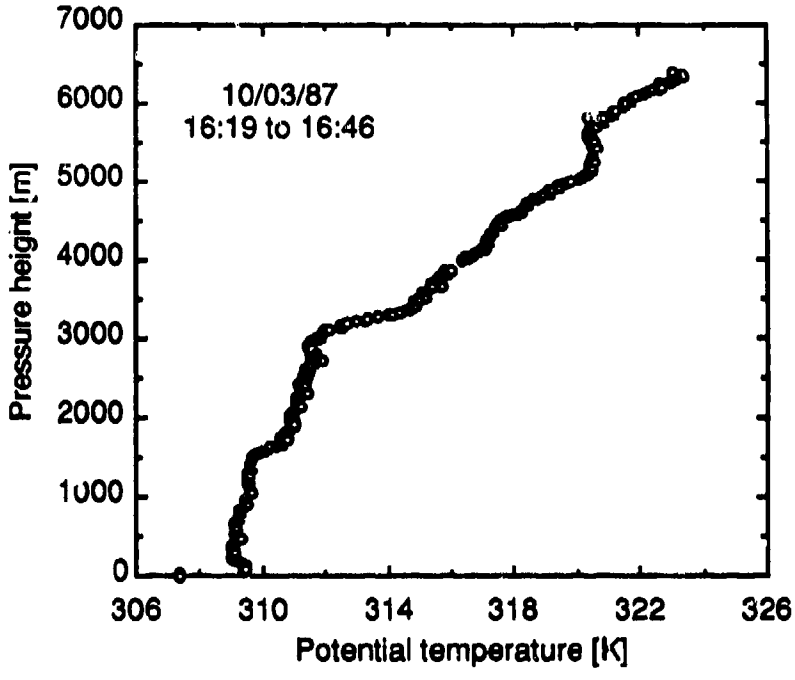

(a)

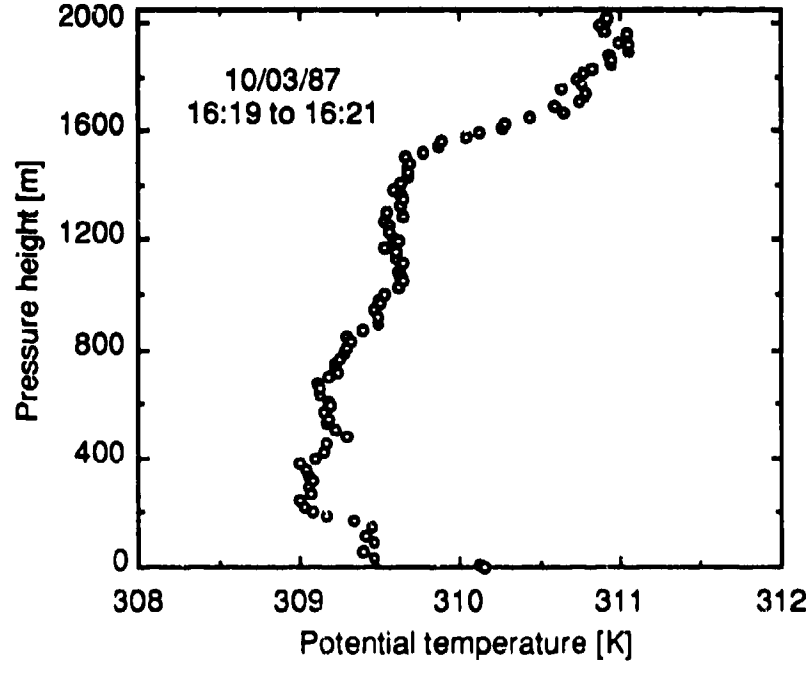

(b)

Figure 3.25 Potential temperature profile for October 3, 1987 (a) to a height of 6500 m and (b) to a height of 2000 m

possible for Test 0921871, since the first sounding was not made until two days later. However, a fairly reliable estimate may by made with the use of spectra data as discussed in the following paragraph. A sounding conducted immediately prior to Test 0923871 provides an accurate estimate for this test based on an observed inversion. Morning soundings are available for the other three convective cases (Tests 0926871, 0928871 and 1002872). The mixing heights determined for all five convective tests are summarized in Table 3.28.

Table 3.28 Mixing heights for unstable Meadowbrook tests.

Test	Times	z_i (m)
0921871	14:30 - 15:01	900
0923871	14:00 – 14:50	410
0926871	12:00 – 13:07	910
0928871	10:29 – 10:54	300
1002872	12:16 – 12:34	520

The peak frequency of the lateral spectra for unstable daytime tests is often associated with the passage of the largest convective cells, which scale to boundary-layer height. The horizontal width of these cells may be inferred by dividing the wind speed at a sufficiently high level by this peak frequency. Since the 16 and 30-m wind speeds do not differ appreciably for the unstable tests, the 30-m wind speed may be thought of as the horizontal velocity of these large convective cells. Figure 3.26 compares the horizontal width of these cells with the mixing heights for the four tests where sounding data are available. The linear agreement is quite remarkable considering the use of the 30-m wind speed and sounding-based mixing-height values. Using these comparisons, the mixing height for Test 0921871 is about 900 m. Relations such as this are most likely terrain dependent, since the slope of the curve shown is simply the aspect ratio of the convective cells.

3.5 Sonic-anemometer Data

3.5.1 Description of Sonic-anemometer Data

The data from the sonic anemometers (designated Sonic A and Sonic B) exist in the form of 10-min averages and were made available to us on nine-track computer tape. These averages were calculated by an on-site data acquisition system which sampled the anemometer outputs at the rate of 20 hz. These data include

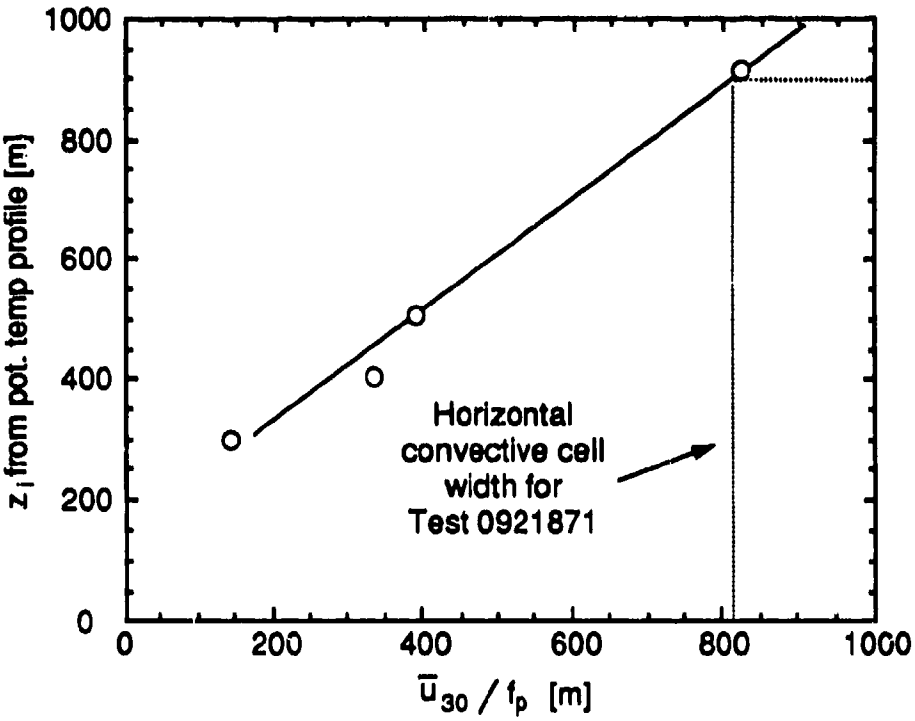

Figure 3.26 Correlation between boundary-layer heights determined using potential temperature profiles and horizontal convective cell widths.

(a) the vector-mean wind speed U [m/s],

(b) the vector-mean wind direction θ [°],

(c) the mean temperature T [°C],

(d) the turbulent kinetic energy E computed from the correlation $\frac{1}{2}(\overline{u'^2} + \overline{v'^2} + \overline{w'^2})$ [m^2/s^2],

(e) the heat flux H given by $\rho C_p \overline{T'w'}$ [W/m^2],

(f) z / L, where z is the measurement height of 7 m and L is the Obukhov Length given by

$$L = \frac{-u_*^3}{\kappa(g/T)Q_0} \quad [m], \text{ and}$$

(g) the friction velocity u_* given by $\sqrt{\overline{u'w'} + \overline{v'w'}}$ [m/s].

3.5.2 Synopsis of Sonic-anemometer Data

Since the sonic anemometer data exist only as 10-min averages, we could not compute averages over the same extended smoke release period which was used in analyzing the surface station data. However, we selected averaging times so that the sonic-anemometer and surface-station averaging periods never differed by more than 5 minutes. These sonic-anemometer test averages are presented in Table 3.29. Simple averages were computed for all values except L. For this parameter, the *average* heat flux and friction velocities were used in conjunction with the definition above. The potential temperature scale θ_*, easily determined from the friction velocity and heat flux (Eqn. 2.9), is also listed in Table 3.29.

Since we wanted the similarity parameters to be representative of the surface-layer properties over the course of the *entire* test, and because some of the 10-min data appear incongruous with those from the same averaging periods, we elected to calculate averages with the inconsistent data removed. These "filtered" averages appear in Table 3.29. The 10-min data and "unfiltered" averages are provided in Appendix A.

As mentioned in the introduction to this chapter, one potential problem of the sonic anemometer data is that they represent turbulent fluxes at a single point as

opposed to estimates derived from vertical profiles, which are inherently integral in nature. This difficulty can be further aggravated by the effects of complex terrain and heterogeneous meteorology. The sonic anemometer data presented for the unstable releases show that this is not a serious problem in the valley floor at the Meadowbrook site. Sonic A typically measured 50% higher heat fluxes and slightly higher friction velocities. These measurements combine to give slightly lower estimates of L. The similarity between the fluxes measured at these two locations indicate that, for unstable conditions, these quantities are not greatly influenced by the regional terrain and are more representative of the local terrain, which is similar around both sonics. Unfortunately, this comparison is only available for unstable conditions, since Sonic A was not operated during the night.

Two mixed-layer scaling parameters w_* and T_* may be easily computed for the convective periods from the sonic-anemometer data and estimates of the boundary-layer height. These relationships are described in Section 2.4, but are restated for the convenience of the reader

$$w_* = u_* \left(- \frac{z_i}{\kappa L} \right)^{1/3}, \tag{3.24}$$

and

$$T_* = \frac{\overline{T'w'}}{w_*}. \tag{3.25}$$

Estimates of these parameters along with the length scale ratio ($-z_i / L$) are given in Table 3.30 for the five unstable tests.

3.6 Discussion of Results

One of the primary goals of the AMADEUS smoke dispersion experiments is to assess the effects of terrain on near- and far-field aerosol dispersion. In view of this goal, the applicability of similarity scaling to the Meadowbrook data is explored, and comparisons of these data to flat-terrain results are made.

3.6.1 Velocity Profiles

Unstable Conditions

Figure 3.27 shows wind profiles for the five unstable tests plotted with respect to ln(z). Profiles for all tests except Test 0928871 demonstrate roughly logarithmic pro-

Table 3.29 Summary of sonic anemometer data for Meadowbrook dispersion tests. Filtered averages are shown.

Test -Sonic	U [m/s]	θ [°]	T [°C]	E [m^2/s^2]	H [W/m^2]	u_* [m/s]	L [m]	θ_* [°C]
0921871-A	4.80	275	42.1	2.17	143.0	0.88	-429	-0.146
0921871-B	3.79	303	38.9	2.53	132.1	0.77	-310	-0.152
0923871-A	2.42	268	34.0	1.54	199.7	0.86	-284	-0.204
0923871-B	2.95	270	30.8	1.25	174.6	0.62	-120	-0.245
0925871-B	0.51	106	15.6	0.10	-15.86	0.20	44.2	0.066
0926871-A	4.92	306	29.1	1.92	270.6	0.80	-169	-0.293
0926871-B	3.66	299	25.8	2.59	183.1	0.74	-197	-0.212
0927871-B	0.44	42	10.4	0.08	8.00	0.14	-30.0	-0.047
0927872-B	0.92	48	8.9	0.18	-13.49	0.24	89.9	0.046
0928871-A	2.54	262	28.8	0.27	115.3	0.23	-9.39	-0.433
0928871-B	3.11	269	25.8	0.28	65.77	0.17	-6.62	-0.332
0930871-B	1.06	67	17.1	0.15	-18.28	0.19	31.8	0.081
1001871-B	0.95	65	18.5	0.22	-34.7	0.26	44.5	0.112
1002871-B	1.05	56	17.5	0.07	-12.5	0.11	9.41	0.095
1002872-A	2.02	276	33.6	0.93	170.8	0.55	-87.4	-0.272
1002872-B	3.32	252	30.6	0.52	132.8	0.39	-39.8	-0.296
1003871-B	0.50	105	16.8	0.18	3.14	0.27	-838	-0.010

Table 3.30 Convective scales for the five unstable tests. These results are based on the filtered averages.

		Sonic Anemometer A			Sonic Anemometer B		
Test	z_i [m]	$-z_i / L$	w_*	T_*	$-z_i / L$	w_*	T_*
0921871	900	2.09	1.52	0.084	2.90	1.49	0.079
0923871	410	1.44	1.31	0.131	3.42	1.26	0.120
0926871	910	5.38	1.90	0.124	4.69	1.67	0.095
0928871	300	32.2	0.99	0.099	45.5	0.82	0.069
1002871	520	5.97	1.35	0.110	13.0	1.24	0.092

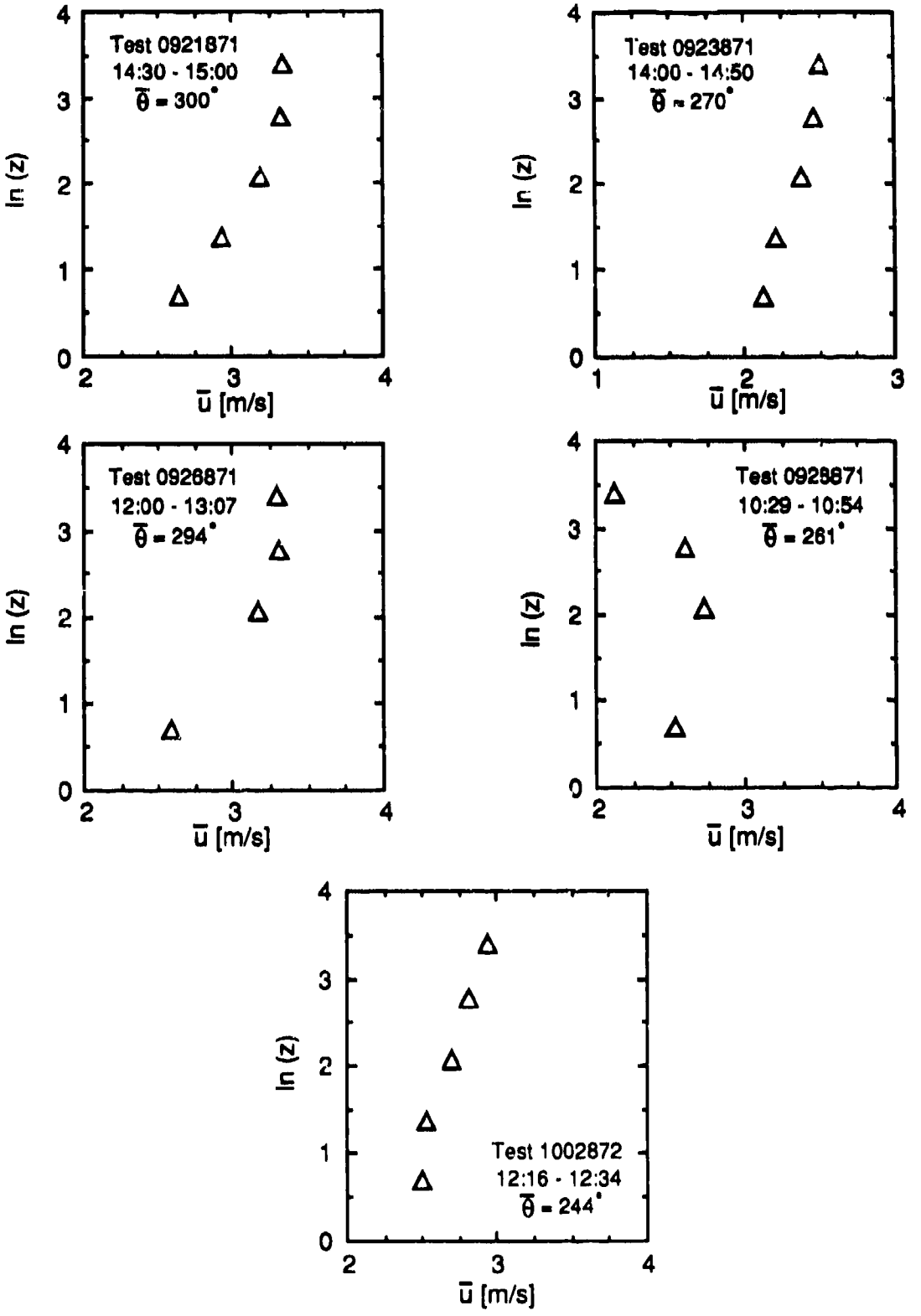

Figure 3.27 Wind profiles measured at 30-m micrometeorological tower during the unstable dispersion tests at Meadowbrook. Smoke release times and average directions are also given.

files at the lower levels, although perturbations exist around the 4- and 8-m levels for Tests 1002872 and 0923871. The profile for Test 0928871 is clearly non-ideal and exhibits a wind speed maxima at the 8-m level, indicating effects other than surface-induced shear and convection are present.

The minor perturbations present in the profiles for Tests 0923871 and 1002872 are characteristic of changes in roughness length at some distance upwind. A change in roughness length is, in effect, a change in surface stress which will cause the formation of an internal boundary layer. Friction velocities will typically vary among the internal boundary layers and cause perturbations, or kinks, in logarithmic profiles. Panofsky and Peterson (1972) further discuss this effect in analyzing data from the 125-m Risø tower in Denmark.

Due to the regionally irregular terrain and the proximity of the micrometeorological tower to Paynes Creek, abnormal profile features may be characteristic of the area. In order to determine the directional variation for daytime profiles, averaged ratios of the 2, 4, 8, and 16-m wind speeds to that of the 30-m level from 6 different directions have been computed and are shown in Figure 3.29. Figure 3.28 shows the six, upslope-flow directional increments into which these profiles are segregated. In this context, upslope flow denotes wind directions from 180° to 360°. Data from four days, encompassing the time period 11:00 to 17:00, were used in computing these profiles. Data from other days were not considered due to missing wind speeds, mainly at the 4-m level. In order to ensure unbiased results, profiles for which the minimum wind speed was less than 1 m/s were excluded, although 95% of the profiles were above this threshold. One-standard-deviation error bars on the ratios, 30-m wind speed statistics, and the percentage of included data from each directional increment are also provided in Figure 3.29.

These mean profiles clearly show influence of differential roughness and jetting phenomena often associated with buoyancy-induced slope flow. The most striking feature of the profiles from directions 240° to 360° is wind speed maximums below the 30-m level. The profile for directions 330° to 360° actually has the average wind speed minimum at 30 m! The standard deviations for the profile ratios are fairly high, indicating the shape of these profiles changes considerably over time. Profiles from 180° to 270° contain small, lower-level perturbations, most likely caused by Paynes Creek. These perturbations show good agreement with those of Tests 0923871 and 1002872. Comparison of the profiles for Tests 0921871 and 0926871 to the average profiles is also good, indicating test conditions were characteristic of the norm. The

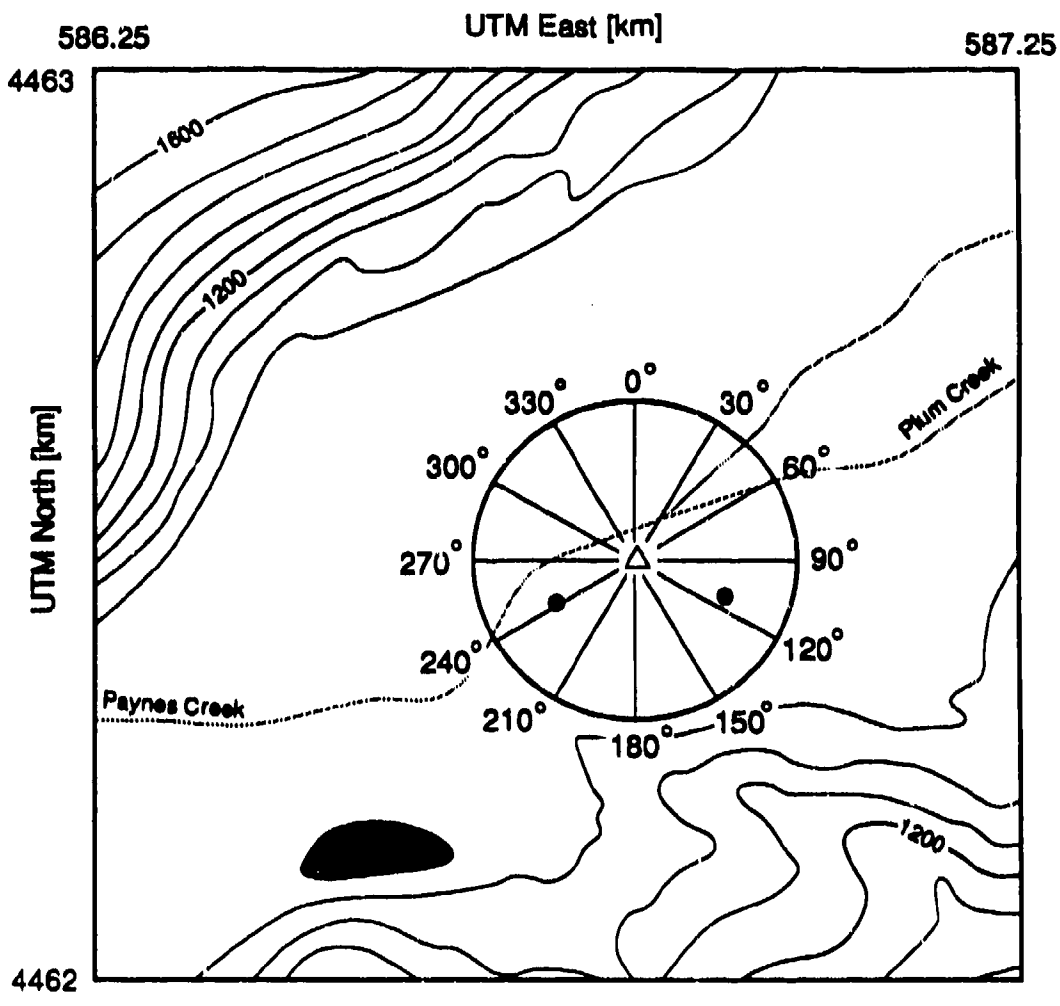

Legend

△ 30-m Micrometoerological tower

● Surface station A102

● Sonic Anemometer B

Figure 3.28 Upslope and downslope directional increments used in the profile analysis. Proceeding clockwise, the downslope and upslope directions span 0° - 180° and 180° - 360° respectively. The horizontal scale is in Universal Transverse Mercator coordinates with the grid marked in km. Elevations are in feet above sea level with contour lines at increments of 40 feet. The topographical information is taken from the USGS map of Inskip Hill, California.

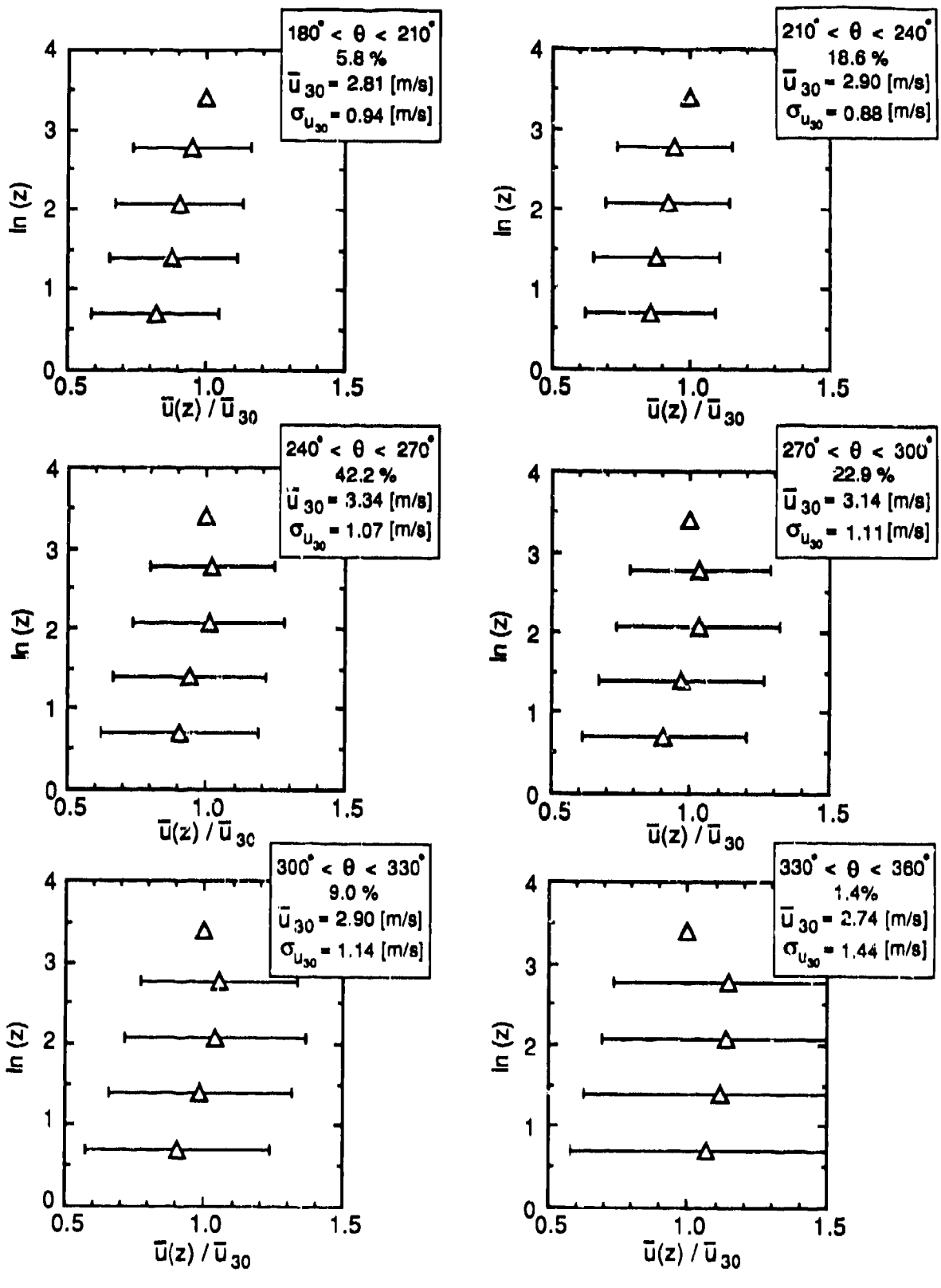

Figure 3.29 Daytime mean profile ratios for upslope flow directions along with percentage of data from each directional increment. One standard deviation error bars and 30-m wind speed statistics are also given. These data are averaged from four days encompassing time periods from 11:00 to 17:00.

jet-like profile for Test 0928871 is possibly a resultant of transitional effects, since that test occurred only an hour and a half after morning transition.

Stable Conditions

Profiles for five of the seven stable tests are shown in Fig 3.30. The other two tests are not included, because many of their average wind speeds were below anemometer thresholds of around 0.3 m/s. All profiles contained wind speeds below 1 m/s at lower tower levels, and significant bias errors due to non-cosine directional response of the propeller anemometers may have occurred. These errors can be largely ignored at higher wind speeds. Another problem not encountered in the unstable tests are large vertical variations in wind direction, with deviations between levels often exceeding 20°. Due to the possibilities of large directional errors in the propeller anemometers, the directions given in Figure 3.30 are those of the wind vane at the 10-m level. Despite these potential problems, the profiles for all tests except Test 0927871 are nicely logarithmic at the lower levels and display characteristics similar to those for stable conditions on flat, homogeneous terrain. The abnormal profile for Test 0927871 could be the result of the 30° wind direction variation among the levels (see Table 3.19).

In an analysis similar to that done for the unstable tests, mean profiles were computed for six downslope-flow directions ranging from 0° to 180° (see Fig. 3.28). Figures 3.31 and 3.32, for time periods encompassing 20:00-00:00 and 03:00-07:00 respectively, show the averaged wind profiles delineated by direction. The directions used for the separation of the data were those of the 10-m wind vane. Two separate time periods were selected to provide data on late-night and early-morning periods, for which different profile characteristics may be present. For both time periods, data from five days were used in the analysis; however, a majority of wind-speed measurements in the early morning period were below the 1-m/s threshold, and their profiles were not included in the averages. This omission of these early-morning data reduced the number of samples in three of the directional increments to less than 20, so their averaged profiles are not deemed statistically significant and thus are not shown.

The profiles from the two time periods are virtually identical in form, although the 30-m wind speeds are significantly higher during the late-night period. The higher wind speeds early at night probably result from the stronger buoyancy forces caused by the intense radiational cooling during this time. The directional distributions, as well as the ratio standard deviations, are nearly indistinguishable.

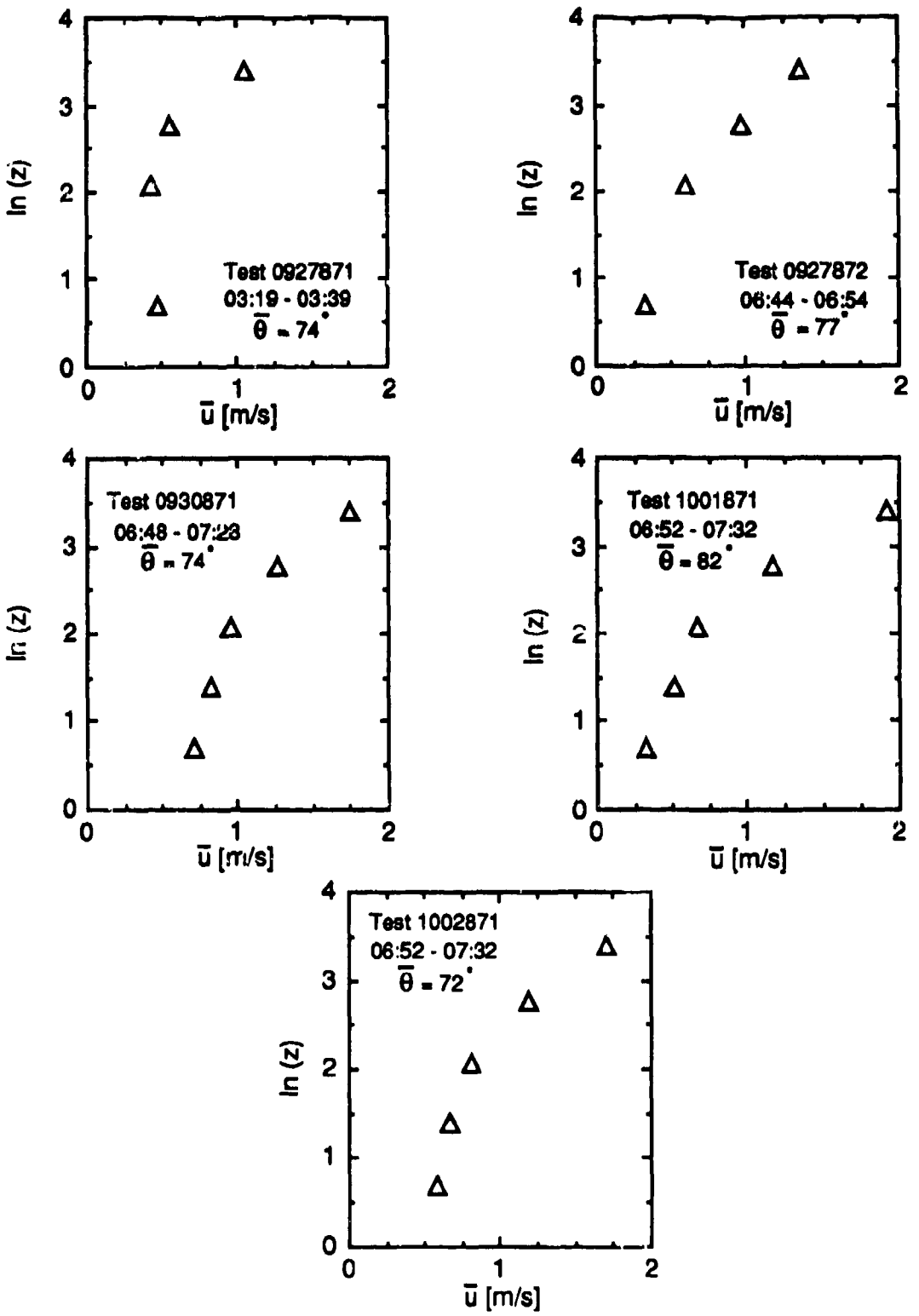

Figure 3.30 Wind profiles measured at 30-m micrometeorological tower during stable dispersion tests at Meadowbrook. Profiles for Tests 0925871 and 1003871 not shown due to near-calm conditions. Smoke release times and 10-m wind directions are also given.

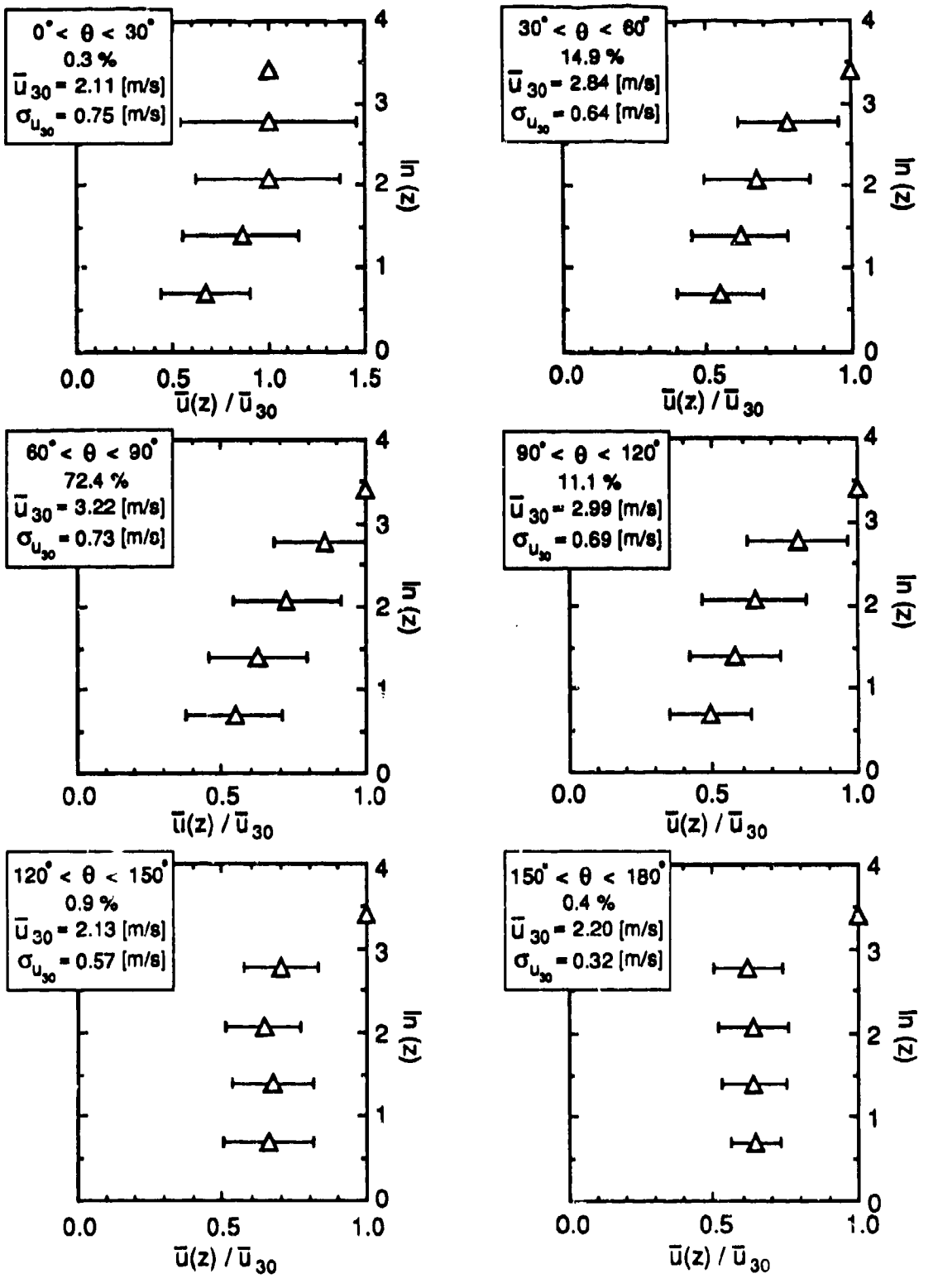

Figure 3.31 Late-night mean profiles for downslope directions along with percentage of data from each directional increment. One standard deviation error bars and 30-m wind speed statistics are also given. These data are averaged from five days encompassing time periods from 20:00 to 00:00.

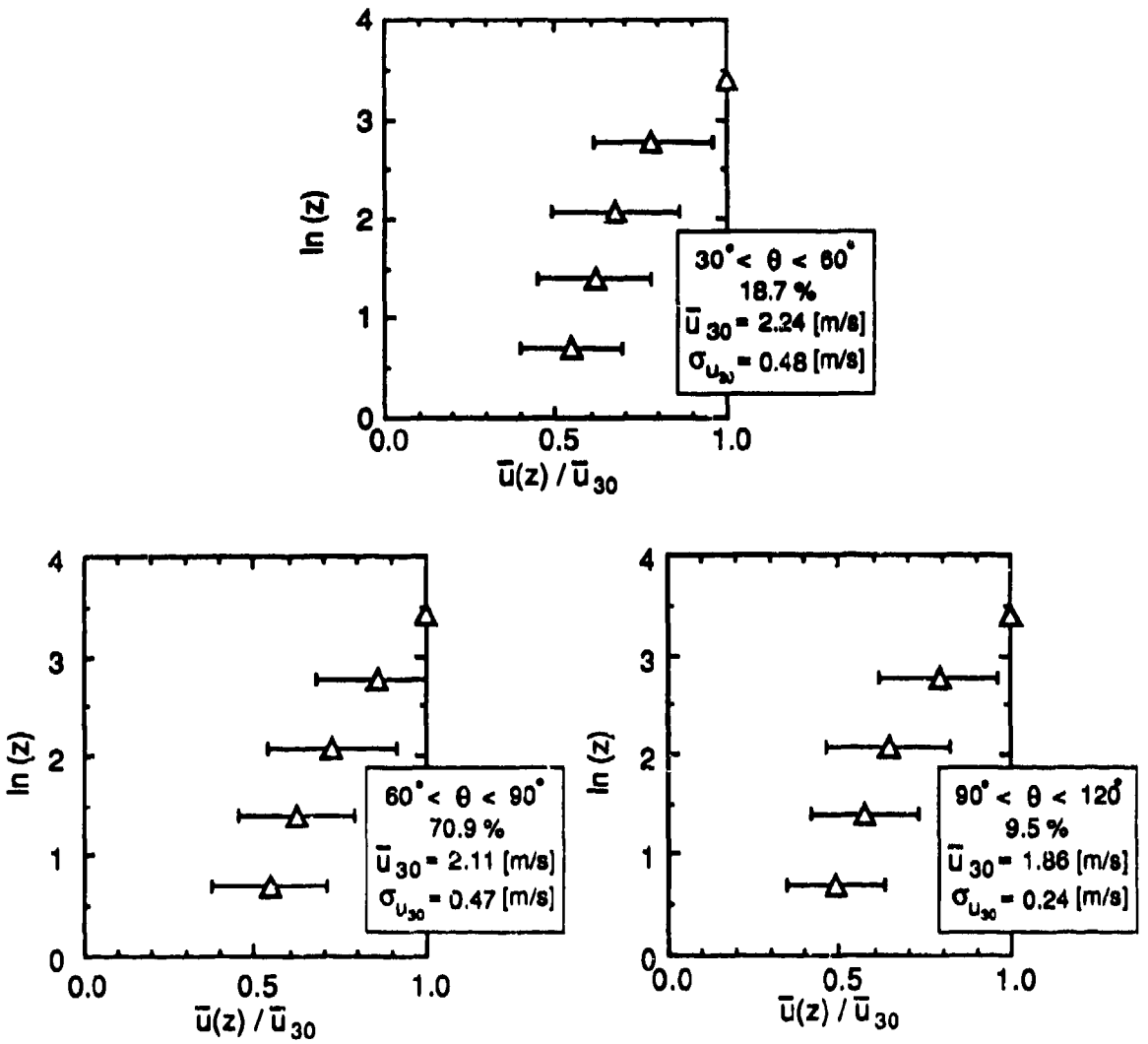

Figure 3.32 Early morning mean profile ratios for downslope flow directions along with percentage of data from each directional increment. One standard deviation error bars and 30-m wind speed statistics are also given. These data are averaged from five days encompassing time periods from 03:00 to 07:00.

As previously mentioned, many data for the nighttime periods were below the threshold of 1 m/s and were excluded from the averages. This criteria eliminated 55% of the late-night data and over 80% of the early-morning data. If we define wind-speed intermittency as the fraction of time that the wind speed is above 1 m/s, we can investigate how these intermittencies vary with time and direction. Table 3.31 shows the wind-speed intermittencies for the 2, 8 and 30-m levels of the micrometeorological tower. These data coincide with those used for the profile ratios. The low, early-morning intermittencies at the 2 and 8-m levels are indicative of a weak wind field in which cool, dense air pools near the ground. However, the 30-m early-morning intermittencies are actually higher than those at night, indicating that, although weaker, the core of the drainage flow is more established and flows consistently. Low-level intermittencies are very small for the sidewall directions.

In early morning, interesting behavior occurs in the 120° - 180° directional range, where intermittencies are lowest at the 8-m level. Further investigation into these data showed that the wind direction between the 2- and 30-m levels varied by 60°-75°. This large directional variation could result from the incursion of weak, shallow sidewall flows into the main valley at the 2- to 8-m levels. The shear zones, where the sidewall flows and the main drainage flows meet, may have very low wind speeds and thus, very low intermittencies. Sidewall flows typically have depths less than 15 m and, in the main valley at Meadowbrook, would only exert their influence when the low-level, drainage flow stagnates.

Table 3.31 Wind speed intermittencies for late night and early morning time periods. These data were measured on the micrometeorological tower.

	Intermittencies for time periods 20:00 - 00:00			Intermittencies for time periods 03:00 - 07:00		
Direction	2-m	8-m	30-m	2-m	8-m	30-m
$0° < \theta < 30°$	0.06	0.10	0.44	0.02	0.05	0.68
$30° < \theta < 60°$	0.33	0.54	0.81	0.13	0.23	0.92
$60° < \theta < 90°$	0.50	0.80	0.93	0.19	0.42	0.96
$90° < \theta < 120°$	0.24	0.59	0.88	0.10	0.18	0.96
$120° < \theta < 150°$	0.20	0.30	0.67	0.08	0.03	0.86
$150° < \theta < 180°$	0.11	0.19	0.44	0.16	0.00	0.72

3.6.2 Methods for Flux Determination

The proximity of the micrometeorological tower to Sonic A provides an excellent opportunity for the comparison of fluxes measured directly (with Sonic B) to those inferred from other measurements. Three alternative methods are considered in this analysis: (a) Irwin and Binkowski's bulk Richardson number method, (b) Niewstadt's profile fitting method, and (c) an the eddy correlation technique using the low-resolution micrometeorological-tower data. The method of Irwin and Binkowski as well as Nieuwstadt's profile method are discussed in Section 2.3. The eddy-correlation technique is essentially what the sonic anemometer employs and is discussed briefly in Section 3.1.

Before the Ri_b or profile method may be attempted, the roughness length must be estimated. In a complex terrain setting such as this, there are many issues which should be addressed as was discussed in Chapter 2. The mean velocity profiles described in the last section are somewhat useful, but extrapolation of the profiles to their zero wind speeds provide unreasonably low roughness heights (< .001 m) considering the heterogeneity of the terrain. The only other *empirical* method available to us is the EPA-recommended correlation presented in Section 2.3 and repeated here for convenience

$$\frac{\sigma_u}{u} = \frac{1}{\ln [z/z_o]}.$$

This provides reasonable but inconsistent roughness length estimates of 0.3 to 0.9 m for unstable tests and 0.1 to 0.2 m for stable tests. These results, however, may not be reliable, since the method is recommended for wind speeds above 5 m/s, and our data do not meet this criteria. For lack of a better method and to keep matters simple, we will use roughness lengths of 0.5 m/s for directions of 60° to 240° (southerly flow) and 1.0 m for the remaining directions. Two roughness lengths are necessary to account for the influence of the Paynes Creek creekbed on the flow.

The results of these comparisons are shown in Table 3.32. Results for Niewstadt's profile fitting method are not shown, since this algorithm failed to converge or gave extremely low Obukhov Lengths for all tests. The non-ideal profiles and large roughness lengths are probably to blame for these poor results. However, this method does converge to more reasonable (but still poor) values in some cases, if the roughness length based on a profile extrapolation is used. As emphasized in the previous paragraph, these are *very* small roughness lengths and do not have physical significance in this terrain. The eddy-correlation technique significantly underestimated fric-

tion velocity, and yielded negative heat-flux values for three of the five tests. The magnitudes of the Obukhov Lengths are rather consistent with those from the sonic, but the errors in sign are troubling, indicating that either the 1-s data are not feasible for use with this technique, or the temperature probes on the tower did not actually have a 1-hz response time. Irwin and Binkowski's method provided reasonable estimates of Obukhov Length but grossly overestimated friction velocity values. Unreasonably large roughness length estimates on the order of 2 - 5 m would lower these friction velocity estimates to a reasonable value, but they would also increase Obukhov Length estimates to near neutral values.

Table 3.32 Comparison of friction velocity and Obukhov Length as given by sonic anemometer and 2 alternative techniques.

	Sonic B		Eddy correlation		Irwin and Binkowski	
Test	u_*	L	u_*	L	u_*	L
0921871	0.77	-310	0.22	-131	1.95	-265
0923871	0.62	-120	0.16	66.2	1.68	-111
0926871	0.80	-197	0.31	281	1.07	-406
0928871	0.17	-6.62	0.07	6.62	1.25	-28
1002871	0.39	-39.8	0.17	-130	1.57	-124

No data for stable tests are presented owing to even poorer results than those for the unstable tests. For these tests the eddy-correlation technique yielded friction velocity estimates of less than 0.05 m/s and meaningless heat-flux values. Irwin and Binkowski's method yields Obukhov Lengths of zero for all tests, since Ri_b is greater than the critical value of around 0.21 for all tests. Profile fitting was not attempted.

3.6.3 Variance and Spectra

Unstable Standard Deviations

The flat-terrain, variance and spectra correlations presented in Section 2.5.1 may be used in conjunction with the sonic-anemometer-measured flux data to determine the applicability of similarity-based scaling in a complex-terrain setting such as the Meadowbrook Site. Figures 3.33 and 3.34 show σ_u and σ_v normalized by u_* and plotted against z/z_i. Højstrup's relations for these statistics for two different values of z_i/L, encompassing the values found occurring in our data, are presented for comparison. These correlations agree with the data fairly well for the mean-wind velocity variations.

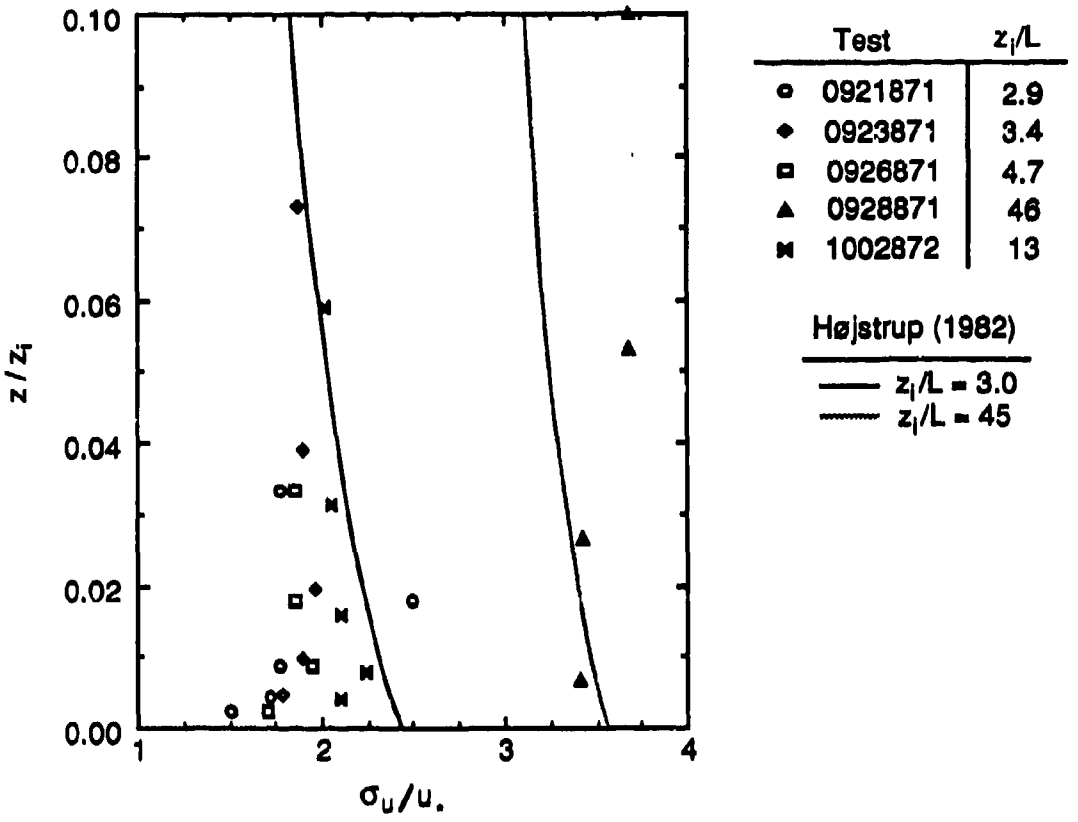

Figure 3.33 Mean-wind velocity standard deviations for unstable tests as compared with the similarity-based empirical relation by Højstrup (1982). Curves given represent approximate upper and lower bounds of z_i/L for our data.

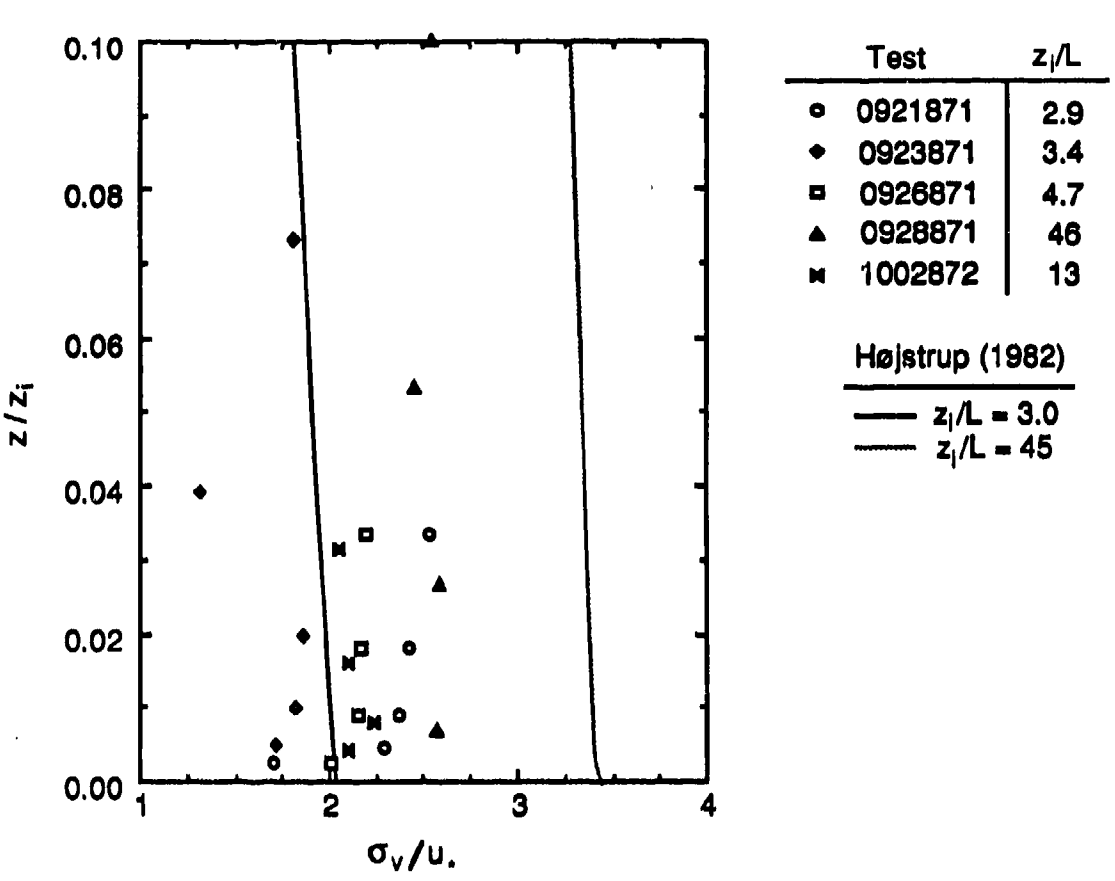

Figure 3.34 Tranverse velocity standard deviations for unstable tests as compared with the similarity-based empirical relation by Højstrup (1982). Curves given represent approximate upper and lower bounds of z /L for our data.

The correct estimate for Test 0928871 is especially encouraging. However, the increase of variance with height contradicts the trends that Højstrup's relations predict. The correlations between our data and the empirical functions for the transverse velocity are not as good, with a dependence on z_i/L failing to manifest itself. Much of this discrepancy may result from the effects of the valley in constraining the transverse velocity fluctuations.

Figure 3.35 shows σ_w normalized by u_* and plotted against ζ. Empirical relations from both Højstrup and Panofsky are shown for comparison. All relations overpredict the actual values of σ_w/u_* computed from test data, although, with the exception of Test 1002872, the proper dependency on z_i postulated by Højstrup is realized. The overprediction of σ_w/u_* is likely the result of terrain influences on friction velocity. The large convective cells, which contribute most to σ_w are probably influenced little by terrain in the middle of the Paynes Creek valley, whereas the friction velocity may be raised due to complex-terrain influence in the surface layer. Since the near surface variations in the horizontal velocity components are probably affected similar to friction velocity, this scaling did not produce such a wide disparity between the data and the models for the horizontal velocity standard deviations.

Stable Standard Deviations

Using the concept that the standard deviations for three velocity components should scale directly to friction velocity in neutral to moderately stable conditions, a direct relationship between these is explored. Standard deviations of the wind components measured on the 8-m level of the micrometeorological tower are compared to the friction velocities measured by the sonic anemometer in Table 3.33. Only the 8-m level on the micrometeorological tower is considered, since it is close to the 7-m sonic anemometer height, and consideration of only these data would reduce inconsistencies caused by height-dependent variations of friction velocity. Also, ζ values at this level, as measured by the sonic anemometer, are fairly small (< 1), approaching the criteria of moderate stability.

Table 3.33 also gives the correlation coefficients defined as

$$\rho = \frac{\overline{(\bar{u}_* - u_*)(\bar{\sigma}_i - \sigma_i)}}{\sigma_{u_*}\,\sigma_{\sigma_i}} , \qquad (3.26)$$

where the subscript "i" denotes each velocity component. Not only do the proportionality constants vary considerably between the tests, but the correlation coefficients

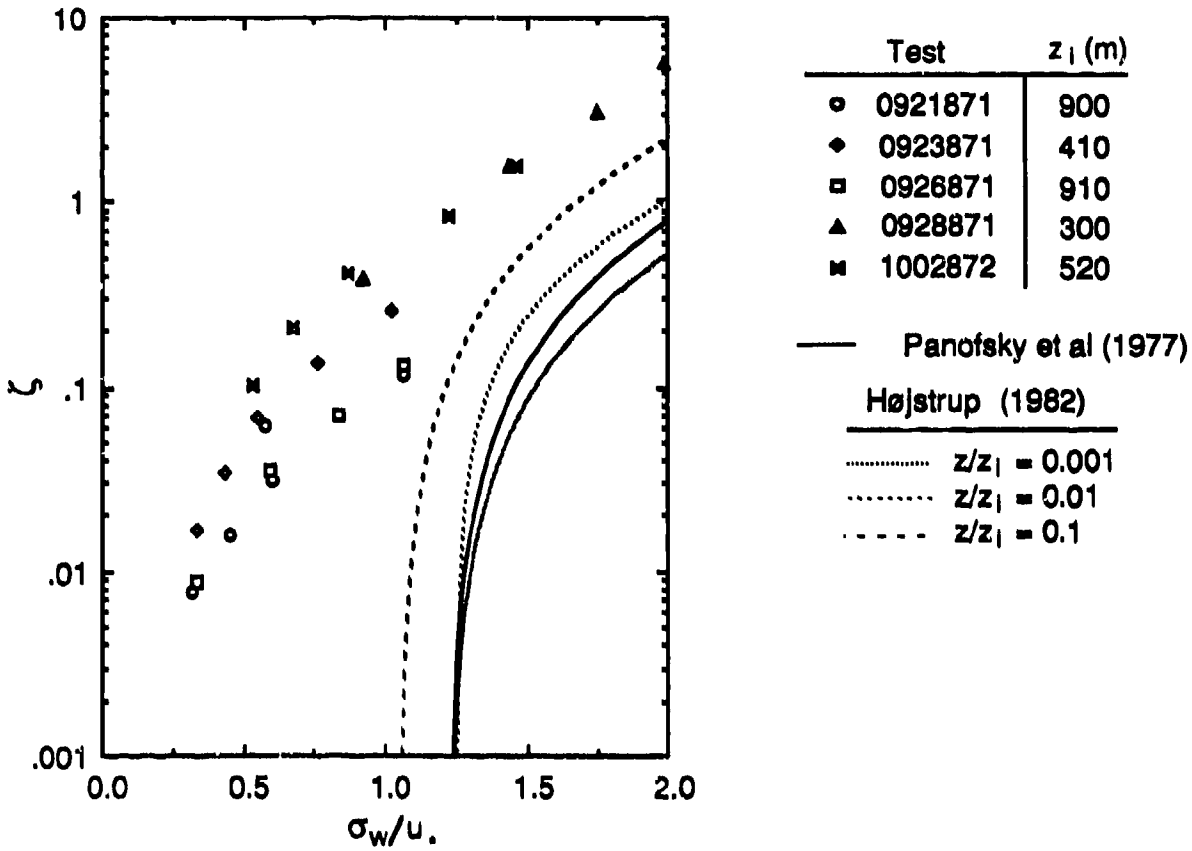

Figure 3.35 Vertical velocity standard deviations as compared with similarity-based empirical relations by Højstrup (1982) and Panofsky (1977). Boundary-layer height information provided for the comparison of influence on z/z_i.

indicate that a relationship between u_* and the velocity fluctuations is relatively poor, especially for the mean-wind direction. The correlation coefficient of 0.72 between σ_v and friction velocity indicates a moderate degree of consistency, but the correlation is still unimpressive. The general absence of a relationship between friction velocity and variance could be indicative of several things. These include: propeller-anemometer error caused by near threshold wind speeds; higher stabilities than indicated by the sonic anemometer, resulting in failure of the method; and subtle effects on u_* caused by far-upstream conditions. Considering the terrain and the highly stable conditions, as indicated by Ri_b values, all three of these effects were probably experienced.

Table 3.33 Friction velocities, wind-component standard deviations, and their ratios along with correlation coefficients for the stable tests.

Test	u_*	σ_u	σ_v	σ_w	σ_u/u_*	σ_v/u_*	σ_w/u_*
0925871	0.2	0.28	0.31	0.058	1.40	1.55	0.29
0927871	0.14	0.27	0.42	0.082	1.64	3.00	0.58
0927872	0.24	0.49	0.42	0.115	2.04	1.75	0.48
0930871	0.19	0.33	0.42	0.096	1.74	2.21	0.51
1001871	0.26	0.42	0.5	0.125	1.62	1.92	0.47
1002871	0.11	0.49	0.29	0.096	4.45	2.64	0.87
1003871	0.27	0.39	0.48	0.114	1.44	1.78	0.42
ρ		0.14	0.73	0.55			

Spectra

Figures 3.36 and 3.37 show a comparison between the unstable spectra for Tests 0921871 and 0923871 and the similarity-based predictions of Højstrup. These two tests were chosen for analysis, since their stability characteristics were similar. The spectra for the tests are also similar, but their agreement with the spectral model is relatively poor. The discrepancies are especially evident at the high-frequency end of the spectra, where the data completely fail to converge on a single curve in the inertial subrange. The raw spectra, given in Section 3.3.2, seem invariant with height, and the incorporation of reduced frequency adds a height and mean-wind speed dependence. The wind speed, however, varied little with height, so this scaling acted to *separate* the curves in this region. The agreement of the spectra between the two tests provides evidence that similarity-based scaling might apply, but the poor comparison of our data to the flat-terrain relations highlights the need for terrain considerations.

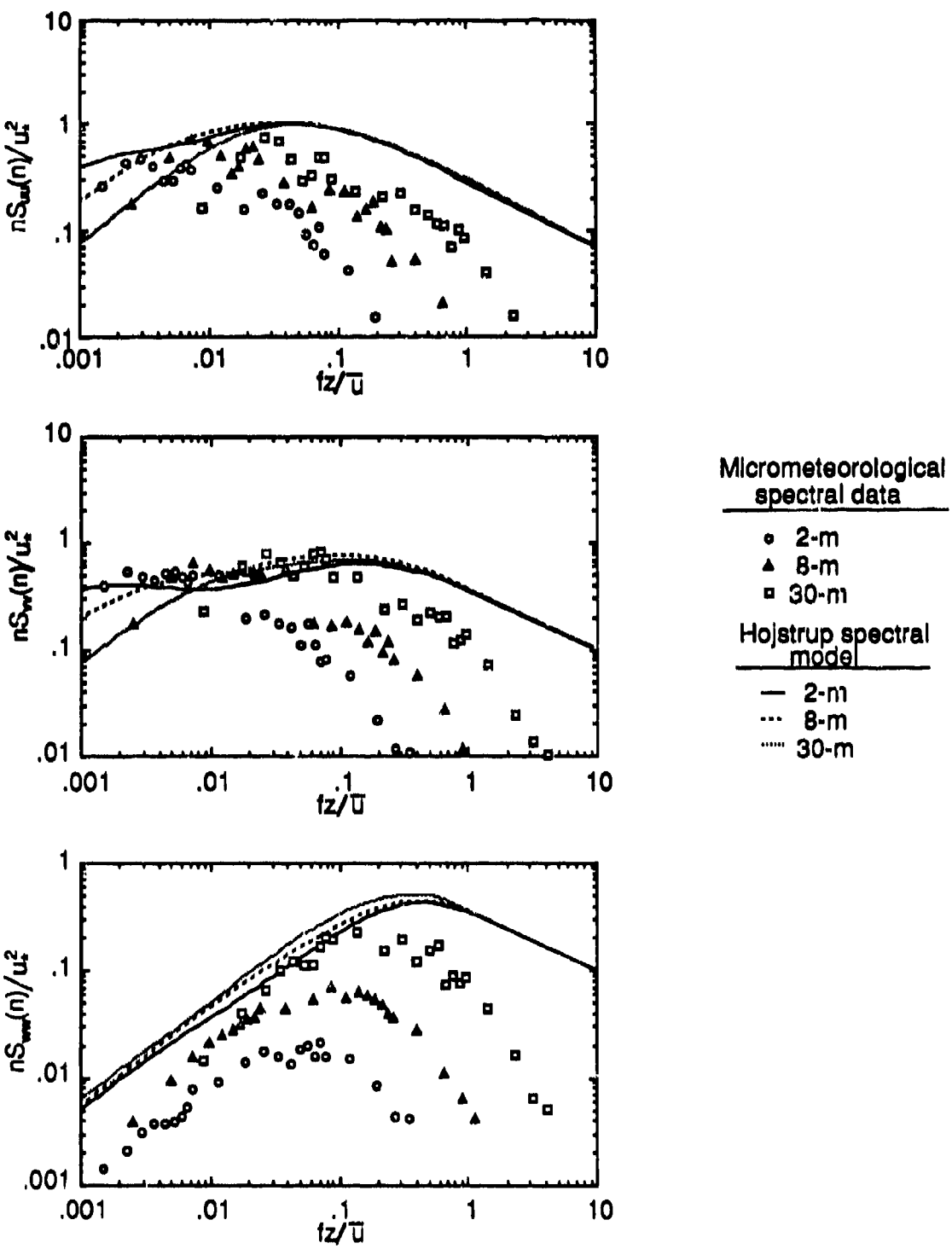

Figure 3.36 Comparison of spectra for Test 0921871 with similarity-based spectra model by Hojstrup's (1982)

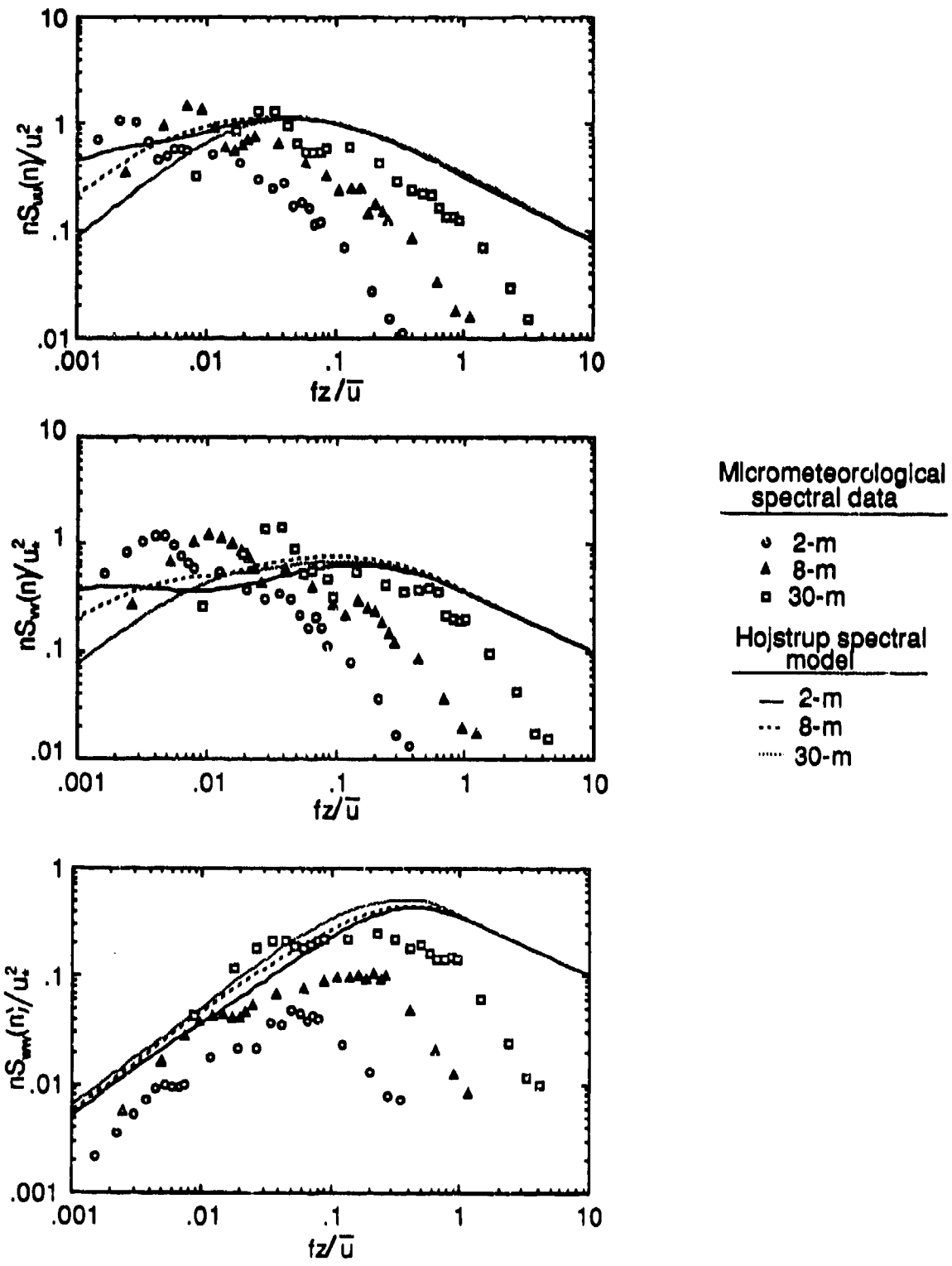

Figure 3.37 Comparison of spectra for Test 0923871 with similarity-based spectra model by Hojstrup's (1982).

4. NOCTURNAL DRAINAGE FLOWS AT MEADOWBROOK

As briefly discussed in Chapter 2, flat-terrain similarity scaling is of uncertain use in the analysis of nocturnal drainage flows. In fact, a definitive concept of stability, which is firmly established in flat-terrain meteorology, is itself somewhat elusive. A cursory inspection of the surface-station data given in Section 3.2 shows an extreme inhomogeneity in wind speed, temperature, and bulk Richardson number for the night-time dispersion tests. Such spatial variations, which are not significant in the daytime trials, underscore the complexities involved in characterizing near-surface atmospheric stability in complex terrain during the night.

4.1 Drainage Flows

4.1.1 Factors Influencing Flow Development

Even though radiative cooling is the primary factor influencing the development of nocturnal drainage flows, their characteristics may be influenced by a variety of additional atmospheric conditions as well as physical terrain features. The atmospheric effects can be delineated into two groups, those which reduce radiational cooling and those which physically erode or impede the formation of the drainage flows. Radiational cooling may be directly affected by cloud cover, local humidity, and soil characteristics, whereas the flows may be physically affected by upper-level winds, which may be either geostrophic or from larger drainage flow systems. The terrain effects are mainly confined to slope and surface characteristics, but can be extended to include large-scale terrain features, which may couple with upper-level winds to produce effects such as the entrainment of upper-level air or the creation of large circulations.

Atmospheric moisture and cloud cover are expected to significantly affect radiational cooling, although few observations comparing these constituents to radiational data exist. Observational studies into these effects are hindered by not only the inhomogeneous and time-dependent nature of atmospheric moisture content, but also the expense and difficulty incurred in obtaining the required data such as vertical profiles of water-vapor mixing ratio as well as cloud-base heights and cloud depths. Numerical studies have demonstrated that, when excluding external effects, the depth and strength of downslope flows decreased non-linearly when either the fraction of cloud cover increased or the cloud-base height decreased (Ye et al. 1990a). These

studies have also revealed that the impact of high clouds (cirrus, alto stratus, etc.) is almost negligible, even if overcast.

4.1.2 Drainage Flow Similarity

Although no generalized similarity theory exists for predicting the wind profiles and boundary-layer depths of drainage flows, there exists strong evidence that local site-specific scaling is plausible. Numerical studies have demonstrated that drainage flow boundary-layer depths are insensitive to terrain steepness, although their strengths are indeed dependent on steepness (Ye et al., 1990b). These same studies have shown that drainage-flow characteristics are predominantly dependent on local phenomena, as opposed to large scale atmospheric conditions. Almost all observational and numerical studies have shown that drainage flows exhibit low-level jets. These jets have been shown to be typical of free-shear jet boundaries in that turbulent kinetic energy is minimized at the jet maximum and momentum fluxes change sign across the boundary (Horst and Doran, 1988). Clements et al. (1990) present tethered-balloon data recorded during the ASCOT programs in 1984 and 1988, which demonstrate that the height of the jet boundaries were relatively constant with respect to location from night to night. During these same nights, however, the maximum velocities and boundary-layer depths varied considerably. These observations strongly suggest that the lower and upper depths of valley flows are decoupled, and local similarity scales, such as that proposed by Nieuwstadt (1984) and discussed in Section 2.2, might be applicable.

4.2 The Meadowbrook Drainage Flow System

Before the dispersion of fog-oil smoke can be properly assessed and modeled, the Plum Creek drainage flow characteristics, as well as the factors influencing them, should be investigated. In this section we will attempt to quantify the drainage flow strengths and associated thermal stabilities and try to relate these to each other and the conditions in the regional terrain. Data from 7 of the 14 surface stations on the Meadowbrook site will be used in this analysis. Stations A105, A109 and A110 are located in regions above the Plum and Paynes Creek valleys and will be used in determining the conditions outside of the local valley system. Stations A106, A107, and A108, will be used for determining flow characteristics in the Plum Creek valley, where the "stable" smoke releases were conducted. Station A102 will be used solely

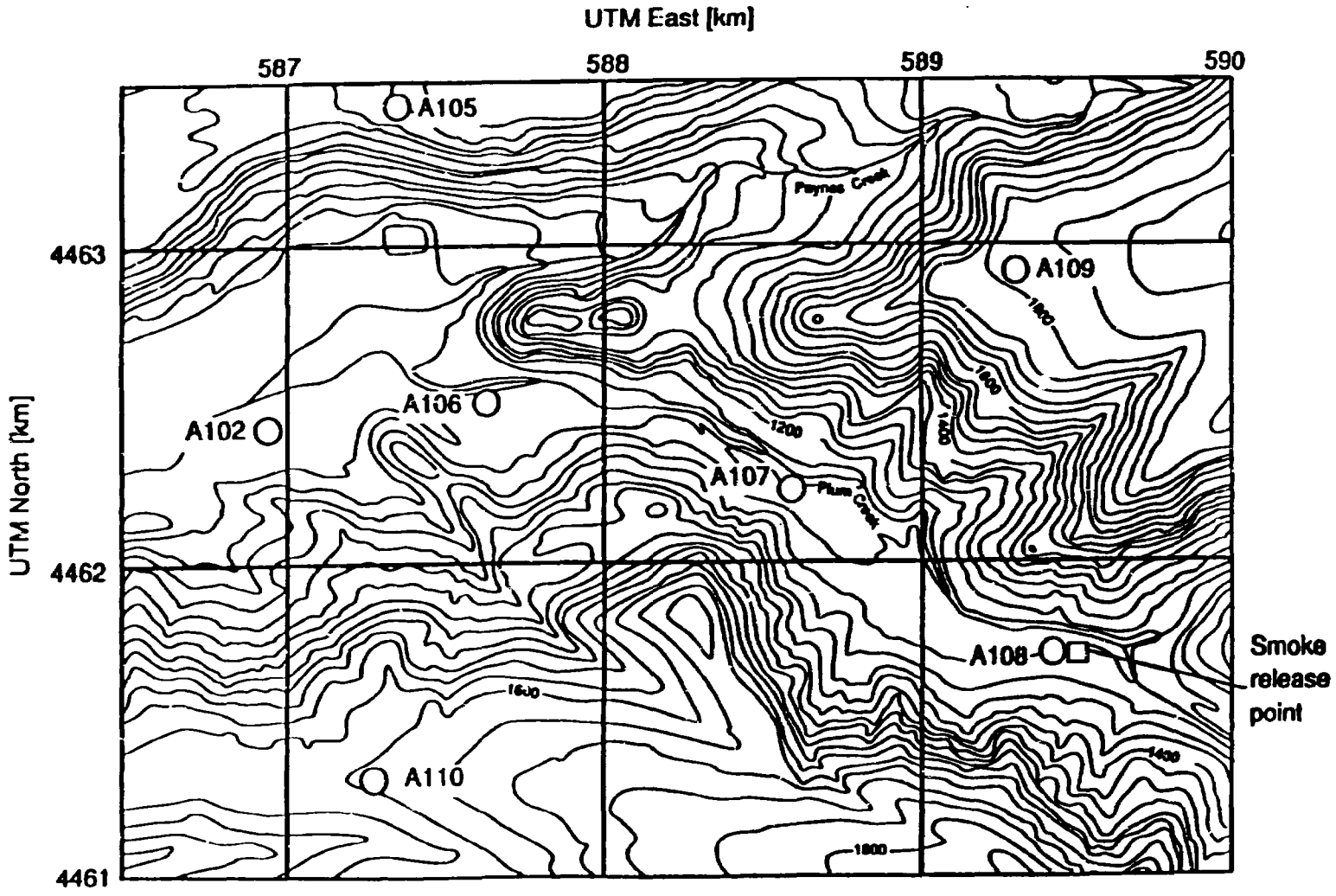

Figure 4.1 Topographical map showing the 7 surface stations used in the analysis of nocturnal flows at the Meadowbrook Site. Elevations are in feet above sea level with contour lines at increments of 40 feet. The horizontal scale is in Universal Transverse Mercator coordinates, with the grid marked in km. The topographical information is taken from the USGS map of Inskip Hill, California.

for a representative 10-m temperature on the main Paynes Creek valley floor. The locations of these stations are shown in Figure 4.1.

In Section 4.2.1, two measures of thermal stability are discussed. One of these is the difference in temperatures between the 10 and 2-m levels at an individual station. This local temperature difference will be referred to as ΔT_i where the subscript "i" denotes the station. The second measure of thermal stability will be the temperature difference between the ridge-top regions and the valley floor. This regional-scale surface-temperature difference will be referred to as $\forall T_i$ where the subscript "i" denotes the station whose 10-m temperature difference with respect Station A102 is being considered.

These quantities are employed in Section 4.2.2 where flow characteristics in the Plum Creek valley are analyzed. The primary goal of this analysis is to determine if the drainage-flow characteristics are most affected by local, valley-scale or mesoscale phenomena. Also, the relationship between local ΔT and regional $\forall T$ is examined. The strength of the flows are inferred with the 10-m wind-speed averages. These 10-m wind speeds should adequately represent the night-to-night, drainage-flow strength variations, since, as was discussed in Section 4.1.2, some degree of wind profile similarity for valley flows has been observed.

4.2.1 Thermal Stability Issues

Some of the problems associated with the classification of stability at the Meadowbrook site can be examined in Figure 4.2. Shown here are 10-m temperature records for Stations A102 and A109 during a 24-hour period from noon on September 21, 1987 to noon the following day. Temperatures at the 10-m level as well as ΔT's for each station are shown. During the day the 10-m temperatures measured at Stations A102 and A109 are very similar, and neither show strong variations with time. However, the temperature difference between the two stations ($\forall T_{A109}$) jumps ten degrees during the first hour after sunset and becomes as much as 15 °C shortly before sunrise. In addition to this temperature disparity, the temperature fluctuations at the individual stations are an order of magnitude larger during the night.

The magnitudes and fluctuations of the ΔT's also exhibit differences with respect to stations and times of day. In the daytime, ΔT_{A109} is larger and more erratic, but during the night ΔT_{A102} shows greater and more randomly fluctuating values. At times, ΔT_{A102} approached 5 °C (indicating a near-ground lapse rate of 0.6 °C/m !) but at other times is less than 1 °C, underscoring the strength and variability of the lower valley stratifications.

Since the primary driving mechanism for nocturnal drainage flows is the long wavelength radiational cooling of the sloping terrain, these regional temperature variations, such as $\forall T_{a109}$, might be related to characteristics of the drainage flows. Regional thermal stability may be directly coupled with the Plum and Paynes Creek system or could be influenced by larger scale (mesoscale) drainage flows which arise from the higher elevations to the east of the site.

Near-ground temperature differences ΔT are indicative of local thermal stability, and when combined with wind speeds, are measures of hydrodynamic stability through the Richardson number concept. These temperature differences reflect not only radiational cooling at a particular location, but also the turbulent mixing of the warmer drainage core into the heavily-stratified, near-ground air at that point. As is evident in Figure 4.2, this local stratification can exhibit strong fluctuations in small time periods, and as was seen with the surface-station data, stratification and Ri_b are very spatially inhomogeneous. Unfortunately, our surface stations lacked radiation and humidity sensors and our on-site cloud cover data is relatively limited, so we cannot assess these effects on the local cooling. This might not be a significant problem, however, since the entire area was very dry and relatively free of low cloud cover for the duration of the experiments.

4.2.2 Flow Characterization

Large, nocturnal temperature variations between stations and strongly fluctuating values of ΔT, such as those shown in Figure 4.2, were not unusual at the Meadowbrook site. Realizing that these temperature gradients usually exist, we desire to relate the ΔT and $\forall T$ values to the drainage-flow strength in the Plum Creek valley, where the "stable" fog-oil smoke releases were conducted. However, the significant fluctuations in the temperature fields require a systematic averaging scheme to be established before data comparisons can be made.

In a manner similar to that done in the analysis of the micrometeorological profiles for stable conditions, surface station temperature and velocity data are analyzed in two separate groups, which encompass the four-hour segments 20:00 - 00:00 and 03:00 - 07:00. Two separate time periods were selected to provide data on the late-night and early-morning periods, during which different flow regimes may be present, while four hour time spans were chosen to provide sufficient statistical accuracy.

In Figure 4.2, it can be seen that the near-surface cooling is very strong early in the night and continually weakens until sunrise. As a consequence, the wind speeds

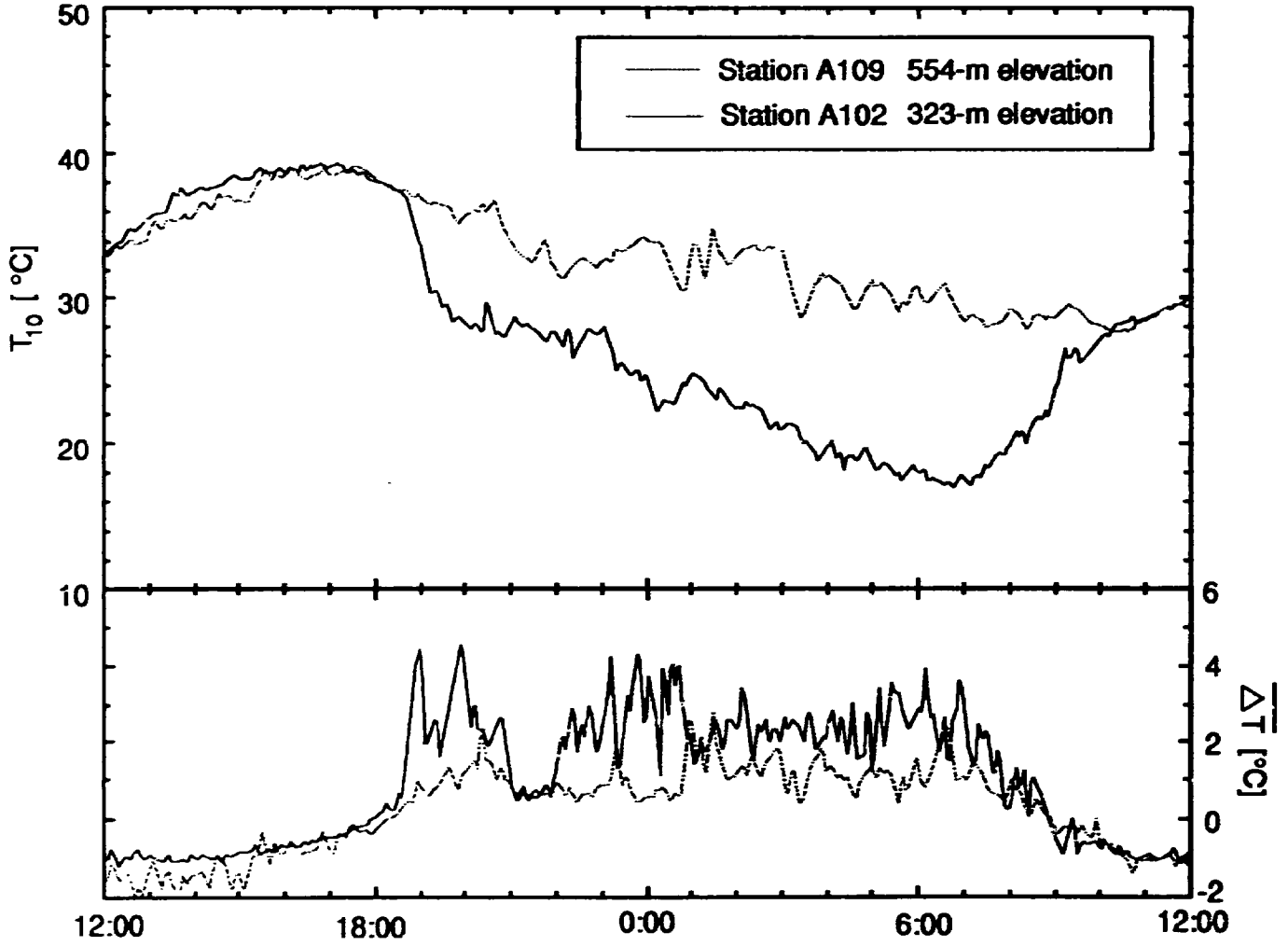

Figure 4.2 10-m temperatures and temperature differences between the 10 and 2-m levels measured at Stations A102 and A109 on Septemper 21-22, 1987. The curves represent linearly-interpolated, 5-min averages.

are generally higher during the late-night hours when the gravity induced buoyancy forces are highest. However, the temperature differences $\forall T$ and ΔT are highest early in the morning, when wind speeds are lower and stratification is more firmly established. The early morning is also of the most interest to us, since most of the Plum Creek dispersion tests took place after 06:00.

Characterization of intra-valley stratification

The first issue that needs to be addressed is whether the average temperature differences $\forall T$, as assessed by the three higher elevation surface stations, yield the same night-to-night trends. Since A109 is the highest of these stations, $\forall T_{A109}$ is compared with $\forall T_{A105}$ and $\forall T_{A110}$. These average temperature differences, for both late night and early morning time periods, are shown in Figure 4.3. Only 10 of the 16 days in the AMADEUS experiment are used with these data, since Station A109 was only operational for 10 days. From the data shown in Figure 4.2 and the associated correlation coefficients, it appears that $\forall T_{A110}$ is correlated very well to $\forall T_{A109}$. The temperature difference $\forall T_{A105}$, however, followed the same general trend as $\forall T_{A109}$ but significant discrepancies exist. These are important observations, since they indicate that the temperatures at Stations A110 and A109 are influenced by the same processes, and strongly suggest that mesoscale influences are present which serve to partially decouple the conditions at Station A105 from those at Stations A109 and A110.

Relationships Between Regional Thermal Stability and Plum Creek Data

A comparison of $\forall T_{A110}$ with the average wind speeds at the Plum Creek Stations A106, A107 and A108 for both late night and early morning periods is shown in Figure 4.4. Station A110 is used as the upper-level station for these comparisons, since data from this station are available for all 16 days of the AMADEUS experiments. The most prominent trend shown in these data is that the velocity maxima occur for all three surface stations for moderate temperature differences (5 – 7 °C). These maxima occur for slightly different values of $\forall T_{A110}$ depending on whether late night or early morning periods are being considered.

Before these observation can be properly assessed, the interaction between $\forall T_{A110}$ and ΔT_{106}, ΔT_{107} and ΔT_{108} needs to be considered. Figure 4.5 shows the comparison between $\forall T_{A110}$ and the ΔT values for the three Plum Creek surface stations. For the nighttime hours, a slight positive correlation is present between $\forall T_{A110}$

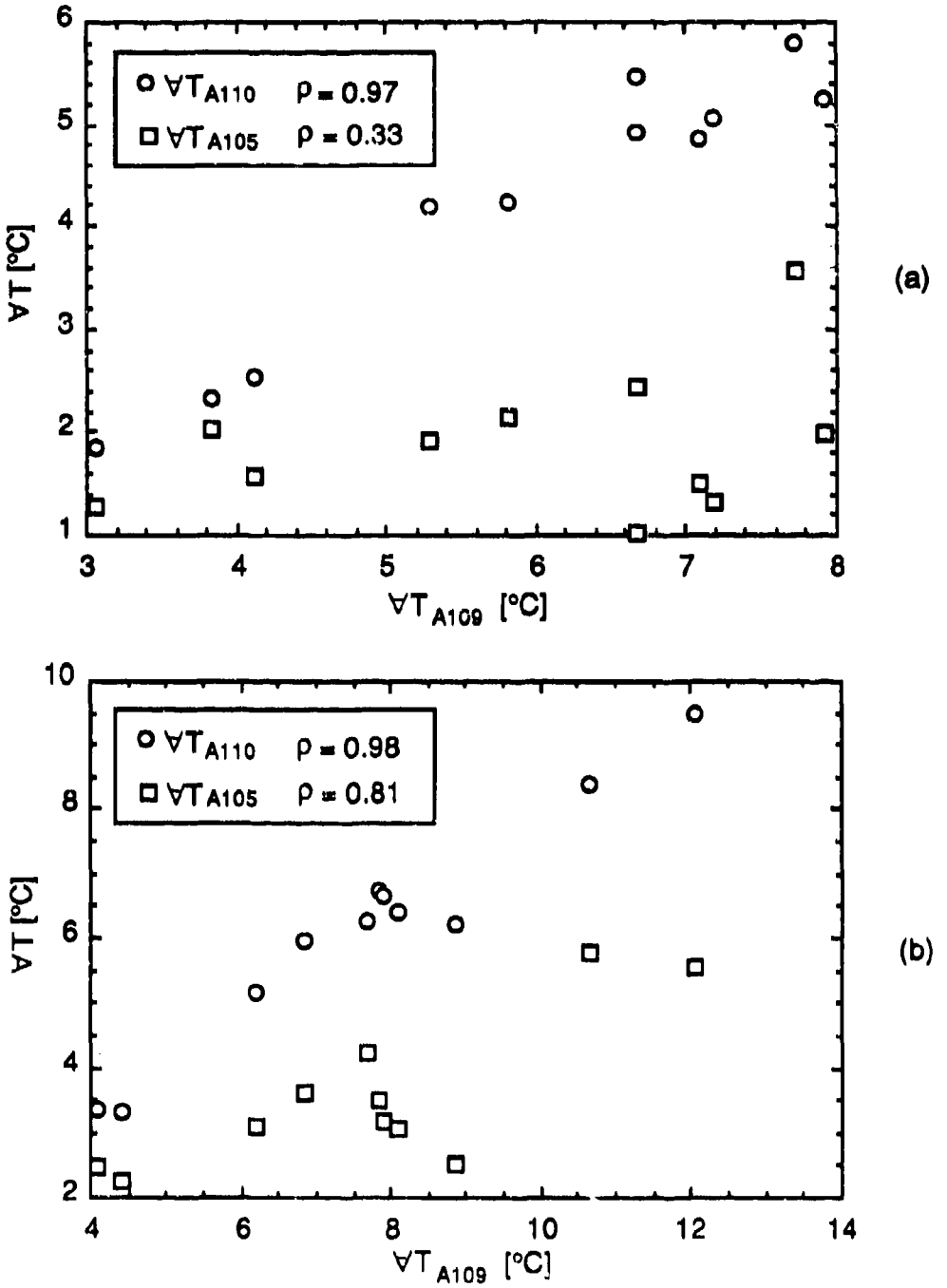

Figure 4.3 Correlation between the intra-valley temperature differences computed using Station A109 and those computed using Stations A105 and A110. Plot (a) is for the time period from 20:00 to 00:00 and plot (b) is for the time period from 03:00 to 07:00. These data are from the 10 days that Station A109 was in operation.

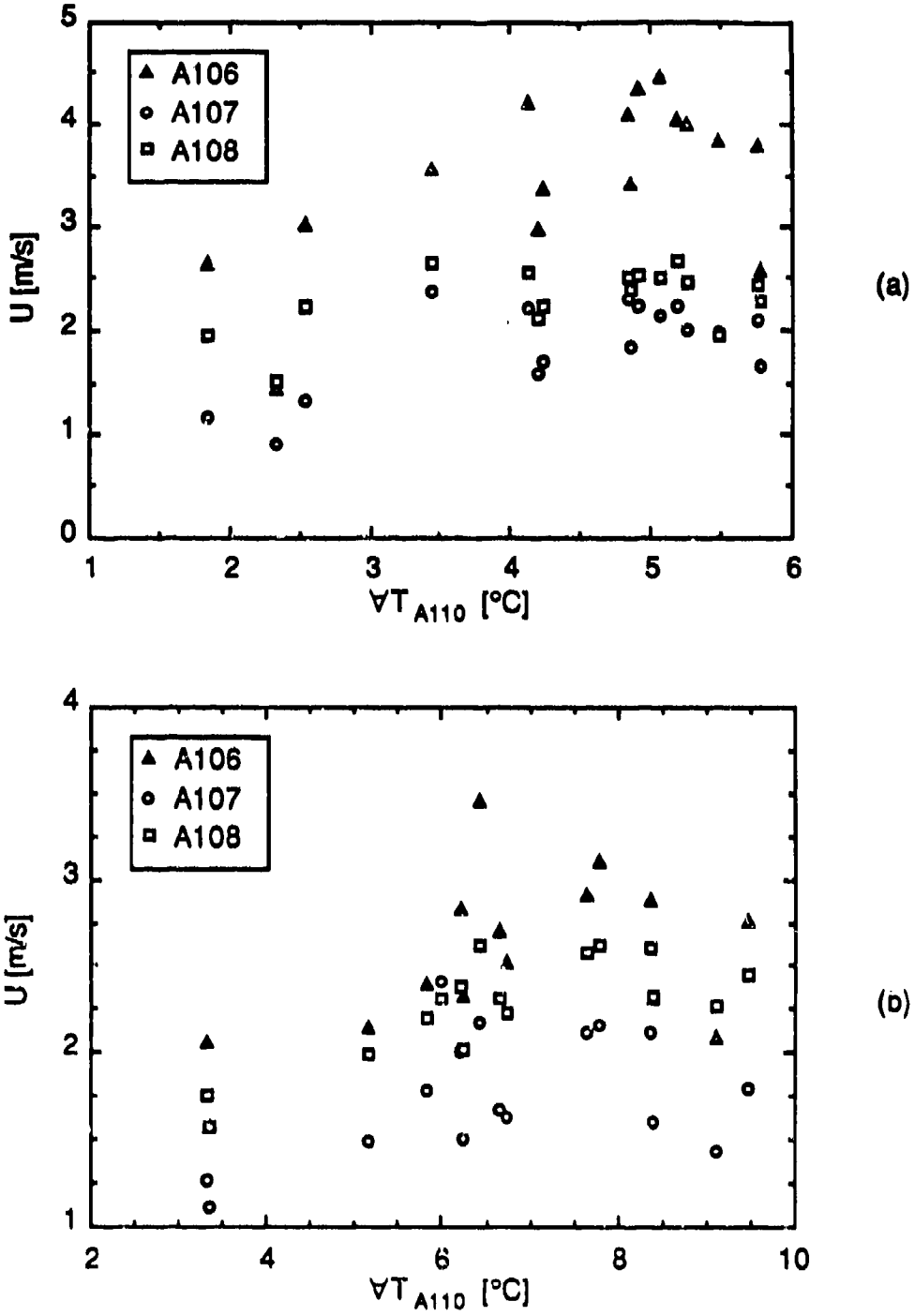

Figure 4.4 Correlation between 10-m wind speeds at Stations A106, A107 and A108 and intra-valley temperature differences. Plot (a) is for the time period from 20:00 to 00:00 and plot (b) is for the time period from 03:00 to 07:00. These data are from all 16 days of the AMADEUS experiments.

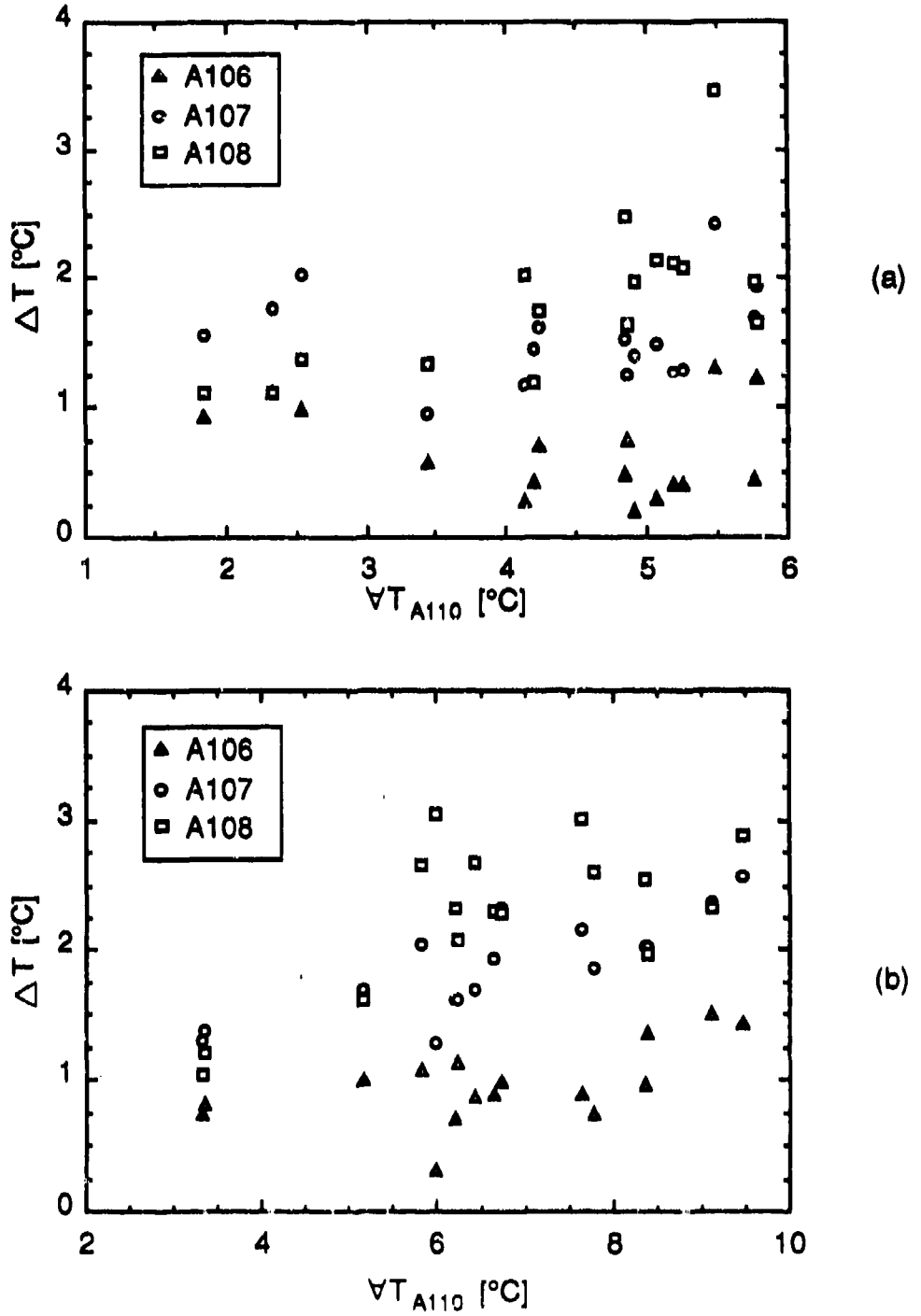

Figure 4.5 Correlation between near-ground temperature differences at Stations A106, A107 and A108 and intra-valley temperature differences. Plot (a) is for the time period from 20:00 to 00:00 and plot (b) is for the time period from 03:00 to 07:00. These data are from all 16 days of the AMADEUS experiments.

and the ΔT's, except for ΔT_{A106}. During the morning hours a weak positive correlation is evident between these temperature difference quantities, although the ΔT's do not show significant increases for $\forall T_{A110}$ above 6 °C. The lack of strong positive correlations between these thermal stability measures indicate a decoupling of the local and regional surface thermal stabilities. However, there does appear to be correlation when both the regional and local stratifications are weak. These weak stratifications are probably indicative of weak cooling, and a relationship between the regional and local stratifications is likely for these conditions.

Relationships Between Lapse Rates and Wind Speeds in Plum Creek

Near-ground temperature stratification ΔT_{A108} is plotted against the wind speeds at Stations A106, A107 and A108 in Figure 4.6. The Plum Creek valley wind speeds appear to generally increase with increasing stratification at Station A108, although, close examination of the wind speed data for Stations A107 and A108 shows that for the higher stratifications, the wind speeds actually decrease a little or at least remain the same. A similar functional relationship appears in Figure 4.7, which depicts the comparison between wind speeds at the Plum Creek stations and ΔT_{A107}. With these data, the wind speeds at the Plum Creek stations actually decrease with increasing ΔT_{A107} during the night and exhibit a maximum for moderate values of ΔT_{A107} in the morning.

These unusual effects can be explained by assuming that these local stratifications do not drive the flow, but are directly affected by the flow strength *and* local cooling. The differences in the relations between the valley wind speeds and the stratifications at Stations A107 and A108 most likely result from surface vegetation differences in the areas surrounding these stations. Station A107 was nestled in an area populated by large numbers of small trees and was fairly close to Plum Creek, whereas Station A108 was in the middle of a field with little vegetation for several hundred meters upwind. The enhanced vertical mixing caused by increased roughness around Station A107 acts to disrupt the near-ground temperature inversion at higher wind speeds, so that the near-ground stratification at this station was not maximized when cooling was the strongest. This effect is also seen at Station A108, but not to such a large degree. These observations lead to the conclusion that the local stratification in the Plum Creek valley is strongly affected by the valley flow (not vice versa), and that local stability may indeed be at a maximum when regional cooling is not at its strongest.

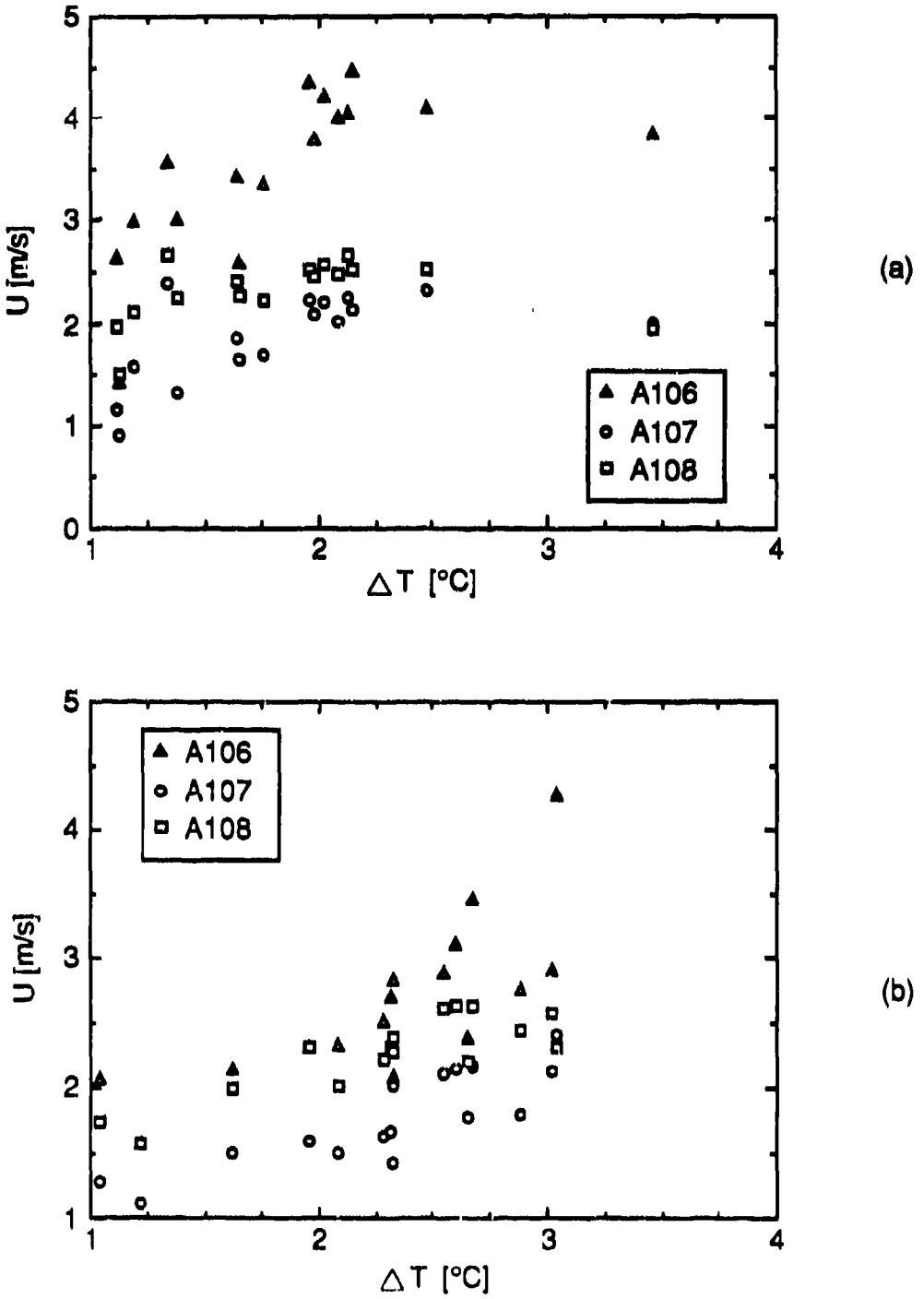

Figure 4.6 Correlation between 10-m wind speeds at Stations A106, A107 and A108 and near ground temperature differences at Station A108. Plot (a) is for the time period from 20:00 to 00:00 and plot (b) is for the time period from 03:00 to 07:00. These data are from all 16 days of the AMADEUS experiments.

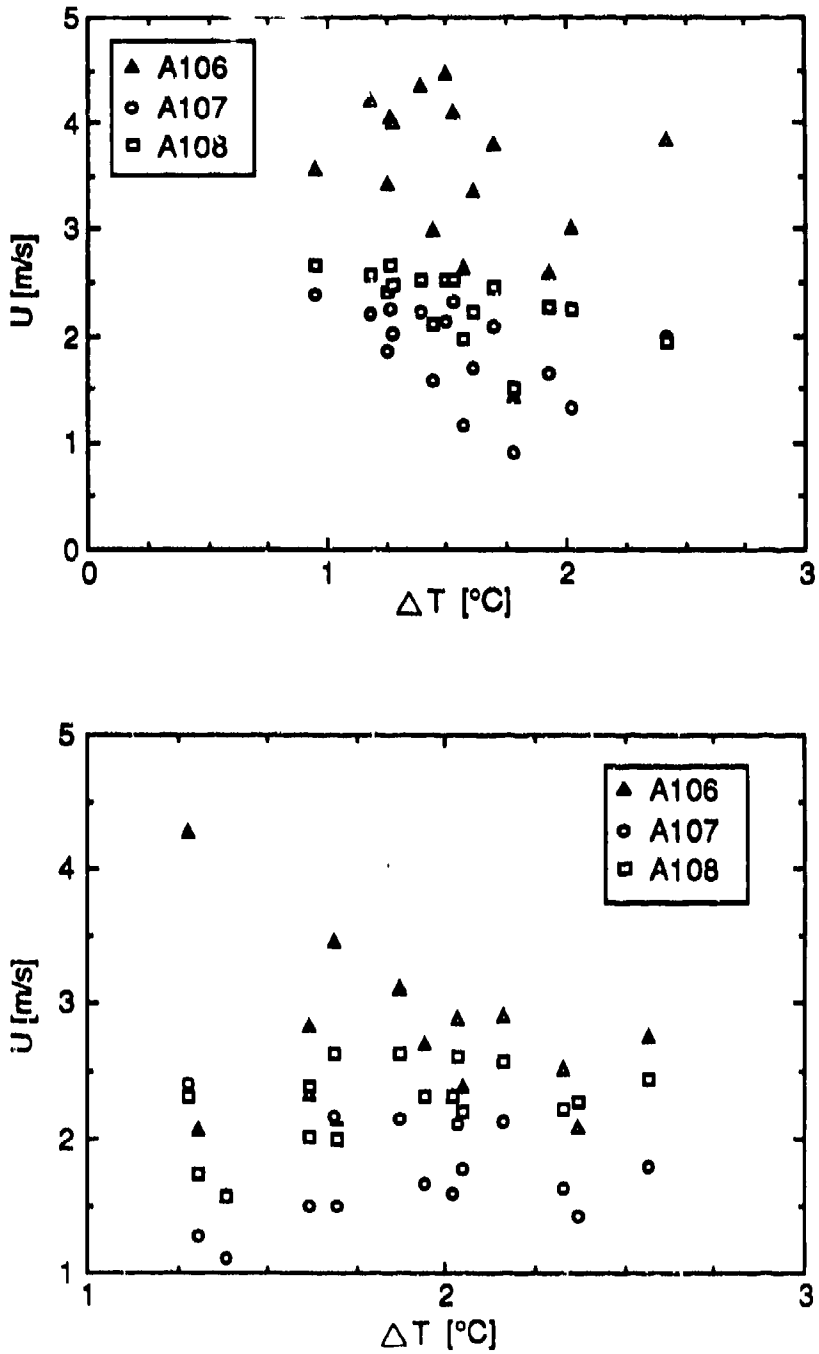

Figure 4.7 Correlation between 10-m wind speeds at Stations A106, A107 and A108 and near ground temperature differences at Station A107. Plot (a) is for the time period from 20:00 to 00:00 and plot (b) is for the time period from 03:00 to 07:00. These data are from all 16 days of the AMADEUS experiments.

External Forcing

The data comparisons presented up to this point illustrate the complexities involved in the Meadowbrook drainage flow system. Since the mechanisms controlling drainage flow strengths have not adequately been explained, external influences need to be examined. There is a problem here, however, in that our resources in this regard are very few, consisting of three widely separated 10-m surface stations. With these stations, we cannot conclusively establish the above-valley flow regimes, but can form ideas of what *may* be affecting the velocity and temperature fields in the valley.

Up to this point in our discussion, the average wind directions have not been considered. For the most part, however, average wind directions are of little interest in drainage flow characterization, since their night-to-night variations are rather small. The Plum Creek valley stations generally exhibited variations of the late-night averages of less than 15° during the whole testing period (with the exception of September 25, 1987). The above valley stations, Stations A105 and A109, also displayed little variation between nights (Station A109, though, was not operational for 6 days and the wind direction data for some of the other days contain many bad data.) Station A110, however, exhibited a comparatively wide variation in the late night and early morning averages, of around 80° and 120°, respectively, throughout the AMADEUS dispersion tests. Figure 4.8 shows the velocities for Stations A106, A107 and A108 plotted with respect to the wind direction at A110. A correlation between θ_{A110} and Plum Creek valley wind speeds is present for both late night and early morning time periods. The wind velocities are significantly higher when the direction at A110 is between 90° and 110°. A second, but less intense, maximum in the velocities may be occurring for directions at Station A110 of about 130°, although this second maximum is not conclusive, since data are sparse in this vicinity.

The wind speeds at Station A110 were also compared with those from the Plum Creek valley and $\forall T_{A110}$. These comparisons reveal a linear correlation between these wind speeds, although the wind speed at Station A110 did not show the same degree of correlation with $\forall T_{A110}$ as did the Plum Creek valley stations.

The correlations between the wind speeds and directions at Station A110 to those of the Plum Creek valley provide evidence of two possible effects which may be occurring. The first is channeling of the flow into the Plum Creek valley when the larger mesoscale drainage flows arrive from a certain directional range. This channel-

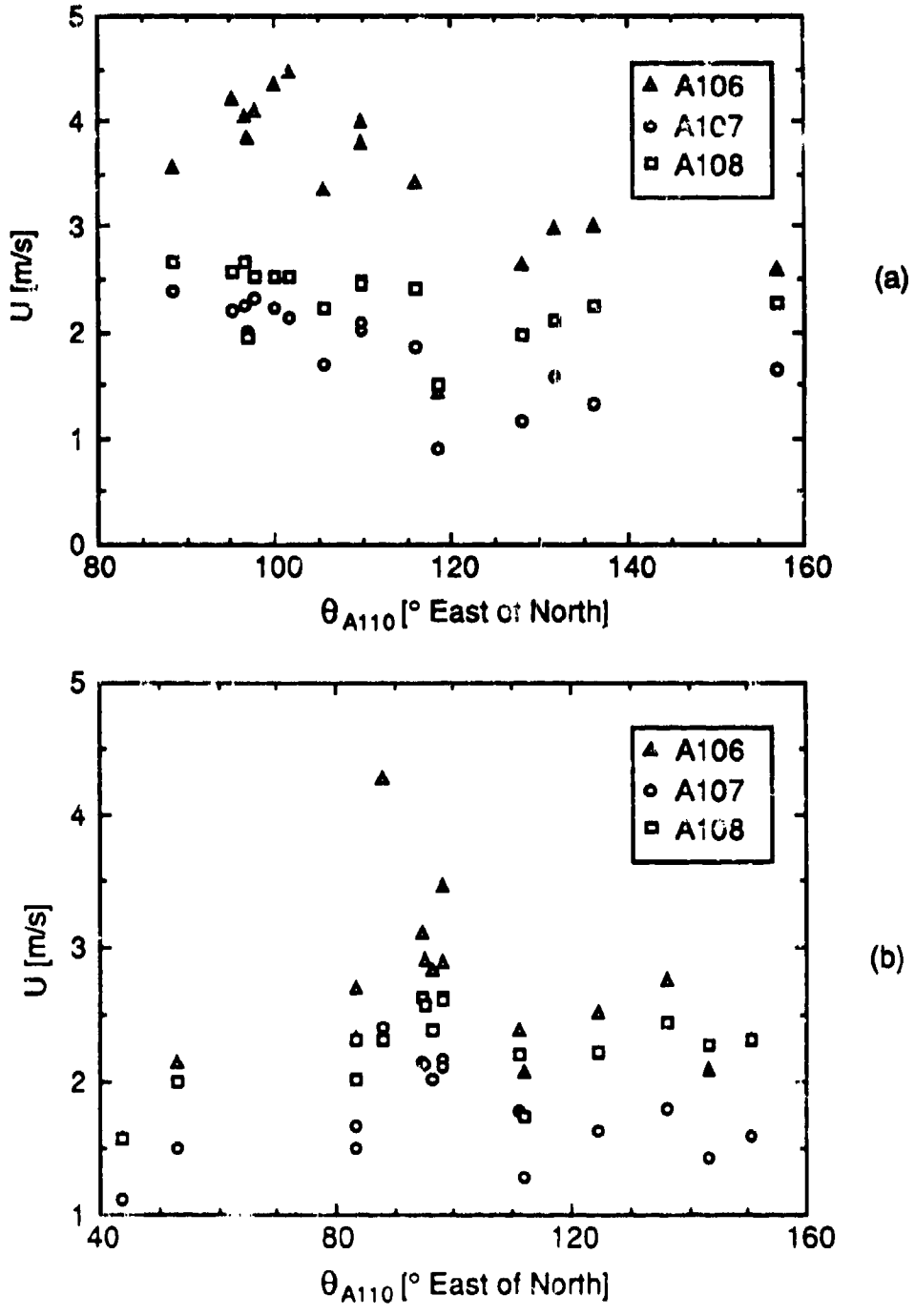

Figure 4.8 Correlation between 10-m wind speeds at Stations A106, A107 and A108 and wind direction at Station A110. Plot (a) is for the time period from 20:00 to 00:00 and plot (b) is for the time period from 03:00 to 07:00. These data are from all 16 days of the AMADEUS experiments.

ing of the flow will raise both the wind velocities at Station A110 and in the Plum Creek valley. A second scenario could be that regional cooling affects the mesoscale flows in such a way that the strongest flows naturally arrive from a certain directional range. These stronger flows could then dominate the regional and local drainage.

The Station A110 directional data are compared with the intra-valley temperature differences in Figure 4.9. A correlation appears to exist for the early-morning time periods, but not for the late-night periods. The single outlier data point in the early morning period ($\forall T_{A110} = 3.5$ °C at $\theta_{A110} = 115°$) is from September 25, 1987 which had very weak cooling and a very poorly established drainage flow. These data, however, do not offer an easy explanation into the external dynamics influencing the intra-valley temperature stratifications. These effects will be further examined in later reports.

Conclusions

The data correlations presented in this section for flow strength and thermal stratification have provided a valuable insight into some of the dynamics influencing the Meadowbrook drainage flows. The major conclusions of this study, in the order explained in the text, are as follows.

(a) As indicated by the differing trends of $\forall T_{A105}$, as opposed to those of $\forall T_{A109}$ and $\forall T_{A110}$, conditions on the northern and southern rims of the larger Paynes Creek valley are partially decoupled. This decoupling probably results from the presence of a large hill (Inskip Hill) to the northeast, and a large ridge to the southeast, of Station A105.

(b) Regional thermal stratifications are decoupled from near ground thermal stratifications in the Plum Creek valley for moderate to strong nocturnal cooling.

(c) The drainage flow strength in the Plum Creek valley acts to disrupt local stratification, when the wind speeds are above a certain threshold. For weaker flows, the stratification is dominated by the local cooling, since the wind speeds are not strong enough to sufficiently agitate the boundary layer. As local terrain roughness increases, the ability of the flow to disrupt the local stratification is greatly enhanced.

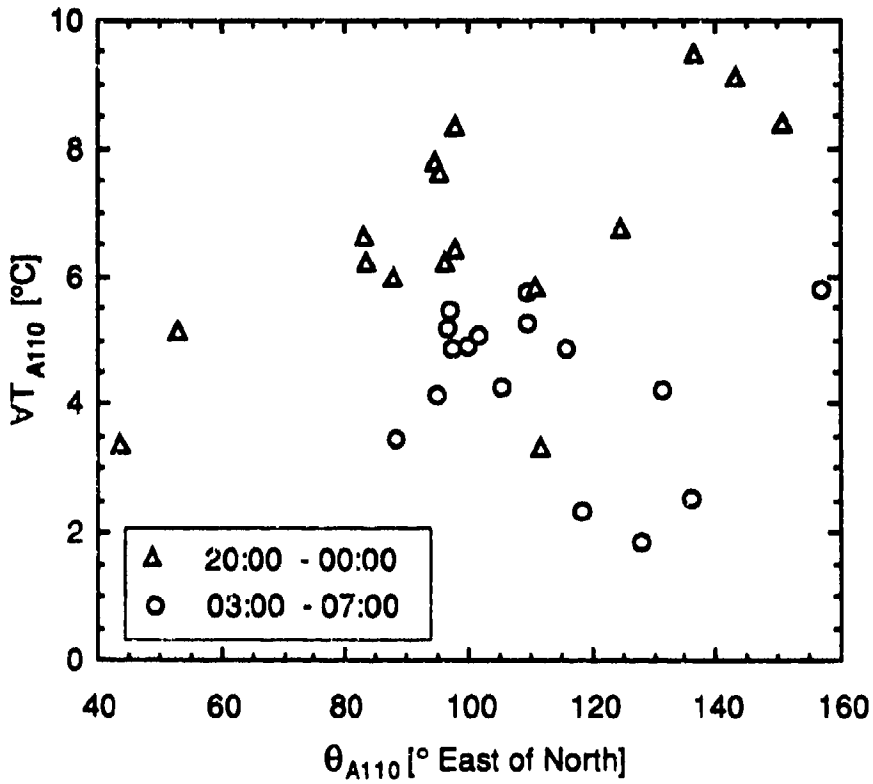

Figure 4.9 Correlation between intra-valley stratification and wind direction at Station A110. These data are from all 16 days of the AMADEUS experiments.

(d) The Plum Creek flow is dominated, or at least strongly coupled to, the larger mesoscale drainage flows which originate from the east. There are two possible scenarios under which this can occur. The first of these is a channeling of the larger mesoscale flow into the Plum Creek valley when the flows approach the valley from certain range of wind directions. Since the velocities at Station A110 are also strongly correlated with those in the Plum Creek valley, a second explanation is that the strengths of the mesoscale and local flows are coupled, and that the directional variations are associated with influences of regional cooling and stability on the mesoscale flow.

(e) The intra-valley stratifications are most likely influenced by a combination of local cooling and external forces. Local stratification would tend to dominate in weak cooling, and the external flows would act to enhance or erode the stratifications in stronger cooling, when mesoscale flows are well established.

5. SUMMARY AND CONCLUSIONS

This report summarizes our analysis of the AMADEUS meteorological data which has been carried out to date. Our efforts in this regard have included the reduction, analysis and archiving of data from the following meteorological instrumentation employed during each of the smoke and tracer release periods:

1. An array of 14 surface stations (instrumented at a height of 10 m) was used to map the horizontal variation of the wind field over the site.

2. A micrometeorological tower was used to determine vertical profiles of wind and temperature to a 30-m height and to provide indirect measures of atmospheric stability through fluctuations in the wind velocity and temperature.

3. Two sonic anemometers were used to directly measure the vertical momentum and heat flux through the atmospheric boundary layer and thus provide additional data by which to characterize atmospheric stability.

4. Instrumented balloons were used to provide wind and temperature profiles to a height of several kilometers and allowing the thickness of the atmospheric boundary layer to be determined.

Preliminary results obtained from the reduction of on-site meteorological instrumentation are given in Chapter 3. This preliminary reduction of the data included: (i) computation of averages of the surface-station and micrometeorological measurements (wind speed, wind direction, temperature), (ii) stability characterization by analysis of bulk Richardson numbers and wind direction standard deviations, (iii) examination of vertical heat and momentum fluxes from sonic-anemometer data, (iv) analysis of spectra computed using 1-hz micrometeorological data and (v) determination of boundary-layer height from the instrumented balloon soundings.

These data strongly reflect the upslope-downslope flow regimes characteristic of mountain-valley terrain. Results for the unstable tests are internally consistent, showing little variation in temperature and wind speed over the site. Velocity fluctuations, however, do not entirely conform to flat-terrain empirical models which are based on measured surface fluxes. Terrain effects probably act to raise friction velocities, raise mean-wind velocity fluctuations and limit transverse velocity fluctuations. Indirect methods for obtaining fluxes produced poor results, although Irwin and Binkowski's bulk Richardson number method produced consistent estimates of Obukhov length for four of the five unstable dispersion tests.

Results for late night and early morning tests were very incoherent except for the fact that downslope drainage flow was almost always observed. During most stable tests, wind speeds varied by a factor of ten, bulk Richardson numbers varied by a factor of 50 and temperatures varied by more than 10 °C over the Meadowbrook Site. Variations such as these highlight the site-specific nature of nocturnal drainage flows and eliminate the possibility of characterizing the meteorological conditions of the site by means of simple and conventional methods.

The mechanisms influencing the nocturnal drainage flows were analyzed in detail. This analysis led to the following observations: (i) Conditions on the northern and southern rims of the larger Paynes Creek Valley are partially decoupled. This decoupling probably results from the presence of a large hill (Inskip Hill) to the northeast, and a large ridge to the southeast, of Station A105. (ii) Regional thermal stratifications are decoupled from near ground thermal stratifications in the Plum Creek valley for moderate to strong nocturnal cooling. (iii) Local thermal stratification does not influence drainage flow strength in the Plum Creek valley. In fact, the drainage flow strength in this valley acts to disrupt local stratification when the wind speeds are above a certain threshold. This disruption of the local stratification was greatly enhanced by increased roughness in the local terrain. (iv) The Plum Creek flow is strongly coupled to the larger mesoscale drainage flows which originate from the east. There are two possible scenarios under which this coupling can occur. One scenario is that the larger mesoscale flow is channeled into the Plum Creek valley when the mesoscale flow approaches the valley from a certain range of wind directions. Another scenario is that the strengths of the mesoscale and local flows are coupled, and that the directional variations are associated with influences of regional cooling and stability on the mesoscale flow. (v) The intra-valley stratifications are most likely influenced by a combination of local cooling and external forces. Local stratification would tend to dominate in weak cooling, and the external flows would act to enhance or erode the stratifications in stronger cooling, when these flows are more well established.

As of this writing, there are still unresolved issues, offering additional avenues of research. Some of the unresolved issues which may have important implications for dispersion modeling are: (i) the characterization of velocity covariances for both unstable and stable conditions, (ii) the effects and characterization of local stratification and stability fluctuations in stable conditions and (iii) the effects of tree canopies on turbulence and stability.

APPENDIX A: 10-MIN DATA FROM SONIC ANEMOMETERS

Tables A.1 - A.12 show the 10-min sonic anemometer data used for computing averages for the fog-oil dispersion tests. Times shown for each data segment mark the start of the ten-minute averaging periods. Data for times marked with an asterisk (*) were excluded in filtered averages.

Table A.1 Sonic-anemometer data for Test 0921871. Smoke was released from 14:30 to 15:00. The unstable release point was used. Data for times marked with an asterisk (*) are not included in the filtered averages.

(a) Sonic Anemometer A

Start Time	U [m/s]	θ [°]	T [C]	E [m^2/s^2]	H [W/m^2]	z / L	u_* [m/s]	1/L [m^{-1}]
14:25*	4.35	287	41.8	1.54	150.09	-0.40	0.29	-0.057
14:35	4.42	276	42.2	2.45	174.67	-0.01	1.07	-0.001
14:45	4.20	278	41.9	2.02	115.54	-0.02	0.78	-0.003
14:55	5.33	275	42.2	2.20	205.73	-0.01	1.00	-0.001
15:05	5.26	269	42.1	1.99	75.95	-0.02	0.68	-0.003
Average	4.71	277	42.0	2.04	144.40	-0.026	0.76	-0.004
Filtered	4.80	274.50	42.10	2.17	142.97	-0.016	0.88	-0.002

(b) Sonic Anemometer B

Start Time	U [m/s]	θ [°]	T [C]	E [m^2/s^2]	H [W/m^2]	z / L	u_* [m/s]	1/L [m^{-1}]
14:25	3.55	307	38.5	2.52	94.32	-0.01	0.99	-0.001
14:35*	3.26	295	38.7	1.59	123.05	-0.38	0.28	-0.054
14:45	3.67	316	39.0	2.14	128.87	-0.01	0.99	-0.001
14:55	3.17	302	39.0	2.26	159.15	-0.14	0.42	-0.020
15:05	4.75	288	38.9	3.20	146.21	-0.03	0.66	-0.004
Average	3.68	301	38.8	2.34	130.32	-0.033	0.67	-0.005
Filtered	3.79	303.15	38.85	2.53	132.14	-0.023	0.77	-0.003

Table A.2 Sonic-anemometer data for Test 0923871. Smoke was released from 14:00 to 15:31. The smoke moved off the grid at 14:50. The unstable release point was used. Data for times marked with an asterisk (*) are not included in the filtered averages.

(a) Sonic Anemometer A

Start Time	U [m/s]	θ [°]	T [C]	E [m^2/s^2]	H [W/m^2]	z / L	u_* [m/s]	1/L [m^{-1}]
13:55	2.57	275	33.4	1.63	263.95	-0.03	0.83	-0.004
14:05	3.06	275	33.7	1.57	260.07	-0.02	0.94	-0.003
14:15	2.98	298	33.8	0.77	192.79	-0.10	0.51	-0.014
14:25*	3.08	273	34.1	0.79	172.00	-2.66	0.16	-0.380
14:35	3.21	282	34.3	1.13	148.80	-0.06	0.57	-0.009
14:45	1.84	240	34.6	2.86	163.03	0.00	1.46	0.000
14:55	0.83	238	34.6	1.30	169.50	-0.02	0.87	-0.003
Average	2.51	268.71	34.07	1.44	195.73	-0.035	0.76	-0.005
Filtered	2.42	268.00	34.07	1.54	199.69	-0.025	0.86	-0.004

(b) Sonic Anemometer B

Time	U [m/s]	θ [°]	T [C]	E [m^2/s^2]	H [W/m^2]	z / L	u_* [m/s]	1/L [m^{-1}]
13:55	3.08	268	30.1	1.29	147.50	-0.03	0.72	-0.004
14:05	2.90	276	30.5	1.23	173.38	-0.03	0.70	-0.004
14:15	3.87	265	30.6	1.07	150.09	-0.14	0.42	-0.020
14:25	2.69	303	30.8	1.28	161.73	-0.36	0.32	-0.051
14:35	3.58	277	31.0	0.91	200.55	-0.07	0.59	-0.010
14:45	2.22	249	31.3	1.93	261.36	-0.06	0.66	-0.009
14:55	2.33	251	31.3	1.06	127.83	-0.04	0.63	-0.006
Average	2.95	269.67	30.80	1.25	174.63	-0.070	0.58	-0.010

Table A.3 Sonic-anemometer data for Test 0925871. Only Sonic Anemometer B operated. Smoke was released from 00:18 to 01:03. The stable release point was used. Data for times marked with an asterisk (*) are not included in the filtered averages.

Time	U [m/s]	θ [°]	T [C]	E [m^2/s^2]	H [W/m^2]	z / L	u_* [m/s]	1/L [m^{-1}]
00:15	0.45	352	15.5	0.08	-16.95	0.12	0.22	0.017
00:25	0.65	47	15.5	0.08	-6.34	0.05	0.21	0.007
00:35	0.63	36	15.6	0.04	-8.35	0.14	0.16	0.020
00:45*	0.19	195	15.5	0.05	29.63	-0.37	0.18	-0.053
00:55	0.28	25	15.5	0.11	-37.65	0.09	0.31	0.013
01:05	0.52	71	15.7	0.19	-10.03	0.42	0.12	0.060
Average	0.45	121	15.6	0.09	-8.28	0.082	0.20	0.012
Filtered	0.51	106.16	15.56	0.10	-15.86	0.158	0.20	0.023

Table A.4 Sonic-anemometer data for Test 0926871. Smoke was released from 12:00 to 13:07. The unstable release point was used. No filtering was deemed necessary for this test.

(a) Sonic Anemometer A

Time	U [m/s]	θ [°]	T [C]	E [m^2/s^2]	H [W/m^2]	z / L	u_* [m/s]	1/L [m^{-1}]
11:55	5.00	308	28.4	1.50	282.06	-0.16	0.50	-0.023
12:05	4.15	314	28.6	1.88	258.77	-0.02	0.99	-0.003
12:15	4.02	307	28.9	2.46	209.61	-0.01	1.27	-0.001
12:25	5.35	311	29.0	1.75	284.65	-0.19	0.47	-0.027
12:35	5.12	306	29.4	2.11	304.06	-0.03	0.87	-0.004
12:45	5.21	294	29.8	1.91	367.46	-0.11	0.61	-0.016
12:55	5.60	304	29.7	1.85	187.61	-0.02	0.92	-0.003
Average	4.92	306	29.1	1.92	270.60	-0.041	0.80	-0.006

(b) Sonic Anemometer B

Time	U [m/s]	θ [°]	T [C]	E [m^2/s^2]	H [W/m^2]	z / L	u_* [m/s]	1/L [m^{-1}]
11:55	3.26	308	24.8	3.87	200.55	-0.01	1.02	-0.001
12:05	3.77	300	24.9	1.55	156.56	-0.07	0.53	-0.010
12:15	2.14	321	25.6	2.52	163.03	-0.02	0.83	-0.003
12:25	3.62	322	25.5	1.54	155.26	-0.10	0.49	-0.014
12:35	4.17	278	25.9	3.20	195.37	-0.05	0.65	-0.007
12:45	4.88	264	26.2	2.28	188.91	-0.04	0.72	-0.006
12:55	3.39	315	26.3	2.11	157.85	-0.05	0.61	-0.007
13:05	4.04	284	26.9	3.68	247.13	-0.01	1.08	-0.001
Average	3.66	299	25.8	2.59	183.08	-0.036	0.74	-0.005

Table A.5 Sonic-anemometer data for Test 0927871. Only Sonic Anemometer B operated for this test. Smoke was released from 03:19 to 03:39. The stable release point was used.

Time	U [m/s]	θ [°]	T [C]	E [m²/s²]	H [W/m²]	z / L	u. [m/s]	1/L [m⁻¹]
03:15*	0.33	113	11.1	0.08	-8.59	0.35	0.12	0.050
03:25	0.32	36	10.5	0.08	1.91	-0.17	0.09	-0.024
03:35	0.23	65	10.5	0.09	13.33	-0.21	0.17	-0.030
03:45	0.76	26	10.3	0.06	8.77	-0.15	0.16	-0.021
Average	0.41	60	10.6	0.08	3.86	-0.112	0.14	-0.016
Filtered	0.44	42.33	10.43	0.08	8.00	-0.232	0.14	-0.033

Table A.6 Sonic-anemometer data for Test 0927872. Only Sonic Anemometer B operated for this test. Smoke was released from 06:44 to 06:54. The stable release point was used. No filtering was deemed necessary for this test.

Time	U [m/s]	θ [°]	T [C]	E [m²/s²]	H [W/m²]	z / L	u. [m/s]	1/L [m⁻¹]
06:45	1.24	27	8.8	0.18	17.08	-0.41	0.15	-0.059
06:55	0.91	69	9.3	0.23	-46.71	0.14	0.30	0.020
07:05	0.61	47	8.5	0.12	-10.84	0.05	0.26	0.007
Average	0.92	48	8.9	0.18	-13.49	0.078	0.24	0.011

Table A.7 Sonic-anemometer data for Test 0928871. Smoke was released from 10:29 to 10:54. The unstable release point was used. Data for times marked with an asterisk (*) are not included in the filtered averages.

(a) Sonic Anemometer A

Time	U [m/s]	θ [°]	T [C]	E [m^2/s^2]	H [W/m^2]	z / L	u_* [m/s]	1/L [m^{-1}]
10:25	2.38	261	28.4	0.19	105.97	-1.38	0.18	-0.197
10:35	2.64	268	28.6	0.30	101.44	-0.80	0.21	-0.114
10:45*	2.96	265	28.8	0.20	93.68	-10.28	0.09	-1.469
10:55	2.60	257	29.4	0.32	138.44	-0.32	0.31	-0.046
Average	2.65	263	28.8	0.25	109.88	-1.674	0.20	-0.154
Filtered	2.54	262.00	28.80	0.27	115.28	-0.753	0.23	-0.106

(b) Sonic Anemometer B

Time	U [m/s]	θ [°]	T [C]	E [m^2/s^2]	H [W/m^2]	z / L	u_* [m/s]	1/L [m^{-1}]
10:25	2.69	266	25.7	0.24	72.07	-1.28	0.16	-0.183
10:35	3.10	269	25.9	0.26	67.80	-1.18	0.16	-0.169
10:45	3.54	272	25.9	0.34	57.45	-0.57	0.19	-0.081
10:55*	3.45	262	26.2	0.22	69.87	-6.83	0.09	-0.976
Average	3.20	267.05	25.93	0.27	66.80	-1.561	0.15	-0.223
Filtered	3.11	268.70	25.83	0.28	65.77	-1.056	0.17	-0.150

Table A.8 Sonic-anemometer data for Test 0930871. Only Sonic Anemometer B operated for this test. Smoke was released from 06:48 to 07:28. The stable release point was used. No filtering was deemed necessary for this test.

Time	U [m/s]	θ [°]	T [C]	E [m^2/s^2]	H [W/m^2]	z / L	u_* [m/s]	1/L [m^{-1}]
06:45	1.33	57	17.1	0.18	-57.32	0.38	0.22	0.054
06:55	1.42	72	17.1	0.14	-7.34	0.30	0.12	0.043
07:05	1.14	55	17.2	0.07	-6.31	0.06	0.19	0.009
07:15	1.14	36	17.3	0.11	2.68	-0.07	0.14	-0.010
07:25	1.01	72	17.0	0.16	-20.05	0.39	0.16	0.056
07:35	0.33	109	16.6	0.23	-21.35	0.06	0.30	0.009
Average	1.06	67	17.1	0.15	-18.28	0.208	0.19	0.029

Table A.9 Sonic-anemometer data for Test 1001871. Only Sonic Anemometer B operated for this test. Smoke was released from 06:52 to 07:32. The stable release point was used. No filtering was deemed necessary for this test.

Time	U [m/s]	θ [°]	T [C]	E [m^2/s^2]	H [W/m^2]	z / L	u_* [m/s]	1/L [m^{-1}]
06:45	1.07	40	18.8	0.20	-13.84	0.04	0.29	0.006
06:55	0.77	92	18.2	0.24	-41.15	0.45	0.19	0.064
07:05	0.41	76	18.6	0.09	-38.69	0.34	0.20	0.049
07:15	1.46	45	18.5	0.32	-54.21	0.07	0.39	0.010
07:25	0.85	73	18.6	0.24	-55.90	0.23	0.26	0.033
07:35	1.14	65	18.4	0.21	-4.52	0.03	0.23	0.004
Average	0.95	65	18.5	0.22	-34.72	0.156	0.26	0.022

Table A.10 Sonic-anemometer data for Test 1002871. Only Sonic Anemometer B operated for this test. Smoke was released from 07:17 to 07:47. The stable release point was used. No filtering was deemed necessary for this test.

Time	U [m/s]	θ [°]	T [C]	E [m^2/s^2]	H [W/m^2]	z / L	u_* [m/s]	1/L [m^{-1}]
07:15	0.66	14	17.4	0.04	-2.65	0.73	0.06	0.104
07:25	0.81	56	17.7	0.05	-12.40	0.58	0.12	0.083
07:35	1.50	70	17.7	0.06	-6.30	0.56	0.09	0.080
07:45	1.45	65	17.3	0.06	-9.17	0.25	0.14	0.036
07:55	0.85	76	17.2	0.13	-31.83	0.62	0.16	0.089
Average	1.05	56	17.5	0.07	-12.47	0.743	0.11	0.106

Table A.11 Sonic-anemometer data for Test 1002872. Smoke was released from 12:16 to 12:34. The unstable release point was used. Data for times marked with an asterisk (*) are not included in the filtered averages.

(a) Sonic Anemometer A

Time	U [m/s]	θ [°]	T [C]	E [m^2/s^2]	H [W/m^2]	z / L	u_* [m/s]	1/L [m^{-1}]
12:15	1.80	270	33.2	0.77	135.86	-0.16	0.39	-0.023
12:25*	2.09	275	33.8	0.64	179.85	-1.49	0.20	-0.213
12:35	2.23	281	34.1	1.08	205.73	-0.04	0.70	-0.006
Average	2.04	275	33.7	0.83	173.81	-0.170	0.43	-0.024
Filtered	2.02	275.50	33.65	0.93	170.80	-0.080	0.55	-0.011

(b) Sonic Anemometer B

Time	U [m/s]	θ [°]	T [C]	E [m^2/s^2]	H [W/m^2]	z / L	u_* [m/s]	1/L [m^{-1}]
12:15	3.19	244	30.3	0.38	103.90	-0.20	0.33	-0.029
12:25*	3.15	251	30.7	0.64	175.97	-7.12	0.12	-1.017
12:35	3.45	260	31.0	0.66	161.73	-0.13	0.44	-0.019
Average	3.26	252	30.7	0.56	147.20	-0.727	0.30	-0.061
Filtered	3.32	251.75	30.65	0.52	132.82	-0.176	0.39	-0.025

Table A.12 Sonic-anemometer data for Test 1003871. Only Sonic Anemometer B operated for this test. Smoke was released from 06:56 to 07:27. The stable release point was used. Data for times marked with an asterisk (*) are not included in the filtered averages.

Time	U [m/s]	θ [°]	T [C]	E [m^2/s^2]	H [W/m^2]	z / L	u_* [m/s]	1/L [m^{-1}]
06:55	0.27	199	16.6	0.15	-2.46	0.01	0.30	0.001
07:05	0.67	59	16.6	0.26	18.11	-0.03	0.37	-0.004
07:15	0.55	58	17.1	0.14	-6.24	0.03	0.25	0.004
07:25*	0.49	264	17.4	0.12	18.89	-0.35	0.16	-0.050
Average	0.50	145	16.9	0.17	7.08	-0.029	0.27	-0.004
Filtered	0.50	105.43	16.77	0.18	3.14	-0.008	0.31	-0.001

REFERENCES

André, J. C., G. De Moor, P. Lacarrère, G. Therry and R. du Vachat, 1978: "Modeling the 24-Hour Evolution of the Mean and Turbulent Structures of the Planetary Boundary Layer," Journal of the Atmospheric Sciences, 35, 1861-1883.

André, J. C. and L. Mahrt, 1982: "The Nocturnal Surface Inversion and Influence of Clear-air Radiative Cooling," Journal of the Atmospheric Sciences, 39, 864-878.

Arritt, R. W. and R. A. Pielke, 1986: "Interactions of Nocturnal Slope Flow with Ambient Winds," Boundary-Layer Meteorology, 37, 183-195.

Arya, S. P. S., 1984: "Parametric Relations for the Atmospheric Boundary Layer," Boundary-Layer Meteorology, 30, 57-73.

Arya, S. P. S. and E. J. Plate, 1969: "Modeling of the Stably Stratified Atmospheric Boundary Layer," Journal of the Atmospheric Sciences, 26, 656-665.

Barr, S. and M. M. Orgil, 1989: "Influence of External Meteorology on Nocturnal Drainage Winds," Journal of Applied Meteorology, 28, 497-517.

Beljaars, A. C. M., 1987: "On the Memory of Wind Standard Deviation for Upstream Roughness," Boundary-Layer Meteorology, 38, 95-101.

Benoit, R., 1977: "On the Integral of the Surface Layer Profile-Gradient Functions," Journal of Applied Meteorology, 16, 859-860.

Brost, R. A. and J. C. Wyngaard, 1978: "A Model Study of the Stably Stratified Planetary Boundary Layer," Journal of the Atmospheric Sciences, 35, 1427-1440.

Brown, D. F. and W. E. Dunn, 1990: Analysis of Meteorological Data from the AMADI US Smoke Dispersion Experiments, work completed under contract no. 90PP0819, University of Illinois, Urbana, IL

Busch, N. E., 1973: "On the Mechanics of Atmospheric Turbulence," in: Workshop on Micrometeorology, Haugen, D. A. (ed.), American Meteorological Society, 1-65.

Busch, N. E. and H. A. Panofsky, 1968: "Recent Spectra of Atmospheric Turbulence," Quarterly Journal of the Royal Meteorological Society, 94, 132-148.

Businger, J. A., 1973: "Turbulent Transfer in the Atmospheric Surface Layer," in: Workshop on Micrometeorology, Haugen, D. A. (ed.), American Meteorological Society, 67-100.

Businger, J. A, 1984: "Equations and Concepts," in: Atmospheric Turbulence and Air Pollution Modeling, Nieuwstadt, F.T.M. and H. van Dop (eds.), D. Reidel, Boston, 1-36.

Businger, J. A., J. C. Wyngaard, Y. Izumi and E.F. Bradley, 1971: "Flux-Profile Relationships in the Atmospheric Surface Layer," Journal of the Atmospheric Sciences, 28, 181-189.

Businger, J. A. and S. P. S. Arya, 1974: "Height of the Mixed Layer in the Stably Stratified Planetary Boundary Layer," Advances in Geophysics, 18A, 73-92.

Calder, K. L., 1949: "The Criterion of Turbulence in a Fluid of Variable Density, with Particular Reference to Conditions in the Atmosphere," Quarterly Journal of the Royal Meteorological Society, 75, 71-88.

Calder, K. L., 1966: "Concerning the Similarity Theory of A. S. Monin and A. M. Obukhov for the Turbulent Structure of the Thermally Stratified Surface layer of the Atmosphere," Quarterly Journal of the Royal Meteorological Society, 92, 141-146.

Carson, D. J., 1973: "The Development of a Dry Inversion-Capped Convectively Unstable Boundary Layer," Quarterly Journal of the Royal Meteorological Society, 99, 450-467.

Caughey, S. C., 1977: "Boundary Layer Turbulence Spectra in Stable Conditions," Boundary-Layer Meteorology, 11, 3-14.

Caughey, S. C., 1984: "Observed Characteristics of the Atmospheric Boundary Layer," in: Atmospheric Turbulence and Air Pollution Modeling, Nieuwstadt, F.T.M. and H. van Dop (eds.), D. Reidel, Boston, 107-158.

Caughey, S. J. and S. G. Palmer 1979: "Some Aspects of Turbulence Structure Through the Depth of the Convective Boundary Layer," Quarterly Journal of the Royal Meteorological Society, 105, 811-827.

Caughey, S. J., J. C. Wyngaard and J. C. Kaimal, 1979: "Turbulence in the Evolving Stable Boundary Layer," Journal of Atmospheric Sciences, 36, 1041-1052.

Clements, W. E., W. M. Porch, T. A. Grant and J. A. Archuleta 1990: "Drainage Flow Characteristics in Neighboring Valleys," in: Fifth Conference on Mountain Meteorology, American Meteorological Society, 224-230.

Deardorff, J. W., 1970: "Convective Velocity and Temperature Scales for the Unstable Planetary Boundary Layer and for Rayleigh Convection," Journal of the Atmospheric Sciences, 27, 1211-1213.

Deardorff, J. W. and G. E. Willis, 1975: "A Parameterization of Diffusion into the Mixed Layer," Journal of Applied Meteorology, 14, 1451-1458.

Derbyshire, S. H., 1990: "Nieuwstadt's Stable Boundary Layer Revisited," Quarterly Journal of the Royal Meteorological Society, 116, 127-158.

Finnigan, J. J. and D. Fua, 1984: "The Interaction Between an Internal Gravity Wave and Turbulence in the Stably-stratified Nocturnal Boundary Layer," Journal of the Atmospheric Sciences, 41, 2409-2436.

Finnigan, J. J., 1988: "Kinetic Energy Transfer Between Internal Gravity Waves and Turbulence," Journal of the Atmospheric Sciences, 45, 486-505.

Fitzjarrald, D. R., 1984: "Katabatic Wind in Opposing Flow," Journal of the Atmospheric Sciences, 41, 1143-1158.

Garrett, A. J., 1981: "Comparison of Observed Mixed-layer Depths to Model Estimates Using Observed Temperatures and Winds and MOS Forecasts," Journal of Applied Meteorology, 20, 1277-1283.

Garrett, A. J. and R. A. Brost, 1981: "Radiative Cooling Effects within and Above the Nocturnal Boundary Layers," Journal of the Atmospheric Sciences, 38, 2730-2746.

Gryning, S.E., A.A.M. Holtslag, J.S. Irwin and B. Sivertsen, 1987: "Applied Dispersion Modeling Based on Meteorological Scaling Parameters," Atmospheric Environment, 21, 79-81.

Hoffert, M. I. and Y. C. Sud, 1976: "Similarity Theory of the Buoyantly Interactive Planetary Boundary Layer with Entrainment," Journal of the Atmospheric Sciences, 33, 2130-2151.

Højstrup, J., 1982: "Velocity Spectra in the Unstable Planetary Boundary Layer," Journal of Atmospheric Science, 39, 2239-2248.

Holtslag, A. A. M. and F. T. M. Nieuwstadt, 1986: "Scaling the Atmospheric Boundary Layer," Boundary-Layer Meteorology, 36, 201-209.

Horst, T. W. and J. C. Doran, 1986: "Nocturnal Drainage Flow on Simple Slopes," Boundary-Layer Meteorology, 34, 263-286.

Horst, T. W. and J. C. Doran, 1988: "The Turbulent Structure of Nocturnal Slope Flow," Journal of Atmospheric Science, 45, 605-616.

Hunt, J. C. R., J. C. Kaimal and J. E. Gaynor, 1985: "Some Observations of Turbulence in Stable Layers," Quarterly Journal of the Royal Meteorological Society, 111, 793-815.

Irwin, J.S. and F. C. Binkowski, 1981: "Estimation of the Monin-Obukhov Scaling Length Using On-Site Instrumentation," Atmospheric Environment, 15, 1091-1094.

Kaimal, J. C., 1978: "Horizontal Velocity Spectra in an Unstable Surface Layer," Journal of Atmospheric Science, 35, 18-23.

Kaimal, J. C., J. C. Wyngaard, Y. Izumi, O. R. Cote, 1972: "Spectral Characteristics of Surface-Layer Turbulence," Quarterly Journal of the Royal Meteorological Society, 98, 563-389.

Kaimal, J. C., J. C. Wyngaard, D. A. Haugen, O. R. Coté and Y. Izumi, 1976: "Turbulence Structure in the Convective Boundary Layer," Journal of the Atmospheric Sciences, 33, 2152-2169.

Khalsa, S. J. S., 1980: "Surface-layer Intermittency Investigated with Conditional Sampling," Boundary-Layer Meteorology, 19, 135-153.

Klug, W., 1968: "Diffusion in the Atmospheric Surface Layer: Comparison of Similarity Theory with Observations," Quarterly Journal of the Royal Meteorological Society, 94, 555-562.

Klug, W., 1965: "Diabatic Influence on Turbulent Wind Fluctuations," Quarterly Journal of the Royal Meteorological Society, 91, 215-217.

Korrell, A., H. A. Panofsky and R. J. Rossi, 1982: "Wind Profiles at the Boulder Tower," Boundary-Layer Meteorology, 22, 295-312.

Leyi, Z. and H. A. Panofsky, 1983: "Wind Fluctuations in Stable Air at the Boulder Tower," Boundary-Layer Meteorology, 25, 353-362.

Mahrt, L., 1985: "Vertical Structure and Turbulence in the Very Stable Boundary Layer," Journal of the Atmospheric Sciences, 42, 2333-2349.

Mahrt, L., 1989: "Intermittency of Atmospheric Turbulence," Journal of the Atmospheric Sciences, 46, 79-95.

Mahrt, L. and D. H. Lenschow, 1976: "Growth Dynamics of the Convectively Mixed Layer," Journal of the Atmospheric Sciences, 33, 41-51.

Manton, M. J. and W. R. Cotton, 1977: "Parameterization of the Atmospheric Surface Layer," Journal of the Atmospheric Sciences, 34, 331-334.

McCutchan, M. H., 1979: "Determining the Diurnal Variation of Surface Temperature in Mountainous Terrain," Journal of Applied Meteorology, 18, 1224-1229.

Miles, J. W., 1961: "On the Stability of Heterogeneous Shear Flows," Journal of Fluid Mechanics, 10, 496-508.

Miles, J. W., 1986: "Richardson's Criterion for the Stability of Stratified Shear Flow," Physics of Fluids, 29, 3470-3471.

Monin, A. S., 1959: "General Survey of Atmospheric Diffusion," Advances in Geophysics, 6, 29-40.

Monin, A. S. and A. M. Yaglom, 1971: Statistical Fluid Mechanics: Mechanics of Turbulence, 1, 419-421, (MIT Press, Cambridge, Massachusetts).

Monin, A. S. and A. M. Obukhov, 1954: "Basic Laws of Turbulent Mixing in the Ground Layer of the Atmosphere," translated from Akademiia Nauk SSSR, Leningrad, Geofizicheskii Institut, Trudy, 151, 163-187, in AIAA Selected Reprint Series, vol IX, Aerophysics of Air Pollution, (American Institute of Aeronautics and Astronautics, New York).

Nappo, C. J., 1991: "Sporadic Breakdowns of Stability over Simple and Complex Terrain," Boundary-Layer Meteorology, 54, 69-87.

Nieuwstadt, F. T. M., 1978: "The Computation of the Friction Velocity and the Temperature Scale from Temperature and Wind Velocity Profiles by Least-square Methods," Boundary-Layer Meteorology, 14, 235-246.

Nieuwstadt, F. T. M., 1980: "Application of Mixed-layer Similarity to the Observed Dispersion from a Ground Level Source," Journal of Applied Meteorology, 19, 157-162.

Nieuwstadt, F. T. M., 1984: "The Turbulent Structure of the Stable, Nocturnal Boundary Layer," Journal of the Atmospheric Sciences, 41, 2202-2216.

Nieuwstadt, F. T. M. and A. G. M. Driedonks, 1979: "The Nocturnal Boundary Layer: A Case Study Compared with Model Calculations," Journal of Applied Meteorology, 18, 1397-1405.

Panofsky, H. A., 1962: "Scale Analysis of Atmospheric Turbulence at 2 m," Quarterly Journal of the Royal Meteorological Society, 88, 57-69.

Panofsky, H. A. and B. Prasad, 1965: "Similarity Theories and Diffusion," International Journal of Air and Water Pollution, 9, 419-430.

Panofsky, H. A. and E. L. Petersen, 1972: "Wind Profiles and Change of Terrain Roughness at Risø," Quarterly Journal of the Royal Meteorological Society, 98, 845-854.

Panofsky, H. A., D. Larko, R. Lipschutz, G. Stone, E. F. Bradley, A. J. Bowen and J. Højstrup, 1982: "Spectra of Velocity Components over Complex Terrain," Quarterly Journal of the Royal Meteorological Society, 108, 215-230.

Panofsky, Hans A. and John A. Dutton, 1984: Atmospheric Turbulence - Models and Methods for Engineering Applications, (John Wiley and Sons, New York).

Panofsky, H. A., D. Larko, R. Lipschutz, G. Stone, E. F. Bradley, A. J. Bowen and J. Højstrup, 1982: "Spectra of Velocity Components over Complex Terrain," Quarterly Journal of the Royal Meteorological Society, 108, 215-230.

Paulson, C. A., 1970: "The Mathematical Representation of Wind Speed and Temperature Profiles in the Unstable Atmospheric Surface Layer," Journal of Applied Meteorology, 9, 857-861.

Pendergast, M. M., 1984: "Meteorological Fundamentals," in Atmospheric Science and Power Production, D. Randerson, ed., Weather Service Nuclear Support Office, National Oceanic and Atmospheric Administration, United States Department of Commerce, (Technical Information Center, Office of Scientific and Technical Information, United States Department of Energy).

Randerson, D., (Ed.), 1984: Atmospheric Science and Power Production, Weather Service Nuclear Support Office, National Oceanic and Atmospheric Administration, United States Department of Commerce, (Technical Information Center, Office of Scientific and Technical Information, United States Department of Energy).

Rao, K. S. and M. A. Schaub, 1990: "Observed Variations of σ_θ and σ_ϕ in the Nocturnal Drainage Flow in a Deep Valley," Boundary-Layer Meteorology, 51, 31-48.

Rhines, P. B., 1979: "Geostrophic Turbulence," Annual Review of Fluid Mechanics, 11, 401-441.

Schotz, S. and H. A. Panofsky, 1980: "Wind Characteristics at the Boulder Atmospheric Observatory," Boundary-Layer Meteorology, 19, 155-164.

Sedefian, L. and E. Bennet, 1980: "A Comparison of Turbulence Classification Schemes," Atmospheric Environment, 14, 741-750.

Shinn, J. H. , R. T. Cederwall, F. J. Gouveia and K. R. Chapman, 1989: "Micrometeorology of Slope Flows in a tributary Conyon During the 1984 ASCOT Experiment," Journal of Applied Meteorology, 28, 569-577.

Smith, F. B. and R. M. Blackall, 1979: "The Application of Field Experimental Data to the Parameterization of Dispersion Plumes from Ground-level and Elevated Sources," Mathematical Modeling of Turbulent Diffusion in the Environment, Series Vol. 9, Fay, J. A. and D. P. Hoult (eds.), AIAA Press, New York.

Sutton, O. G., 1932, "A Theory of Eddy Diffusion in the Atmosphere," Proceedings of the Royal Society, A, 135, 143-165.

Sykes, R. I. and L. Hatton, 1976: "Computation of Horizontal Trajectories Based on the Surface Geostropic Wind," Atmospheric Environment, 10, 925-934.

Taylor, G. I., 1927: "Turbulence," Quarterly Journal of the Royal Meteorological Society, 53, 201-212.

Tennekes, H., 1973: "The Logarithmic Wind Profile," Journal of the Atmospheric Sciences, 30, 234-238.

Tennekes, H., 1984: "Similarity Relations, Scaling Laws and Spectral Dynamics," in: Atmospheric Turbulence and Air Pollution Modeling, Nieuwstadt, F.T.M. and H. van Dop (eds.), D. Reidel, Boston, 37-68.

Tennekes, H. and J. L. Lumley, 1972: A First Course in Turbulence, (The MIT Press, Cambridge, Massachusetts).

Whiteman, C. D., K. J. Allwine, L. J. Fritschen, M. M. Orgil and J. R. Simpson, 1989: "Deep Valley Radiation and Surface Energy Budget Microclimates. Part 1: Radiation," Journal of Applied Meteorology, 28, 414-426

Wyngaard, J. C., 1984: "Boundary Layer Modeling," in: Atmospheric Turbulence and Air Pollution Modeling, Nieuwstadt, F. T. M. and H. van Dop (eds.), D. Reidel, Boston, 69-106.

Wyngaard, J. C., 1985: "Structure of the Planetary Boundary Layer and Implications for its Modeling," Journal of Climate and Applied Meteorology, 24, 1131-1142.

Wyngaard, J. C. and S. F. Clifford, 1978: "Estimating Momentum, Heat and Moisture Fluxes from Structure Parameters," Journal of the Atmospheric Sciences, 35, 1204-1211.

Yamada, T., 1976: "On the Similarity Functions A, B and C of the Planetary Boundary Layer," Journal of the Atmospheric Sciences, 33, 781-793.

Yamada, T., 1979: "Prediction of the Nocturnal Surface Inversion Height," Journal of Applied Meteorology, 18, 526-531.

Ye, Z. J., M. Segal, J. R. Garrett and R. A. Pielke, 1989: "On the impact of Cloudiness on the Characteristics of Nocturnal Downslope Flows," Boundary-Layer Meteorology, 49, 23-52.

Ye, Z. J., M. Segal, J. R. Garrett, M. Segal and R. A. Pielke, 1989: "On the Impact of Atmospheric Thermal Stability on the Characteristics of Nocturnal Downslope Flows," Boundary-Layer Meteorology, 51, 77-97.

Yu, Tsann-Wang, 1978: "Determining Height of the Nocturnal Boundary Layer," Journal of Applied Meteorology, 17, 28-33.

Zeman, O., 1979: "Parameterization of the Dynamics of Stable Boundary Layers and Nocturnal Jets, Journal of the Atmospheric Sciences, 36, 792-804.

DOCUMENT DISTRIBUTION LIST

No. of Copies	
15	Commander U.S. Army Biomedical Research and Development Laboratory ATTN: SGRD-UBZ-RA Fort Detrick Frederick, MD 21702-5010
3	Commander U.S. Army Medical Research and Development Command ATTN: SGRD-RMI-S (Ms. Mary Frances Bostian) Fort Detrick Frederick, MD 21702-5012
1	Commander U.S. Army Laboratory Command Army Research Office ATTN: SLCRO-GS (Dr. Walter Bach, Jr.) P.O. Box 12211 Research Triangle Park, NC 27709-2211
1	Battelle-Pacific Northwest Laboratory ATTN: Dr. Peter Van Voris P.O. Box 999 Richland, WA 99352
1	Commander U.S. Army Environmental Hygiene Agency ATTN: HSHB-ME-AA (Mr. Jeff Kirkpatrick) Aberdeen Proving Ground, MD 21010-5423
1	Commander Chemical Research, Development and Engineering Center ATTN: SMCCR-ST (Mr. Ron O. Pennsyle) Aberdeen Proving Ground, MD 21010-5423
1	Commander U.S. Army Atmospheric Science Laboratory ATTN: SLCAS-BA-M (Dr. Ron Cionco) White Sands Missile Range, NM 88002-5501
1	Commander Dugway Proving Grounds ATTN: STEDP-MT-M (James F. Bowers) Dugway, UT 84022-5000

1 Commander
U.S. Army Materiel Command
ATTN: AMSCG-5
5001 Eisenhower Avenue
Alexandria, VA 22333-2300

1 Commander
U.S. Army Materiel Command
ATTN: AMCEN-A
5001 Eisenhower Avenue
Alexandria, VA 22333-2300

1 HQDA
ATTN: DASG-PSP-E
5111 Leesburg Pike
Falls Church, VA 22041-3258

1 HQDA
ATTN: DAEN-RDM
20 Massachusetts Ave, NW
Washington, DC 20314-5000

1 Commander
U.S. Army Forces Command
ATTN: AFEN-FDE
Fort McPherson, GA 30330

1 Commander
U.S. Army Construction Engineering Research Laboratory
ATTN: CERN-EN
Champaign, IL 61820-1305

1 Commander
U.S. Army Training and Doctrine Command
ATTN: ATEN-FN
Fort Monroe, VA 23651